Integrated Design and Manufacturing of Thermoelectric Generator for Energy Harvesting

A Dissertation Presented
by

Gaosheng Fu

to
The Graduate School
in Partial Fulfillment of the
Requirements
for the Degree of

Doctor of Philosophy

in
Mechanical Engineering
Stony Brook University

May 2015

Stony Brook University

The Graduate School

Gaosheng Fu

We, the dissertation committee for the above candidate for the
Doctor of Philosophy degree, hereby recommend
acceptance of this dissertation.

Prof. Lei Zuo - Dissertation Advisor
Department of Mechanical Engineering

Prof. Jon Longtin – Committee Chair
Department of Mechanical Engineering

Prof. David Hwang – Committee Member
Department of Mechanical Engineering

Mr. James Kierstead – Outside Committee Member
Brookhaven National Lab

This dissertation is accepted by the Graduate School

Charles Taber
Dean of the Graduate School

Integrated Design and Manufacturing of Thermoelectric Generator for Energy Harvesting

by

Gaosheng Fu

Doctor of Philosophy

in

Mechanical Engineering

Stony Brook University

2015

Abstract: This dissertation addresses the critical issue of energy crisis by proposing thermal energy harvesting through thermoelectric materials and device. Thermoelectric generators are solid state devices that generate electricity under a temperature gradient. By using thermoelectric material, the wasted heat energy could be converted into electricity to increase vehicle fuel efficiency and to power sensors, depends on the quality and quantity of input heat energy. The scientific innovation is based on recent advance on various kinds of thermoelectric material and novel fabrication method to increase energy efficiency of different situations. The proposed thermal energy harvesting methods are realized in three applications in this dissertation.

Majority of the dissertation work is in automobile application. More than two thirds of the energy is wasted as vehicle exhaust and the average exhaust temperatures at highway driving cycle and city driving cycle are around 500~650 degree Celsius and 200~400 degrees Celsius. The proposed integrated design and manufacture of thermoelectric generator using thermal spray take advantages of environmental friendly and low cost magnesium silicide material. Magnesium silicide layers have been successfully synthesized by Atmospheric Plasma Spray and Vacuum Plasma Spray which has been shown to be an effective way to reduce thermal conductivity of material compared with conventional hot press method. The scientific highlights are 1) by comparing different thermal spray method, the VPS is identified to give best result due to limited oxidation and better microstructure; 2) the interface influence on the thermal conductivity, electrical conductivity and Seebeck coefficient has been intensively studied in this dissertation; 3) the prototype of flat geometry thermoelectric generator was fabricated using thermal spray method for the first time to demonstrate the ability of novel fabrication of TEG by thermal spray method.

In thin film thermoelectric application, filled skutterudite as the state of art high temperature thermoelectric material is investigated in this work. Yb filled CoSb3 skutterudite thin film has been synthesized using DC magnetron sputtering method. The results showed 30% of figure of merit is achieved compared to same bulk material.

In nuclear application, the designed energy harvester can still provide self-sustainable power to monitor the critical parameters of the nuclear power plant or fuel cycle facilities when a severe accident or massive loss of grid power happens. The commercial Hi-z TEG is used together with novel heat sink design to provide power for the wireless communication. The nuclear radiation including gamma, neutron and ion radiation effect on thermoelectric material, thermoelectric module and other electronic component has been intensively studied. Results show proper radiation shielding is need for TEG system during nuclear application.

TABLE OF CONTENT

TABLE OF CONTENT v

LIST OF TABLES ix

LIST OF FIGURES x

ACKNOWLEDGEMENTS xiv

1 INTRODUCTION 1

- 1.1 Background 2
- 1.2 Motivation 5
  - 1.2.1 Thermal energy harvesting from automobile exhaust 5
  - 1.2.2 Thin film thermoelectric 7
  - 1.2.3 Thermal energy harvesting from nuclear environment 8
- 1.3 Objective 9
- 1.4 Thesis Organization 11

2 LITERATURE REVIEW 12

- 2.1 Thermal Energy Harvesting and Application 12
  - 2.1.1 Automobile exhaust heat energy from automobile 12
  - 2.1.2 Thin film thermoelectric energy harvesting 26
  - 2.1.3 Thermal energy recovery in nuclear power plant 27
- 2.2 Popular Thermoelectric Materials 29
  - 2.2.1 Bismuth Telluride 29
  - 2.2.2 Magnesium silicide 31
  - 2.2.3 Iron disilicide 41
  - 2.2.4 Manganese silicide 45
  - 2.2.5 Filled skutterudite 48
  - 2.2.6 Others 51

3 MATERIAL PREPARATION AND CHARACTERIZATION 52

- 3.1 Thermal Spray Technology 52

3.1.1 Thermal spray principle 53
3.1.2 System overview 54
3.1.3 Plasma spraying 56
3.1.4 High velocity oxygen fuel spraying (HVOF) 59
3.1.5 Cold spray 60
3.1.6 Summary 61
3.2 Thin Film Technique 62
3.2.1 Physical vapor deposition (PVD) 62
3.2.2 Chemical vapor deposition (CVD) 63
3.2.3 Lithography 64
3.2.4 Etching 64
3.3 Background of Ionization Radiation 65
3.3.1 Gamma radiation 66
3.3.2 Neutron radiation 67
3.3.3 Ion beam radiation 68
3.4 Materials Characterization 69
3.4.1 X-ray diffraction (XRD) analysis, scanning electron microscopy (SEM) 70
3.4.2 Transmission electron microscopy (TEM) 73
3.4.3 Thermal conductivity measurement 74
3.4.4 Electrical properties measurement 76
3.4.5 Seebeck coefficient measurement 83
4 THERMAL SPRAY OF THERMOELECTRIC MATERIAL 89
4.1 Pre-experiment of Mg_2Si 89
4.1.1 Experiment 89
4.1.2 Results and discussion 90
4.1.3 Conclusion 94
4.2 Air Plasma Spray (APS) of Mg_2Si 94
4.2.1 Experiment 94
4.2.2 Results and discussion 96
4.2.3 Conclusion 102
4.3 Vacuum Plasma Spray (VPS) of Mg_2Si 103

4.3.1 Methods ... 103
4.3.2 RESULTS AND DISCUSSIONS ... 105
4.3.3 CONCLUSIONS ... 114
4.4 Thermal Spray of Fe2Si and Thermoelectric Property ... 114
4.4.1 Experiment ... 115
4.4.2 Results and discussion ... 115
4.4.3 Conclusion ... 115
4.5 Thermal Spray of Filled Skutterudite and Thermoelectric Property ... 116
4.5.1 Experiment ... 116
4.5.2 Results and discussion ... 117
4.5.3 Conclusion ... 119
5 DC-SPUTTERING OF FILLED SKUTTERUDITE ... 119
5.1 Experiment Methods ... 119
5.2 Results and Discussions ... 122
5.2.1 Phase composition of filled skutterudite thin film before and after heat treatment ... 122
5.2.2 SEM results of dc-sputtered filled skutterudite thin film samples ... 123
5.2.3 Thermoelectric properties of dc-sputtered filled skutterudite thin film samples ... 124
5.3 Conclusions ... 131
6 PRELIMINARY THERMOELECTRIC GENERATOR DESIGN AND OPTIMIZATION IN AUTOMOBILE APPLICATION ... 132
6.1 Integrated Design of TEG ... 132
6.1.1 Heat transfer modeling ... 132
6.1.2 Electrical resistance modeling ... 135
6.1.3 TEG module geometry optimization ... 136
6.1.4 Result and sensitivity analysis ... 138
6.1.5 Conclusion ... 143
6.2 Fin design and electric output power estimation ... 144
6.2.1 Basic heat transfer calculations ... 144
6.2.2 Fin design ... 147
6.2.3 Analytic solution of electric power output ... 148
6.2.4 FEA analysis and numerical results ... 149

6.2.5 Conclusion 151

7 THERMOELECTRIC GENERATOR APPLICATION AND RADIATION EFFECT IN NUCLEAR POWER PLANT........ 152

7.1 Overall Design 152

7.1.1 Design Challenges........ 153

7.1.2 Experimental Setup 155

7.2 Nuclear Radiation 157

7.2.1 Gamma and neutron radiation effect........ 158

7.2.2 Ion beam radiation effect 160

7.3 Design Guideline for Radiation Shielding 170

7.3.1 Gamma and X-rays Shielding design........ 171

7.3.2 Neutron shielding design 174

7.3.3 Alpha and Beta Particles shielding design 176

7.3.4 Shielding design guideline 177

8 CONCLUSION........ 178

8.1 Exhaust Heat Review 178

8.2 Thermal Spray of Magnesium Silicide 179

8.3 Thermoelectric Generator Model and Design........ 180

8.4 Thin Film Thermoelectric Material Fabrication 181

8.5 Radiation Influence on TEG Application in Nuclear Environment........ 182

9 FUTURE WORK........ 183

9.1 Thermal Spray of Other Materials 183

9.1.1 Filled skutterudite thermal spray........ 183

9.1.2 Higher manganese silicide and oxides 184

9.1.3 Oxides 185

9.2 Optimize Thin Film Filled Skutterudite Thermoelectric 185

9.3 Through thickness measurement........ 186

9.4 Thermoelectric Prototype Shielding Design in Nuclear Application........ 188

REFERENCE........ 189

LIST OF TABLES

Table 2-1 Characters of different driving cycles........13
Table 2-2 Exhaust gas temperature and gas flow rate[33]........22
Table 2-3 Perforce of an ambient temperature of 35 °C[34]........22
Table 2-4 Comparison of the information........25
Table 2-5 Properties of Mg_2Si/Ge/Sn [73]........32
Table 2-6 Electrical properties of Bi-doped Mg_2Si at 300K [79]........38
Table 2-7 Chemical components of C_O doped $FeSi_2$ powders [17]........42
Table 2-8 Plasma spraying conditions for FeSi2 [17]........43
Table 2-9 Maximum Void Occupancy in PureCoSb [73]........48
Table 4-1 Thermal spray parameters........90
Table 4-2 Concentrations of different composition in powder and coatings........92
Table 4-3 Plasma spray parameters........95
Table 4-4 Sample synthesis parameters and powder information.........95
Table 4-5 Hall Effect measurement of APS and hot press samples........99
Table 4-6 Plasma spray parameters........103
Table 4-7 Sample synthesis parameters and powder information........104
Table 4-8 Hall Effect measurement of hot press and VPS samples........109
Table 5-1 DC magnetron sputtering parameters........120
Table 5-2 Sample synthesis method and post process.........120
Table 5-3 Room temperature Hall Effect for 860nm thin film at different heat treatment temperature........125
Table 5-4 Room temperature Hall Effect for 1020K heat treated thin film at different thicknesses........125
Table 6-1 Parameters of the thermoelectric module........139
Table 6-2 Design Parameters of the Heat Exchanger........148
Table 7-1 Electricity requirement for each circuit component........153
Table 7-2 Core and steam generator inlet/outlet temperature in different SMRs........156
Table 7-3 Threshold of radiation for different electronic components........157
Table 7-4 Radiation level at different locations in nuclear plants........157
Table 7-5 electrical properties of N, P type material before and after radiation........160
Table 7-6 Sample synthesis method, ion fluence and displacements per atoms (dpa) based on SRIM-2008 calculation.........161
Table 7-7 Ion irradiation parameter, ion range, electronic and nuclear energy loss and the ratio of the ENSP as evaluated by full cascade calculation based on SRIM-2008........162
Table 7-8 Room temperature Hall Effect for two type thin film at different fluence........167
Table 7-9 Measured and predicted attenuation coefficients determined by photoelectric peaks (E. Bashandy, 1962)........172

LIST OF FIGURES

Figure 1.1 Thermoelectric generator conversion module [8] 5
Figure 1.2 Energy consumption for vehicle operation[9] 6
Figure 1.3 Integrated design and manufacturing of TEG (Courtesy of Prof. Lei Zuo) 10
Figure 2.1 Exhaust thermal power at FTP-75[26] 15
Figure 2.2 Temperature of exhaust gas measured in front of and behind the catalytic converter[26] 15
Figure 2.3 Engine exhaust temperature at NEDC[28] 16
Figure 2.4 Engine exhaust mass flow rate at NEDC[28] 16
Figure 2.5 Exhaust temperature and at NEDC [29] 17
Figure 2.6 Exhaust thermal power at NEDC [29] 17
Figure 2.7 Temperature of exhaust at HWFET and FTP72 driving cycle 18
Figure 2.8 Mass flow rate of exhaust at HWFET and FTP72 18
Figure 2.9 Exhaust temperature of a light duty truck at FTP72 driving cycle [30] 19
Figure 2.10 Exhaust thermal power of a light duty truck at FTP72 driving cycle [30] 20
Figure 2.11 Exhaust temperature at constant driving speed with different configuration [31] 21
Figure 2.12 Exhaust temperature at different engine load [33] 23
Figure 2.13 Mass flow rate in term of engine load and speed [35] 24
Figure 2.14 Phase Diagram of Mg_2Si (courtesy of *National Physical Laboratory*) 32
Figure 2.15 The comparison of the good thermoelectrics with the solid state solution under discussion[72] 33
Figure 2.16 Attritor mill used for mechanical alloying [75] 34
Figure 2.17 X-ray diffraction patterns for solid-state-reacted, mechanically alloyed and hot pressed (a) Mg_2Si (b) $Mg_2Si:Bi_{0.02}$ (c) $Mg_2Si:Sb_{0.03}$ (d) $Mg_2Si:Te_{0.03}$ (e) $Mg_2Si:Se_{0.02}$ [76] 35
Figure 2.18 Changes in the electrical conductivity of n-type $Mg_2Si:Xm$ with temperature [76] 35
Figure 2.19 Changes in the Seebeck coefficient of n-type $Mg_2Si:Xm$ with temperature [76] 36
Figure 2.20 Changes in the thermal conductivity of n-type Mg2Si:Xm with temperature [76] 36
Figure 2.21 Changes in the dimensionless-figure-of-merit of n-type with temperature [76] 37
Figure 2.22 Bi atom concentration (x) dependence of carrier concentration at 300K [79] 38
Figure 2.23 Electrical resistivity of Bi-doped Mg_2Si and non-doped Mg_2Si as a function of temperature [79] 39
Figure 2.24 Seebeck coefficient (S) of Bi-doped Mg_2Si and non-doped Mg_2Si as a function of temperature [79] 39
Figure 2.25 Thermal conductivity (k) of Bi-doped Mg_2Si and non-doped Mg_2Si as a function of temperature [79] 40
Figure 2.26 Dimensionless figure of merit (ZT) of Bi-doped Mg_2Si and non-doped Mg_2Si as a function of temperature [79] 40
Figure 2.27 Phase diagram of Fe-Si alloy [83] 42
Figure 2.28 Plasma spray-formed $FeSi_2$ thermoelectric device [17] 43
Figure 2.29 Thermoelectric power of spray-formed and hot press 5% Co doped $FeSi_2$. [17] 43

Figure 2.30 (a) Electrical conductivity; (b) thermal conductivity; and (c) Seebeck of Co-doped FeSi2 [19] 44
Figure 2.31 (a) Electrical conductivity; (b) thermal conductivity; and (c) Seebeck coefficient of Al-doped FeSi2 [19] 45
Figure 2.32 Relative figure-of-merit, Z, of plasma spray formed FeSi2 as a function of annealing time [19] 45
Figure 2.33 A schematic of half a unit cell of $Mn_{15}Si_{26}$ I: positions of Mn atoms; II: positions of Si atoms; III: positions of Mn and Si atoms [73] 46
Figure 2.34 Phase diagram of Mn-Si [84]... 46
Figure 2.35 Crystal structures of Nowotny chimney ladder (NCL) phases of manganese silicides and their comparison with the parent TiSi2 structure [86]... 47
Figure 2.36 Band structure of CoSb3. The dashed line indicates Ef [73]... 49
Figure 2.37 Band structure of the filled skutterudite CeFe4Sb12. The dashed line indicates Ef [73]........ 49
Figure 2.38 Carrier density vs. filling fraction for various filler ions. [73] 49
Figure 3.1 Principle of thermal spraying [109]... 53
Figure 3.2 Illustration of thermal sprayed coatings [109]... 53
Figure 3.3 Powder flame spray gun cross section (Courtesy of Steven)................................... 54
Figure 3.4 Wire/rod spray gun cross section (Courtesy of Sulzer company) 54
Figure 3.5 Diagram of electric arc wire spray (Courtesy of Sulzer company) 55
Figure 3.6 Diagram of plasma spray (Courtesy of U of Toronto) 56
Figure 3.7 Diagram of high velocity oxy-fuel spray (Courtesy of Steven Ort) 56
Figure 3.8 Plasma spray setup (Courtesy of Zircotec)... 57
Figure 3.9 Vacuum plasma spray (Courtesy of Matthias Zepper)... 59
Figure 3.10 HVOF sparying (Courtesy of Ruppex)... 60
Figure 3.11 The cold spray process (Courtesy of U.S. Army Research Laboratory) 61
Figure 3.12 Bragg's law [119]... 70
Figure 3.13 Principle of SEM (Courtesy of Purdue U).. 71
Figure 3.14 SEM facility (Courtesy of Susan)... 72
Figure 3.15 Principle of EDX (Courtesy of Muso).. 73
Figure 3.16 Measuring principle of thermal diffusivity by laser flash method [122]................ 74
Figure 3.17 Thermal conductivity testing machine.. 75
Figure 3.18 Thermal conductivity testing machine with pump 75
Figure 3.19 Van der pauw contact placement (Courtesy of Wikimedia Commons) 79
Figure 3.20 Van der Pauw method (Courtesy of Vladislav).. 80
Figure 3.21 Diagram of Hall Effect (Courtesy of George State U) 81
Figure 3.22 Hall Effect Measurement System 82
Figure 3.23 Four IV curves (Courtesy of Sbyrnes).. 83
Figure 3.24 CM460 Semi-Automatic Probe Station (Courtesy of Signatone)........................... 83
Figure 3.25 Seebeck testing machine with temperature controller 84
Figure 3.26 Lateral view of sample mounting 86
Figure 3.27 Oblique view of sample mounting.. 86

Figure 3.28 Vacuum pump of Seebeck testing system 87
Figure 4.1 XRD of APS (a) and VPS (b) coating 91
Figure 4.2 SEM of APS samples: a) R1961, b) R1962, c) B006 92
Figure 4.3 SEM of VPS samples: a) VPS003, b) VPS004, c) VPS101 93
Figure 4.4 Seebeck coefficient of un-doped Mg_2Si by a) APS and b) VPS 93
Figure 4.5 XRD of powder, hot press and thermal spray samples 96
Figure 4.6 SEM cross sections of APS and hot press samples 97
Figure 4.7 Thermal conductivity of Mg_2Si by APS and hot press 98
Figure 4.8 Electrical conductivity of Mg_2Si by APS and hot press 99
Figure 4.9 Seebeck of Mg_2Si by APS and hot press 100
Figure 4.10 ZT of Mg_2Si by APS and hot press 102
Figure 4.11 XRD of powder with nominal Mg ratio (P1), Mg-rich (P2) and VPS samples 105
Figure 4.12 SEM cross sections of VPS and hot press samples 106
Figure 4.13 Thermal conductivity of Mg_2Si by VPS and hot press 107
Figure 4.14 Electrical conductivity of Mg_2Si by VPS and hot press 108
Figure 4.15 Temperature dependent of hot pressed and VPS samples 110
Figure 4.16 Current-Voltage (IV) curve measurement of hot press and VPS samples at room temperature 111
Figure 4.17 Seebeck of Mg_2Si by VPS and hot press 111
Figure 4.18 Seebeck coefficient variation due to carrier concentration change at room temperature 112
Figure 4.19 . ZT of Mg_2Si by VPS and hot press 113
Figure 4.20 Thermal sprayed iron silicide (courtesy of Dr. Kentaro Shinoda and Prof Sanjay Sampath) 115
Figure 4.21 Vapor pressure of several element 116
Figure 4.22 SEM of skutterudite powder 117
Figure 4.23 XRD of as quenched powder, as sprayed and heat treated samples 117
Figure 4.24 Splat of as quenched powder by APS 118
Figure 4.25 Cross section of skutterudite coating by APS 118
Figure 5.1 XRD of DC magnetron sputtered filled skutterudite thin film and target with different heat treatment 122
Figure 5.2 EDS of as-sputtered filled skutterudite thin film on Si substrate sample Y1 123
Figure 5.3 SEM surface image of filled skutterudite thin film a) as deposited Y1 sample, b) 620K heat treated Y2 sample, c) 870K HT Y3 sample and d) 1020K HT Y4 sample 124
Figure 5.4 Electrical conductivity of 1020K heat treatment Yb doped CoSb3 thin film with different thicknesses 126
Figure 5.5 Seebeck of 1020K heat treatment Yb doped CoSb3 thin film with different thicknesses 127
Figure 5.6 Thermal conductivity measurement including a)TCR of Au and b) example of temperature oscillations, ΔT, measured in the 3 ω method at 300 K on the Yb doped CoSb3 film and the reference sample 128
Figure 5.7 Thermal conductivity of Yb doped CoSb3 film with different thickness with temperature dependent 129
Figure 5.8 Figure of Merit, ZT of Yb filled CoSb3 films with different thicknesses 130

Figure 6.1 Integrated design concept (courtesy of Prof. Lei Zuo) 132
Figure 6.2 Scheme of the TEG layers 133
Figure 6.3 thermoelectric couple in the system 133
Figure 6.4 Thermal resistance network of the TEG module 134
Figure 6.5 Optimal leg length for maximum power output 139
Figure 6.6 Optimal air gap for maximum power output 140
Figure 6.7 Sensitivity analysis of ceramic layer 140
Figure 6.8 Sensitivity analysis of inner exhaust pipe radius 141
Figure 6.9 Sensitivity analysis of electrical contact resistance 141
Figure 6.10 Influence of hot source temperature 142
Figure 6.11 Influence of heat sink temperature to optimal leg length 142
Figure 6.12 Different TE material influence on power output 143
Figure 6.13 Heat flow through a TEG 145
Figure 6.14 Thermal Resistance Network of TEG System 146
Figure 6.15 Diagram of cylindrical TEG System Cross Section 147
Figure 6.16 Example of Fin Design 147
Figure 6.17 Temperature Distribution of Pipe with TEG at Entrance End 150
Figure 6.18 Temperature Distribution of Pipe with TEG at Exit End 150
Figure 7.1 Operation during normal and off-normal conditions [8] 152
Figure 7.2 The enclosure for system circuits [8] 154
Figure 7.3 Temperature distribution along the test stand [8] 156
Figure 7.4 Thermal conductivity of N,P type material before and after gamma radiation. 159
Figure 7.5 XRD of Bi2Te3 (left, a) and Sb2Te3 (right, b) thin film before and after ion beam irradiation shows an irradiation-induced reorientation and enhancement of crystallinity as the ion fluence increases 163
Figure 7.6 TEM of Bi2Te3 a) before radiation N0, b) after radiation N3 and Sb2Te3 c) before radiation P0, d) after radiation P3 164
Figure 7.7 Electrical resistivities of Bi2Te3 (a) and Sb2Te3 (b) thin film after bombardment decrease to some extent and then increase after the ion fluence of $5x10^{15}$/cm2 166
Figure 7.8 Room temperature electrical conductivity for Bi2Te3 and Sb2Te3 samples at various ion fluences 167
Figure 7.9 Seebeck of Bi2Te3 (a) and Sb2Te3 (b) thin film before and after bombardment 168
Figure 7.10 Room temperature PF of Bi2Te3 and Sb2Te3 thin film increases when ion fluence increases and the peak achieves between 1 and $5x10^{15}/cm^2$ 169
Figure 7.11 Half Value Layer Thickness for Shielding Materials Using a Cobalt 60 Source (courtesy of W. J. Quapp) 173
Figure 9.1 EDX of as-sprayed skutterudite 184
Figure 9.2 In plane electrical conductivity of Mg2Si by APS 187
Figure 9.3 Through thickness electrical conductivity of Mg2Si by APS 187

ACKNOWLEDGEMENTS

First of all, I would like to give my most sincere thanks to my advisor, Prof. Lei Zuo, who pointed out a bright path on my long research journey. I won't forget the first time I talked with him and how he impressed me on the research. He gave me a second chance to continue my PhD career at Stony Brook University and my real research work started when I joined his group. Prof. Zuo always tells us we are as smart as people in MIT, the only difference is they are working harder. Another important character I learned from him is he never gave up and he questions everything.

Second, I must thank my wife, Qin Wei, who gives me meticulous care and consistent encouragement. I still remember those somber days that I fought alone. It's her accompany and support that bring me endless power to do better on research. Also, it's her love and dedication that make me never surrender during struggling days.

Third, I would like to thank my parent and my younger uncle who supported and loved me for more than 20 years. Without their caring, I can never be so lucky and I am glad they are proud of me and I will never let them down.

I would like to thank Prof. Richard Gambino, Prof. Jon Longtin, Prof. David Hwang, Dr. Ming Lu and Mr. James Kierstead to serve on my thesis committee. Their knowledgeable insights and suggestions greatly enrich my thesis. Special thanks go to Prof. Sanjay Sampath from SBU, Michael Heibel from Westinghouse, Prof. Jie Lian from RPI, Yongqiang Wang from Los Alamos National Laboratory and Robert Willson from VPS company for the valuable discussions.

I also want to thank Drs. Jim Quinn, Vladimir Samuilov, Fernando Camino, Kim Kisslinger and Fuxing Ye for help with experiments and samples of this project.

I would like to thank Drs. Xiaoya Shi, Yikai Chen who have worked or helped with me on the projects and all the team members from Prof. Zuo's lab. Those moments spent together will be my best memories. In addition, I would like to thank Prof. Yu Zhou who gave me the chance to come to study in United States.

This thesis research is partially supported by NSF/DOE Thermoelectrics Partnership of NSF Grant #1048744, NYSERDA Contract 21180, the DOE Nuclear Engineering University Program (NEUP) CFP-13-5479 and CFP-12 3331.

1 INTRODUCTION

Thermoelectric generators (TEG) are devices that can directly convert heat into electricity without any moving parts. TEGs could potentially benefit the thermodynamic systems and increase overall efficiency when used in waste heat recovery applications. The absence of moving parts, modular capabilities and wide range of working temperatures makes thermoelectric generators attractive for energy generation applications. They have been considered for application on, power plant waste heat recovery, vehicle exhausts and other energy recovery from wasted heat in thermodynamic cycles. Until recently, thermoelectric devices have been only used by niche applications because of their low efficiencies, expensive materials and time consuming manufacturing process. As better materials are developed, and module efficiencies increase, an efficient synthesis method is desirable to reduce manufacturing time and cost to optimize potential electrical power generation applications. Extensive research has been done on synthesis of thermoelectric material, such as hot press, spark plasma sintering, vertical Bridgeman method and solid state reaction. But most of these methods are either time consuming or could not provide large amounts for industrial application.

For automobile application, as a flexible, industry-scalable and cost-effective manufacturing process, thermal spray has been traditionally used for protective barrier coating. Thermal spray has a very high quenching rate (10^6-7 K/sec) similar as the melt spinning which may improve the thermoelectric properties. An integrated design and manufacturing of thermoelectric devices on the exhaust system using thermal spray has been proposed in this thesis. As an innovative technology for thermoelectric material synthesis, thermal spray including atmospheric plasma spray (APS) and vacuum plasma spray (VPS) has been investigated for the feasibility of synthesis thermoelectric material like magnesium silicide, iron silicide and skutterudites. This thesis focus on the parameters for thermal spray that influence thermoelectric property and characterization of thermal sprayed thermoelectric material is compared with traditional hot press method.

For thin film application, as the size and power density requirements are dramatically changing for electronics, conventional bulk thermoelectric technology will lose its advantages for the microelectronics applications. Conversely, thin film thermoelectric modules focused on localized temperature control as well as self-sustained power generation. These thin film thermoelectric modules take the advantages of semiconductor processing techniques to create a nano-structured thermoelectric thin film. As the Internet of Things (IoT) develops, more embedded thermoelectric energy harvesting modules are needed for a variety of applications due to its advantage of compactness and free of maintenance compared with using regular battery.

In nuclear power plant application, accidents (Chernobyl, Three Mile Island, and Fukushima Daiichi) have casted a shadow on the history and future of nuclear power. Safety thus rightfully remains an enormous concern in the development and operations of nuclear power plants and fuel cycles. In the Fukushima event, one major concern was a total loss of power at the plant, leading to catastrophic failure of reactor systems and loss of coolants. As a result, sensing and actuation systems stopped working. Increasingly research is going on recently to develop thermoelectric-driven sensing technologies to power sensor and communication packages in the event of massive power loss.

1.1 Background

Thermoelectric devices are solid state devices that generate electricity under a temperature gradient of the thermoelectric device. Thermoelectric devices are based on the Seebeck Effect [1] and Peltier Effect [2]. The Seebeck Effect governs the operation of each thermoelectric device which contains two different thermoelectric materials. These are arranged electrically in series and thermally in parallel. The junctions of the dissimilar conductors are kept at different temperatures which introduces an open circuit voltage V_{oc} as follows:

$$V_{oc} = S\ (T_H - T_C) \tag{1.1}$$

Where S is the difference in Seebeck coefficient of the two thermoelectric materials and has the units of V/K, and T_H and T_C are the absolute temperatures of hot and cold side which are in Kelvin. This effect was observed firstly by Thomas Johann Seebeck, a German physicist in early 1800s. When an electric load is applied in the system, electric current is generated by the temperature gradient. Almost in the same time period, French physicist Jean Charles Athanase Peltier made an independent discovery on Seebeck effect. Peltier Effect was discovered in 1834 by Jean Peltier which was the reverse effect of the Seebeck. When passing current through the dissimilar conductor, one side can be heated or cooled, depending on the direction of current. The Peltier coefficient, Π, is defined as the ratio of the rate of heating or cooling to the electrical current passing through the junction, as

$$\Pi = \frac{1}{I}\frac{\delta Q}{dt} = ST \qquad (1.2)$$

Where δQ/dt is the heat flow per unit time and I is the electrical current. Depending on current direction, heat can be absorbed or released at the junction of two conductors. Thomson Effect [3] was observed in 1851 by Thomson. Thomson predicted the cooling or heating of a homogeneous conductor will result from the flow of an electrical current when posing a temperature difference. Thomson coefficient β is defined as the rate of heat transferred per unit of temperature gradient per unit of current. The rate of heat transferred, Q_β, also known as Thomson heat, in a uniform conductor is proportional to the electrical current. Below is the relation:

$$dQ_\beta = (\int \beta dT)\, Idt \qquad (1.3)$$

The Thomson effect relates the Seebeck and Piltier coefficients. Thermoelectric power generation based on the Seebeck effect [1] and refrigeration based on Peltier effect [2] are two possible application of thermoelectric material. Figure 1.1 shows the thermoelectric energy conversion module. In the power generation mode, where the Seebeck effect is equipped, temperature difference is applied at one side of the device. As a result, a voltage is generated across the thermoelectric device that can be used to convert part of the heat into electrical power. The Peltier effect is the reverse effect of the Seebeck. In the refrigeration mode, in which the Peltier effect is operated, an external electric source forces the electrons and holes move away from the cold side of the module for cooling. The heat absorption or dissipation may create a temperature gradient in the system depending on its thermal resistance. The factor determines how efficient thermoelectric material is the thermoelectric figure of merit ZT. It characterizes the effectiveness of a specific thermoelectric material in terms of its electrical and thermal material properties. The figure of merit is expressed as

$$ZT = \frac{S^2\sigma}{\kappa}T \qquad (1.4)$$

Where σ is the electrical conductivity, κ is the thermal conductivity, and T is the absolute average temperature of the device. The thermal conductivity comes from two parts: electrical contribution κ_e and lattice contributionκ_L, which is shown as

$$\kappa = \kappa_e + \kappa_L \qquad (1.5)$$

The electrical conductivity and electronic thermal conductivity are correlated via the Wiedemann-Franz relationship

$$L = \frac{\kappa}{\sigma T} \tag{1.6}$$

Here, people usual choose the Lorentz number L = $2.44*10^{-8}V^2K^{-2}$. Researchers investigated extensively on how to improve ZT by minimizing κ_L while preserving electrical conductivity and Seebeck coefficient. ZT for materials has remained below unit for decades but in recent years, ZT of new materials has reached values greater than two. These increases in the figure of merit are a result of studies in supperlattice or nanostructures of thermoelectric materials [4-6].

$$\sigma = \mathrm{ne}\mu \tag{1.7}$$

For single carrier type, homogenous, and isotropic material, the electrical conductivity is given by carrier concentration n, carrier mobility μ and electron charge e shown in equation 1.7. Carrier concentration and mobility can be characterized using hall measurement system by measure hall coefficient R_H. For electron as main carrier, the hall coefficient is

$$\mathrm{R_H} = -1/\mathrm{ne} \tag{1.8}$$

Compare Hall Effect coefficient and electrical conductivity, electron mobility μ can be expressed as follow

$$\mu = -\sigma \mathrm{R_H} \tag{1.9}$$

The Seebeek coefficient is defined in several different ways depending on the situation. A common definition from Busch and Winkler [7] is given below for n-type thermoelectric material with

$$\mathrm{S} = -\,\mathrm{k/e}\,(5/2 + \mathrm{r} + \ln \mathrm{N_c/n}) \tag{1.10}$$

Here k is Boltzmann constant, r is exponent of the power function in the energy-dependent ($\tau=\varepsilon^r$) relaxation time expression, and N_c is the effective density of states in the valence band. Seebeck coefficient is affected by carrier concentration.

Modules consist of a group of thermoelectric semiconductor legs, connected electrically in series and thermally in parallel as is shown in Figure 1.1. The ends of the leg pairs are typically connected by a conductor, ex Cu. On top of these conductors an electrically insulating but thermally conductive material (ex, AlN, ten times higher thermal conductivity than Al_2O_3, BeO has an even higher conductivity however it’s toxic) is attached to prevent electrical shorting of the leg pairs.

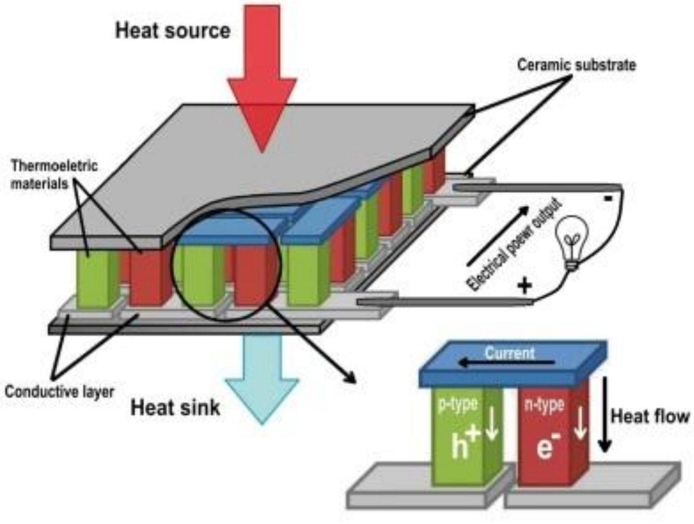

Figure 1.1 Thermoelectric generator conversion module [8]

1.2 Motivation

1.2.1 Thermal energy harvesting from automobile exhaust

In automobile exhaust application, people are trying to improve thermoelectric devices in their efficiencies and power outputs for most effective operating conditions. As these advances are made, applications for these devices need to be explored. Their implementation into industry could lead to a success of power recovered from waste heat in a lot of different applications. Turbine and compressor exhausts, manufacturing plants, power utilities and automobile exhausts are prime examples of applications that could benefit from a thermoelectric system. Most of these systems use nonrenewable resources as their source of fuel either directly or indirectly.

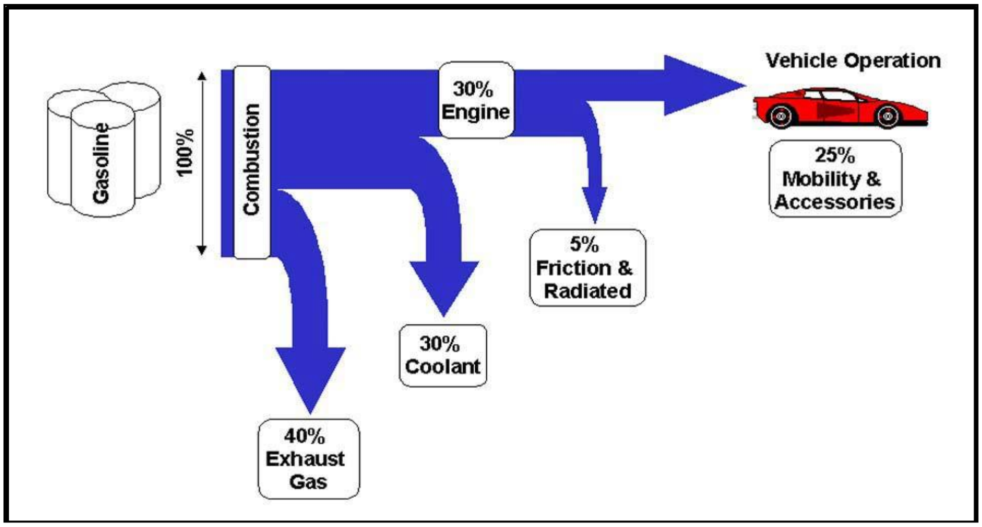

Figure 1.2 Energy consumption for vehicle operation[9]

Figure 1.2 indicates at least 40 percent of the energy is wasted as engine exhaust [9]. Exhaust also contaminates environment, so lots of organizations regulate the emission of vehicles based on their size and usage. Various measures have been taken to make use of the exhaust heat of vehicles, for example Rankine cycle [10], mechanical turbocharger [11], electric turbocharger [12] and thermoelectric generator [13], so as to reduce the emission and provide some amount of driving power to vehicles. Besides, absorptive refrigeration uses a source of heat to provide the energy needed to drive the cooling process. All of these method calls for the information about the engine exhaust, including heat quantity and heat quality. The amount of heat energy, temperature and mass flow rate of the exhaust are essential information for the materials, components, and devices research of thermoelectric generators. As a solid state energy converter, the thermoelectric generators (TEG) show great promise in vehicle engine exhaust energy recovery. As DOE report indicated, 350-390 watts of electricity recovery can provide 3 and 4% fuel efficiency improvement for a truck Chevy Suburban and a BMW sedan[14].

The successful development of thermoelectric generators (TEGs) for automotive applications requires advances on several fronts: (a) abundant, low cost, and high-ZT thermoelectric (TE) materials, (b) industry scalable material synthesis and device fabrication process, and (c) cost efficient and reliable integration into existing vehicle systems. An innovative approach is proposed to address all of these challenges. Recent investigations by one of the team members at BNL demonstrated that thermoelectric and mechanical performance of filled skutterudites and Mg_2Si can be significantly enhanced by non-equilibrium synthesis, such as melt-spinning followed by spark plasma synthesis (SPS) or hot pressing

[15]. Equally important is the manufacturing process required to fabricate TEGs for vehicle applications that are reliable, inexpensive, and perform well. This presents a novel fabrication process based on thermal spray that can fabricate layered, patterned mesoscale structures conformally (non-flat) and directly onto exhaust components to fabricate complete TEG devices. Thermal spray technology and its recent innovations, namely direct writing and laser micromachining offer new avenues for integration. Recent work in Japan and Germany has also shown that silicide thermoelectrics are feasible for thermal spray-based fabrication and assembly [16-19]. The similarities in quench rates between melt spinning and thermal spray should allow preservation of the quenched non-equilibrium nanostructures required for improved ZT over bulk values as demonstrated by the groups mentioned above. However, we need to investigate the thermal cycle effect on thermoelectric properties for these materials prepared with rapid quench method.

1.2.2 Thin film thermoelectric

In thermoelectric device applications a high value of the figure of merit (ZT) is desirable for greater efficiency. For thermoelectric devices, a ZT value of above 3 or 4 at the room temperature is required to be competitive with the conventional methods. For the thermoelectric applications Bi2Te3has become a material of particular interest, since it gives the highest ZT value of 0.68 at room temperature in its bulk form. It has been predicted that low-dimensional topologically protected modes in line dislocations can significantly increase ZT. Many different approaches have been proposed and attempted to improve the thermoelectric performance of Bi2Te3, namely, by suppressing the lattice thermal conductivity by tuning carrier concentration, by engineering the band structure, and by reducing the device dimensionality. The recent reports of the mechanical exfoliation and growth of quintuple layers of Bi2Te3 and Bi2Se3 motivate this study and underscore the importance of developing thermoelectric properties of thin films. In thin film application, superlattice thermoelectric technologies in the Bi2Te3 material system can potentially enable efficient thermoelectric refrigeration and air conditioning using high cooling power density superlattice devices as well as lead to compact power conversion devices. People discussed the state of the art in these materials and highlight the state of transition of these materials into device prototypes for both cooling and power conversion. A ZT of 1.4 in fully fabricated p–n couples, using p-type Bi2Te3/Sb2Te3 and n-type Bi2Te3/Bi2TexSe3 superlattices has been reported, from heat-to electrical power conversion efficiency measurements. The concept denoted as high active-flux has been developed and validated for the use of the high active heat-flux (200 to 2500 W/cm^2) superlattice devices, with relatively simple heat-exchanger systems, and is applicable for both cooling and power conversion. Superlattice cooling modules with cooling power densities in excess of 150 W/cm2 at the module level have been demonstrated. The transitioning of high ZT of thin-film materials to improvements in cooling performance has involved solving a series of issues related to the intrinsic superlattice thermoelectric couple as well as optimizing several electrical and thermal interfaces within the p– n couple and between the couple and external interfaces.

Heat also plays crucial role limiting current electronic device development. In this work, the proposed thin film thermoelectric will be used to solve the heat management problem by convert thermal energy from the “hot spot” to electricity. On the other hand, the developed thin film thermoelectric material can be used as localized cooling element for some electronic components. The scientific motivation of thin film work lies on the recent popular on low dimensional material and device. The low dimension structures as well as the interfaces influence on the overall thermoelectric properties are the main concern of thin film thermoelectric work. Another topic associated with thin film thermoelectric is suppressing of the phonon transport for low dimensional thermoelectric material. This dissertation targets to explore the relationship between thin film thickness and thermal properties of thin films. There is lots of interesting and promising phenomenon at low dimensional scale, surely the thermoelectric material will be no exceptional and this work will present the findings form the proposed thin film thermoelectric work.

1.2.3 Thermal energy harvesting from nuclear environment

In nuclear application, energy harvesting and wireless communication provide a promising opportunity to revolutionize nuclear sensors and instrumentations and to benefit reactor design and fuel cycle facilities by reducing the cost of power, wiring and signal transmission or eliminating battery replacement. More importantly, when a severe accident or massive loss of grid power happens, the energy harvester can still provide self-sustainable power to monitor the critical parameters of the nuclear power plant or fuel cycle facilities.

Several recent studies have reported on the radiation effect on thermoelectric material, thermoelectric module and related power electronics. Back to 1960s, Corelli et al [20] reported the radiation from the spent fuel can affect the physical properties of the thermoelectric materials, which then influence the power production from the TEG. At 1961, Kilp et al [21] reported, when the thermoelectric material was irradiated at reactor ambient temperatures, increase of electrical resistivity and Seebeck coefficient but overall reduction of the power factor. Carstens et al [22] reported gamma radiation effect on the commercial Hi-Z modules which use bismuth telluride based alloy and DC-DC converters. The results showed that TEG is not affected by gamma radiation at a dose rate of 170 Rad/min; while DC-DC converter cannot operate normally at the presence of gamma radiation. Up to now, few researchers studied neutron radiation effects on thermoelectric material. However, high neutron dose radiation test is not practical due to limited neutron irradiation access as well as the complexity of post irradiation testing. As an alternative investigation method, ion radiation has been used to simulate the neutron radiation effect especially for displacement damage.

1.3 Objective

For automobile exhaust application, we present an integrated effort to make transformative advances in low cost thermoelectric materials coupled with novel design, fabrication and assembly. The strategy involves device integration directly onto exhaust components enabling robust, durable performance. Furthermore the flexibility of thermal stray approach allows for depositing on conformal (non-flat) surfaces, allowing the use of traditional round exhaust components and for the design of novel conformal TEG devices, as shown in Figure 1.3.

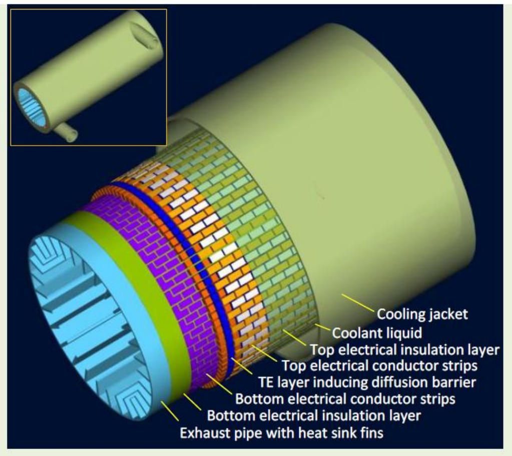

Figure 1.3 Integrated design and manufacturing of TEG (Courtesy of Prof. Lei Zuo)

As shown in figure 1.3, we propose to directly fabricate thermoelectric generator on exhaust pipe by thermal spray method. For the isolation part, laser micro-machining will be involved. On the exhaust pipe, the first layer is bottom electrical insulation layer, then bottom electrical conducting layer, then thermoelectric layer. On top of n/p type thermoelectric layer, there will be another conducting and insulation layer. In order to reduce the cold side temperature, a cooling jacket is added into the system. To date, in most vehicle TEG approaches, flat, prefabricated modules are placed in contact with a custom exhaust component/heat exchanger to provide waste heat for the devices. While impressive gains have been made with this approach, and proof-of-concept vehicles have been showcased [23], high-volume, low cost, and high-reliability TEG devices still require innovative approaches for wide spread adaptation on production vehicles. The proposed single step, integrated strategy involving non-equilibrium synthesis, 3D conformal deposition and rapid formation of patterned structures is potentially game-changing, and is very suitable for large scale waste heat TEG applications. Our unique approach to the materials development and deposition provides, in turn, new processing opportunities that provide for new system level. The results in an innovation cascade in which all facets of the research development benefit from advances in previous steps: materials to synthesis then device design and followed with thermal analysis and device fabrication. Our approach also favors TE materials that are proven, plentiful, inexpensive, and well characterized versus high-performance but rare, expensive, difficult to produce and manufacturing intensive materials. To compliment this approach, our process is ideally suited for high volume manufacturing, and is readily scalable. Although the absolute performance may not be as high as more exotic superlattice materials [6], larger exhaust system areas can be outfitted with our TEGs and at much lower cost, with the end result that total electricity production can exceed that of the traditional approach of using high-cost, high-ZT modules. Indeed the overarching goal of the proposed approach is to provide a pathway for large-scale, low-cost, mass production of TEGs for automotive systems.

For thin film application, we are targeting of preparation of Yb filled skutterudite thin film growth using DC magnetron sputtering and measurement of thermoelectric properties including thermal conductivity, electrical conductivity, Seebeck coefficient and figure of merit are reported from room temperature to 700K. The selection of using DC magnetron sputtering lies in its high deposition rate as well as it can maintain the target material composition.[24] More importantly, magnetron sputtering provides dense microstructure which surpasses most of other thin film deposition techniques.[25] The parameters of DC magnetron sputtering and post heat treatment on sputtered sample have been optimized experimentally and Yb filled CoSb3 has first time been successfully deposited using sputtering and characterized comprehensively. From the thin film filled skutterudite deposition, a good thermoelectric as well as robust fabrication parameter is desirable in this work.

For nuclear power plant application, the objective is to develop a self-powered sensing and actuation system that is powered by intrinsic heat from reactor components. The key concept is to use thermoelectric generators that can be integrated directly onto key nuclear components, including pipes, pump housings, heat exchangers, reactor vessels, and shielding structures, as well as secondary-side components. The package will include a thermoelectric generator (TEG), microcontroller, signal processing, and a wireless radio package, and will be environmentally hardened to survive radiation, flooding, vibration, mechanical shock (explosions), corrosion, and excessive temperature. The energy harvested from the intrinsic heat of reactor components can power sensors, provide bi-directional communication, recharge batteries for other safety systems, and actuate valves, pumps, and other devices when all other power sources are unavailable. Such an approach is intrinsically fault tolerant: in the event that system temperatures increase, the amount of available energy will increase, which will make more power available for applications. The system can also be used during normal conditions to provide enhanced monitoring of key system components.

1.4 Thesis Organization

This thesis presents thermoelectric material fabrication as well as its application in automobile exhaust recovery, thin film and nuclear power plant situations. Section 2 compiles the information of literature on thermal energy harvesting and application in automobile exhaust, thin film and nuclear power plant and popular thermoelectric materials people has been using. Section 3 introduces sample preparation using thermal spray, thin film technique, nuclear radiation process as well as characterization method. Section 4 explains in detail about the experiment procedures and thermoelectric properties of thermal sprayed samples including silicide and skutterudite. Section 5 discusses about dc-sputtering of filled skutterudite thin film preparation and thermoelectric results. Section 6 talks about optimization of device geometry parameter and estimation of the electric output based on optimal thermoelectric material in automobile application. Section 7 summarizes the design of thermoelectric generator and nuclear radiation effect on material/device in nuclear power plant application. Section 8 concludes the thermoelectric material fabrication and overall application. Section 9 discusses some future work that will improve our thermal sprayed thermoelectric material.

2 LITERATURE REVIEW

2.1 Thermal Energy Harvesting and Application

2.1.1 Automobile exhaust heat energy from automobile

This part aims at a review of heat quantity and heat quality of different size vehicles in various driving conditions. Section 2.1.1 introduces the standard driving test cycles in US and Europe. Section 2.1.2 presents the heat quantity and quality profile including detailed information about the vehicles and driving conditions. Section 2.1.3 draws some general conclusion of the engine exhaust based on this survey.

2.1.1.1 Driving cycle

Vehicles produce various kinds of engine exhaust when driving at different driving cycles. According to EPA, the typical US driving cycles are FTP-72 (federal test procedure), FTP-75, SFTP-

US06 (Supplementary federal test procedure), HWFET (Highway Fuel Economy Test), and FTP transient. Besides, the NEDC (New European Driving Cycle) is widely used, which consists of four repeated ECE-15 driving cycles and an extra-urban driving cycle. In this standard driving cycle, detailed test procedures are illustrated including cold start phase, transient phase, hot start phase and the duration for each phase as well as for idle. Table 2-1 list those popularly used driving cycles in the emission test and engine exhaust test.

Table 2-1 Characters of different driving cycles

Cycle	Test condition	Duration (s)	Distance (mi)	Aver. Speed (mph)	Maxi. Speed (mph)
FTP-72	Urban	1369	7.5	19.6	56.7
FTP-75	Urban, aggressive	1874	11.04	21.2	56.7
SFTP-US06	Aggressive	596	8.01	48.4	80.3
HWFET	Highway	765	10.26	48.3	60.0
Transient	Highway	1200	6.4	18.6	N/A
ECE-15	urban	195	0.6	11.6	31.1
EUDC	suburban	400	4.3	38.9	74.6

According to Table 2-1, each driving cycle has its own focus. To represent a practical automobile on the road, one usually needs to combine some of these test procedures. They are not simply categorized as urban driving cycles or highway driving cycles, and sometime whether they use AC or not should be considered. So later in the analysis of the vehicle engine exhaust, the specific driving conditions should be taken into account.

2.1.1.2 Exhaust of engine

Engine exhaust mainly depends on the size of the vehicle since heavy duty vehicles consume more fuel. The amount of heat that can be converted to electricity plays crucial role in the thermoelectric generators. Since the size of the vehicle varies, the electricity needed for basic usage, like spark ignition, and the need for the optional usage, like HVAC is quite different. In this case, it’s necessary to examine the engine exhaust according to the vehicle size. The exhaust temperature varies at different locations. Generally speaking, after the catalytic converter the temperature decreases as the gas flows along the pipe to its tail. But catalytic converters require a gas stream of certain temperature for operation. Too much heat extraction from upstream of catalytic converter leads to increased pollution. Actually, the difference between before and after the catalytic converter is not obvious, because it depends on the engine load and engine speed.

2.1.1.3 Mid-sized sedan

A mid-size sedan is referred to equal to or greater than a compact in North America. BMW research group has presented the engine exhaust profile at the 2005 DEER conference at Chicago. The selected vehicle platform is BMW 530i, MY2006 which has an inline six cylinder engine with 3.0L displacement. The test cycles are FTP-75 and NEDC. Figure 2.1 shows the exhaust thermal power for FTP-75 test cycle[26] and one can find the average thermal power is around 7KW.

The temperature test is based on different engine load and speed which is shown in Figure 2.2. P1 is the measured point in front of catalytic converter and P2 is the one behind. The test engine speeds are 1000, 3000 and 6000 RPM which are indicated in different colors in Figure 2.2. At low engine load or speed, the temperature goes up at both P1 and P2 if engine speed and load increases. However, the temperature doesn’t change much before and after the catalytic converter as shown in figure 2.2.

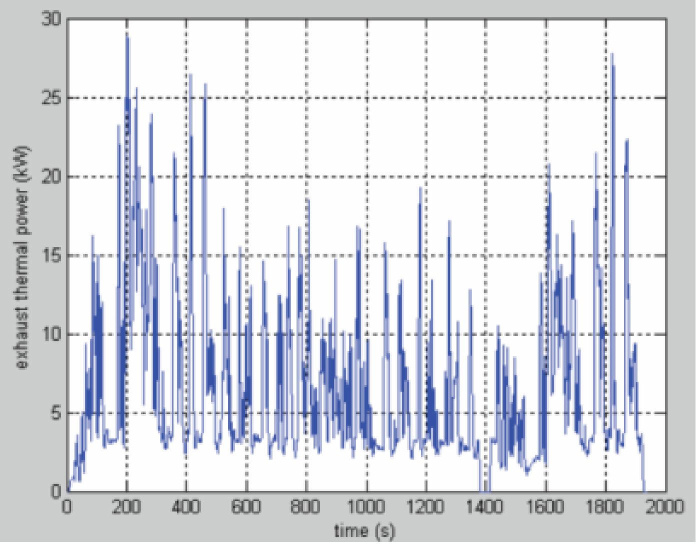

Figure 2.1 Exhaust thermal power at FTP-75[26]

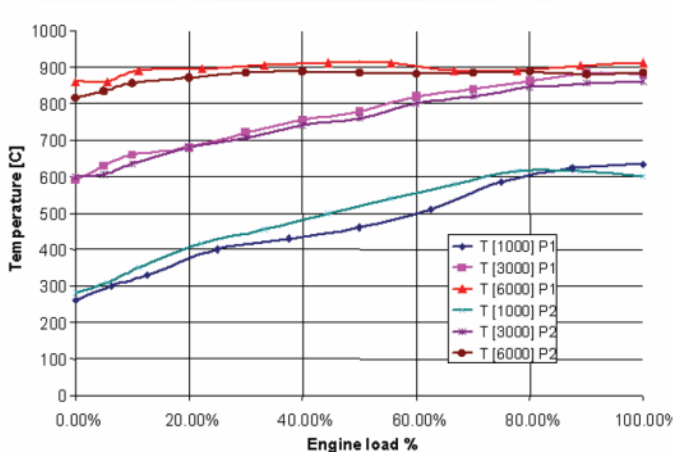

Figure 2.2 Temperature of exhaust gas measured in front of and behind the catalytic converter[26]

The other test is NEDC driving cycle which was presented in 2011. The exhaust thermal power is 3.8KW[27]. The exhaust temperature and mass flow rate is shown in figure 2.3. The temperature ranges from 300 to 580 Celsius degree.

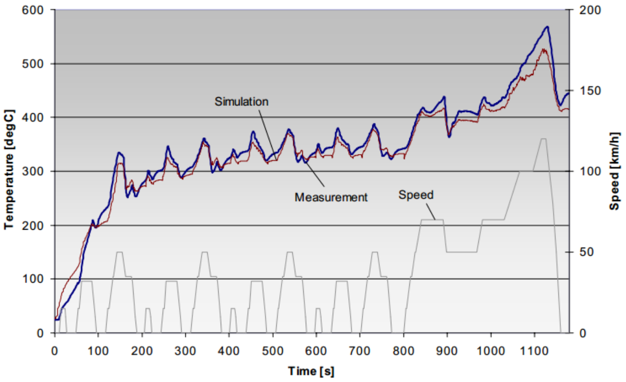

Figure 2.3 Engine exhaust temperature at NEDC[28]

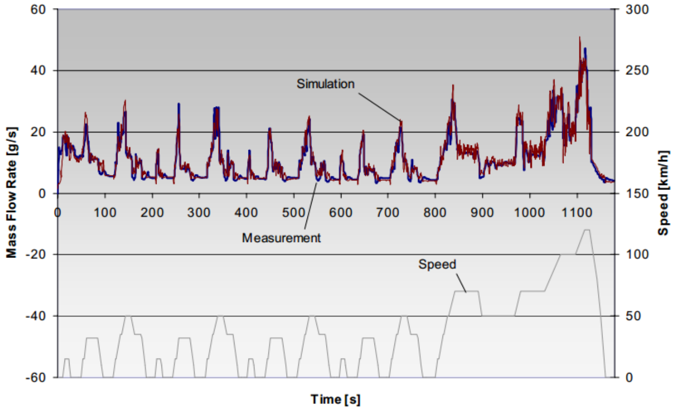

Figure 2.4 Engine exhaust mass flow rate at NEDC[28]

Nissan Research Center tested the exhaust based on Nissan Quasqai1.5 L diesel vehicle at NEDC driving cycle[29]. The temperature of the exhaust at this driving condition is shown below in Figure 2.5. In these figures, the temperature was recorded at points 1-4 (reading from top to bottom). The four temperature measurement points are 1) the engine exhaust manifold, 2) after the catalytic converter, 3) at the silencer box and 4) at the exhaust tail. The temperature is not very high since the engine is just 1.5 L.

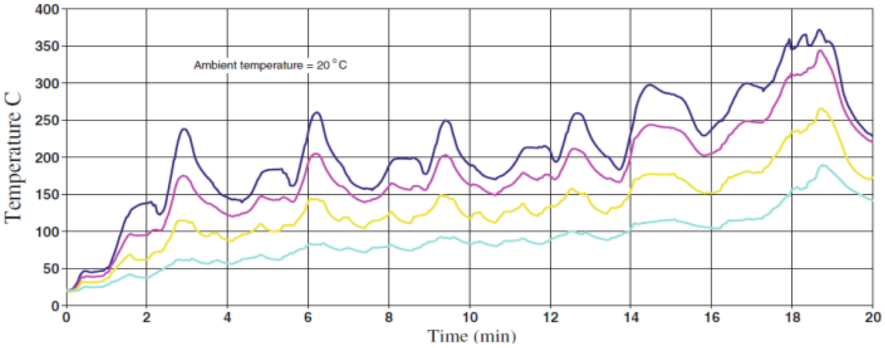

Figure 2.5 Exhaust temperature and at NEDC [29]

Figure 2.6 shows the exhaust thermal power of Nissan vehicle at NEDC. The average exhaust energy for the urban cycle is 1.5KW and for Ex-urban cycle is 7KW. All the measurements were conducted at an ambient temperature with 20 Celsius degree.

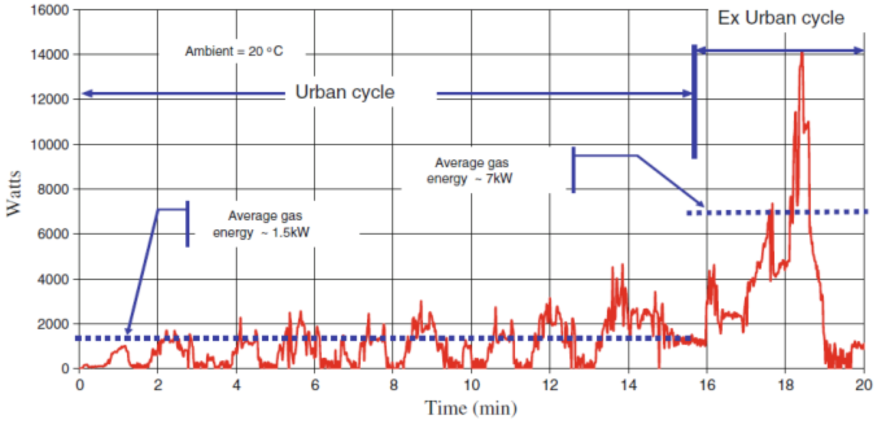

Figure 2.6 Exhaust thermal power at NEDC [29]

Another vehicle manufacture company provides their measurement data of temperature and mass flow rate of the exhaust. Figure 2.7 shows the temperature of the exhaust at HWFET and FTP72 driving cycles. FTP72 is an urban driving test which lasts longer. The temperature ranges from 550 to 800 and 550 to 850 degree C at HWFET and FTP72 respectively. It’s on a hot start, so the temperature begins around 550 degree C.

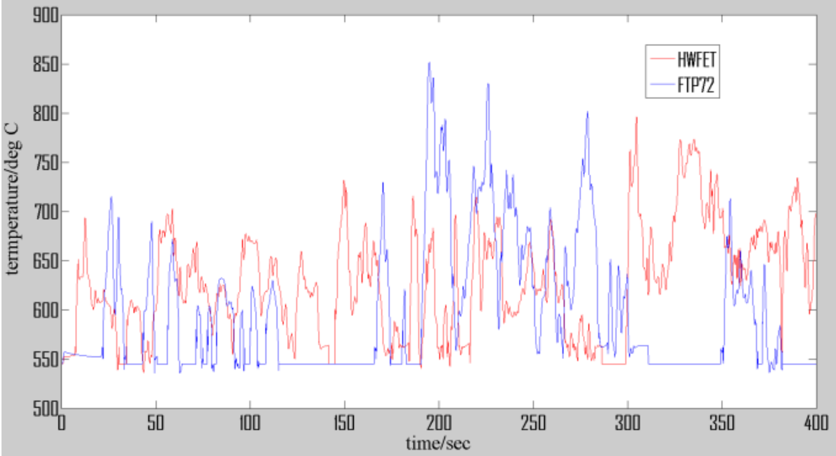

Figure 2.7 Temperature of exhaust at HWFET and FTP72 driving cycle

They also provide us the measurement data of mass flow rat at HWFET and FTP72 driving cycle. The average mass flow rate is around 20g/sec at HWFET and 10g/sec at FTP72. Highway driving condition has greater mass flow rate than urban driving condition.

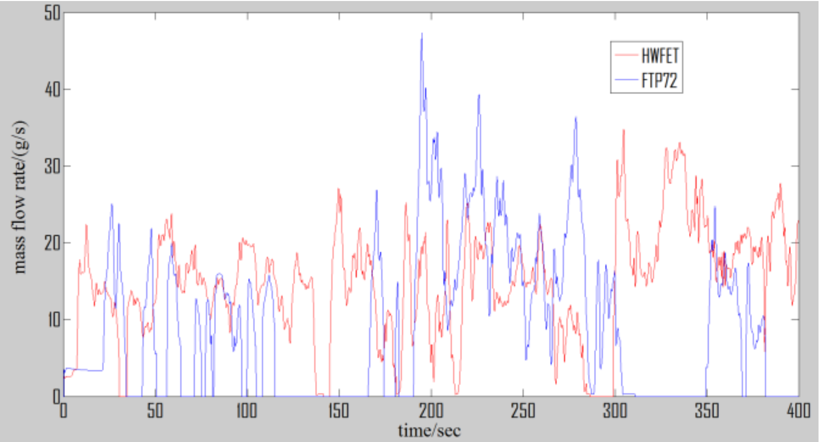

Figure 2.8 Mass flow rate of exhaust at HWFET and FTP72

2.1.1.4 Light duty trucks

Light trucks or light duty trucks are the U.S. classification for trucks or truck-based vehicles with a payload capacity of less than 4,000 pounds. U.S. has lots of light duty trucks, and their emission is between mid-size sedans and heavy duty trucks. Several researches has been done on this type of vehicle, the following content is a brief review of those works. In 2009 Thermoelectric Applications Workshop, GM presented a test result based on Chevy Suburban[30]. The driving cycle chosen was city driving cycle FTP72. Figure 2.9 indicates 4 groups of data of temperature measurement based on FTP72. Even though there is some deviation of those data, the average exhaust temperature keeps the same around 500 degrees Celsius. At the very beginning, it's a cold start, so the temperature increases from ambient temperature. While the repeated cycle gives a hot start of the engine which keep the staring temperature much higher than ambient temperature. The blue curve showed behind the temperature profile is vehicle speed of FTP72.

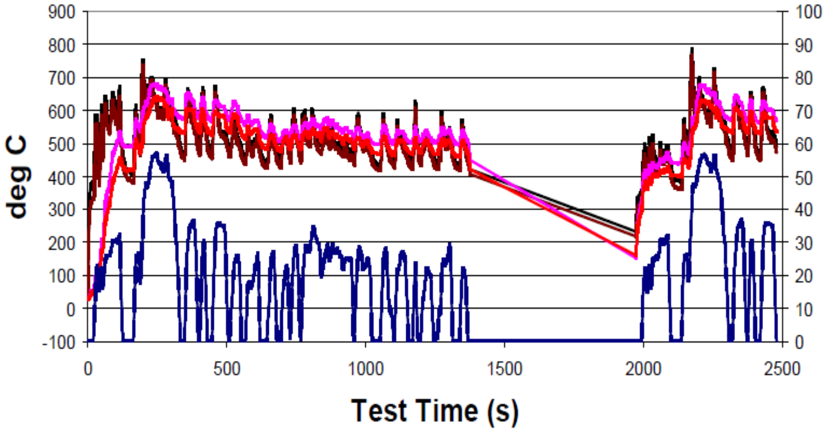

Figure 2.9 Exhaust temperature of a light duty truck at FTP72 driving cycle [30]

In Figure 2.10, the exhaust thermal power is shown at the same driving condition as those in Figure 2.9 and the average is around 15kW.

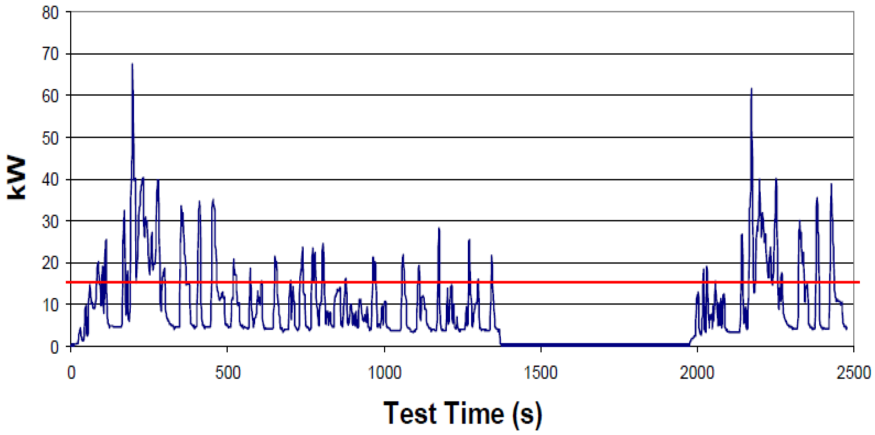

Figure 2.10 Exhaust thermal power of a light duty truck at FTP72 driving cycle [30]

In 2005, researchers in Clarkson University did measurement of the exhaust quantity and quality of GM Sierra pickup with 5.3 L V8 configuration [31]. In Figure 2.11, exhaust temperature at various driving speeds with different configurations has been shown. Configuration A: baseline truck without installation of automobile exhaust thermoelectric generator (AETEG), but the data with this configuration is not shown in the figure. Configuration B: AETEG installed but with the precooling heat exchanger (PCHX) covered. Configuration C: AETEG with exhaust pipes between catalytic converters and the AETEG insulated with Thermo-Tec TM exhaust wrap and aluminum-backed high-temperature glass fiber insulation and the PCHX covered. Configuration D: the AETEG with exhaust insulation and the PCHX uncovered to provide pre-cooling of the engine coolant. In Figure 2.11, the different locations of the measured temperatures are: 1) Txc is the exhaust left and right catalytic converter outlet averaged temperature; 2) Txi is AETEG exhaust heat exchanger inlet temperature; 3) Txo is AETEG exhaust heat exchanger outlet temperature; 4) Tcli is the AETEG coolant loop inlet temperature; 5) Tci is the AETEG coolant heat exchanger inlet temperature; 6) Tco is the AETEG coolant heat exchanger outlet temperature. 7) Txm1 is the exhaust temperature of thermoelectric module 1; 8) Txm4 is the exhaust temperature of thermoelectric module 4; 9) Tcm1 is coolant temperature of thermoelectric module 1; 10) Tcm4 is coolant temperature of thermoelectric module 4. Each measurement has three speed, which is 48.28, 80.47, 112.65 kilometer per hour.

2.1.1.5 Heavy duty trucks

Heavy duty trucks are the U.S. classification for trucks or truck-based vehicles with a payload capacity of more than 26,000 pounds. This type of vehicle provides huge amount of exhaust since they consume more fuel. Hi-z has reported their measurement data on heavy duty diesel engine on the 2001 International Conference on Thermoelectric about the engine exhaust [32]. The engine they choose is Cummins 335 Diesel engine. The test is from 75 to 290 horse power (HP) engine load and 1300 to 2100 RPM of engine speed. They provided the data on 2100 RPM, 335 HP. The exhaust temperature is 627 degrees Celsius and the mass flow rate is 2500 cubic feet per minute (CFM).

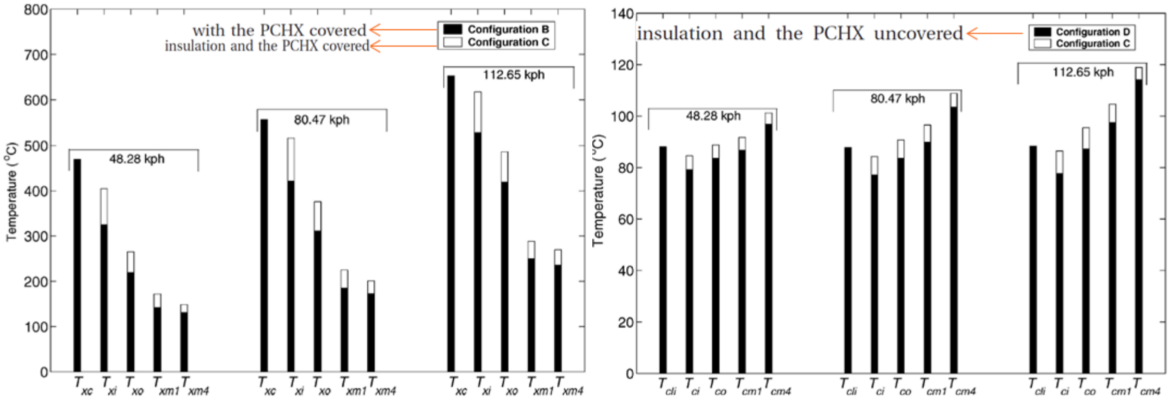

Figure 2.11 Exhaust temperature at constant driving speed with different configuration [31]

Researchers from Kocaeli University reported some of exhaust temperature profiles on a minibus [33]. The test is based on the constant speed and two different engine loads which are 20 percent and 80 percent. The data is shown below in Table 2-2.

Table 2-2 Exhaust gas temperature and gas flow rate[33]

Test No.	Engine speed (rpm)	Inlet temperature of the exhaust gas (°C)		Exhaust gas flow rate (m3/s)
		Engine load 20%	Engine load 80%	
1	750	104	188	0.0278
2	1200	142	230	0.0388
3	1500	200	275	0.0491
4	1800	212	335	0.0589
5	2000	221	410	0.0697
6	2300	243	505	0.0798
7	2570	260	530	0.0911
8	2840	285	570	0.1012

From Table 2-2, one can find that at higher engine loads the temperature is much higher when other conditions remain the same. The mass flow rate of the exhaust is averaged from the different engine loads. Another research in University of Newcastle upon Tyne reported exhaust power and temperature [34]. They explored the theoretical performance of four different configurations of a turbocharger diesel engine and absorption refrigeration unit combination when operating in a high ambient day temperature of 35 degree Celsius. The engine is a caterpillar diesel engine and 2000 rpm of engine speed is applied to get the exhaust thermal power and the temperature. Table 2-3 shows the data.

Table 2-3 Perforce of an ambient temperature of 35 °C[34]

Test No.	Inlet manifold temperature (K)	Exhaust thermal power (kW)	Exhaust temperature (K)
1	434	154.8	1000
2	414	159.6	951
3	334	165.0	890
4	329	167.4	860

The exhaust thermal power is calculated by multiplying the exhaust temperature difference, exhaust mass flow rate and specific heat of the exhaust. To adjust the measurement, a coefficient of 0.97 was applied in this result which showed in Table 2-3. The exhaust temperature is around 900 K and the average of exhaust power is 163kW. This power is considerable when compared with the power in GM's FTP test which is just 15kW.

Internal Combustion Engines Laboratory reported their measurement of exhaust temperature of a heavy duty diesel engine which was tested at several engine speeds [35]. In Figure 2.12, the temperature of the exhaust is shown and "before T/C" means before turbocharger in their turbocharger application. Generally, it's the inlet temperature of exhaust right after the engine. The temperature ranges from 325 to 600 degree Celsius when three different engine speeds 1300, 1700 and 2100 RPM are applied.

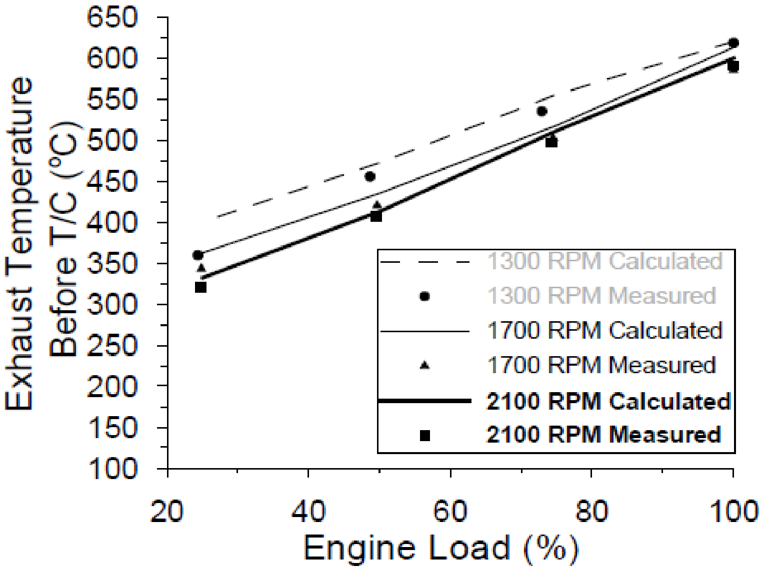

Figure 2.12 Exhaust temperature at different engine load [33]

Beside the temperature the mass flow rate of their test is also shown in Figure 2.13. The mass flow rate is measured at the same condition with that of temperature. It ranges from 0.2 to 0.4 Kg/s.

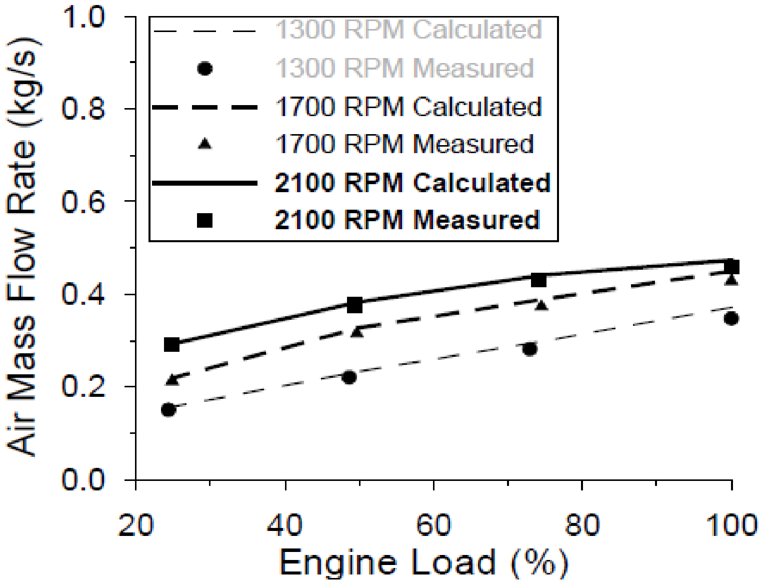

Figure 2.13 Mass flow rate in term of engine load and speed [35]

2.1.1.6 Conclusion

Table 2-4 summarizes the data mentioned above, including the temperature, mass flow rate, and thermal power.

Table 2-4 Comparison of the information

Test information			Test result			References
Vehicle	Type	Test cycle	Aver. Temp (°C)	Mass flow rate (g/s)	Thermal power (kW)	
BMW 530i	Midsize sedan	FTP-75	600		5.0	17
		NEDC	400	16	3.8	
Nissan Qusaqai	Midsize sedan	NEDC	200		2.6	18
		Highway			11	
X	Midsize sedan	FTP-72	580	10		19
X		HWFEL	650	20		
Suburban	LD truck	FTP72	580	25	15	20
GM Sierra pickup	Light Duty truck	48.28 kph	480			21
		80.47 kph	580			
		112.65 kph	640			
Cummins	HD truck	2100 RPM	627	60		22
Minibus	HD truck	20% load	208			23
		80% load	380			
caterpillar	HD truck	2000 RPM	652		162	24
X	HD truck	Const. speed	500	280		25

In summary, the average temperatures at highway driving cycle and city driving cycle are around 500~650 degree Celsius and 200~400 degrees Celsius. The mass flow rate changes a lot according to vehicle size. Typically, the mass flow rate is around 10~25 g/s but the exception occurs when heavy duty trucks are taken into consideration. The thermal power calculated based on the collected data is 3~10 kilowatts. To make meaningful contribution to the fuel efficiency improvement, the conversion efficiency of TEG devices needs to be 8~10% or more since several hundreds of watts of electricity is effective for application. As the exhaust changes in large range at different driving conditions, the TEG is hard to replace the alternator even though the average output of the electrical power from TEG can be several hundred watts. To install the TEG module, locations should be chosen at downstream of catalytic converter since the heat quantity and quality satisfy the requirement for intermediate temperature thermoelectric material and there is no increased pollution due to extracting heat from upstream of catalytic converter.

2.1.2 Thin film thermoelectric energy harvesting

Conventional thermoelectric module, sometimes referred to as - “bulk” modules, have been used for decades in commercial power generation (ex, Hi-z)[36] and temperature control of electronics[37]. However, as the size and power density requirements are dramatically changing for electronics, conventional bulk thermoelectric technology will lose its advantages for the microelectronics applications. Conversely, thin film thermoelectric modules focused on localized temperature control as well as self-sustained power generation.[38],[39] These thin film thermoelectric modules take the advantages of semiconductor processing techniques to create a nano-structured thermoelectric thin film.[40] As the Internet of Things (IoT) develops, more embedded thermoelectric energy harvesting modules are needed for a variety of applications due to its advantage of compactness and free of maintenance compared with using regular battery.[41] The only type of the thin film thermoelectric module that commercially available is based on bismuth telluride alloy which has good performance at room temperature.[42] For energy harvesting application in nuclear or other harsh environment, electronic systems must sustain at high temperature and thermoelectric device based on high temperature materials other than bismuth telluride is desirable.

Filled skutterudite is the state of art high temperature thermoelectric material which known as phonon glass electron crystal-PGEC systems [43]. Nolas et al.[44] reported the bulk Yb filled skutterudite and found ZT close to 1 at 600K for Yb0.19Co4Sb12. Shi et al.[45] investigated multi-filled skutterdite bulk material and got maximum ZT of 1.7 at 850K. One advanced approached for preparing high ZT materials is through quantum well structures with quantum confinement effects in thin films and superlattices.[46],[47] For microdevice applications[48] , it is essential to find these promising “bulk” properties also in skutterudite thin films. Thermoelectric module based on thin film skutterudite material is still under laboratory research level.[49],[50] Anno et al. [51],[52] reported the grown of CoSb3 thin film on Si(100) and GaAs (100) substrate using rf-sputtering. In another study, V. Savchuk et al. [53] studied the structural, electrical, and thermal properties of binary skutterudite CoSb3 thin films deposited using sputtering. The temperature of the transition from the amorphous to crystalline state was found to be around 428K. On the other hand, J. Caylor et al. [54] presented skutterudite (CoSb3 and IrSb3) thin films of high phase purity and crystallinity. Zeipl et al. [55],[56] studied thin layers of Yb filled CoSb3 prepared by pulsed laser deposition (PLD) and get best results on quartz substrate at 470K. Kumar et al. [57] reported In and Yd double filled CoSb3 thin film using PLD and obtained maximum power factor of 0.68 W/m*K at 700K. However, all the studies reported on thin film skutterudite didn’t provide their figure of merit at high temperature which impeded the development for high temperature applications.

2.1.3 Thermal energy recovery in nuclear power plant

Nuclear plants accidents (Chernobyl, Three Mile Island, and Fukushima Daiichi) have cast a shadow on the history and future of nuclear power. Safety issues thus rightfully remain an enormous concern in the development of nuclear power. The Fukushima event, one major concern, as seen in the Fukushima event, was a total lack of power at the plant. As a result, sensing systems stopped working. We are now developing thermoelectric-driven sensing technologies to power sensor and communication packages in the event of total system failure. The target is Small Modular Reactors (SMRs): a new generation of nuclear reactors that are more flexible, standardized, and safer. SMRs are built in modular fashion at factories, and are able to be shipped by truck, train, or barge. There are more than twelve advanced SMRs currently being developed and could be implemented before 2020 [58]. SMRs have many advanced features that minimize opportunities for accidents happening. Integrated advanced technologies such as passive cooling utilizing gravity to provide backup cooling system in unusual circumstances are an integral part of the system design. This project aims at designing an additional backup system for monitoring and low-power actuation when power is lost in nuclear plants. Loss of offsite power in nuclear plants is one of the most frequent incidents in the U.S. A total of 42 separate power-out conditions in the U.S from 1997 to 2004 [59] have been recorded. Among these incidents, 24 caused critical operation conditions and 18 more resulted in a shutdown condition. Although these incidents did not lead to major damage, they had the potential for major accidents if the onsite emergency power generators had also failed. The offsite power source, which is supplied from electric grid, is the primary power source during normal operation. When nuclear plants lose the offsite power source (because of weather-related, plant-centered, grid-related, switchyard-related events, etc.), the onsite power source, e.g. diesel generator, are used. If both power sources become unavailable a station blackout results. The Fukushima Daiichi resulted in a station blackout because the tsunami disabled the emergency diesel generator and the offsite power. Cooling system malfunctions can cause core damage in a short time. In light water reactors for example, peak core temperatures can reach 1,100 K in less than 30 minutes if the cooling system becomes unavailable, with the result that the cladding of the fuel rods can burst at this temperature [60]. Monitoring devices provide important parameters such as pressure, temperature, and radiation that help operators understand the system status in the reactor. It is vitally important to maintain continuous monitoring, particularly during station blackout conditions.

Several recent studies have reported on the radiation effect on thermoelectric material, thermoelectric module and related power electronics. However, high neutron dose radiation test is not practical due to limited neutron irradiation access as well as the complexity of post irradiation testing. As an alternative investigation method, ion radiation has been used to simulate the neutron radiation effect especially for displacement damage. Clapier et al [61] have used existing neutron dose measurements from the bombardments of thick targets by heavy ion beams to study the relationship between the dose rate and the incident energy variable measured in unit of MeV/nucleon. They found that the yield can be fitted by a power law curve in terms of the incident energy variable. Vizkelethy et al [62] reported simulation of neutron displacement damage in bipolar junction transistors using high-energy heavy ion beams. Lewis et al [63] described heavy-ion simulation of neutron damage by simultaneously operating two accelerators to propel two or three ion beams on the target under well-controlled conditions. Kulcinsk et al [64] compared typical examples of pure nickel (Ni) and 316 stainless steel which have been both neutron and ion bombarded. Abromeit [65] used ion beam irradiation to simulate neutron damage and discussed advantages and disadvantages of using different particle irradiations to simulate neutron damage. Ila et al[66-71] reported MeV Si bombardment effect on thermoelectric properties of several monolayer and multilayer thin films.

2.2 Popular Thermoelectric Materials

2.2.1 Bismuth Telluride

Since the observation of a substantial lowering of temperature by means of the Peltier effect in a thermocouple incorporating bismuth telluride, Bi2Te3, this compound has been extensively used in the construction of thermoelectric modules. The performance of these modules has steadily improved, since the original observations, due to a number of factors. When there is only one type of carrier, electrons or positive holes, the Seebeck coefficient at a given temperature falls as the electrical conductivity increases. The Seebeck coefficient and the electrical conductivity are combined in a quantity, $\alpha^2 \sigma$, known as the power factor. One aims to make this parameter as large as possible, though it must be remembered that a large electrical conductivity also implies a large electronic component of the thermal conductivity. Most of the early improvements came about through a reduction in the lattice component of the thermal conductivity, λL. This was achieved through the use of solid solutions of bismuth telluride with the isomorphous compounds antimony telluride and bismuth selenide. The enhanced scattering of phonons in these solid solutions is not usually accompanied by a reduction in the mobility of the charge carriers. This is somewhat surprising since the charge carriers usually possess the larger mean free path. In recent years, further reductions in the lattice conductivity have been obtained by the adoption of nanostructures. One must remember that the electrical and thermal conductivities of bismuth telluride are anisotropic although the Seebeck coefficient does not depend on orientation in the extrinsic or one-carrier regime. The lattice conductivity is about twice as large along the cleavage planes as it is in the perpendicular direction. The anisotropy of the hole mobility is almost the same as that of the lattice conductivity so that, although the electrical and thermal conductivities in aligned crystals are different from those in randomly oriented polycrystalline material, the figure of merit is virtually isotropic for p-type bismuth telluride. On the other hand, the electron mobility is more strongly anisotropic than the lattice conductivity and this means that the figure of merit is significantly less for non-aligned n-type samples than it is for properly oriented material. This is unfortunate since there are practical advantages in making material in polycrystalline form using a sintering process rather than a melt-growth process.

The problem of optimizing the impurity content of bismuth telluride alloys for specific temperatures has been tackled by Kuznetsov in the production of functionally graded thermoelements. Min and Rowe [37] discussed the optimization of Peltier modules for use in power generation but did not treat the question of the composition of the thermoelements. Matsuura and Rowe selected bismuth telluride alloys as the preferred generator materials up to 150 °C but did not consider the optimization of the Seebeck coefficient.

It has generally been found that good n-type bismuth telluride alloys are more difficult to produce than their p-type counterparts. This is in part due to the rather high ratio of the electron mobility parallel to and perpendicular to the cleavage planes. Thus, unaligned polycrystalline specimens are bound to be inferior to aligned crystals, with ZT closer to 0.5 than 1. Nevertheless, such polycrystalline material is attractive from the practical viewpoint. The figure of merit of these alloys is no larger than that of the Bi2Te3-Bi2Se3 alloys and, in their increased energy gap, the latter would appear to be the more promising for higher temperature use. It is expected that the best n-type materials will display some preferential orientation, the most practical production process , for achieving this end, involving hot extrusion . One of the few papers to describe the properties of nanostructured material above room temperature has been published by Bulat et al. [48]. The material was p-type with the composition Bi0.4Sb1.6Te3.The high figure of merit, ZT, equal to 1.25 at about 100 ° C, is attributed to a small lattice conductivity. The sintered material was prepared from powders with a grain size of the order of 100 nm. The importance of the structure of the powders in any sintering process is apparent from the work of Wu et al. [49]. The best results were achieved using flower-like nanosheets yielding ZT of the order of unity over the whole temperature range 300 K to 525 K. Somewhat higher values of ZT were obtained by Xie et al. [50] who combined melt spinning and spark plasma sintering. Most of the early studies of sintered Bi2Te3 alloys made use of large particle sizes to minimize the effect of oxidation [51]. On the other hand, very fine powders are needed in the production of nanostructured material. This problem has been tackled successfully by Nguyen et al. using a spark erosion technique. Samples of p-type

Bi0.5Sb1.5Te3 made by sintering these powders have yielded a ZT value of 1.36 at 360 K. Non-aligned n-type materials with the formula LixBi2Se0.3Te2.7 has been prepared by Chen et al. [53]using a sintering method. The authors claim that the use of Li as a dopant improves ZT by about 25%.However, the observed value of 0.8, while quite high for non-aligned material, is no better than other workers have achieved. A significant feature of this work is the maintenance of a reasonably high ZT value up to a temperature of 500 K. Kim et al. produced n-type nanocomposites of bismuth seleno-telluride by introducing Bi2Se3nanoparticle inclusions into bulk Bi2Te3. The reduction in the lattice conductivity was reflected in arise of ZT at 320 K from 0.56 to 0.75. Measurement of the thermoelectric properties covered temperatures up to nearly 600 K. However, ZT fell continuously with increasing temperature over the whole range. This was largely because the Seebeck coefficient was continuously decreasing. That this should have occurred with a Seebeck coefficient of no more than -150 μV/K at 320 K is entirely unexpected and may indicate non-uniformity of composition. Part of the sample could have displayed mixed conduction and part extrinsic conduction, both regions having a low Seebeck coefficient.

2.2.2 Magnesium silicide

Magnesium silicide (Mg_2Si) is an inorganic compound consisting of magnesium and silicon elements and has a face-centered cubic lattice structure. Magnesium silicide powder is dark blue or slightly purple in color and should be sealed in case of oxidation. Magnesium silicide is formed by react silicon dioxide (SiO2), an ingredient found in sand and glass with excessive magnesium. The first product in this reaction is silicon, which then reacts further with magnesium to produce Mg_2Si. In its unit cell, it possesses the antifluorite structure with Si^{4-} ions occupying the corners and face-centered positions of the unit cell and Mg^{2+} ions occupying eight tetrahedral sites in the interior. There are also four equivalent interstitial sites and the phase diagram of Mg_2Si is shown below.

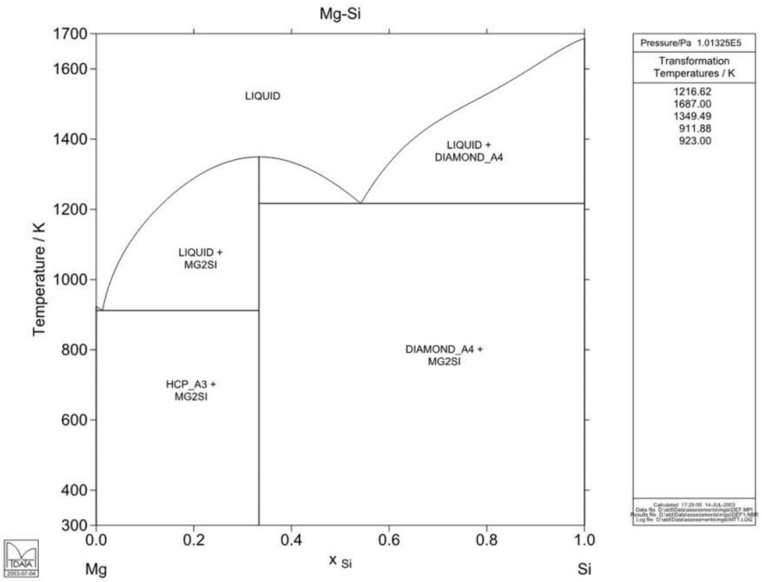

Figure 2.14 Phase Diagram of Mg_2Si (courtesy of *National Physical Laboratory*)

Extensive research has been done to synthesize and solidify Mg_2Si and its solid solutions, Zaitsev et al [72] used direct melting to synthesis polycrystalline $Mg_2Si_{1-x}Sn_x$. The powder was mixed and melted in boron nitride crucibles using high-frequency heating. The diameter of the ingots was about 22 mm and the length, about 20 mm. Long-time annealing was used for homogenization of the samples.

Table 2-5 Properties of Mg_2Si/Ge/Sn [73]

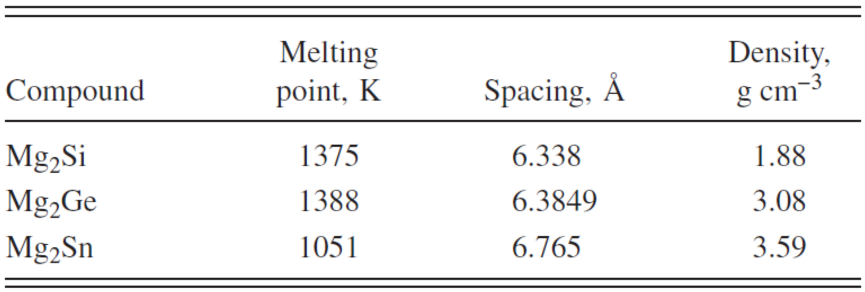

Compound	Melting point, K	Spacing, Å	Density, g cm^{-3}
Mg_2Si	1375	6.338	1.88
Mg_2Ge	1388	6.3849	3.08
Mg_2Sn	1051	6.765	3.59

Table 2-5 shows the physical property of Mg_2Si/Ge/Sn and lattice spacing. Mg_2Si differs a lot with Mg_2Sn in regard to melting point and density. Figure 2.15 shows the figure of merit of several good thermoelectric compared with Zaitsev's work. Below 800K, $Mg_2Si_{0.4}Sn_{0.6}$ has higher ZT than $Mg_2Si_{0.6}Sn_{0.4}$ and both of them show great potential for middle range temperature application.

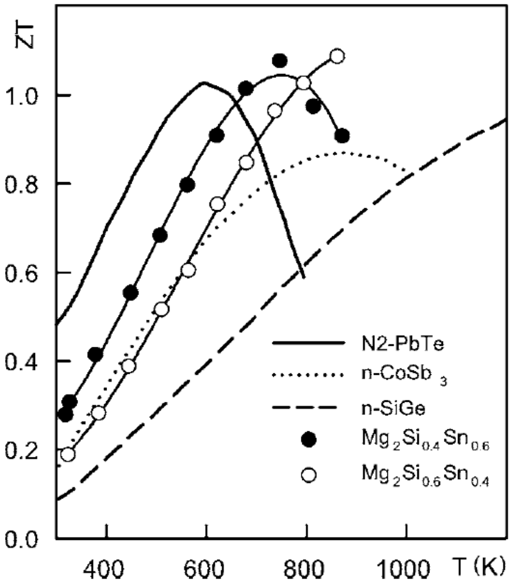

Figure 2.15 The comparison of the good thermoelectrics with the solid state solution under discussion[72]

Riffel and Schilz [74] investigated mechanical alloying method followed by hot-pressing process. It was found that the alloying process during milling develops in one of two different directions. The first one leads to the nominal composition with only a small amount of iron impurities resulting from wear of the milling media. In the second route-which only occurs in the presence of Sn-an abrasive phase is formed and the Fe content may increase up to 50 at%. The Fe is bound in FeSi and consequently, the solid solution has a lack of Si. The hot-pressing was performed at a temperature smaller than the peritectic temperature of the quasibinary Mg_2Si-Mg_2Sn system. A decomposition of the solid solutions occurs, which suggest changes on the miscibility gap in published phase diagrams. However, some transport measurements on the multiphase materials were performed, which revealed lower mobility values and lattice thermal conductivities compared to values published in the literature for single crystalline materials. The mobility of the materials was found to be independent from composition whereas the thermal conductivity decreases with increasing Sn content.

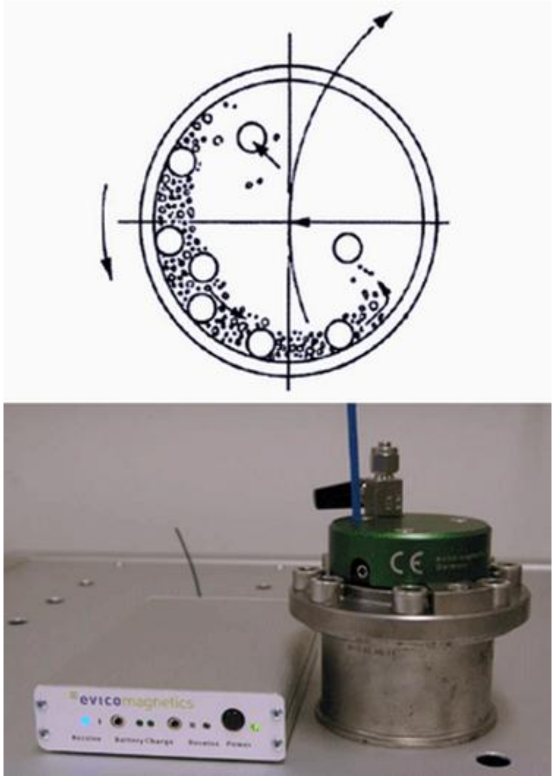

Figure 2.16 Attritor mill used for mechanical alloying [75]

Jung and Kim [76] tried solid state reactions then hot press (HP). High purity Mg powder (< 149 μm, purity 99.99%) and Si powder (<45 μm, purity 99.99%) were weighed at an atomic ratio of 2:1 and mixed homogeneously. The mixed powders were cold-pressed under a pressure of 600 MPa to make pellets, which were reacted in solid state in an alumina crucible with a cover at 773 K for 6 h in a vacuum. The solid-state-reacted Mg_2Si pellets, dopant powders and hardened steel balls (diameter of 5 mm) were loaded at a weight ratio of 20 into a hardened steel vial in an argon atmosphere. These synthesized powders were hot-pressed in a cylindrical graphite die with an internal diameter of 10 mm at 1073 K under a pressure of 70 MPa for 1 h in a vacuum.

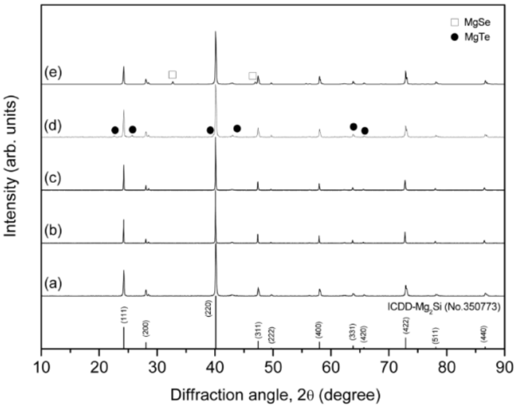

Figure 2.17 X-ray diffraction patterns for solid-state-reacted, mechanically alloyed and hot pressed (a) Mg_2Si (b) $Mg_2Si:Bi_{0.02}$ (c) $Mg_2Si:Sb_{0.03}$ (d) $Mg_2Si:Te_{0.03}$ (e) $Mg_2Si:Se_{0.02}$ [76]

Figure 2.17 showed the phase of those synthesized material was pure except some minor MgTe and MgSe phases which might due to the dopants. Also, by substation of Si instead of Mg atom, the entire doped semiconductor showed n-type.

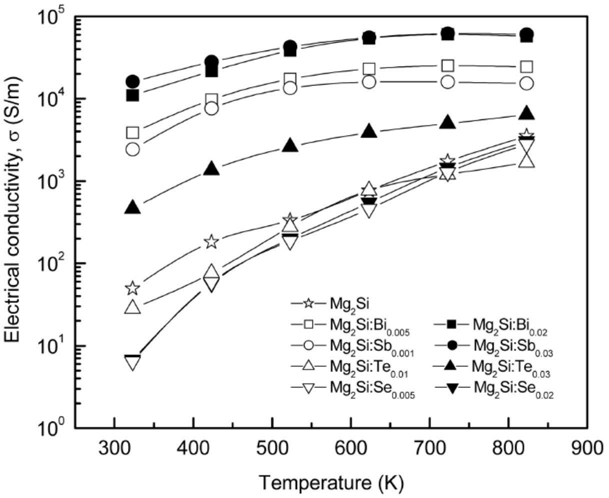

Figure 2.18 Changes in the electrical conductivity of n-type $Mg_2Si:Xm$ with temperature [76]

Figure 2.18 shows the electrical conductivity of different sample with regard to the temperature change. As know, electrical conductivity depends on change carrier concentration and mobility. As a matter of fact, the carrier concentration increases dramatically by doping with other elements while the mobility doesn't change that much. In this figure, people can conclude with higher doping rate, the electrical conductivity is higher.

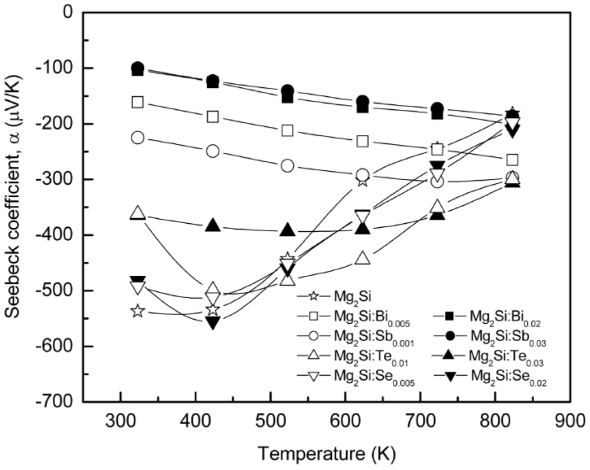

Figure 2.19 Changes in the Seebeck coefficient of n-type Mg_2Si:Xm with temperature [76]

Figure 2.19 shows Seebeck of the samples. For undoped Mg_2Si, the Seebeck coefficient is negative and increase as temperature raise. Bi, Sb, Te and Se doped Mg_2Si showed n-type semiconductor. But the temperature dependence differs far from each other. Mg_2Si doped with Te and Se shows similar dependence to temperature as un-doped samples and Mg_2Si doped with Bi and Sb decreases as temperature increases.

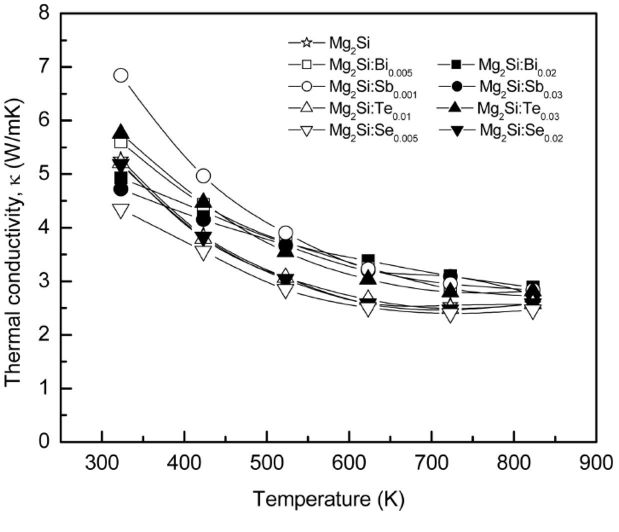

Figure 2.20 Changes in the thermal conductivity of n-type Mg2Si:Xm with temperature [76]

Figure 2.20 shows the thermal conductivity of those samples. The difference between doped and intrinsic Mg_2Si sample changes from 7 to 4.2 W/mK at room temperature but at high temperatures the difference vanishes. The one doped with Se ratio of 0.005 reflect the lowest thermal conductivity which probably is due to the strongest phonon scattering. The un-doped Mg_2Si has a thermal conductivity of 5.3 W/mK at room temperature by this synthesis method.

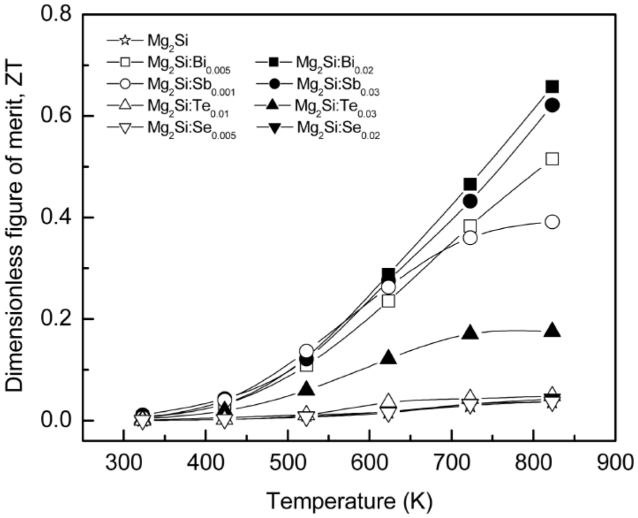

Figure 2.21 Changes in the dimensionless-figure-of-merit of n-type with temperature [76]

Figure 2.21 shows the figure of merit of Mg_2Si with different dopants. Clearly, doped by Bi and Sb can increase the figure of merit of Mg_2Si dramatically. But doped with Te and Se doesn't enhance the figure of merit of Mg_2Si that much. Also, for doped Mg_2Si with Bi and Sb, the higher doping rate has better effect. However, people can't add too much dopant which will deteriorate the property. Overall, Jung *et al* obtained maximum ZT of 0.7 at 830K with Bi doped Mg_2Si.

Kajikawa *et al*. [77, 78] and Tani [79] used spark plasma sintering. Powders of high purity, Mg (>99.9%), Si (>99.999%), and Bi (>99.9%), were used as starting materials. The Mg and Si were mixed in 2:1 ratio and varying an amount of Bi (the molar ratio of Mg_2Si:Bi=1:*x*) were added to each charge. They were ground together, and then heated in a graphite die (15 mm in diameter) at 1023–1053 K for 15 min at 30 MPa under a vacuum of 1×10−3 Torr by the SPS method with a heating rate of 60 K/min. The density of the annealed samples was more than 99% of the theoretical value.[79]

Table 2-6 Electrical properties of Bi-doped Mg_2Si at 300K [79]

x (at%)	Conduction type	Carrier concentration (cm^{-3})	Mobility ($cm^2/V\ s$)	Resistivity (Ωcm)
0.0	N	4.3×10^{17}	204	7.14×10^{-2}
0.1	N	1.8×10^{19}	85.7	3.97×10^{-3}
0.3	N	3.1×10^{19}	91.5	2.22×10^{-3}
0.5	N	4.1×10^{19}	92.4	1.64×10^{-3}
1	N	8.5×10^{19}	63.5	1.16×10^{-3}
2	N	1.1×10^{20}	64.0	8.58×10^{-4}

Table 2-6 listed electrical properties of the Bi doped Mg_2Si at 300K. As known, electrical conductivity depended on carrier concentration and mobility. From the figure, one could find the doped Mg_2Si has two or three magnitude higher of carrier concentration and slightly slower mobility which is probably due to the scattering by impurities involved. Overall, the resistivity decreases when more dopants were added.

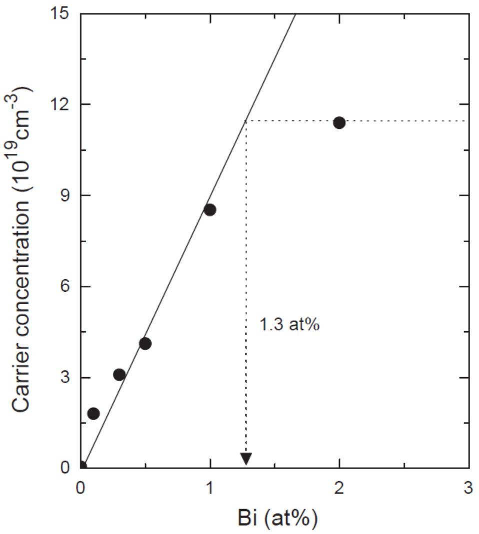

Figure 2.22 Bi atom concentration (x) dependence of carrier concentration at 300K [79]

Figure 2.22 showed the carrier concentration changes due to the doping rate of Bi in Mg_2Si samples. Clearly, at low doping rate, dopants increased the carrier concentration. However, the effect on carrier concentration change vanished when doped Bi with around 1.3%. How dopant influence samples carrier concentration is still unclear and we can only find out the optimal doping rate experimentally.

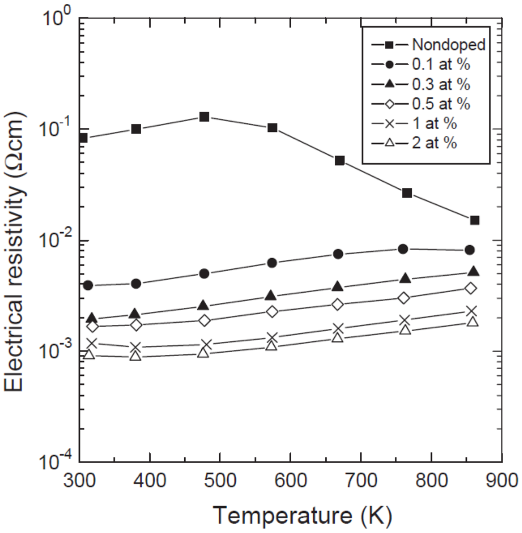

Figure 2.23 Electrical resistivity of Bi-doped Mg_2Si and non-doped Mg_2Si as a function of temperature [79]

The above figure showed electrical resistivity dependence on temperature. Un-doped Mg_2Si showed highest resistivity and as the doped Bi ratio increased, the electrical resistivity decreased. The lowest electrical resistivity shown in the above figure is with 2% of Bi. By adding 2% of Bi in Mg_2Si, the electrical conductivity enhanced 100 times with all the contribution coming from carrier concentration.

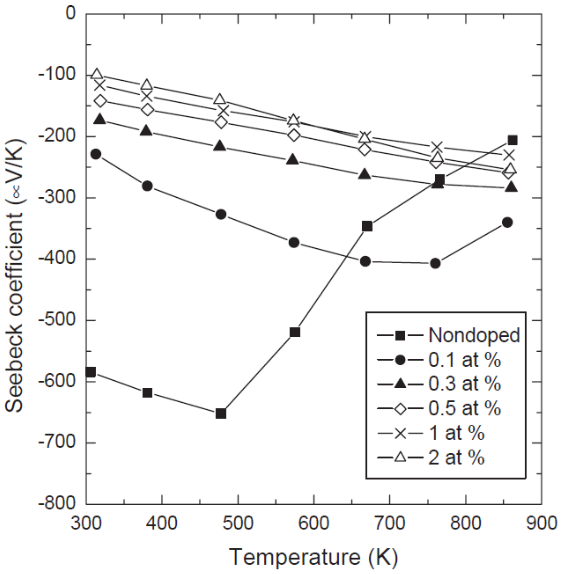

Figure 2.24 Seebeck coefficient (S) of Bi-doped Mg_2Si and non-doped Mg_2Si as a function of temperature [79]

However, the figure 2.24 showed the change of Seebeck as a function of temperature. Generally, it showed an inverse dependence as Bi ratio increased which is due to the Seebeck decrease as carrier concentration increase. Basically, it a tradeoff between electrical conductivity and Seebeck coefficient, higher carrier concentration gives higher electrical conductivity but lower Seebeck. On the other hand, mobility will also increase the electrical conductivity without altering Seebeck.

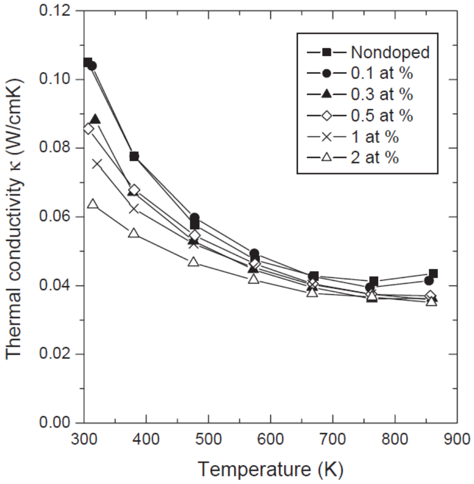

Figure 2.25 Thermal conductivity (k) of Bi-doped Mg_2Si and non-doped Mg_2Si as a function of temperature [79]

Figure 2.25 indicated the thermal conductivity of Bi-doped Mg_2Si versus un-doped Mg_2Si. Doped Mg_2Si showed lower thermal conductivity than non-doped Mg_2Si sample because of phonon scattering by those impurities. The strongest phonon scattering occurs at doping Bi with 2%. Using this method, the thermal conductivity changed from non-doped 10W/mK to 6W/mK at room temperature.

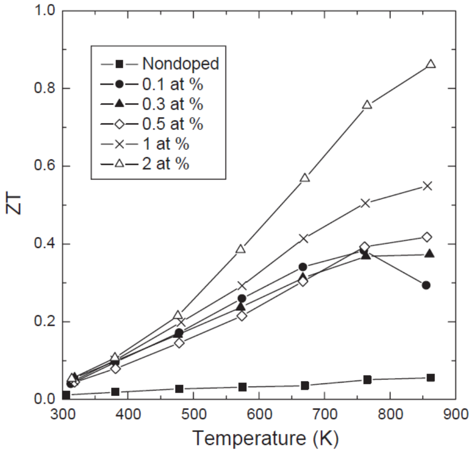

Figure 2.26 Dimensionless figure of merit (ZT) of Bi-doped Mg_2Si and non-doped Mg_2Si as a function of temperature [79]

Figure 2.26 was the figure of merit of doped and non-doped Mg_2Si from 300K to 862K. It clearly showed that with 2% of Bi doping, the figure of merit increase significantly. Generally, the figure of merit increases as Bi content increases. Also, it increases as a function of temperature since figure of merit contains temperature. Tani got maximum ZT of 0.86 at 862K with Bi doped Mg_2Si and showed great potential of mid-temperature range application.

The vertical Bridgman method has also been applied for the single crystal growth by Akasaka *et al*. [80]. Magnesium siliside (Mg_2Si) crystals have been grown using the vertical Bridgman method in a non-wetting growth environment, which is achieved by the use of an anti-adhesion coating on the crucible wall. [80] Tamura *et al*. have also grown Mg_2Si bulk crystals by the vertical Bridgman method using a high-purity Mg (6N-up) source. The grown crystals were single-phase Mg_2Si and had well-developed grains (1–5 mm^3). The Hall mobility of 14,500 cm2/V*sec was observed at 45 K in the crystals grown from 6N-up-Mg. From the optical absorption measurement, we estimated that the indirect energy gap was about 0.66eV at 300 K and about 0.74eV at 4 K [81].

2.2.3 Iron disilicide

The properties of iron disilicide ($FeSi_2$) have been investigated, and it has been shown to be a semiconductor with a thermal energy gap of 0.88 ± 0.04eV. It has been found possible to dope FeSi2 both n and p type by the substitution of suitable elements for iron and silicon. Substitution of cobalt for iron yields an n-type material, and substitution of aluminum for silicon produces a p-type material. These materials have $Z > 2 \times 10^{\sim 4} C^{-1}$ over the temperature range 150-650°C. The materials are oxidation-resistant, thermally stable and mechanically strong. A method of construction is described which exploits the properties of these materials and should produce a cheap, robust generator of high power/weight ratio. [82]

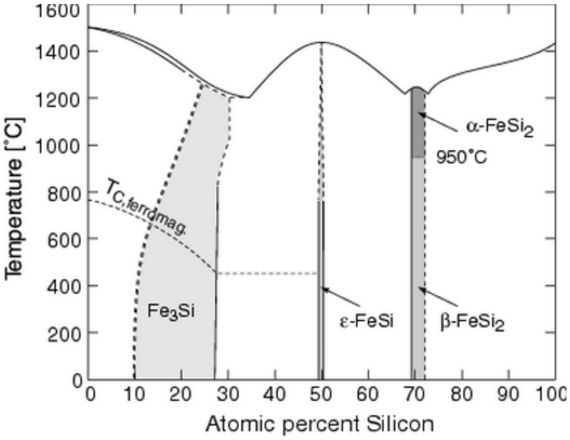

Figure 2.27 Phase diagram of Fe-Si alloy [83]

Figure 2.27 shows the phase diagram of ferrosilicon. Beta-iron disilicide is the phase used for thermoelectric application. As you can see, it’s a very narrow band which means much more attention need to be paid when synthesis this material. H. Katsumata *et al* [16] investigated optical, electrical and structural properties of polycrystalline beta-$FeSi_2$ thin films fabricated by electron beam evaporation of ferrosilicon. Later K. Ueno [17] fabricated $FeSi_2$ by thermal spraying process. Table 2-7 showed the chemical components of Co doped $FeSi_2$ that had been used in their work.

Table 2-7 Chemical components of C_O doped $FeSi_2$ powders [17]

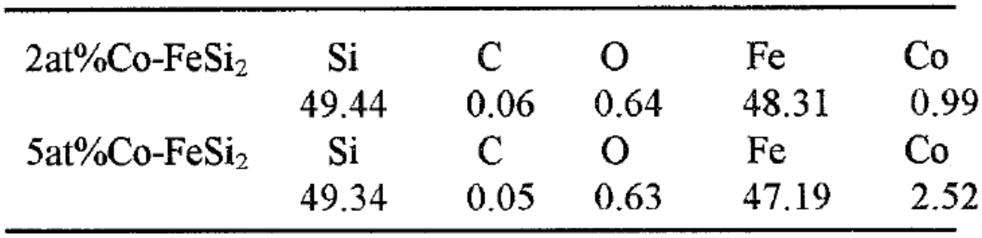

2at%Co-$FeSi_2$	Si	C	O	Fe	Co
	49.44	0.06	0.64	48.31	0.99
5at%Co-$FeSi_2$	Si	C	O	Fe	Co
	49.34	0.05	0.63	47.19	2.52

These powders have the grain size ranging from 20 to 63 µm. The powders were deposited on two stainless steels by spraying. One is a plate (10 x 10 x 0.5 cm), another tube (2.5 cm diameter, 50 cm long). The substrate was blasted by alumina grit after degreasing by organic solvent, and then pre-heated at about 600°C in a plasma spraying chamber filled with inert gas. Plasma spraying was carried out by using Controlled Atmosphere Plasma Spraying (CAPS, Sulzer-Metco Co.,), equipped with a plasma spray gun manipulated by 5-axis robot within the chamber. The spray parameters are listed below.

Table 2-8 Plasma spraying conditions for FeSi2 [17]

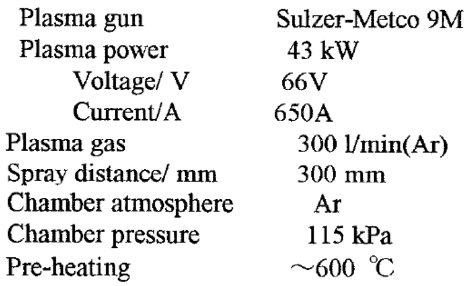

Plasma gun	Sulzer-Metco 9M
Plasma power	43 kW
Voltage/ V	66V
Current/A	650A
Plasma gas	300 l/min(Ar)
Spray distance/ mm	300 mm
Chamber atmosphere	Ar
Chamber pressure	115 kPa
Pre-heating	~600 ℃

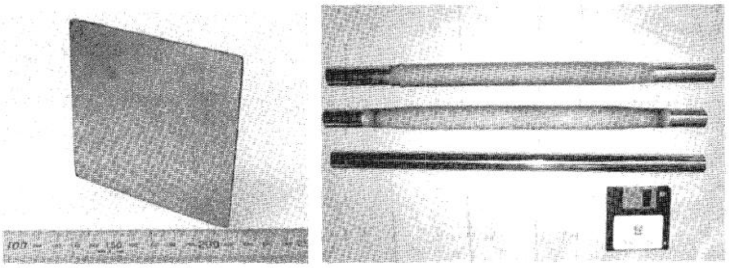

Figure 2.28 Plasma spray-formed $FeSi_2$ thermoelectric device [17]

Figure 2.28 showed some devices fabricated by thermal spray on flat and non-flat surface. Thermal spray is an industrial scalable mass productive method. These results clearly verified the feasibility of fabricating thermoelectric generator using thermal spray method. The challenges are to find best thermoelectric materials that are suitable for thermal spray.

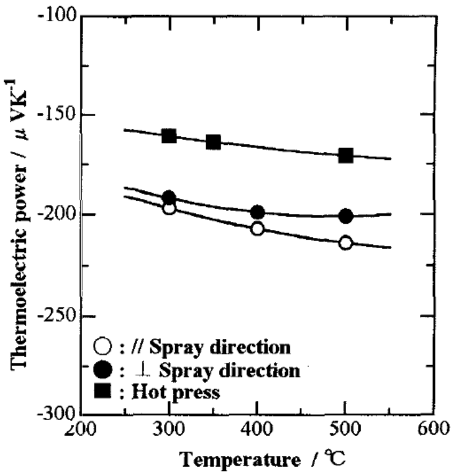

Figure 2.29 Thermoelectric power of spray-formed and hot press 5% Co doped $FeSi_2$. [17]

Figure 2.29 showed the Seebeck coefficient of thermal sprayed FeSi2 versus by traditional hot press method. As can be seen, thermoelectric power of thermal sprayed sample was higher than by hot press. Furthermore, the spray direction showed the highest thermoelectric power from 250C to 550C.

M. Cherigui *et al* [18] investigated structure and magnetic properties of FeSi coatings obtained by HVOF spraying using microcrystalline and nano-crystalline powders. The structure was completely crystalline and for coatings sprayed using nano-crystalline powders, X-ray diffraction showed the crystalline size was lower than that in the coating obtained from microcrystalline powder. FeSi coatings behaved as a soft ferromagnetic.

J. Schilz *et al* [19] concluded that plasma spray forming can indeed be an advantageous tool to form thermoelectric devices. Despite the crude processing method, the resulting properties are not necessarily inferior to those of state-of-the-art material they can even be better under the circumstances met in the present case. However, not every thermoelectric semiconductor is suited to be processed by plasma spraying. If the corrosion resistance of a component is too low, the thermoelectric performance of the resulting samples can be greatly reduced. This may for example hold true for materials such as the highly effective bismuth telluride or bismuth selenide based compounds or those containing magnesium like the promising Mg2(Si, Ge, Sn) solid solutions. Although, besides the already investigated iron disilicide, material combinations like silicon germanium solid solutions or manganese silicides might be favorably processed in the future by plasma spray forming.

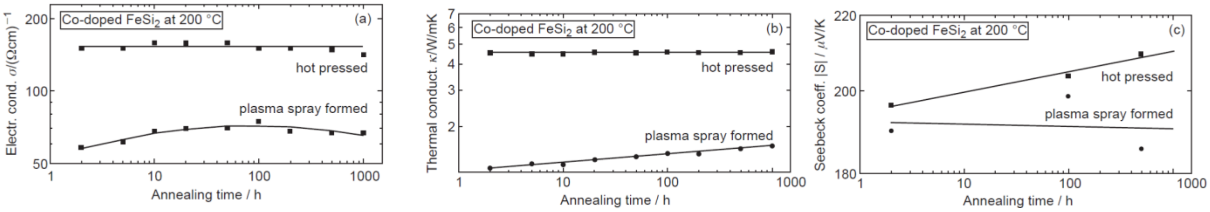

Figure 2.30 (a) Electrical conductivity; (b) thermal conductivity; and (c) Seebeck of Co-doped FeSi2 [19]

Figure 2.30 showed the electrical, thermal and Seebeck of Co-doped FeSi2 as a function of annealing time. Hot pressed sample had higher themal and electrical conductivity because thermal sprayed samples contained lots of pore and crack in the coating. Figure 2.31 showed Al-doped FeSi2 properties and similarly as Co-doped FeSi2, plasma spray formed samples obtained lower electrical and thermal conductivity while the Seebeck didn’t change that much.

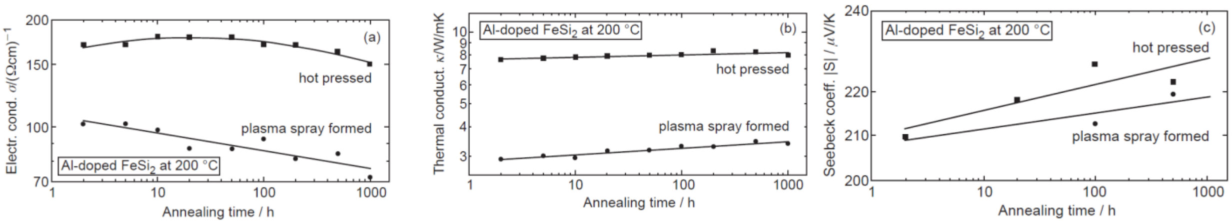

Figure 2.31 (a) Electrical conductivity; (b) thermal conductivity; and (c) Seebeck coefficient of Al-doped FeSi2 [19]

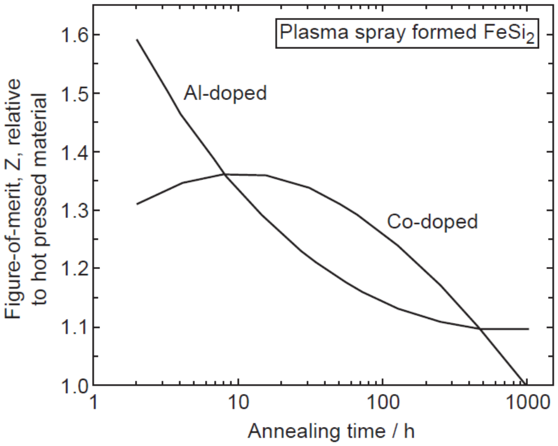

Figure 2.32 Relative figure-of-merit, Z, of plasma spray formed FeSi2 as a function of annealing time [19]

Figure 2.32 showed the relative figure of merit plasma spray formed FeSi2 and both at low and high annealing time, Al-doped got better figure of merit than Co-doped. The above figure clearly addressed the significance of proper annealing time. As a matter of fact, the annealing temperature is also important but the author didn’t discuss in this paper. Even though thermal spray has already been used to prepare FeSi2 thermoelectric materials, the maximum ZT of $FeSi_2$ is too low for practical energy recovery application.

2.2.4 Manganese silicide

Higher manganese silicide is one of the most interesting materials from the point of view of its structure and thermoelectric properties. Careful study of the phase diagram of the Mn–Si system shows that higher manganese silicide (HMS) can be produced in aperitectic reaction at 1428 K and its composition was determined to be $MnSi_{1.72}$ .The homogeneity region of HMS has been found to be very narrow (not more than 0.3%). The method of HMS formation has been confirmed by other researchers;

however, the composition of HMS was reported to be different in different papers and the consensus is that HMS can exist over the composition range of $MnSi_{1.70}$ to $MnSi_{1.77}$. [73]

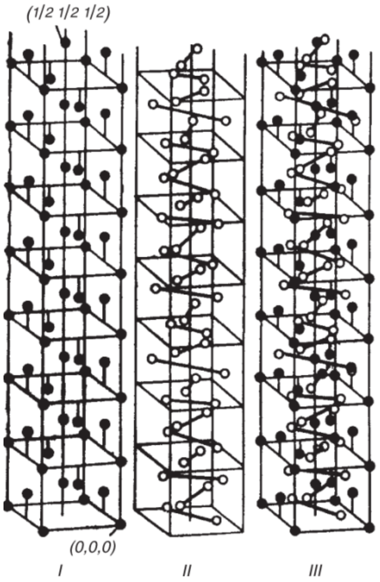

Figure 2.33 A schematic of half a unit cell of $Mn_{15}Si_{26}$ I: positions of Mn atoms; II: positions of Si atoms; III: positions of Mn and Si atoms [73]

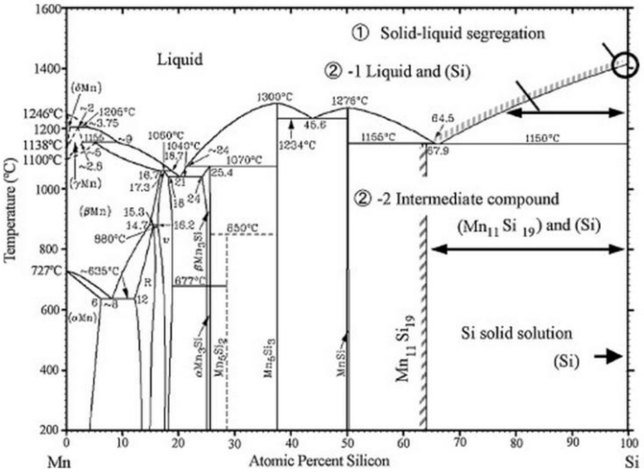

Figure 2.34 Phase diagram of Mn-Si [84]

Tsutomu Kojima *et al* grew crystal of manganese silicide with a Si/Mn ratio near 1.73 by the Bridgman method followed by chemical transport. The Bridgman as grown boule was observed to have a lamellar structure identified to be composed of a MnSi precipitate and a $Mn_{15}Si_{26}$ matrix. The chemical transport was carried out by using crushed grains of the Bridgman boule as starting material and $CuCl_2$ as transport agent. Homogeneous single crystals of $Mn_{15}Si_{26}$ having an average linear size of 0.5 mm were grown on the colder zone. The crystals were identified by X-ray technique as well as by electron probe micro analysis. [85] Song Jing *et al* reported the synthesis, structural identification, and electrical properties of the first one dimensional (1-D) nanomaterials of a semiconducting higher manganese silicide ($MnSi_{2-x}$) with widths down to 10 nm via chemical vapor deposition of the single-source precursor $Mn(CO)_5SiCl_3$. [86]

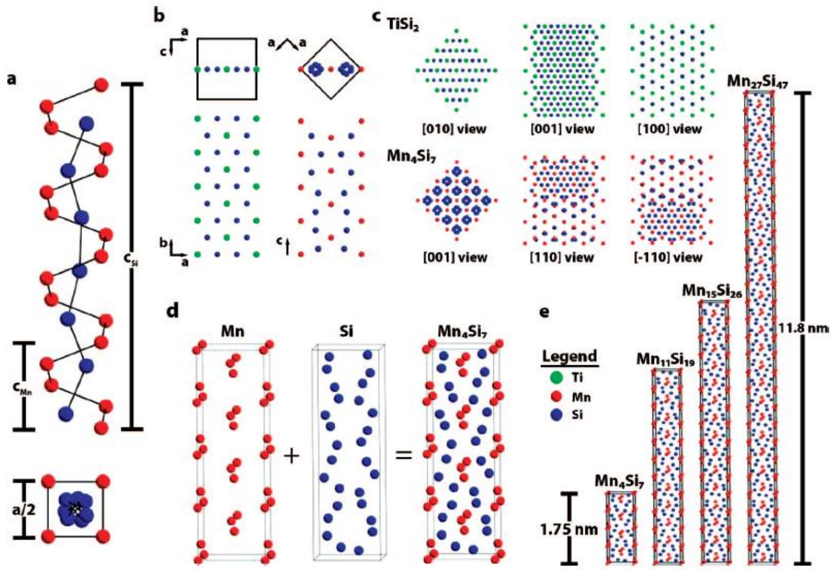

Figure 2.35 Crystal structures of Nowotny chimney ladder (NCL) phases of manganese silicides and their comparison with the parent TiSi2 structure [86]

Figure 2.35 showed (a) Visualization of the NCL structures of MnSi2-x with the Si sublattice (cSi) forming the ladder and the Mn sublattice (cMn) forming the chimney sublattice. cSi/cMn ≈ 4 for reported HMS structures. (b) Comparison of the NCL parent structure TiSi2 (left) clearly showing the 3^6 and 6^3 nets of the stacking planes with the simplest HMS phase, Mn4Si7 (right), highlighting the distorted 63 nets associated with the defect NCL structure. (c) Comparison of the TiSi2 structure and the Mn4Si7 along comparable projections revealing NCL supercell characteristics similar to different rotated views of the TiSi2 supercell. This rotation in cell structure is characteristic of the defect Nowotny chimney ladder structures. (d) General NCL structure is formed by combining one sublattice of transition metal atoms with a sublattice of main group atoms. (e) Effects of sublattice periodicity on unit cell size for the four HMS phases completely characterized crystallographically with atomic positions.

2.2.5 Filled skutterudite

In the preceding section, it was pointed out that the skutterudite structure contains two empty voids. The existence of these voids invites an opportunity to insert (fill) foreign species into the skutterudite lattice. The first such filled skutterudite —LaFe4P12—was synthesized in 1977 by Jeitschko and Brown [87]. Shortly after, filled skutterudites were prepared also in the arsenide and antimonide families. Filled skutterudites are compounds with the same crystal structure as CoAs3 in which additional atoms have been added to the empty regions within the unit cell. They take the form RM4X12 where R is a filling atom, M is Fe, Ru, Os, or Co, and X is P, As, or Sb. Appropriate choices of the filling atom result in these atoms “rattling” within the unit cell cage, which significantly depresses the thermal conductivity of the material, while having little effect on electrical conductivity or the Seebeck coefficient.

Table 2-9 Maximum Void Occupancy in PureCoSb [73]

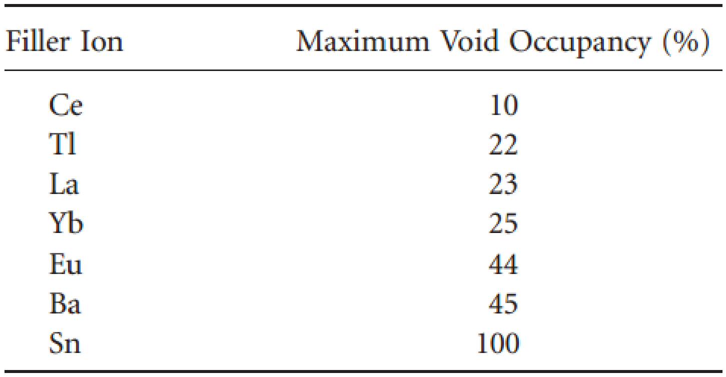

Filler Ion	Maximum Void Occupancy (%)
Ce	10
Tl	22
La	23
Yb	25
Eu	44
Ba	45
Sn	100

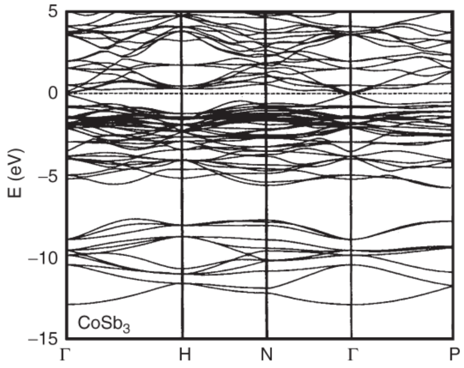

Figure 2.36 Band structure of CoSb3. The dashed line indicates Ef [73]

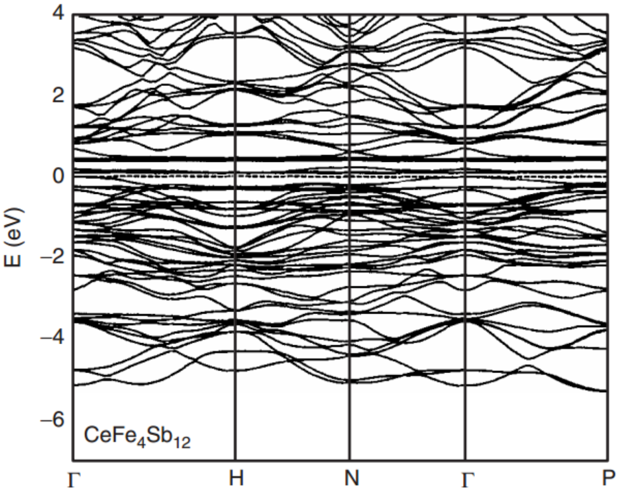

Figure 2.37 Band structure of the filled skutterudite CeFe4Sb12. The dashed line indicates Ef [73]

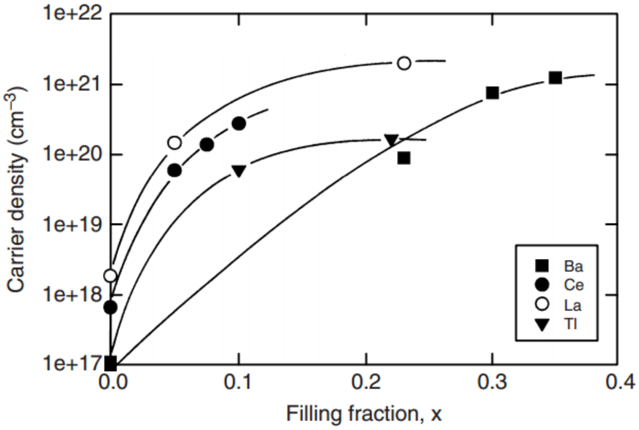

Figure 2.38 Carrier density vs. filling fraction for various filler ions. [73]

Since the early days, alloying isostructural compounds has been the hallmark of research on thermoelectrics. Best conventional thermoelectric materials such as Bi_2Te_3/Sb_2Te_3, PbTe/SnTe, and Si-Ge alloys is directly related to strong phonon scattering, which arises as a consequence of alloy or solid solution formation. Although solid solutions within the family of skutterudites have been demonstrated, [88-90] remarkably, few attempt has been made to fill such structures. The filled solid solution would benefit from both the effect of the filler on the normal phonon modes and the strong point defect scattering, resulting in exceptionally low lattice thermal conductivity for skutterudite material. At the same time, their solid solution would present little additional impedance to the charge transport since the two constituent skutterudite compounds are isoelectronic. In addition to the expected strong phonon scattering which reduces lattice thermal conductivity, solid solutions of skutterudites offer several other important advantages, such as: tailoring the band gap to the desired operational regime, extend the range of rare-earth ions and altering the size of the void that can increase the filling fraction. Alloying can take place either on the sites of the pnicogen atom or on the sites of the metal atom. The range of solubility and the ensuing solubility gap is the major unknown in the formation of solid solutions and people need to carefully explore this. However, strong phonon scattering is often achieved with a relatively low volume fraction and solid solutions can readily be prepared at least up to 10% of $CoAs_3$ and 10% of $IrSb_3$ in $CoSb_3$, respectively.

Each type of filler ions has its own characteristic frequency which reflects its mass, size, and the strength of coupling with the atoms forming the cage, various ion types will have different "spring constants", and thus, different frequencies, and will consequently affect a broader spectrum of phonon modes. In order to reduce lattice thermal conductivity, one needs to scatter as wide a spectrum of heat-carrying phonons as possible. This is the essence of the multiple filling approaches. Clearly, it is beneficial to select filler ions that differ significantly as far as their size and mass is concerned so that the impact on the phonon spectrum. Initial attempts demonstrating the effectiveness of this approach in reducing the lattice thermal conductivity have been made with Ba and Ce, [91] with Ce and Yb [92, 93] and Ce and La, [94] but no systematic studies looking into the effect on all three key transport parameters —resistivity, Seebeck coefficient, and thermal conductivity— have yet been made. Multiple filling is an intriguing approach that should be explored in detail.

People should notice that the effective mass of charge carriers is large. A situation may occur whereby the mean-free path of phonons is comparable or even greater than that of the carriers. The thermoelectric performance might actually be enhanced by improved boundary scattering if this is the case. [95] The best candidate for this situation is filled skutterudites with their large carrier effective masses. By reducing the grain size down to the nanometer scale should achieve large effects and especially changes have been made on the order of a lattice parameter. A recent attempt to demonstrate the concept [96] has targeted binary skutterudites and, indeed, a reduction in the thermal conductivity was achieved. However, a full potential of this approach remains to be tested since the actual size of grains in the experiment was not smaller than about 0.1 mm. Nano-sized particles of skutterudites [97] can be prepared by precipitation from a solution. However, it is a different matter how to prevent their growth in the process of compacting the particles under high pressure at elevated temperatures. In order to gain full benefit of this very promising approach, innovative ways must be found to suppress grain growth.

2.2.6 Others

Oxide materials are considered to be promising for future thermoelectric applications, since they have many advantages such as nontoxicity, thermal stability, high oxidation resistance, etc. Oxide materials had been ignored for a long time by the thermoelectric community because of its low figure of merit which is the intrinsic of non-conducting properties of oxides, but the discovery of $NaxCoO_2$ as a strong candidate thermoelectric material in 1997 [58, 98] lit a fire in the researchers’ minds to explore high-efficiency oxide materials. Cobalt-oxide-based layer-structured crystals including $NaxCoO_2$, $Ca_3Co_4O_9$, and their derivative compounds have been developed as p-type materials having fairly high thermoelectric performance, and the maximum ZT value generated from this compound group has to date reached unity or larger. [99, 100] Additionally, modulated layered cobalt oxides have been found promising as p-type materials. [101, 102] In contrast, the n-type oxide materials so far proposed, such as ZnO:Al [103] and $Zn_5In_2O_8$, [104-106] only show rather low figures-of-merit (ZT , 1) and remain to be further improved, or otherwise novel oxide materials have to be explored. Strontium titanate, $SrTiO_3$ (abbreviated as STO), and its derivative layered compounds, (SrO) $(SrTiO_3)_m$ (m ¼ integer), have recently been shown to exhibit promising high TE performance [107]. Also, the concept of nanoblock integration into a layer-structured hybrid crystal (natural superlattice) is first proposed as our strategy to explore novel TE materials, and then apply it to some of the state-of-the-art oxide materials, such as $NaxCoO_2$, Ca–Co–O system, STO, and its derivatives, to demonstrate how we can improve and enhance their thermoelectric performance. The significance of nanostructure control to give rise to high thermoelectric (TE) performance will be emphasized by employing ZnO material as an example, and an attempt to fabricate oxide TE modules will be discussed.

Recently, Theodore *et al* from Austria manipulated cobalt (II/III) tris (bipyridyl) redox couple through anion exchange has improved its solubility in ionic liquids and 3-methoxypropionitrile (MPN). This has allowed the preparation of electrolytes with high Seebeck coefficients, 1.5–2.2 mV K^{-1}, and thereby excellent prospects for thermal harvesting. The unique physical properties of ionic liquids offer ideal characteristics for their use as electrolytes in thermoelectrochemical cells, particularly for applications involving thermal energy available at temperatures in the 100–200 C range. The power generation characteristics of thermoelectrochemical cells using a series of ionic liquids and MPN with the $Co^{II/III}(bpy)_3(NTf2)_{2/3}$ couple are described. Power densities reached >0.5 W m^{-2} in un-optimized devices, operating with a 130C hot side. The high Seebeck coefficient appears to have its origins in the high-to-low spin transition upon electron transfer in this cobalt complex. [108]

3 MATERIAL PREPARATION AND CHARACTERIZATION

3.1 Thermal Spray Technology

In this thesis, thermal spray was used to deposit thermoelectric material which is an industrial scalable method. In the following section, the principle of thermal spray, different kinds of spray method and its related issues are addressed.

3.1.1 Thermal spray principle

Thermal Spray had long been recognized as one of the techniques to produce surface coatings in a continuous process, in which coating material is combined with heat and kinetic energy, to form a laminate structure of droplets on substrate, where they splat, solidify and increment in vertical direction and eventually build up as a new surface.

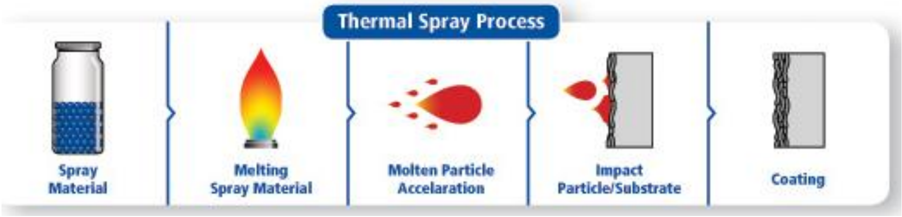

Figure 3.1 Principle of thermal spraying [109]

As shown in figure 3.1, during the spraying, feedstock materials are heated to molten or semi-molten state and are transported by operating media, as droplets, so that the coating materials can deposit on the substrate, to accumulate vertically to form laminated coating.

Substrate materials are of great importance as well. Suitable substrate materials are those which can resist high temperature and impact from high speed droplets in the course of spraying; Substrates need to be processed before spraying since the adhesion of molten particles to the substrate is primarily mechanical bonding, instead of metallurgical bonding; thus pretreatment of substrates that to be coated is important. Surface of substrate can be cleaned by chemical or mechanical methods. Then the surface is roughened in order to provide more mechanical bonding to those molten particles and grit blasting with dry corundum is the normal way to roughen the surface.

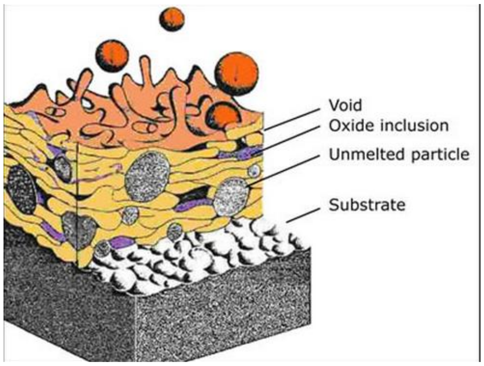

Figure 3.2 Illustration of thermal sprayed coatings [109]

Since the molten particles hit the surface at high speed, they usually deform after hitting the surface. Figure 3.2 shows a typical thermal sprayed coating constitution. For those particles that are not melted during the spray, they will stay in the coating as the splats accumulate around, the un-melted particles will be buried inside the coating. Hot particles will shrink and solidify, and it forms a mechanical bond dominated structure; metallurgical bond happens during the diffusion between particles and substrate and particle to particle, but such bonding mechanism is so small to be neglected.

3.1.2 System overview

Thermal spray processes can be classified into conventional flame spray, electric arc wire spray, plasma spray, high velocity oxy fuel spray, etc [109].

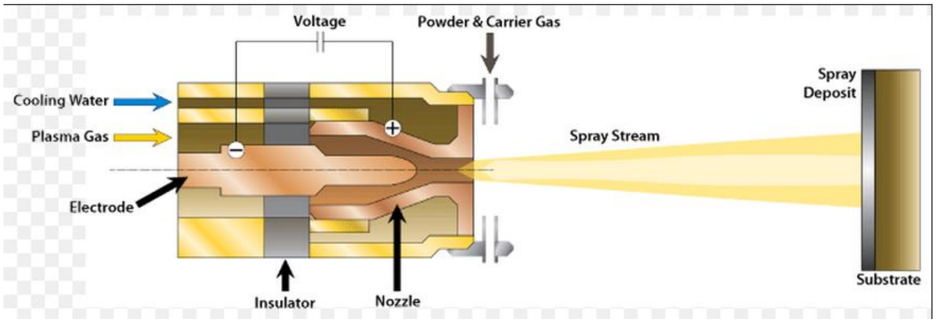

Figure 3.3 Powder flame spray gun cross section (Courtesy of Steven)

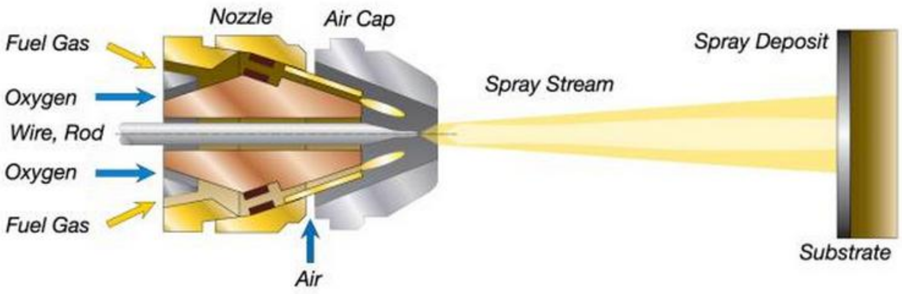

Figure 3.4 Wire/rod spray gun cross section (Courtesy of Sulzer company)

Both powder flame spray [110] and wire flame spray [111] belong to conventional flame spray process [112]. Powder or wire is melted in the flame of gaseous fuel, such as acetylene, propane or hydrogen. Once the feed material is melted, the compressed air can carry the melted and atomized toward the substrate to form layered structure. Not all the materials can be fabricated into wire, the powder flame spray expand the material selection for thermal spray.

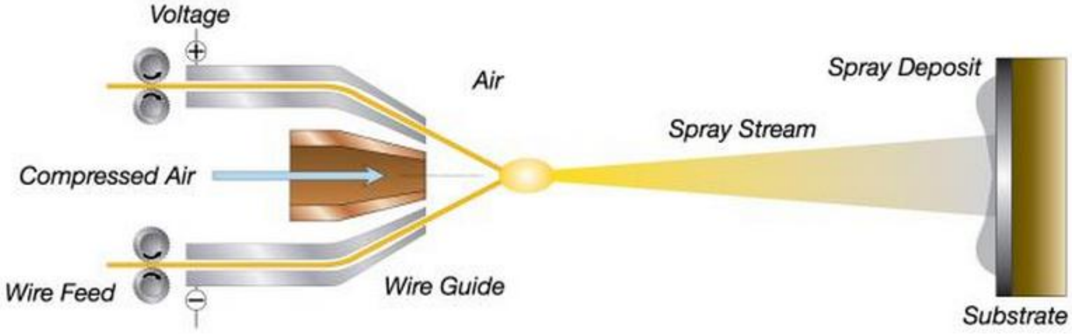

Figure 3.5 Diagram of electric arc wire spray (Courtesy of Sulzer company)

Different from flame spray, electric arc wire spray applied opposite charge to the two wires (shown in Figure 3.5), the contact of these two wires can trigger the melt of the tip; compressed air is then blew into the system to take the melted part to the substrate. Appropriate control of wire feed speed regulates the melt at a constant speed.

The principal of plasma spray [113] shown in figure 3.6 is based on the formation of high temperature plasma. The gas, such as helium, hydrogen, nitrogen or mixtures, flow though the cathode and anode, which are charged by high frequency current, is being ignited by the arc between these electrodes to form plasma plume; coating material is fed outside and is carried by the plasma plume onto the substrate. Since the temperature can reach as high as 16000K, the injected powder can be melted before they reach the substrate. According to special applications, plasma spray varies from atmospheric plasma spray (APS) [114] and vacuum plasma spray (VPS) [115]. One significant advantage of VPS is its low oxidation rate but it requires higher energy input to melt the particles than APS.

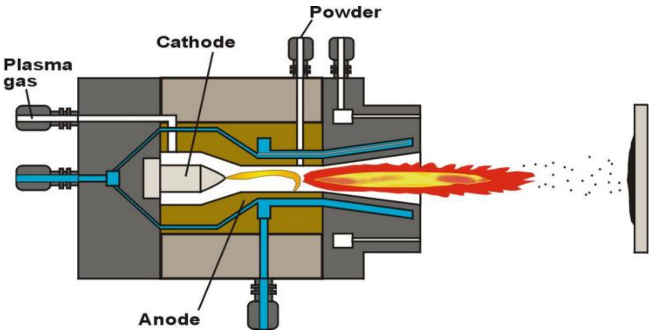

Figure 3.6 Diagram of plasma spray (Courtesy of U of Toronto)

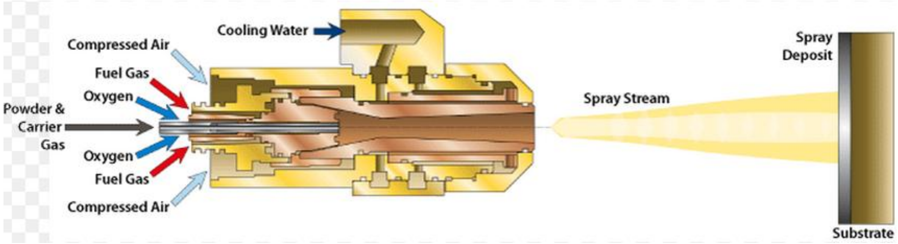

Figure 3.7 Diagram of high velocity oxy-fuel spray (Courtesy of Steven Ort)

High velocity oxy-fuel spray (HVOF) [116] is new to the family of thermal spray processes. It differs from other processes is that it used supersonic air flow jet to carry the melted particles. Fuel gas and compressed air are injected as shown in Fig 3.7. The impact of particles on the substrate is much higher than flame spray which can result more dense coating.

3.1.3 Plasma spraying

In plasma spraying process, the material to be deposited (feedstock) — typically as a powder, sometimes as a liquid, suspension or wire — is introduced into the plasma jet, emanating from a plasma torch. In the jet, where the temperature is on the order of 10,000 K, the material is melted and propelled towards a substrate. There, the molten droplets flatten, rapidly solidify and form a deposit. Commonly, the deposits remain adherent to the substrate as coatings; free-standing parts can also be produced by removing the substrate. There are a large number of technological parameters that influence the interaction of the particles with the plasma jet and the substrate and therefore the deposit properties. These parameters include feedstock type, plasma gas composition and flow rate, energy input; torch offset distance, substrate cooling, etc.

Figure 3.8 Plasma spray setup (Courtesy of Zircotec)

3.1.3.1 Deposit properties

The deposits consist of a multitude of pancake-like lamellae called 'splats', formed by flattening of the liquid droplets. As the feedstock powders typically have sizes from micrometers to above 100 micrometers, the lamellae have thickness in the micrometer range and lateral dimension from several to hundreds of micrometers. Between these lamellae, there are small voids, such as pores, cracks and regions of incomplete bonding which is shown in figure 3.2. As a result of this unique structure, the deposits can have properties significantly different from bulk materials. These are generally mechanical properties, such as lower strength and modulus, higher strain tolerance, and lower thermal and electrical conductivity. Also, due to the rapid solidification, metastable phases can be present in the deposits

3.1.3.2 Applications

This technique is mostly used to produce coatings on structural materials. Such coatings provide protection against high temperatures (for example thermal barrier coatings for exhaust heat management), corrosion, erosion, wear; they can also change the appearance, electrical or tribological properties of the surface, replace worn material, etc. When sprayed on substrates of various shapes and removed, free-standing parts in the form of plates, tubes, shells, etc. can be produced. It can also be used for powder processing. In this case, the substrate for deposition is absent and the particles solidify during flight or in a controlled environment. This technique with variation may also be used to create porous structures, suitable for bone ingrowth, as a coating for medical implants. A polymer dispersion aerosol can be injected into the plasma discharge in order to create a grafting of this polymer on to a substrate surface. This application is mainly used to modify the surface chemistry of polymers.

3.1.3.3 Vacuum plasma spraying

Vacuum plasma spraying (VPS) is a technology for etching and surface modification to create porous layers with high reproducibility and for cleaning and surface engineering of plastics, rubbers and natural fibers as well as for replacing CFCs for cleaning metal components. This surface engineering can improve properties such as frictional behavior, heat resistance, surface electrical conductivity, lubricity, cohesive strength of films, or dielectric constant, or it can make materials hydrophilic or hydrophobic.

The process typically operates at 39–120 °C to avoid thermal damage. It can induce non-thermally activated surface reactions, causing surface changes which cannot occur with molecular chemistries at atmospheric pressure. Plasma processing is done in a controlled environment inside a sealed chamber at a medium vacuum, around 13–65 Pa. The gas or mixture of gases is energized by an electrical field from DC to microwave frequencies, typically 1–500 W at 50 V. The treated components are usually electrically isolated. The volatile plasma by-products are evacuated from the chamber by the vacuum pump, and if necessary can be neutralized in an exhaust scrubber.

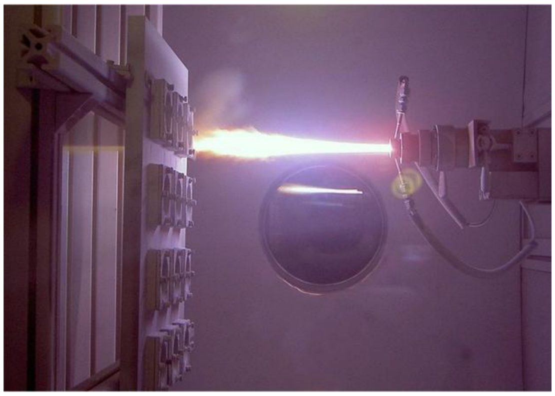

Figure 3.9 Vacuum plasma spray (Courtesy of Matthias Zepper)

3.1.3.4 Changing effects with plasma

At higher energies ionization tends to occur more than chemical dissociations. In a typical reactive gas, 1 in 100 molecules form free radicals whereas only 1 in 106 ionizes. The predominant effect here is the forming of free radicals. Ionic effects can predominate with selection of process parameters and if necessary the use of noble gases.

3.1.4 High velocity oxygen fuel spraying (HVOF)

During the 1980s, a class of thermal spray processes called high velocity oxy-fuel spraying was developed: A mixture of gaseous or liquid fuel and oxygen is fed into a combustion chamber, where they are ignited and combusted continuously. The resultant hot gas at a pressure close to 1 MPa emanates through a converging–diverging nozzle and travels through a straight section. The fuels can be gases (hydrogen, methane, propane, propylene, acetylene, natural gas, etc.) or liquids (kerosene, etc.). The jet velocity at the exit of the barrel (>1000 m/s) exceeds the speed of sound. A powder feed stock is injected into the gas stream, which accelerates the powder up to 800 m/s. The stream of hot gas and powder is directed towards the surface to be coated. The powder partially melts in the stream, and deposits upon the substrate. The resulting coating has low porosity and high bond strength. HVOF coatings may be as thick as 12 mm (1/2"). It is typically used to deposit wear and corrosion resistant coatings on materials, such as ceramic and metallic layers. Common powders include WC-Co, chromium carbide and alumina. The process has been most successful for depositing cermet materials (WC–Co, etc.) and other corrosion-resistant alloys (stainless steels, nickel-based alloys, aluminum, hydroxyapatite for medical implants, etc.).

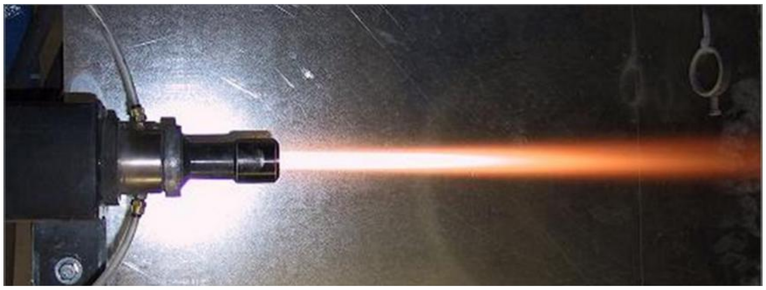

Figure 3.10 HVOF sparying (Courtesy of Ruppex)

3.1.5 Cold spray

In the 1990s, cold spraying (often called gas dynamic cold spray) [117] has been introduced. The method was originally developed in Russia with the accidental observation of the rapid formation of coatings, while experimenting with the particle erosion of the target exposed to a high velocity flow loaded with fine powder in a wind tunnel. In cold spraying, particles are accelerated to very high speeds by the carrier gas forced through a converging–diverging de Laval type nozzle. Upon impact, solid particles with sufficient kinetic energy deform plastically and bond metallurgically to the substrate to form a coating. The critical velocity needed to form bonding depends on the materials properties, powder size and temperature. Soft metals such as Cu and Al are best suited for cold spraying, but coating of other materials (W, Ta, Ti, WC–Co, etc.) by cold spraying has been reported. The deposition efficiency is typically low for alloy powders, and the window of process parameters and suitable powder sizes is narrow. To accelerate powders to higher velocity, finer powders (<20 micrometers) are used. It is possible to accelerate powder particles to much higher velocity using a processing gas having high speed of sound (helium instead of nitrogen). However, helium is costly and its flow rate, and thus consumption, is higher. To improve acceleration capability, nitrogen gas is heated up to about 900 C. As a result, deposition efficiency and tensile strength of deposits increase.

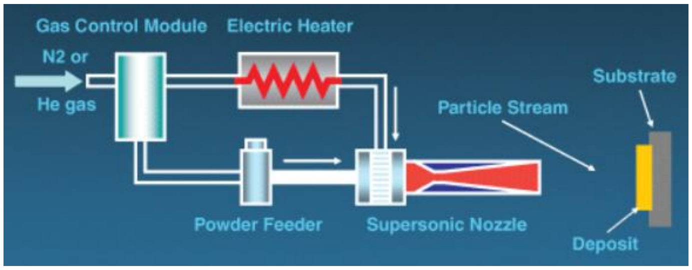

Figure 3.11 The cold spray process (Courtesy of U.S. Army Research Laboratory)

3.1.6 Summary

Even though all the processes can form laminate structure, the density of such structure varies according to different types of spray. HVOF has much higher kinetic energy than other spray process, thus it can result in much denser structure with nearly 0.5% porosity and plasma spray, since it has much higher thermal energy but relatively low kinetic energy, usually it can produce layers with 1-2% percent porosity and to be specific, controlled APS can produce fully dense laminate structure.

During operation, the thermal spray gun travels back and forth over the surface, each time as the gun travels, it can produce a layer of coating with 10 – 20 micrometer thickness. Oxidation happens at this time and melting process. Therefore, oxides can be found in the cross section of the layer. In application, depending on the requirement of the objective, oxidation can be minimized or neglected. The typical way to avoid oxidation is to use VPS; however, VPS cannot achieve zero oxidation percent.

The contamination can be found from 3 sources: raw powder, spray gun and substrate. As mentioned before, the contamination on the substrate can result weak mechanical bonding between coating and substrate. In the coating, contamination, or, impurities may from raw materials or thermal spray gun. Impurities can be trapped in the coatings as the spraying process continues. This can lower the stress of the coating and affect the properties of the coatings. In some cases, impurities can improve the properties but it depends on the purpose of spray.

Post-coat treatment is necessary since the surface of thermal sprayed coating is rough and internal cracks and porosity can affect the mechanical properties, as well we thermal conductivity and electrical conductivity. Polishing and heat treatment are the typical treatment that applied on the coatings. In other word, polishing can smooth the surface in wear protection application and heat treatment can decrease the amount of cracks and porosity.

3.2 Thin Film Technique

A thin film is a layer of material ranging from fractions of a nanometer (monolayer) to several micrometers in thickness. Electronic semiconductor devices and optical coatings are the main applications benefiting from thin-film construction. A familiar application of thin films is the household mirror, which typically has a thin metal coating on the back of a sheet of glass to form a reflective interface. The process of silvering was once commonly used to produce mirrors. A very-thin-film coating (less than about 50 nanometers thick) is used to produce two-way mirrors.

It is useful in the manufacture of optics (for reflective, anti-reflective coatings or self-cleaning glass, for instance), electronics (layers of insulators, semiconductors, and conductors form integrated circuits), packaging (i.e., aluminum-coated PET film), and in contemporary art (see the work of Larry Bell). Similar processes are sometimes used where thickness is not important: for instance, the purification of copper by electroplating, and the deposition of silicon and enriched uranium by a CVD-like process after gas-phase processing. Deposition techniques fall into two broad categories, depending on whether the process is primarily chemical or physical

3.2.1 Physical vapor deposition (PVD)

Physical vapor deposition (PVD) describes a variety of vacuum deposition methods used to deposit thin films by the condensation of a vaporized form of the desired film material onto various workpiece surfaces. The coating method involves purely physical processes such as high-temperature vacuum evaporation with subsequent condensation, or plasma sputter bombardment rather than involving a chemical reaction at the surface to be coated as in chemical vapor deposition. The term physical vapor deposition originally appeared in the 1966 book Vapor Deposition by C. F. Powell, J. H. Oxley and J. M. Blocher Jr. Physical vapor deposition coating is a process that is currently being used to enhance a number of products, including automotive parts like wheels and pistons, surgical tools, drill bits, and guns.

The current version of physical vapor deposition was completed in 2010 by NASA scientists at the NASA Glenn Research Center in Cleveland, Ohio. This physical vapor deposition coating is made up of thin layers of metal that are bonded together through a rig that NASA finished developing in 2010. In order to make the coating, developers put the essential ingredients into the rig, which drops the surrounding atmospheric pressure to one torr. From there, the coating is heated with a plasma torch that reaches 17,540 degrees Fahrenheit or 9,727 degrees Celsius. NASA's PS-PVD is one of only two such facilities in the USA and one of four in the world. In the automotive world, it is the newest alternative to the chrome plating that has been used for trucks and cars for years. This is because it has been proven to increase durability and weigh less than chrome coating, which is an advantage because a vehicle's acceleration and fuel efficiency will increase. Physical vapor deposition coating is gaining in popularity for many reasons, including that it enhances a product’s durability. In fact, studies have shown that it can enhance the lifespan of an unprotected product tenfold.

3.2.2 Chemical vapor deposition (CVD)

Chemical vapor deposition (CVD) is a chemical process used to produce high quality, high-performance, solid materials. The process is often used in the semiconductor industry to produce thin films. In typical CVD, the wafer (substrate) is exposed to one or more volatile precursors, hich react and/or decompose on the substrate surface to produce the desired deposit. Frequently, volatile by-products are also produced, which are removed by gas flow through the reaction chamber. Microfabrication processes widely use CVD to deposit materials in various forms, including: monocrystalline, polycrystalline, amorphous, and epitaxial.

This reaction is usually performed in LPCVD systems, with either pure silane feedstock, or a solution of silane with 70–80% nitrogen. Temperatures between 600 and 650 °C and pressures between 25 and 150 Pa yield a growth rate between 10 and 20 nm per minute. An alternative process uses a hydrogen-based solution. The hydrogen reduces the growth rate, but the temperature is raised to 850 or even 1050 °C to compensate.

3.2.3 Lithography

Lithography (from Greek) is a method of printing originally based on the immiscibility of oil and water. Printing is from a stone (lithographic limestone) or a metal plate with a smooth surface. Lithography can be used to print text or artwork onto paper or other suitable material. Lithography originally used an image drawn with oil, fat, or waxes onto the surface of a smooth, level lithographic limestone plate. In modern lithography, the image is made of a polymer coating applied to a flexible aluminum plate. The image can be printed directly from the plate (the orientation of the image is reversed), or it can be offset, by transferring the image onto a flexible sheet (rubber) for printing and publication.

As a printing technology, lithography is different from intaglio printing wherein a plate is either engraved, etched, or stippled to score cavities to contain the printing ink; and woodblock printing or letterpress printing, wherein ink is applied to the raised surfaces of letters or images. Today, most types of high-volume books and magazines, especially when illustrated in color, are printed with offset, which has become the most common form of printing technology since the 1960s. The word lithography also denotes photolithography, a microfabrication technique used in the microelectronics industry to make integrated circuits and microelectromechanical. Photolithography is one of these methods, often applied to semiconductor manufacturing of microchips. Photolithography is also commonly used for fabricating Microelectromechanical systems (MEMS) devices. Photolithography generally uses a pre-fabricated photomask or reticle as a master from which the final pattern is derived.

3.2.4 Etching

Etching is traditionally the process of using strong acid or mordant to cut into the unprotected parts of a metal surface to create a design in intaglio in the metal. In modern manufacturing, other chemicals may be used on other types of material. As a method of printmaking, it is, along with engraving, the most important technique for old master prints, and remains in wide use today.

In pure etching, a metal plate is covered with a waxy ground which is resistant to acid. The artist then scratches off the ground with a pointed etching needle where he or she wants a line to appear in the finished piece, so exposing the bare metal. The plate is then dipped in a bath of acid, technically called the mordant or etchant, or has acid washed over it. The acid "bites" into the metal where it is exposed, leaving behind lines sunk into the plate. The remaining ground is then cleaned off the plate. The plate is inked all over, and then the ink wiped off the surface, leaving only the ink in the etched lines. The second way to apply hard ground is by liquid hard ground. This comes in a can and is applied with a brush upon the plate to be etched. Exposed to air the hard ground will harden. Some printmakers use oil/tar based bitumen as hard ground, although often bitumen is used to protect steel plates from rust and copper plates from aging. Soft ground also comes in liquid form and is allowed to dry but it does not dry hard like hard ground and is impressionable. After the soft ground has dried the printmaker may apply materials such as leaves, objects, hand prints and so on which will penetrate the soft ground and expose the plate underneath.

3.3 Background of Ionization Radiation

Sunshine is one of the most familiar forms of radiation. It delivers light, heat and suntans. While enjoying and depending on it, we control our exposure to it. Beyond ultraviolet radiation from the sun are higher-energy kinds of radiation which are used in medicine and which we all get in low doses from space, from the air, and from the earth and rocks. It can cause damage to matter, particularly living tissue. At high levels it is therefore dangerous, so it is necessary to control our exposure. Living things have evolved in an environment which has significant levels of ionizing radiation.

Furthermore, many people owe their lives and health to such radiation produced artificially. Medical and dental X-rays discern hidden problems. Other kinds of ionizing radiation are used to diagnose ailments, and some people are treated with radiation to cure disease. Ionizing radiation, such as occurs from uranium ores and nuclear wastes, is part of our human environment, and always has been so. At high levels it is hazardous, but at low levels such as we all experience naturally, it is harmless. Considerable effort is devoted to ensuring that those working with nuclear power are not exposed to harmful levels of radiation from it. Standards for the general public are set about 20 times lower still, well below the levels normally experienced by any of us from natural sources. Background radiation is that ionizing radiation which is naturally and inevitably present in our environment. Levels of this can vary greatly. A lot of our natural exposure is due to radon, a gas which seeps from the Earth's crust and is present in the air we breathe.

3.3.1 Gamma radiation

Gamma radiation, also known as gamma rays, denoted by the Greek letter γ, refers to electromagnetic radiation of an extremely high frequency and is therefore high energy photons. Gamma rays are ionizing radiation, and are thus biologically hazardous. They are classically produced by the decay of atomic nuclei as they transition from a high energy state to a lower state known as gamma decay, but may also be produced by other processes. Paul Villard, a French chemist and physicist, discovered gamma radiation in 1900, while studying radiation emitted from radium. Villard's radiation was named "gamma rays" by Ernest Rutherford in 1903.

Natural sources of gamma rays on Earth include gamma decay from naturally occurring radioisotopes, and secondary radiation from atmospheric interactions with cosmic ray particles. Rare terrestrial natural sources produce gamma rays that are not of a nuclear origin, such as lightning strikes and terrestrial gamma-ray flashes. Additionally, gamma rays are produced by a number of astronomical processes in which very high-energy electrons are produced, that in turn cause secondary gamma rays via bremsstrahlung, inverse Compton scattering and synchrotron radiation. However, a large fraction of such astronomical gamma rays are screened by Earth's atmosphere and can only be detected by spacecraft.

Gamma rays typically have frequencies above 10 exahertz (or >1019 Hz), and therefore have energies above 100 keV and wavelengths less than 10 picometers (10−12 meter), which is less than the diameter of an atom. However, this is not a hard and fast definition, but rather only a rule-of-thumb description for natural processes. Electromagnetic radiation from radioactive decay of atomic nuclei is referred to as "gamma rays" no matter its energy, so that there is no lower limit to gamma energy derived from radioactive decay. This radiation commonly has energy of a few hundred keV, and almost always less than 10 MeV. In astronomy, gamma rays are defined by their energy, and no production process need be specified. The energies of gamma rays from astronomical sources range to over 10 TeV, an energy far too large to result from radioactive decay. A notable example is extremely powerful bursts of high-energy radiation referred to as long duration gamma-ray bursts, of energies higher than can be produced by radioactive decay.

3.3.2 Neutron radiation

Neutrons may be emitted from nuclear fusion or nuclear fission, or from any number of different nuclear reactions such as from radioactive decay or reactions from particle interactions. Large neutron sources are rare, and are usually limited to large-sized devices like nuclear reactors or particle accelerators. Neutron radiation was discovered as a result of observing a beryllium nucleus reacting with an alpha particle thus transforming into a carbon nucleus and emitting a neutron, Be(α, n)C. The combination of an alpha particle emitter and an isotope with a large (α, n) nuclear reaction probability is still a common neutron source.

Cold, thermal and hot neutron radiation is most commonly used for scattering and diffraction experiments in order to assess the properties and the structure of materials in crystallography, condensed matter physics, biology, solid state chemistry, materials science, geology, mineralogy and related sciences. Neutron radiation is also used in select facilities to treat cancerous tumors due to its highly penetrating and damaging nature to cellular structure. Neutrons can also be used for imaging of industrial parts termed neutron radiography when using film, neutron radioscopy when taking a digital image, such as through image plates, and neutron tomography for three-dimensional images. Neutron imaging is commonly used in the nuclear industry, the space and aerospace industry, as well as the high reliability explosives industry.

Neutron radiation is often called indirectly ionizing radiation. It does not ionize atoms in the same way that charged particles such as protons and electrons do (exciting an electron), because neutrons have no charge. However, neutron interactions are largely ionizing, for example when neutron absorption results in gamma emission and the gamma ray (photon) subsequently removes an electron from an atom, or a nucleus recoiling from a neutron interaction is ionized and causes more traditional subsequent ionization in other atoms. Because neutrons are uncharged, they are more penetrating than alpha radiation or beta radiation. In some cases they are more penetrating than gamma radiation, which is impeded in materials of high atomic number. In materials of low atomic number such as hydrogen, a low energy gamma ray may be more penetrating than a high energy neutron.

Neutrons also degrade materials; bombardment of materials with neutrons creates collision cascades that can produce point defects and dislocations in the materials. At high neutron fluences this can lead to embrittlement of metals and other materials, and to swelling in some of them. This poses a problem for nuclear reactor vessels and significantly limits their lifetime (which can be somewhat prolonged by controlled annealing of the vessel, reducing the number of the built-up dislocations). Graphite moderator blocks are especially susceptible to this effect, known as Wigner effect, and have to be annealed periodically; the well-known wind scale fire was caused by a mishap during such an annealing operation.

3.3.3 Ion beam radiation

An ion beam is a type of charged particle beam consisting of ions. Ion beams have many uses in electronics manufacturing (principally ion implantation) and other industries. A variety of ion beam sources exist some derived from the mercury vapor thrusters developed by NASA in the 1960s. Ion beams can be used for sputtering or ion beam etching and for ion beam analysis. Ion beam application, etching, or sputtering, is a technique conceptually similar to sandblasting, but using individual atoms in an ion beam to ablate a target. Reactive ion etching is an important extension that uses chemical reactivity to enhance the physical sputtering effect.

In a typical use in semiconductor manufacturing, a mask can selectively expose a layer of photoresist on a substrate made of a semiconductor material such as a silicon dioxide or gallium arsenide wafer. The wafer is developed, and for a positive photoresist, the exposed portions are removed in a chemical process. The result is a pattern left on the surface areas of the wafer that had been masked from exposure. The wafer is then placed in a vacuum chamber, and exposed to the ion beam. The impact of the ions erodes the target, abrading away the areas not covered by the photoresist.

Focused ion beam (FIB) instruments have numerous applications for characterization of thin film devices. Using a focused, high-brightness ion beam in a scanned raster pattern, material is removed (sputtered) in precise rectilinear patterns revealing a two-dimensional, or stratigraphic profile of a solid material. The most common application is to verify the integrity of the gate oxide layer in a CMOS transistor. A single excavation site exposes a cross section for analysis using a scanning electron microscope. Dual excavations on either side of a thin lamella bridge are utilized for preparing transmission electron microscope samples.

Another common use of FIB instruments is for design verification and/or failure analysis of semiconductor devices. Design verification combines selective material removal with gas-assisted material deposition of conductive, dielectric, or insulating materials. Engineering prototype devices may be modified using the ion beam in combination with gas-assisted material deposition in order to rewire an integrated circuit's conductive pathways. The techniques are effectively used to verify the correlation between the CAD design and the actual functional prototype circuit, thereby avoiding the creation of a new mask for the purpose of testing design changes. Materials science use sputtering for extending surface analytical techniques such as secondary ion mass spectrometry or electron spectroscopy (XPS, AES) so that they can depth profile them.

3.4 Materials Characterization

According to the equation of ZT, the following material properties need to be measured: thermal conductivity, electrical conductivity, Seebeck Coefficient, as shown below:

$$\mathrm{ZT} = \frac{\mathrm{S}^2\sigma}{\kappa}\mathrm{T} \qquad (3.1)$$

S represents Seebeck Coefficient; σ represents electrical conductivity and κ represents thermal conductivity.

3.4.1 X-ray diffraction (XRD) analysis, scanning electron microscopy (SEM)

X-ray crystallography is a method used for determining the atomic and molecular structure of a crystal, in which the crystalline atoms cause a beam of X-rays to diffract into many specific directions. By measuring the angles and intensities of these diffracted beams, a crystallographer can produce a three-dimensional picture of the density of electrons within the crystal. From this electron density, the mean positions of the atoms in the crystal can be determined, as well as their chemical bonds, their disorder and various other information.

Crystals are regular arrays of atoms, and X-rays can be considered waves of electromagnetic radiation. Atoms scatter X-ray waves, primarily through the atoms' electrons. Just as an ocean wave striking a lighthouse produces secondary circular waves emanating from the lighthouse, so an X-ray striking an electron produces secondary spherical waves emanating from the electron. This phenomenon is known as elastic scattering, and the electron (or lighthouse) is known as the scatter. A regular array of scatters produces a regular array of spherical waves. Although these waves cancel one another out in most directions through destructive interference, they add constructively in a few specific directions, determined by Bragg's law [118]:

$$2d\sin\theta = n\lambda \tag{3.2}$$

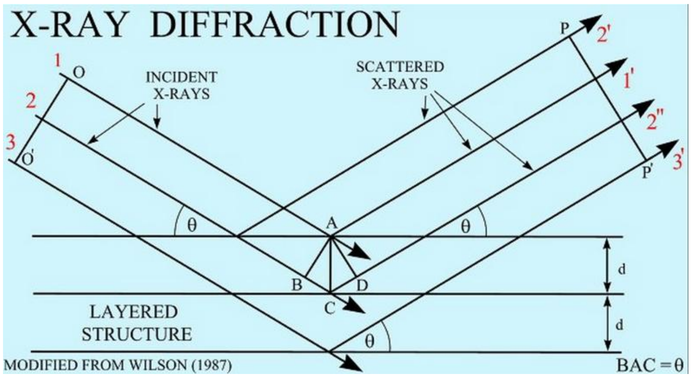

Figure 3.12 Bragg's law [119]

A scanning electron microscope (SEM) is a type of electron microscope that produces images of a sample by scanning it with a focused beam of electrons. The electrons interact with atoms in the sample, producing various signals that can be detected and that contain information about the sample's surface topography and composition. The electron beam is generally scanned in a raster scan pattern, and the beam's position is combined with the detected signal to produce an image. SEM can achieve resolution better than 1 nanometer. Specimens can be observed in high vacuum, in low vacuum, and (in environmental SEM) in wet conditions.

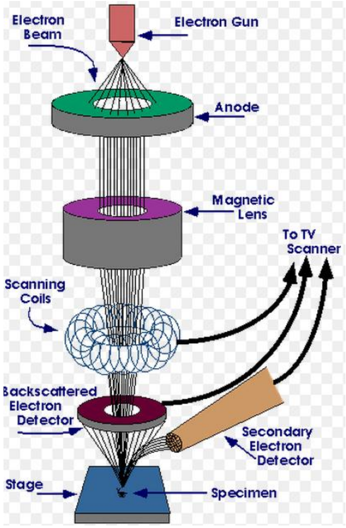

Figure 3.13 Principle of SEM (Courtesy of Purdue U)

The most common mode of detection is by secondary electrons emitted by atoms excited by the electron beam. The number of secondary electrons is a function of the angle between the surface and the beam. On a flat surface, the plume of secondary electrons is mostly contained by the sample, but on a tilted surface, the plume is partially exposed and more electrons are emitted. By scanning the sample and detecting the secondary electrons, an image displaying the tilt of the surface is created.

Figure 3.14 SEM facility (Courtesy of Susan)

Energy-dispersive X-ray spectroscopy (EDS, EDX, or XEDS) [120] is an analytical technique used for the elemental analysis or chemical characterization of a sample. It relies on the investigation of an interaction of some source of X-ray excitation and a sample. Its characterization capabilities are due in large part to the fundamental principle that each element has a unique atomic structure allowing unique set of peaks on its X-ray spectrum. To stimulate the emission of characteristic X-rays from a specimen, a high-energy beam of charged particles such as electrons or protons (see PIXE), or a beam of X-rays, is focused into the sample being studied. At rest, an atom within the sample contains ground state (or unexcited) electrons in discrete energy levels or electron shells bound to the nucleus. The incident beam may excite an electron in an inner shell, ejecting it from the shell while creating an electron hole where the electron was. An electron from an outer, higher-energy shell then fills the hole, and the difference in energy between the higher-energy shell and the lower energy shell may be released in the form of an X-ray. The number and energy of the X-rays emitted from a specimen can be measured by an energy-dispersive spectrometer. As the energy of the X-rays are characteristic of the difference in energy between the two shells, and of the atomic structure of the element from which they were emitted, this allows the elemental composition of the specimen to be measured.

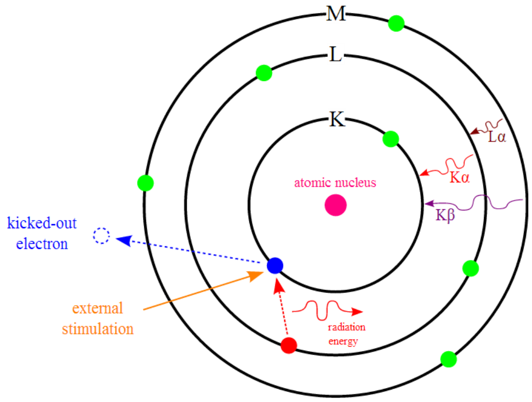

Figure 3.15 Principle of EDX (Courtesy of Muso)

3.4.2 Transmission electron microscopy (TEM)

Transmission electron microscopy (TEM) is a microscopy technique in which a beam of electrons is transmitted through an ultra-thin specimen, interacting with the specimen as it passes through. An image is formed from the interaction of the electrons transmitted through the specimen; the image is magnified and focused onto an imaging device, such as a fluorescent screen, on a layer of photographic film, or to be detected by a sensor such as a CCD camera.

TEMs are capable of imaging at a significantly higher resolution than light microscopes, owing to the small de Broglie wavelength of electrons. This enables the instrument's user to examine fine detail—even as small as a single column of atoms, which is thousands of times smaller than the smallest resolvable object in a light microscope. TEM forms a major analysis method in a range of scientific fields, in both physical and biological sciences. TEMs find application in cancer research, virology, materials science as well as pollution, nanotechnology, and semiconductor research.

At smaller magnifications TEM image contrast is due to absorption of electrons in the material, due to the thickness and composition of the material. At higher magnifications complex wave interactions modulate the intensity of the image, requiring expert analysis of observed images. Alternate modes of use allow for the TEM to observe modulations in chemical identity, crystal orientation, electronic structure and sample induced electron phase shift as well as the regular absorption based imaging.

3.4.3 Thermal conductivity measurement

3.4.3.1 Bulk samples

Thermal conductivity of our samples are measured using laser flash method [121]. The laser flash analysis or laser flash method is used to measure thermal diffusivity of a multiplicity of different materials. An energy pulse heats one side of a plane-parallel sample. The temperature rise on the backside due to the energy input is time-dependent detected. The higher the thermal diffusivity of the sample, the faster the energy reaches the backside. A state-of-the-art laser flash apparatus (LFA) to measure thermal diffusivity over a broad temperature range is shown on the right hand side. In a one-dimensional, adiabatic case the thermal diffusivity α is calculated from this temperature rise as follows:

$$\alpha = 0.1388 \cdot \frac{d^2}{t_{1/2}} \tag{3.3}$$

Here, d is the thickness of the sample and $t_{1/2}$ is the time to half maximum.

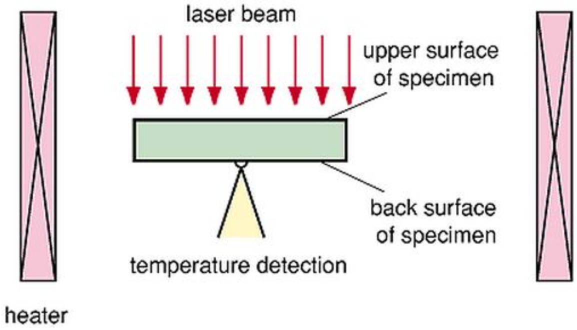

Figure 3.16 Measuring principle of thermal diffusivity by laser flash method [122]

The laser flash method was developed by Parker et al. in 1961 [123]. In a vertical setup a light source (e.g. laser, flashlamp) heats the sample from the bottom side and a detector on top detects the time-depedent temperature rise. For measuring the thermal diffusivity, which is strongly temperature-dependent, at different temperatures the sample can be placed in a furnace at constant temperature. Perfect conditions are homogenous material, a homogenous energy input on the front side a time-dependent short pulse - in form of a Dirac delta function. Several improvements on the models have been made. In 1963 Cowan takes radiation and convection on the surface into account [124].

Figure 3.17 Thermal conductivity testing machine

Figure 3.18 Thermal conductivity testing machine with pump

The red cylinder on the top of the machine is used for liquid nitrogen container, which is used for cooling purposes during the experiment. Remember that laser flash will be flashed during the experiment; liquid nitrogen can be used as proper cooling material because 1) it has low temperature 2) it evaporates only be become gaseous nitrogen which is not being viewed as contamination. A vacuum pump is connected to the testing chamber and the testing chamber has to be vacuumed every time before start to run. After vacuum the chamber, the nitrogen tank, which is the black tank on the right hand side of the picture needs to be turn on so that the testing chamber can be filled with nitrogen as protection gas. At the same time, there is water cooling system in the machine so that the testing chamber can be cooled when needed and at the same time, protect the machine from overheating.

3.4.3.2 Thin film samples

One popular technique for thermoelectric materials is a 3ω-method, in which a thin metal strip evaporated on the sample acts as heat source and a thermometer. The heater is driven with AC current at frequency ω, which causes heat source to oscillate at frequency 2ω. By monitoring AC voltage as a function of the frequency of the applied AC current thermal conductivity can be determined. The measured voltage will contain both ω and 3ω components, because the Joule heating of the film causes small perturbation to its resistance with frequency 2ω.

Thermal conductivity is determined by the linear slope of ΔT vs. log(ω) curve. The main advantages of the 3ω-method are minimization of radiation effects and easier acquisition of the temperature dependence of the thermal conductivity than in the steady-state techniques. Although some expertise in thin film patterning and microlithography is required, this technique is considered as the best pseudo-contact method available

3.4.4 Electrical properties measurement

The measurement of electrical conductivity is based on the flowing three equations:

$$\mathrm{R} = \frac{\mathrm{V}}{\mathrm{I}} \tag{3.4}$$

$$\rho = \mathrm{R}\frac{\mathrm{A}}{\mathrm{L}} \tag{3.5}$$

$$\sigma = \frac{1}{\rho} \tag{3.6}$$

The first equation is Ohm’s law; R is electrical resistance, V is voltage across the measured sample and “I” is the current that flows through the sample. The unit of R is Ohm, Ω. The second equation is Pouillet’s law; ρ is electrical resistivity, R is electrical resistance, A is the area of the cross section of the specimen and L the length of the specimen; electrical resistivity has a unit of ohm•meter, Ω•m. The third equation is the definition of electrical conductivity; electrical conductivity is expressed as σ, it is inversely proportional to electrical resistivity. It has an SI unit of Siemen per meter (S/m).

Electrical resistivity can be measured by “two probes method” and “four probes method”, and electrical conductivity can be calculated according the third equation above.

3.4.4.1 Two probes method

For a long and wire-like specimen with uniform structure and composition, or a sample of parallelepiped shape with uniform structure and composition, the electrical resistivity can be measured by applying an electrical current across the specimen and measure the electrical voltage at the two ends of the specimen. Combining above equations, the electrical resistivity can be written as:

$$\rho = \frac{V}{I}\frac{A}{L} \tag{3.7}$$

All the measurement can be completed by using multi-meter. The two probe can be placed at X and Y positions to apply current. The blue bar is the specimen that is to be measured. However, there are limitations about two-probe method: the contact between two probe and specimen can be the reason of error; this method can only measure wire-like sample and at the same time, if the wire is too thin, it will be more difficult to contact the two probes; In addition, two probe is not as accurate as four probe because in four probe method, the voltage meter have large impedance.

3.4.4.2 Four probes method

Four-probe method eliminates the limitations of two-probe method. It can measure sample with various shapes. The typical set up of this method is equal-distance placement of four in-line probes, or points, the spacing of between every two probes is usually 1 mm. Current is applied through the outer two probes and is measured; at the same time, the inner two probes measure the electrical voltage between these two points and then calculate the electrical resistivity.

In four probes method, the outer probes source the current through the sample; the inner probes measure the voltage. One need to be noted is that the surface condition is very sensitive to the measurement because contaminations, such the oxidation of the surface can contribute increase of resistivity or, affect the contact between the probes and sample.

3.4.4.3 Thin film resistivity measurement

When measuring resistivity of a large specimen, the equation of the electrical resistivity can be written as follow [125]:

$$\rho = \frac{V}{I} 2\pi s \tag{3.8}$$

It is assumed that the thickness of the sample is larger than the distance between every two probes; usually it is five times larger; here, s stands for the distance between every two probes.

In this project, electrical conductivity usually takes place at a conducting substrate or non-conducting substrate. The equations for these conditions are:

$$\rho = \frac{\rho_0}{G_6(t/s)} \tag{3.9}$$

$$\rho = \frac{\rho_0}{G_7(t/s)} \tag{3.10}$$

In these two cases, ρ0 stands for the electrical resistivity of large specimen. The denominators of the two equations are value of functions which can be found in the literature. When the ratio of thickness over distance is small, they can be replaced by such formula:

$$G_7(t/s) = \frac{2s}{t} \ln 2 \tag{3.11}$$

Insert equation 3.11 into 3.10, the electrical conductivity can be written as:

$$\rho = \frac{\pi t}{\ln 2} \frac{V}{I} = 4.5324 \cdot t \cdot \frac{V}{I} \tag{3.12}$$

Meanwhile, all the parameter can also be found in the literature[126].

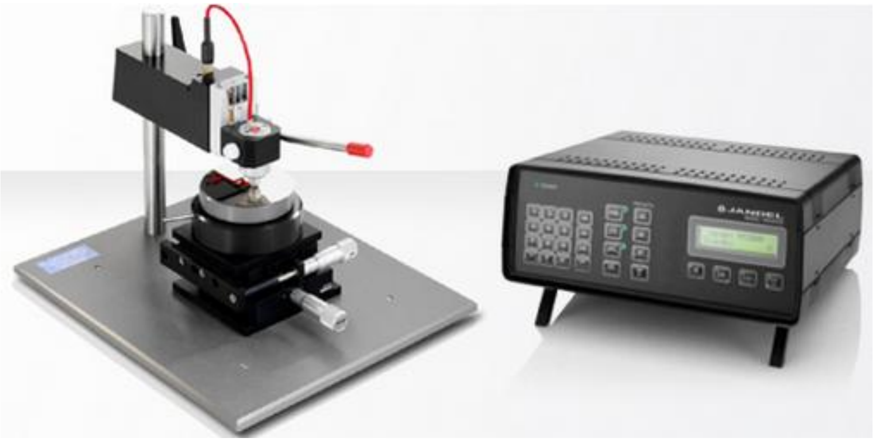

Figure 3.19 Multi Height Microposition Probe with RM3000 Test Unit

3.4.4.4 Van der Pauw method

The van der Pauw Method is a technique commonly used to measure the resistivity and the Hall coefficient of a sample. Its power lies in its ability to accurately measure the properties of a sample of any arbitrary shape, so long as the sample is approximately two-dimensional (i.e. it is much thinner than it is wide) and the electrodes are placed on its perimeter.

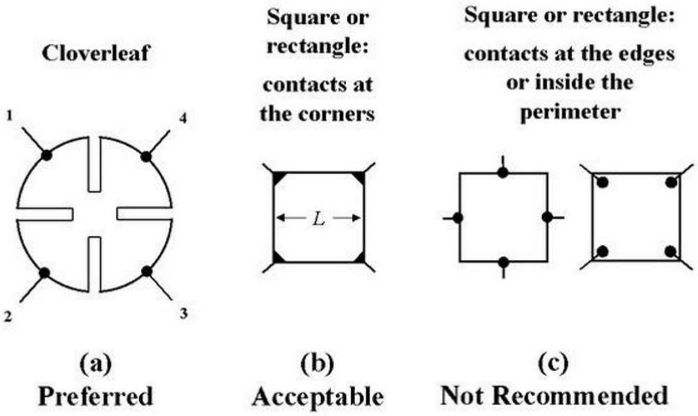

Figure 3.19 Van der pauw contact placement (Courtesy of Wikimedia Commons)

In order to use the van der Pauw method, the sample thickness must be much less than the width and length of the sample. In order to reduce errors in the calculations, it is preferable that the sample is symmetrical. There must also be no isolated holes within the sample. The measurements require that four ohmic contacts be placed on the sample. Certain conditions for their placement need to be met: a) they must be on the boundary of the sample (or as close to it as possible). b) They must be infinitely small. Practically, they must be as small as possible; any errors given by their non-zero size will be of the order D/L, where D is the average diameter of the contact and L is the distance between the contacts. In addition to this, any leads from the contacts should be constructed from the same batch of wire to minimize thermoelectric effects. For the same reason, all four contacts should be of the same material.

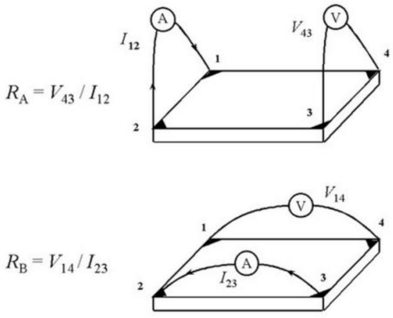

Figure 3.20 Van der Pauw method (Courtesy of Vladislav)

By measure from different direction, see R_A and R_B in the above figure, the correct resistance value can be obtained by some average.

3.4.4.5 Hall Effect measurement

The Hall effect is the production of a voltage difference (the Hall voltage) across an electrical conductor, transverse to an electric current in the conductor and a magnetic field perpendicular to the current. It was discovered by Edwin Hall in 1879. [127]

The Hall coefficient is defined as the ratio of the induced electric field to the product of the current density and the applied magnetic field. It is a characteristic of the material from which the conductor is made, since its value depends on the type, number, and properties of the charge carriers that constitute the current.

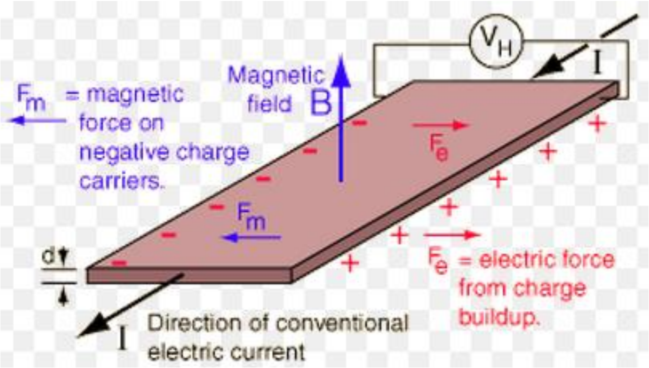

Figure 3.21 Diagram of Hall Effect (Courtesy of George State U)

The Hall Effect is due to the nature of the current in a conductor. Current consists of the movement of many small charge carriers, typically electrons, holes, ions or all three. When a magnetic field is present that is not parallel to the direction of motion of moving charges, these charges experience a force, called the Lorentz force.[3] When such a magnetic field is absent, the charges follow approximately straight, 'line of sight' paths between collisions with impurities, phonons, etc. However, when a magnetic field with a perpendicular component is applied, their paths between collisions are curved so that moving charges accumulate on one face of the material. This leaves equal and opposite charges exposed on the other face, where there is a scarcity of mobile charges. The result is an asymmetric distribution of charge density across the Hall element that is perpendicular to both the 'line of sight' path and the applied magnetic field. The separation of charge establishes an electric field that opposes the migration of further charge, so a steady electrical potential is established for as long as the charge is flowing.

In the classical view, there are only electrons moving in the same average direction both in the case of electron or hole conductivity. This cannot explain the opposite sign of the Hall Effect observed. The difference is that electrons in the upper bound of the valence band have opposite group velocity and wave vector direction when moving, which can be effectively treated as if positively charged particles (holes) moved in the opposite direction to that of the electrons. For a simple metal where there is only one type of charge carrier (electrons) the Hall voltage VH is given by

$$V_H = -\frac{IB}{net} \tag{3.13}$$

where I is the current across the plate length, B is the magnetic field, t is the thickness of the plate, e is the elementary charge, and n is the charge carrier density of the carrier electrons.

Figure 3.22 Hall Effect Measurement System

3.4.4.6 IV curve measurement

A current–voltage characteristic or I–V curve (current–voltage curve) is a relationship, typically represented as a chart or graph, between the electric current through a circuit, device, or material, and the corresponding voltage, or potential difference across it. In electronics, the relationship between the direct current (DC) through an electronic device and the DC voltage across its terminals is called a current–voltage characteristic of the device. Electronic engineers use these charts to determine basic parameters of a device and to model its behavior in an electrical circuit. These characteristics are also known as VI curves, referring to the standard symbols for current and voltage. A more general form of current–voltage characteristic is one that describes the dependence of a terminal current on more than one terminal voltage difference; electronic devices such as vacuum tubes and transistors are described by such characteristics. [128]

The simplest VI characteristic involves a resistor, which according to Ohm's Law exhibits a linear relationship between the applied voltage and the resulting electric. However, even in this case environmental factors such as temperature or material characteristics of the resistor can produce a non-linear curve.

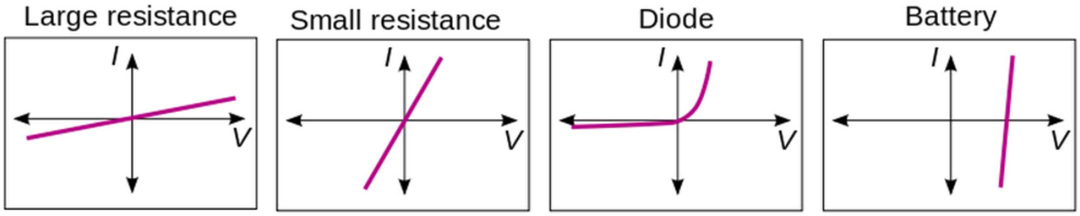

Figure 3.23 Four IV curves (Courtesy of Sbyrnes)

The transconductance and Early voltage of a transistor are examples of parameters traditionally measured with the assistance of an I–V chart, or laboratory equipment that traces the charts in real time on an oscilloscope.

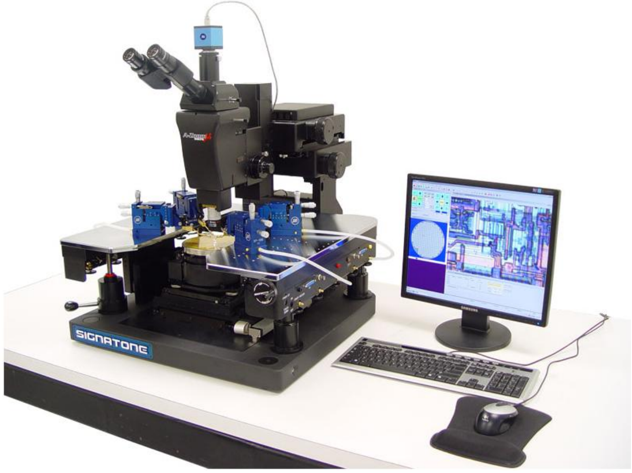

Figure 3.24 CM460 Semi-Automatic Probe Station (Courtesy of Signatone)

3.4.5 Seebeck coefficient measurement

The measurement of Seebeck Coefficient is always difficult to achieve because this measurement is based on the electrical voltage respond and temperature difference across the sample. Usually the unit of electrical voltage is micro volt which is on the noise level. In this project, the equipment for measuring Seebeck Coefficient is from MMR Technologies as shown below:

Figure 3.25 Seebeck testing machine with temperature controller

As introduced above, the Seebeck coefficient relates to temperature difference and is a response to the thermoelectric voltage. Therefore, it can be defined as follow:

$$S = -\frac{\Delta V}{\Delta T} \tag{3.14}$$

Where, ΔV and ΔT are voltage difference and temperature difference.

According to this equation, the value of S can be deduced. One way to calculate Seebeck from MMR technology [129] is as follow:

$$V_1 = S_1 \times \Delta T \tag{3.15}$$

$$V_2 = S_2 \times \Delta T \tag{3.16}$$

Where, the subscripts 1 and 2 represent sample and reference. Both these two materials have same temperature difference, thus:

$$S_1 = S_2 \times \frac{V_1}{V_2} \tag{3.17}$$

Note that the temperature difference is small, so is the thermoelectric voltage, any noise could affect the result of the measurement and such noise can hardly be removed since they may come from small parts in the measuring equipment, such as wires, connectors. Thus the direct measurement will not render high accuracy; however, the accuracy can be improved by taking two different measurements, using different sets of power parameter. The equation can be expressed as follow:

$$V_1(P_1) = S_1 \times \Delta T(P_1) + \Delta V_1 \tag{3.18}$$

$$V_2(P_1) = S_2 \times \Delta T(P_1) + \Delta V_2 \tag{3.19}$$

Where ΔV1 and ΔV2 are the undesired thermoelectric voltages, called offset voltage, produced by the equipment; P1 is the power that applied to the heater at the first time. The other set of measurement can be expressed as:

$$V_1(P_2) = S_1 \times \Delta T(P_2) + \Delta V_1 \tag{3.20}$$

$$V_2(P_2) = S_2 \times \Delta T(P_2) + \Delta V_2 \tag{3.21}$$

The offset voltages can be assumed to be the same because these offset voltages are caused by the dissipated heat from the heater; the immediate power change in the heater will only affect the sample and reference area. Based on the combination of equations 3.20 and 3.21, the overall value of Seebeck coefficient can be obtained:

$$S_1 = S_2 \frac{\{V_1(P_1) - V_1(P_2)\}}{\{V_2(P_1) - V_2(P_2)\}} \tag{3.22}$$

In order to acquire accurate data during the measurement, the temperature control is of key importance. MMR Technologies uses a secondary heating process to eliminate such noise. During the measurement, the calculation is based on the temperature difference across the sample; however, such temperature difference is not generated by the heater located below the sample but from the resistor in the front of the sample. For example, from temperature range 300K to 350K, the first heater brings up the temperature of the sample and reference to 350K and at this time, the secondary heater differentiate the sample and reference temperature to 1 – 3K, which is based on the different materials and power input.

Samples for Seebeck measurement were polished before testing. Sample size should be no longer than 4 mm in length and the diameter is variable as long as you have same reference with the same diameter. In fact, it’s hard to make the coatings into cylindrical shape. So during the experiment, sample was made into rectangular shape with square side of 0.5-0.7mm and 4mm in length. Since the polishing techniques were exactly same as polishing the substrate, the glue had to be used. Once the polishing was done, the glue needed to be washed off by acetone completely; otherwise it will affect the result of the measurement. Remember that the Seebeck Coefficient measurement requires a sample and a reference material (constantan wire) at the same time. The total volume of the sample should be tailored same as reference to draw same amount heat during measurement.

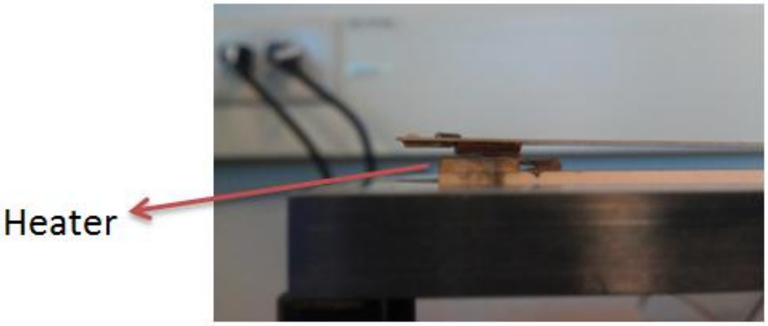

Figure 3.26 Lateral view of sample mounting

The sample and reference material were place on the thermal stage in V shape as discussed before by applying silver paste to adhere them on the stage. Silver paste need be placed before you can adhere you sample or reference on the stage. Multi-time silver paste layer is needed to give good adhesion. At the same time, the resistance of the resistor located on the top of the thermal stage needed to be checked, whose value should be 100 ohms, because sometime the silver paste may short the resistor and malfunction. After the silver paste was complete dry, the thermal stage can be put into the vacuum chamber for vacuum.

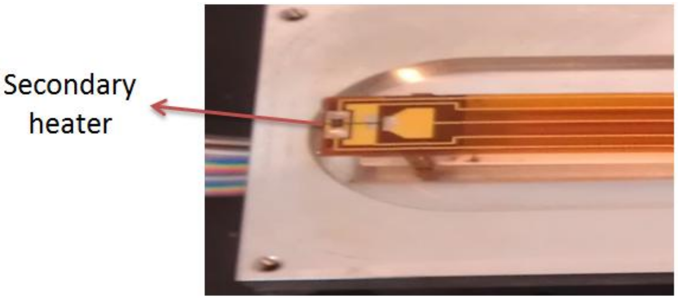

Figure 3.27 Oblique view of sample mounting

The heater in the vacuum chamber is called “refrigerator” because the primarily purpose was to cool down the samples. However, it worked as heater (see Fig 3.30) which could go up to 730 K because we are measuring above room temperature. In order to have a reliable heat transfer between the heater and the thermal stage, thermal paste should be applied in the contacting surface. Reliable thermal paste should be dense because the bottom of the thermal stage may not be flat and dense thermal paste can fill up the gap of the thermal stage and still has good contact at the end of the test. This is extremely important when using the ceramic thermal stage.

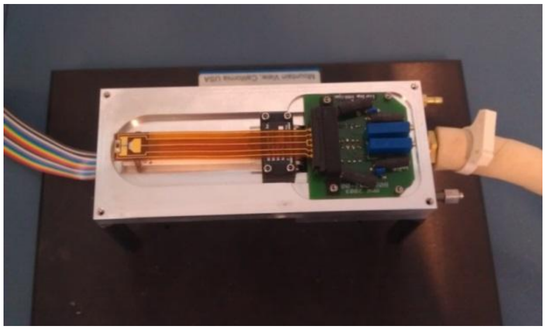

Figure 3.29 Seebeck testing machine in vacuum chamber

After putting the thermal stage into the vacuum chamber, the chamber is sealed and the vacuum is turned on. Figure 3.32 showed the vacuum pump which can vacuum the vacuum chamber. The pressure of the chamber is around 20-30 mTorr after evacuate for 15 minutes. Turn on the pump, the pressure gauge can read the pressure inside the chamber. At the same time, the machine needed to be warmed up. To guarantee the measurement, double click the icon of K-20 on the desktop of the computer, and then check the connection between the computer and the machine; click “test” button on the software, then click “TS” button to check the sensor type, if it tell you the type of the sensor, which should be RTD256, it means the sensor works fine. Then to check the connection, by clicking “TE”, if the connection is good, it should tell you the current temperature; if any one of them does not work, try to restart the software. If the problem is still there, disconnect all the ports and re-connect them after 5 seconds, and follow the same procedure to test the machine. If everything is ok, click “start” to start monitoring the temperature and then set up the destine temperature. In the experiment, the starting temperature was usually around 300K and the destine temperature for heating up was 302-303K, or any temperature that below your experiment temperature. The whole warming process takes 10 minutes. It would be better to warm the machine every time before the test.

Figure 3.28 Vacuum pump of Seebeck testing system

After 10 minutes warming up, turn off the K-20 software and double click the SB-100 icon to control the Seebeck testing machine. Same as using the K-20 software check the connection before start using the machine; the first thing need to be checked is connection. “TC” can tell the connection, if the software says “communication is OK”, it means you can go to the next step; if not, restart software or disconnect and re-connect the ports. Then click “TE”, it should check the sensor and tells the temperature now which should be the destine temperature; then check the voltage of the sample and reference. “GV1” can tell you the voltage of the reference and “GV2” tells you the voltage of the sample. Both of the voltages should be within the plus or minus 100 µV but the standard that was used during the experiment was around plus or minus 50 µV. At this time, if the voltage is not within this range, the measurement should be terminated because it will not give accurate measurement; one of the typical reasons for this is bad sample mounting; if the voltage is ok, the measurement can begin.

Click the setting menu and set the starting temperature and final temperature, and temperature step as well. The operation delay and initial delay were used as default, 30 sec for each of them; the power input is 60mW for kapton thermal stage and 130mW for ceramic thermal stage. After setting up the parameters, click “play” button in the software. The way to check if the measurement is correct is to see the temperature difference. The correct one should be above 1K, if not, try to improve the power input, if nothing changes which means the sample mounting was not good. Then try to check the fuse at back of machine. Note that the incorrect resistance of the resistor that located on the top of the stage can also cause the short of the fuse. As the temperature goes up, the Seebeck Coefficient should change along with it. If not, it could because of the bad heat transfer between the heater and thermal stage or the bad sample mounting.

4 THERMAL SPRAY OF THERMOELECTRIC MATERIAL

An innovative, integrated approach towards cost effective and industrially-scalable thermoelectric generators (TEGs) for vehicle applications has been proposed. It based on thermal spray technology to directly fabricate TE structures in a layered fashion onto exhaust components for robust and durable performance. The fabrication will involve a novel extension to the thermal spray process, namely direct write thermal spray coupled with laser micromachining to create 2D and 3D mesoscale TE structures. The non-equilibrium thermal spray process will provide deposited thermoelectric material. Further, the manufacturing process itself is readily scalable for industrial volumes required for practical implementation of vehicle TEGs. This concept starts with high-ZT materials based on Mg2Si and filled skutterudites that have their native ZT increased significantly by using rapid quenching to form non-equilibrium embedded nanostructures that suppress phonon transport and boost ZT. These materials are abundant, environmentally friendly and relatively inexpensive. Using advanced thermal spray facilities and process control, these strategies will be transitioned to the thermal spray process for device level integration for production scale volumes. In our approach, the interface adhesion between material layers is intrinsically strong, with no adhesives or mechanical pressure required. Cylindrical exhaust components (or virtually any conformal surface) can be readily fabricated, making integration into existing vehicle exhaust systems straightforward and inexpensive.

4.1 Pre-experiment of Mg_2Si

4.1.1 Experiment

Mg_2Si powder (purity > 98%) purchased from YHL New Energy CO.,Ltd (Zhejiang China) was used to deposit coatings on aluminum/titanium plates of size 40 x 25 x 2mm. The grain sizes of the powder range from 10 to 80 μm. The purer powders were not used because 1) starting from the low purity powder, proper thermal spray parameters can be found; 2) the purer Mg_2Si powder is very expensive and was not available with the required powder size and shape. For APS, Sulzer Metco F4-MB plasma torch and SG100 were used and for VPS the Plasma-Technik A-3000S VPS System is used. The parameters of the thermal sprays are shown in Table 4-1.

Table 4-1 Thermal spray parameters

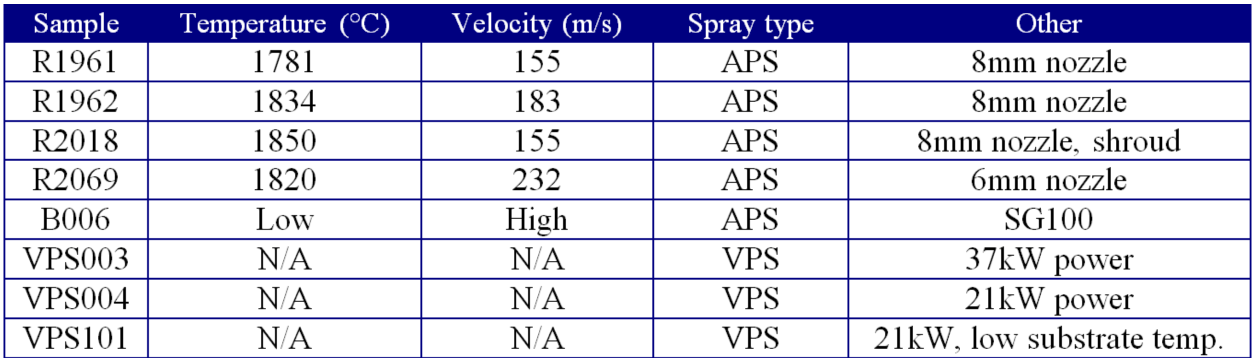

Sample	Temperature (°C)	Velocity (m/s)	Spray type	Other
R1961	1781	155	APS	8mm nozzle
R1962	1834	183	APS	8mm nozzle
R2018	1850	155	APS	8mm nozzle, shroud
R2069	1820	232	APS	6mm nozzle
B006	Low	High	APS	SG100
VPS003	N/A	N/A	VPS	37kW power
VPS004	N/A	N/A	VPS	21kW power
VPS101	N/A	N/A	VPS	21kW, low substrate temp.

The sample phase was analyzed by X-ray diffraction (XRD) (PAD-V, SCITAG Ing., CA, USA) utilizing Cu Kα radiation. The composition is calculated using MDI Jade software. Coating images were observed using a Scanning electric microscope (SEM) (Leo-1550-SFEG, Carl Zeiss SMT Ltd, Cambridge UK). Seebeck coefficient is measured using MMR's SB-100 Seebeck Measurement System and K20 temperature controller (MMR Technologies, CA). The substrate of the sprayed coating is polished and a 1x1x4mm long bar free standing sample is used for Seebeck measurement.

4.1.2 Results and discussion

4.1.2.1 Phase composition of thermal sprayed coatings

The XRD results of the APS are compared with the feed stock powder which is shown in in Figure 4.1(a). As can be seen, thermal spray results in oxidation, which is generally detrimental to thermoelectric properties. Samples R1961 and R1962 are both APS with 8mm nozzle, but R1962 is in higher temperature and velocity, which gave higher concentration of Si. The reaction between Mg_2Si and O2 is around 450 °C, while the temperature during thermal spray is significantly higher than this. The reaction is:

$$Mg_2Si + O2 \xrightarrow{450\ °C} MgO + Si$$

Several techniques have been tried to reduce the oxidation of Mg_2Si during the spray process, including APS with a shroud (R2018), APS with a smaller nozzle (R2069) and APS with an SG100 gun (B006). From table 4-2, we see APS with shroud does help but the improvement is limited. APS with smaller nozzle (R2069) has better result but oxidation is still too high for thermoelectric applications. We tried another set of high velocity low temperature APS using SG100 gun with internal powder passage to avoid oxidation. The XRD result of B006 is very consistent with the feedstock powder, although very small MgO and Si peak are found. The reason B006 shows Mg peak is low temperature and high velocity condition which suppress the oxidation of Mg. Meanwhile, the internal passage of powder in SG100 gun can further eliminate the chance of reaction between powder and ambient air.

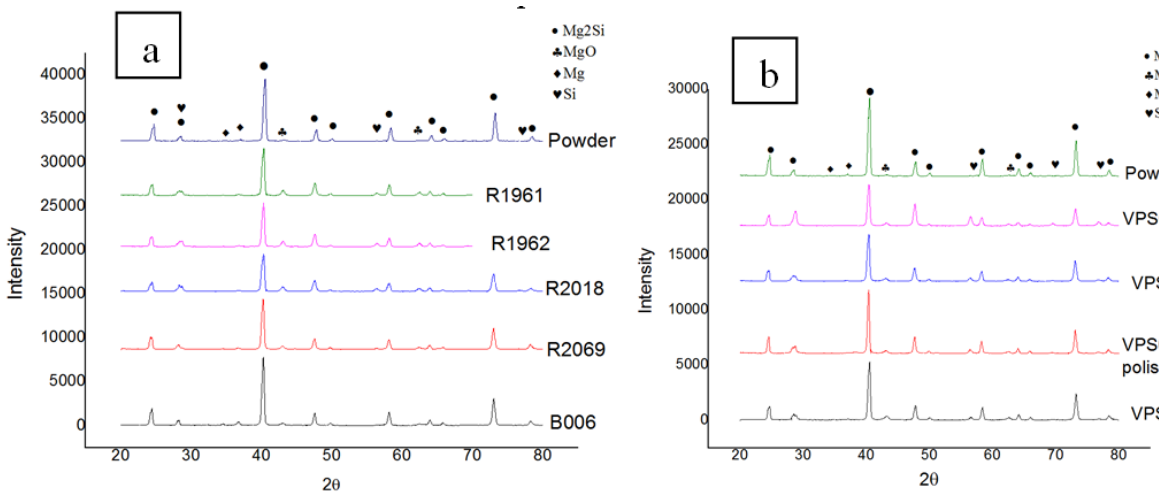

Figure 4.1 XRD of APS (a) and VPS (b) coating

In attempt to reduce the oxidation during the spray, VPS was used to prepare Mg_2Si samples. Figure 4.1(b) shows the XRD results for VPS. Improvement can be seen, that the lower O2 concentration helped reduce oxidation in APS. Normally, the VPS has higher temperature than APS because of lower heat convection in the vacuum chamber. Mg has a very high vapor pressure, so high temperate in VPS can evaporate Mg and leave Si behind. This is why VPS coatings have higher concentration of Si. It appears to be difficult to completely avoid oxidation and Si by VPS. VPS101 is the most recent coating fabricated using 21kW and substrate temperature control method.

Table 4-2 Concentrations of different composition in powder and coatings

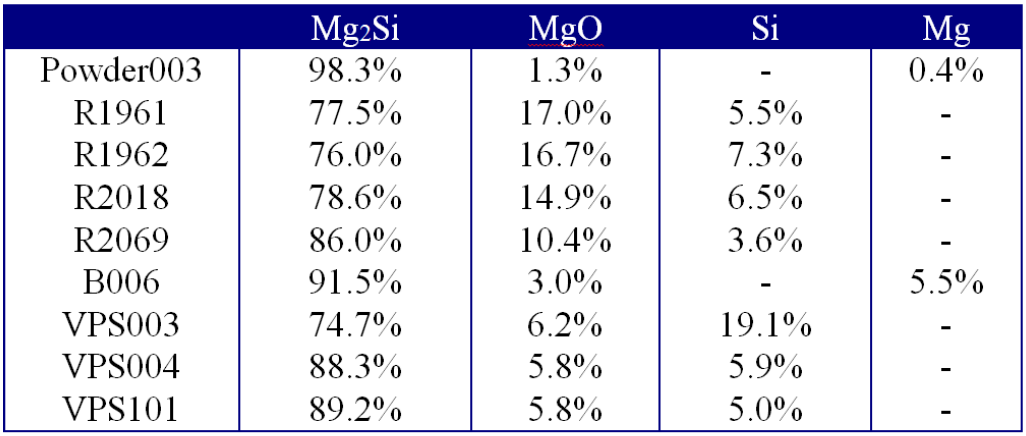

	Mg_2Si	MgO	Si	Mg
Powder003	98.3%	1.3%	-	0.4%
R1961	77.5%	17.0%	5.5%	-
R1962	76.0%	16.7%	7.3%	-
R2018	78.6%	14.9%	6.5%	-
R2069	86.0%	10.4%	3.6%	-
B006	91.5%	3.0%	-	5.5%
VPS003	74.7%	6.2%	19.1%	-
VPS004	88.3%	5.8%	5.9%	-
VPS101	89.2%	5.8%	5.0%	-

From figure 4.1 and Table 4-2, VPS did reduce some oxidation but the concentration is still far too high for practical applications. Part of the issue may be the high reactivity and vapor pressure of Mg. The vacuum produced during VPS is around 10-4 Torr hence a small quantity of oxygen will still be present that can react with Mg at high processing temperatures. More investigation of VPS for Mg_2Si is needed to decide whether it is a viable approach for thermal spraying of Mg_2Si materials for thermoelectric applications.

4.1.2.2 SEM result of thermal sprayed coatings

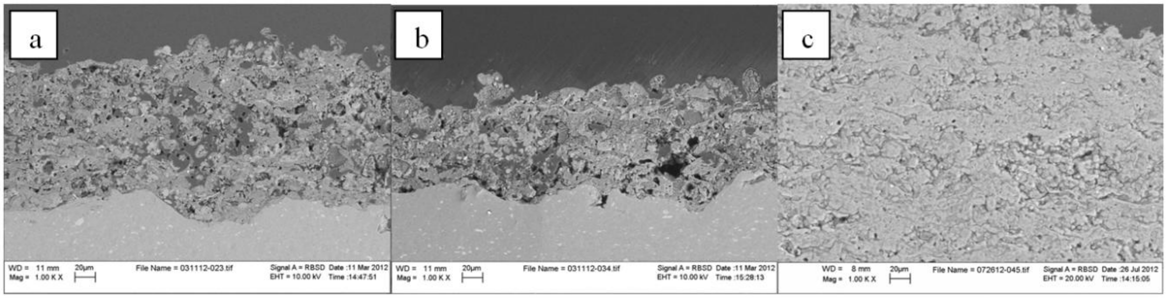

Figure 4.2 SEM of APS samples: a) R1961, b) R1962, c) B006

Figure 4.2 shows SEM images of several APS samples. The low temperature high speed APS (B006) gives a denser microstructure, while bonding in R1961 and R1962 is quite poor. B006 shows softening instead of melting; this condition just softens the powder. Figure 4.3 shows the higher temperature results in a denser coating. VPS003 and VPS004 were sprayed at 21kW and 17kW without substrate temperature control. VPS101 was sprayed at 21kW with a large metal plate attached to substrate to maintain the substrate temperature.

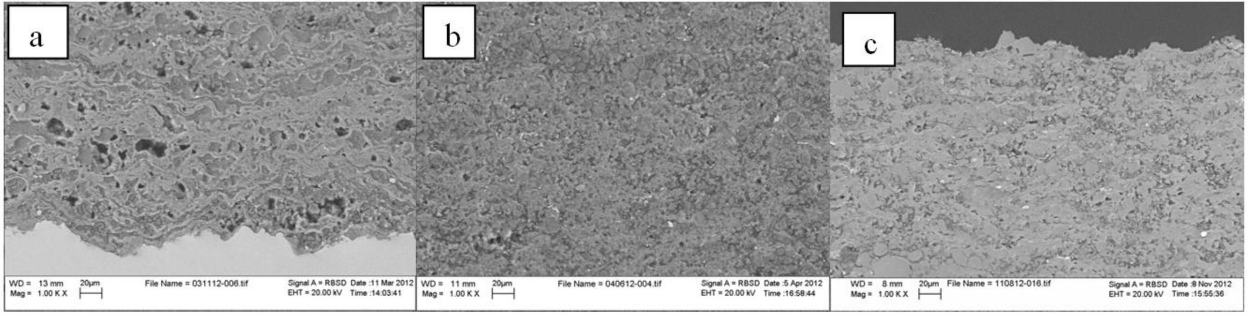

Figure 4.3 SEM of VPS samples: a) VPS003, b) VPS004, c) VPS101

4.1.2.3 Thermoelectric properties of Mg_2Si

Thermoelectric properties include thermal conductivity, electrical conductivity and Seebeck coefficient. The power factor is the combination of Seebeck and electrical conductivity given by □S2. Due to the low coating thickness of Mg_2Si samples prepared by thermal spray, not all of the samples could be characterized for the thermoelectric properties. We have shown reduction in thermal conductivity before and the followings are some Seebeck results for APS and VPS samples.

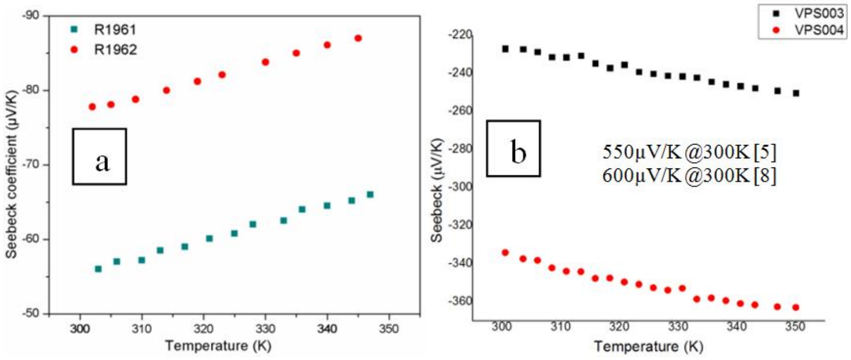

Figure 4.4 Seebeck coefficient of un-doped Mg_2Si by a) APS and b) VPS

Figure 4.4 shows the Seebeck coefficient of undoped Mg_2Si prepared by APS and VPS. Typically, the higher purity thermoelectric gives the higher Seebeck coefficient. Our sample has MgO, Si and/or Mg in the coating, which may be responsible for the significant decrease in the Seebeck coefficient. The result shows that undoped Mg_2Si is n type semiconductor and VPS has higher Seebeck which may due to higher purity.

4.1.3 Conclusion

Mg_2Si layers have been synthesized by thermal spray, which has been shown to be an effective way to reduce the thermal conductivity of material in our previous investigation due to phonon scattering by pores and cracks in the coating. However, the air-sensitive element Mg can form large amount of oxide during the spray process, which may decrease Seebeck coefficient. VPS results showed an improvement in the reduction of oxidation thus increased the Seebeck coefficient. But high temperature due to poor heat transfer during the VPS process causes Mg to evaporate, which results in high concentration of Si in the coating. XRD results clearly showed that low temperature and high speed is useful to reduce the oxide in spray. VPS can achieve relative high Seebeck coefficient by choosing appropriate power.

4.2 Air Plasma Spray (APS) of Mg_2Si

4.2.1 Experiment

Mg_2Si powder (> 98%) purchased from YHL New Energy CO. Ltd (Zhejiang China) was used to deposit samples on aluminum substrate of size 40 x 25mm x 2mm. The grain sizes of the original powder range from 10 to 270 μm. It was sieved from 53-180 μm as feedstock powder. We use 98% purity powder to investigate thermal spray parameters since large amount higher purity Mg_2Si powder is very expensive and is not available with the desired powder size and shape. A 40 kW plasma spray system (SG-100, Miller Thermal, USA) was used to deposit the Mg_2Si feedstock powder. Argon was the main plasma forming gas and helium the power carrier gas.

Table 4-3 Plasma spray parameters

Plasma gas	Argon
Carrier gas	Helium
Current (A)	450
Flow rate (SLPM)	105
Flow rate (SLPM)	34.8
Raster (mm/s)	500
Pulse (s)	2
Step (mm)	2
Powder feed rate (g/min)	5-8
Stand-off distance (mm)	100

As comparison, the hot pressed sample using same above powder and 5% Mg rich powder from the same company. Table 4-4 listed all the samples synthesized by thermal spray or hot press and its annealing condition.

Table 4-4 Sample synthesis parameters and powder information.

Sample	Synthesis	Condition	Annealing	Other
P1	(Powder)	N/A	None	Normal ratio
P2	(Powder)	N/A	None	Mg rich
A1	APS	LTHV	None	Normal ratio
A2	APS	LTHV	Vacuum, 400 ^{o}C, 1h	Normal ratio
A3	APS	LTHV	Vacuum, 400 ^{o}C, 20h	Normal ratio
H1	HP	800 ^{o}C, 30MPa	None	Normal ratio
H2	HP	800 ^{o}C, 30MPa	None	Mg rich

The sample phase was analyzed by X-ray diffraction (XRD) (PAD-V, SCITAG Inc., CA, USA) utilizing Cu Kα radiation and energy dispersive X-ray spectroscopy (EDS) (Leo-1550-SFEG, Carl Zeiss SMT Ltd, Cambridge UK). The cross-section morphologies of the sample were observed using a scanning electric microscope (SEM) (Leo-1550-SFEG, Carl Zeiss SMT Ltd, Cambridge UK).The electrical conductivity were measured by the four-probe method through PPMS (Physical Property Measurement System, Quantum Design) in the temperature range of 300 to 380K and Seebeck coefficient was measured using MMR Seebeck S100 controller with a K20 temperature controller. Thermal conductivity was measured using flash method (Anter/TA FS3500 flashline, DE). To investigate contribution to electrical conductivity, the carrier concentration and hall mobility were measured using Hall Effect Measurement System (Lakeshore 8404, Lake Shore Cryotronics, Inc, OH).

4.2.2 Results and discussion

4.2.2.1 Phase composition

Phase composition of powder, hot pressed and thermal sprayed samples

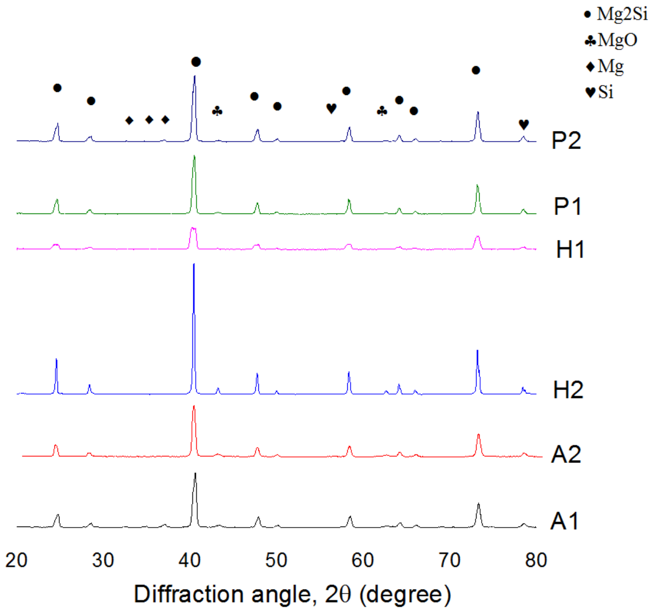

Figure 4.5 XRD of powder, hot press and thermal spray samples

Figure 4.5 shows the XRD of powder, APS and hot press samples. The reaction temperature between Mg_2Si and O2 is around 450 °C, while the temperature during thermal spray is significantly higher than this. In order to avoid serious oxidation, APS with the SG100 gun which can perform high velocity and low temperature is equipped to suppress the reaction rate of Mg_2Si by internal powder distributor. Hot press was performed in vacuum with a heating rate of 5K/min and naturally cooling rate around 3-5K/min. The XRD result clearly shows APS is very consistent with the feedstock powder, although very small MgO and Si peak are found. A1 is as-sprayed sample without heat treatment. Mg peak was found in the sample which may come from the original powder. Vacuum heat treatment APS (A2) didn’t show any Mg peak which may be due to the oxidation or volatilization of Mg during heat treatment. Hot press sample with both powders showed no clear Mg peak, however Mg rich powder resulted in more MgO peak which may due to the oxidation during vacuum hot press. Be aware that, XRD can only show composition above certain amount. Some impurity with small percentage may not be shown in the XRD.

4.2.2.2 Microstructure

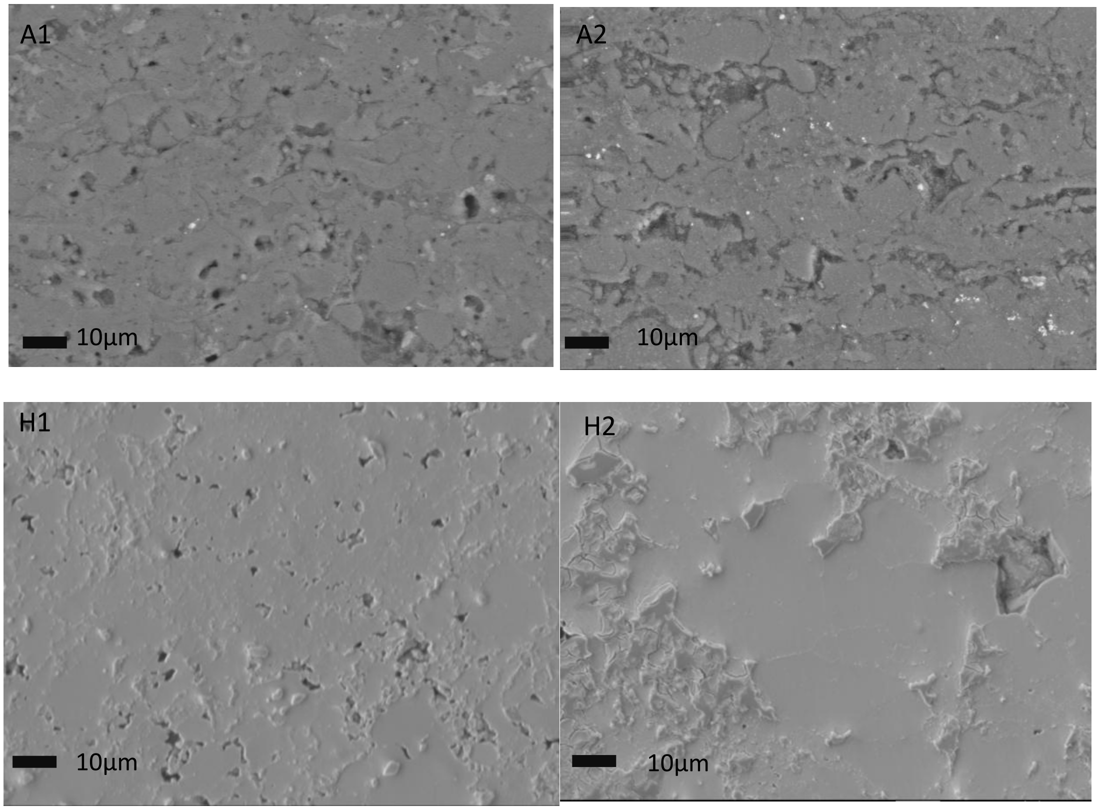

Figure 4.6 SEM cross sections of APS and hot press samples

Figure 4.6 shows of several cross section SEM images of APS and hot press samples. It can be clearly seen that APS samples (A1) lots of pores and cracks compared with hot press samples (H1 & H2). Heat treatment APS sample (A2) doesn't anneal this defect much and the low heat treatment temperature could be the reason. APS samples clearly show some un-melted particles because the condition for this thermal spray is low temperature and high velocity. It simply softened the powder particles instead of melting them, which avoided Mg_2Si from oxidation during the process. SEM of hot press samples indicates Mg rich powder has denser microstructure and this is due to the ductile-brittle system of Mg_2Si. Hot press was both performed at 30MPa for two kinds of raw powder and the structure is not fully dense, however the cracks and pores are still far less than APS samples.

4.2.2.3 Thermal conductivity

Thermoelectric properties including thermal conductivity, electrical conductivity and Seebeck coefficient were characterized and compared between APS and hot press samples.

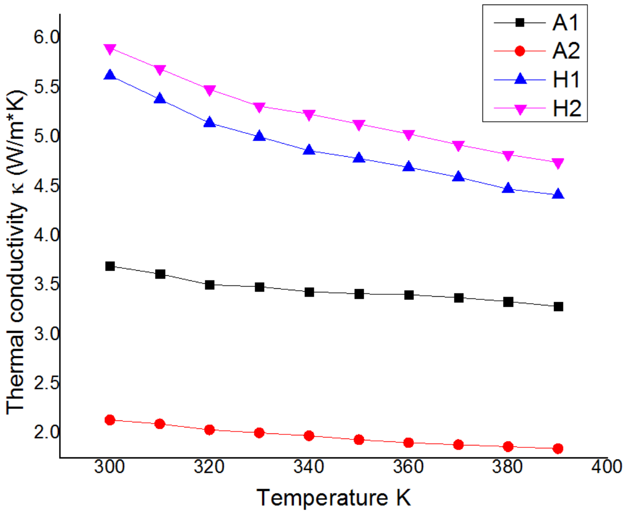

Figure 4.7 Thermal conductivity of Mg_2Si by APS and hot press

Figure 4.7 shows the thermal conductivity of Mg_2Si prepared by APS and hot press. The thermal conductivity is measured from room temperature to 390K under the flow of nitrogen gas. Figure 4.7 clearly shows thermal sprayed samples (A1 & A2) have low thermal conductivity compared with hot press sample and this is due to the pores and cracks in the sample for enhanced phonon scattering[130]. Beside lattice part of thermal conductivity, electronic part can also affect the thermal conductivity due to the heat carried by electrons. This electronic part of thermal conductivity is responsible for the lower thermal conductivity of A2, because A1 has more electron concentration than A2 which can be seen from the Hall Effect measurement later. All the APS samples have lower thermal conductivity than hot press samples, likely the lattice thermal conductivity is dominant in these samples.

4.2.2.4 Electrical conductivity

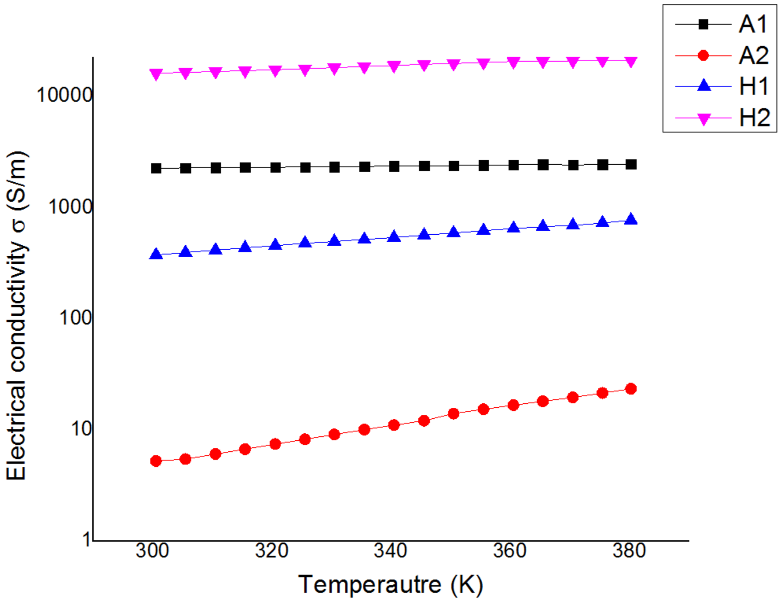

Figure 4.8 Electrical conductivity of Mg_2Si by APS and hot press

Figure 4.8 shows the values of APS and hot press samples vary a lot and after heat treatment the electrical conductivity reduce significantly. Electrical conductivity is measured from 300K to 390K using PPMS. For APS sample, A1 has much higher conductivity than A2. For hot press sample, H2 has higher conductivity than H1, which is due to the 5% more Mg from the raw powder. In order to understand the mechanisms and key parameters that affect electrical conductivity. Hall Effect measurement at room temperature was taken and the result is listed in table 4-5.

Table 4-5 Hall Effect measurement of APS and hot press samples

Sample	Carrier concentration n (1/cc)	Mobility μ (cm^2/V*s)	Conductivity □ (S/m)
A1	4.27E20	0.15	1025
A2	8.26E17	0.51	6.7
A3	1.24E17	0.52	1.03
H1	2.26E18	13.3	481
H2	2.58E19	26.7	11025

Even though the absolute value showed with Hall Effect equipment and PPMS on electrical conductivity are not exactly same due to noise and equipment error, the trend is similar which can explain the influence on the electrical conductivity. Table 4-5 showed APS sample without heat treatment (A1) has highest carrier concentration and A3 has the lowest. Hall Effect measurement shows the mobility of the APS is low compared with conventional hot press samples. Generally, mobility is dominant by phonon scattering at high temperature and ionized impurity scattering at low temperature for single crystal. The sample in this study is highly disordered and the mobility could be far less than single crystal. The low mobility of APS sample may also due to the contamination of the thermal spray gun and original impurities in the raw powder. During process, magnesium will evaporate more than impurity like iron, nickel and manganese which has been detected in the APS sample and raw powder using EDS. The increased concentration of ionized impurity will scattering electron more which will reduce mobility. The impurity cooper could be from erosion of thermal spray nozzle since the cooper was only found in APS sample. More investigation of the percentage of each sample needed to be examined to fully understand why APS sample has much lower carrier mobility. After heat treatment in vacuum, the mobility is increased which may due to the grain size growth. However, during the annealing, Mg_2Si and Mg will still react with residual oxygen in the vacuum chamber which decrease the carrier concentration in sample A2 and A3. Heat treatment does help on increase the mobility but the temperature seems not high enough to anneal the pore/cracks in the as-sprayed sample. More heat treatment with oxygen getter at various elevated temperature will be useful to investigate the influence for electron mobility in APS samples.

4.2.2.5 Seebeck coefficient

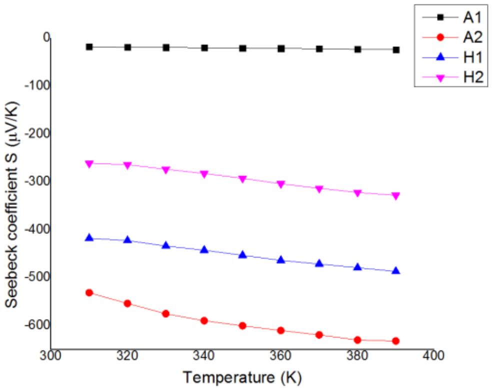

Figure 4.9 Seebeck of Mg_2Si by APS and hot press

Figure 4.9 shows the Seebeck of APS and hot press samples. Seebeck has been reported to be not influenced by the microstructure; rather it more depends on phase composition[131]. Typically, Seebeck coefficient is inversely proportional to electrical conductivity due to the opposite dependence of carrier concentration [7]. Figure 4.9 and table 4-3 clearly showed that with the increased carrier concentration, the Seebeck coefficient decreased and this could be explain with the inverse dependence on carrier concentration in Seebeck equation. As temperature increase, the Seebeck coefficient increase in absolute value. All the negative Seebeck coefficient shows un-doped Mg_2Si is n-type semiconductor. Seebeck coefficient of as-sprayed sample (A1) is very low because the carrier concentration is too high. After heat treatment, some of the Mg vaporized or oxidized so A2 has lower carrier concentration and the Seebeck increased dramatically. For hot press, Mg rich sample (H2) has lower Seebeck coefficient because it has higher carrier concentration when other conditions are similar. Hot press sample has carrier concentration between A1 and A2 and also the Seebeck coefficient is between A1 and A2.

4.2.2.6 Figure of merit

Since the microstructure doesn’t change significantly during annealing, carrier mobility doesn’t increase much. As a whole, electrical conductivity reduce significantly during the annealing. Even with the increase of Seebeck coefficient due to the loss of carrier concentration, A2 still has very low electrical conductivity. However, figure 4.10 shows figure of merit of APS and HP samples. Overall, APS sample has lower ZT than hot press sample even with much reduce thermal conductivity and this is because as-sprayed sample has very low Seebeck coefficient and heat treatment sample has very low electrical conductivity. For APS, vacuum annealed sample (A2) has higher ZT compared with as-sprayed (A1). Even though A1 has much higher electrical conductivity than A2, the Seebeck coefficient of A1 is 25 times less than A2. Also, A2 has only half thermal conductivity of A1 which results in that A2 has higher ZT than A1. For hot press, normal ratio powder sample (H1) has lower ZT than 5% more Mg powder sample (H2). H2 has much higher electrical conductivity than H1 and noticing that Seebeck difference and thermal conductivity between them is not that much, thus H2 has higher ZT than H1. APS with heat treatment can increase figure of merit and can be even promoted by proper doping. Anneal at higher temperature can increase the mobility more and proper doing can tune the optimal carrier concentration of APS samples to improve the thermoelectric property of APS samples.

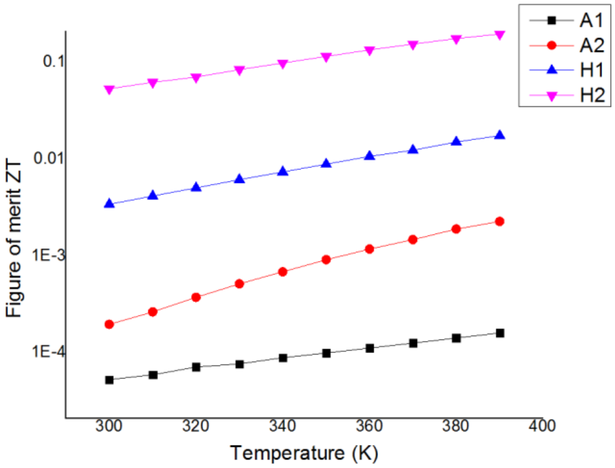

Figure 4.10 ZT of Mg_2Si by APS and hot press

4.2.3 Conclusion

Magnesium silicide (Mg_2Si) layers have been firstly synthesized by Atmospheric Plasma Spray (APS), which has been shown to be an effective way to reduce the thermal conductivity of material compared with conventional hot press method. Even though Mg_2Si is very sensitive to air and temperature, the APS using SG100 gun very successfully keeps the composition the same as raw powder. In our investigation, reduced thermal conductivity of Mg_2Si material is obtained most likely due to phonon scattering by pores and cracks in the APS samples. Thermal conductivity, electrical conductivity, Seebeck coefficient and figure of merit are all compared between APS and hot press from 300K to 390K. Carrier concentration and hall mobility are measured to understand influence of electrical conductivity by different methods. Carrier concentration is a tradeoff between electrical conductivity and Seebeck coefficient. Heat treatment under vacuum at 400 degree Celsius helps to tune the concentration but doesn’t change mobility significantly. Seebeck coefficient increases with the decrease of carrier concentration if phase remain the same. Thermal conductivity of APS is lower than hot press samples. Vacuum annealed APS sample gives very high Seebeck coefficient. Carrier concentration need to be tuned and carrier mobility need to be increased to achieve a better ZT. As a preliminary result, APS achieved 10% in ZT compared with hot pressed sample and higher percentage will obtained by properly control carrier concentration and higher temperature annealing of APS sample. Besides mass production and cost effective, thermal spray can directly fabricate thermoelectric material on exhaust pipe which makes it worth of more investigation.

4.3 Vacuum Plasma Spray (VPS) of Mg_2Si

4.3.1 Methods

The Mg_2Si powder was purchased from *YHL New Energy Co., Ltd* (Zhejiang China). All samples were deposited onto on 40 x 25mm x 2mm aluminum/Titanium substrates. The grain size of the original powder ranges from 20 to 270 μm which is measured by SEM. The powder purity was stated 98% by the company; a higher purity would desirable for this work to minimize thermoelectric property degradation due to impurities, but it was found that such powders were both very expensive and not readily available with the desired powder size and shape. A second, Mg-rich powder that contains 5%wt excess Mg from the same company was also used in this work to compensate for evaporation and oxidation losses of Mg during both the VPS and hot-press processes. The hot-pressed samples were fabricated using the same powder as vacuum thermal spray.

A Plasma-Technik A-3000S VPS system (Plasmatechnik, Wohlen, Switzerland) was used to deposit the Mg_2Si feedstock powder. In order to keep the substrate temperature as low as possible, substrates were attached to a large aluminum plate to provide a low-temperature heat sink. A mixture of Ar, He and H_2 are used as the main plasma-forming gas, and Ar is used as the powder carrier gas. Details of the spray process are shown in Table 4-7.

Table 4-6 Plasma spray parameters

Plasma gas	Ar/He/He
Carrier gas	Ar
Current (A)	600~1000
Carrier gas flow rate (L/min)	5
Powder feed rate (lb/hr.)	1
Stand-off distance (mm)	250~350

Table 4-6 summarizes all of the samples synthesized by thermal spray and hot press techniques used in this work. The relative density was directly measurement of mass and volume.

Table 4-7 Sample synthesis parameters and powder information

Sample	Synthesis	Condition	Density	Powder
P1	(Powder)	N/A	N/A	Nominal ratio
P2	(Powder)	N/A	N/A	5% Mg rich
V1	VPS	18kW	79%	Nominal ratio
V2	VPS	18kW	82%	Mg rich
V3	VPS	21kW	83%	Nominal ratio
H1	HP	800 ^{o}C, 30MPa	85%	Nominal ratio
H2	HP	800 ^{o}C, 30MPa	90%	Mg rich

The sample phase was analyzed by X-ray diffraction (XRD) (PAD-V, SCITAG Inc., CA, USA) utilizing Cu Kα radiation and energy-dispersive X-ray spectroscopy (EDS) (Leo-1550-SFEG, Carl Zeiss SMT Ltd, Cambridge, UK). The cross-section morphologies of the sample were observed using a scanning electric microscope (SEM) (Leo-1550-SFEG, Carl Zeiss SMT Ltd, Cambridge, UK). The electrical conductivity were measured by Keithley digital multimeter (Model 2700, Keithley Instruments, Inc., OH, USA) and heated using High Temperature Probe Station (MBE-Komponenten AO500, DR. EBERL MBE-KOMPONENTEN GMBH, Germany) from 300 to 700K. Low-temperature electrical conductivity was measured using a Physical Property Measurement System (Quantum Design, CA, USA) using the four-probe method. *IV* curve measurement was performed by probe station (Signatone, Gilroy, CA) Seebeck coefficients were measured using an MMR Seebeck S100 controller with a K20 temperature controller (MMR Technologies, Inc., CA, USA). Thermal conductivity was measured using a laser flash method (FS3500, TA Instrument, Inc., DE, USA). To investigate its contribution to electrical conductivity, the carrier concentration and Hall mobility were measured with a Hall Measurement System (8404, Lake Shore Cryotronics, Inc., OH, USA) using the Van der Pauw method.

4.3.2 RESULTS AND DISCUSSIONS

4.3.2.1 Phase composition of raw powder, hot pressed and thermal sprayed samples

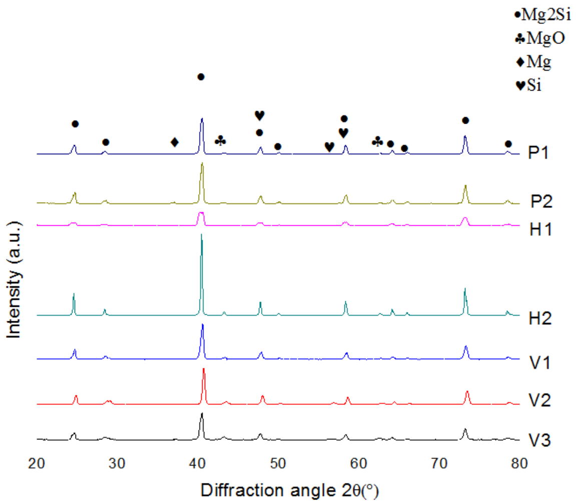

Figure 4.11 XRD of powder with nominal Mg ratio (P1), Mg-rich (P2) and VPS samples

Figure 4.11 shows the XRD of the feedstock powder, and the samples made by VPS and hot press. The reaction temperature between Mg_2Si and O_2 is around 450 ^{o}C, while the temperature during thermal spray is significantly higher than this. In order to avoid significant oxidation, the plasma spray was operated under vacuum that can suppress the oxidation of Mg_2Si.

Sample V1 and V2 are as-sprayed samples at 18kW powder with different feedstock powder, while V3 is at 21kW with nominal ratio powder. The XRD results show that the VPS samples have a composition highly consistent with the feedstock powder, although small MgO and Si peaks are observed. XRD of V3 showed small Si peak which due to the higher temperature of the chamber to assist reaction of Mg_2Si and residual oxygen from the chamber.

The hot press sample fabrication was done in vacuum with a heating rate of 5 ^{o}C /min and cooling rates of 3–5^{o}C/min. Hot press samples using both nominal powder and Mg-rich powder showed no clear Mg peak, however the Mg-rich powder resulted in more MgO peaks, which may due to the oxidation during vacuum hot press. Small quantities of impurities may not be observed due to XRD limitation on small concentration. Plasma emission spectroscopy will be considered later since it can observe the composition better.

4.3.2.2 SEM results of thermal sprayed samples

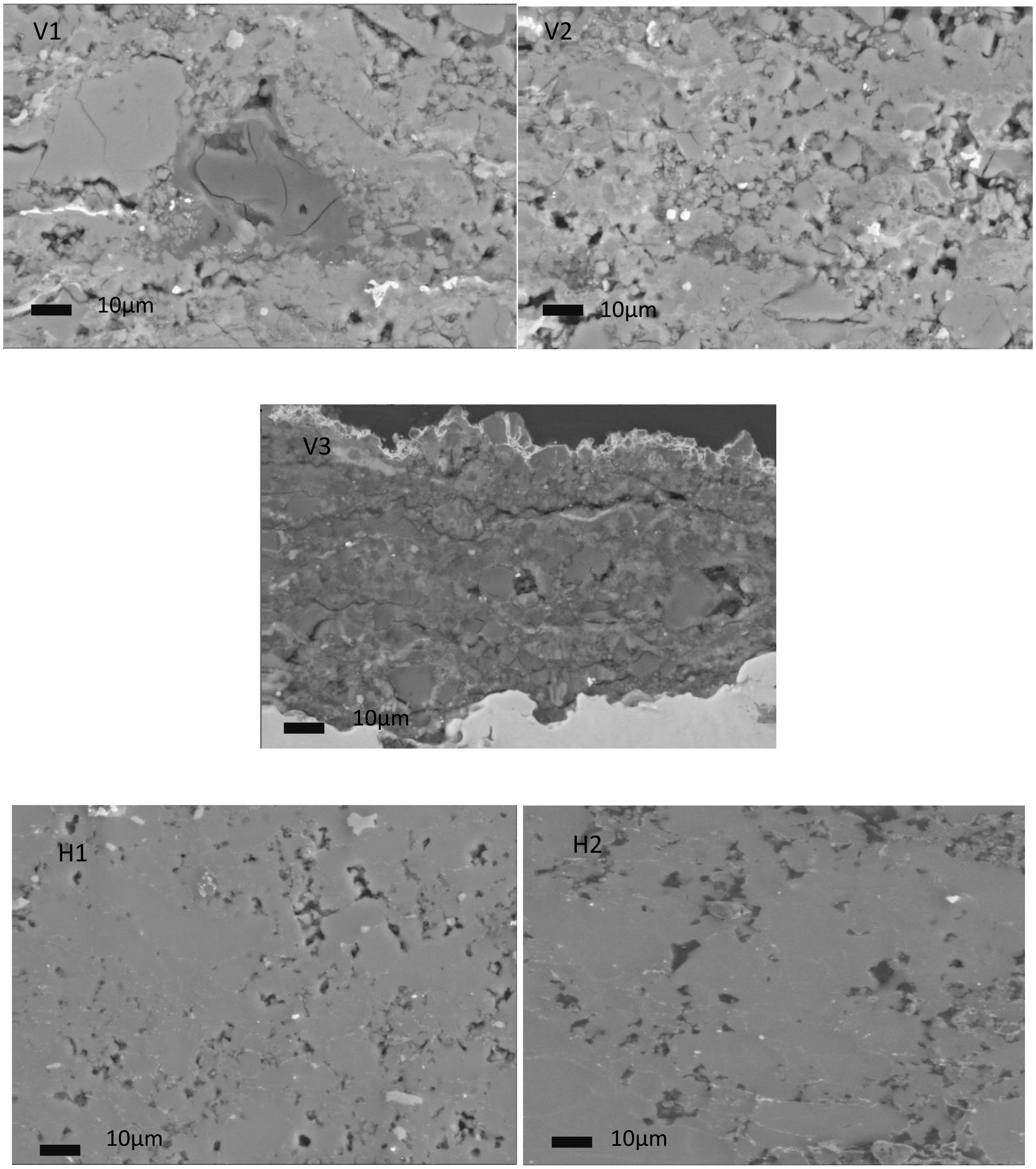

Figure 4.12 SEM cross sections of VPS and hot press samples

Figure 4.12 shows the cross section SEM images of VPS samples V1, V2, V3, and hot press samples H1 and H2. It can be seen that the VPS samples have a large number of pores and cracks compared with hot press samples (H1 & H2). The three VPS images show evidence of un-melted particles, which can be explained by the low power conditions. Such spray conditions tend to avoid Mg_2Si oxidation during the process. SEM images of the hot-press samples indicate that the Mg-rich powder has a denser microstructure, which is likely due to the ductile-brittle system of Mg_2Si. The hot pressing process was performed at 30MPa for both powders. Although the samples were not fully dense, far less cracks and pores were found when compared to the VPS samples.

4.3.2.3 Thermoelectric properties of Mg_2Si

Thermoelectric properties including thermal conductivity, electrical conductivity and Seebeck coefficient were characterized and compared between VPS and hot press samples.

a) Thermal property

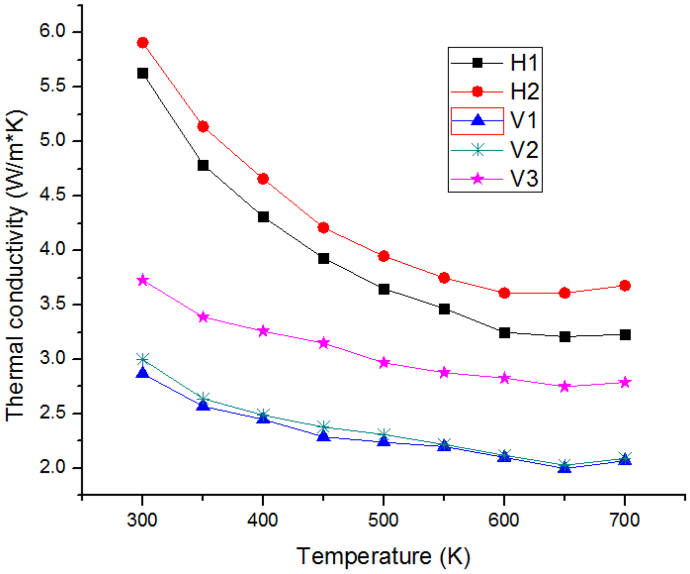

Figure 4.13 Thermal conductivity of Mg_2Si by VPS and hot press

Figure 4.13 shows the thermal conductivity of Mg2Si prepared by VPS and hot press. The thermal conductivity is measured from 300–700K in a nitrogen environment. Thermal-sprayed samples V1, V2 and V3 have a thermal conductivity at least 40% lower than the hot press samples. This is likely due to the large numbers of pores and cracks in the sample that enhance phonon scattering.[130, 132, 133] Electrons also contribute to the thermal conductivity. V1 and V2 both have condition of spray power

18kW, and the reduced thermal conductivity in sample V1 is likely because of the reduced electronic contribution due to the lower electron concentration from the Hall measurements as discussed in the following.

b) Electrical property

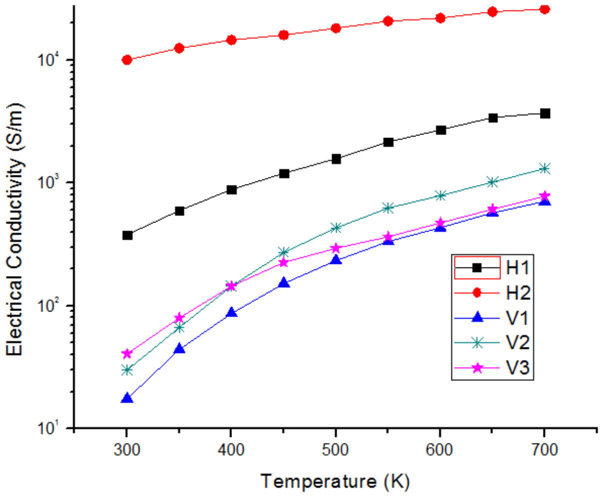

Figure 4.14 Electrical conductivity of Mg_2Si by VPS and hot press

Electrical conductivity was measured from 300–700K using high temperature probe station. The measured electrical conductivity for VPS and hot press samples are shown in Figure 4.14. As can be seen, the variation in electrical conductivity is significant in the samples. For VPS sample, V2 with Mg rich powder has a little higher conductivity than V1 with nominal ratio powder because the carrier concentration is higher, which can be seen from Hall Effect measurement.

For the hot press samples, H2 has higher conductivity than H1, which is most likely due to the additional Mg present in the raw powder. In order to understand the mechanisms and key parameters that affect electrical conductivity, Hall Effect measurements at room temperature were made, with the results shown in Table 4-8.

Table 4-8 Hall Effect measurement of hot press and VPS samples

Sample	Carrier concentration, $\boldsymbol{n}$ (10^{17}/cm^3)	Mobility, $\boldsymbol{\mu}$ (cm^2/V·s)	Conductivity, □ $= \boldsymbol{ne\mu}$ (S/m)
H1	22.6	13.31	481
H2	258	26.72	11,040
V1	8.24	1.31	17.3
V2	10.5	1.74	29.3
V3	7.94	3.14	40
Tani[79]	4.3	204	1,404

The calculated electrical conductivities $\sigma = ne\mu$ in Table 4-8 based on the Hall measurements are in good agreement with the electrical conductivity measurements shown in Figure 4.14 at 300 K. The VPS sample with Mg rich powder (V1) has higher carrier concentration than Mg nominal powder (V1) at same thermal spray power. The mobility of the VPS samples at 21kW (V3) is higher than the VPS sample at 18kW (V1) with same feedstock powder because higher power gives much denser microstructure. Since hot press samples have relative density around 85~90% from Table 4-7 which is much higher than VPS samples, the mobility for hot press samples are significantly higher than VPS samples. The samples in this study are highly disordered, with the result that the mobility is far less than other bulk material (i.e. SPS method) which is shown in Table 4-8. Generally, mobility is determined by phonon scattering at high temperatures and ionized impurity scattering at low temperatures for semiconductor materials.[134] In order to understand the scattering mechanism of electrons, low temperature electrical conductivity is measured from 5-400K.

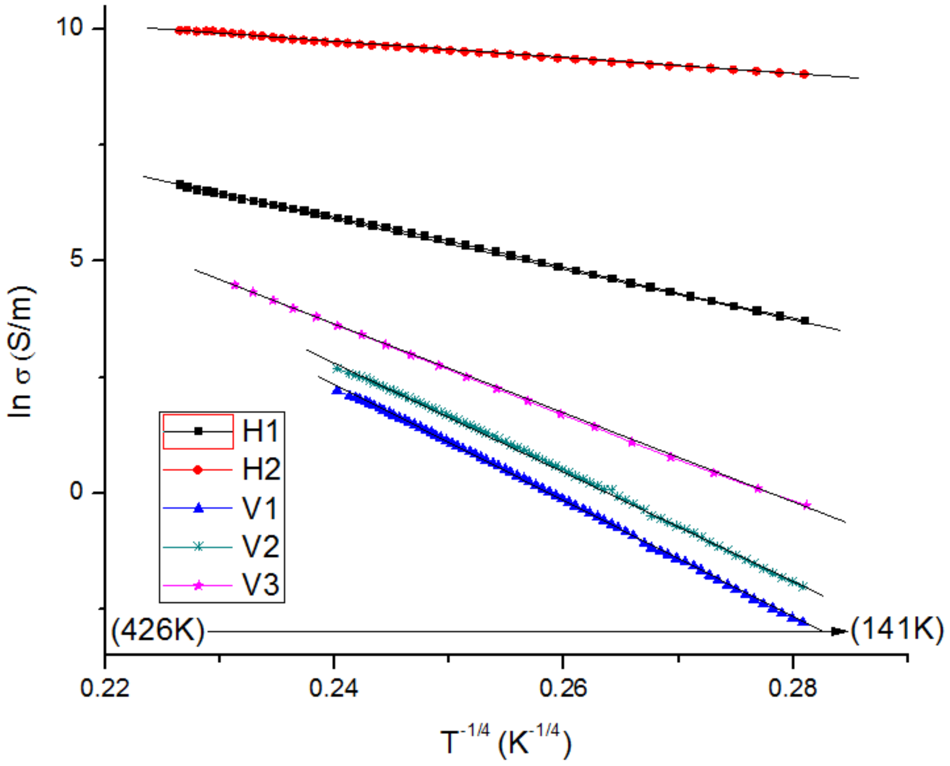

Figure 4.15 Temperature dependent of hot pressed and VPS samples

Figure 4.15 shows the temperature dependence of electrical conductivity from 140K to 400K. This temperature range shows extrinsic region mainly including boundaries, impurities and other defects scattering. We analyzed the data by fitting with power functions as shown in figure 4.15. All of them showed variable range hopping effect.[135] Generally, hopping mechanism take place when $ln\sigma = C\ (1/T)^{-1/N}$, here C is some constant number and N (1, 2, 3, 4) = 1+D (0, 1, 2, 3) dimensional hopping effect. These samples showed 3D variable range hopping effect since N equals to 4. This is expected since no low dimensional structure material or technique has been used. While, the hot press sample showed much higher conductivity than VPS samples, the Current-Voltage (IV) curve was measured to further understand the electron transport mechanism.

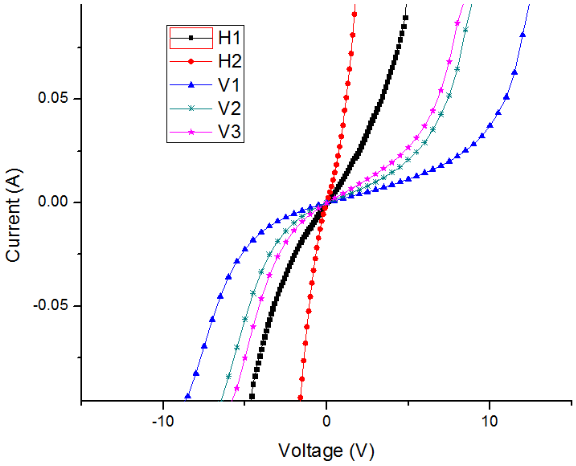

Figure 4.16 Current-Voltage (IV) curve measurement of hot press and VPS samples at room temperature

XRD result clearly shows all of the samples; especially the VPS samples contain MgO inside as an insulator. As a matter of fact, the oxidation of thermal sprayed samples is much worse and evenly distributed in the coating in which the electrons are difficult to travel. However, as shown in Fig. 4.16 for VPS samples, when applying higher current (larger than 5-10V), there is some conduction through the MgO from charge carriers caused by impurities or point defects in the MgO but at low voltages these carriers "freeze out" and become localized so the MgO conductivity drops down. While, the resistance doesn’t change that much for hot pressed samples because hot press method will not involve as much oxidation as VPS do.

c) Seebeck coefficient

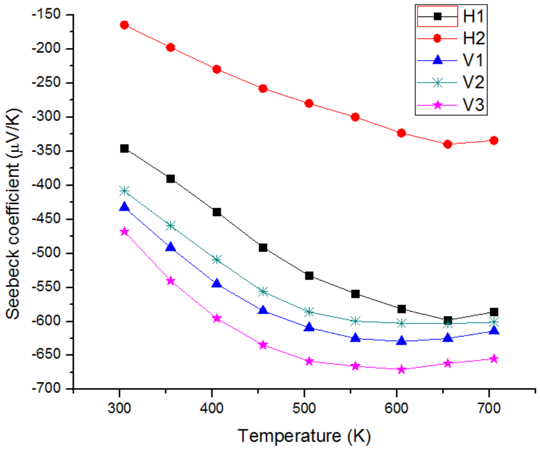

Figure 4.17 Seebeck of Mg_2Si by VPS and hot press

Figure 4.17 shows the measured Seebeck coefficient for the VPS and hot-press samples. Seebeck coefficient of stacking faults abundant films at room temperature were found comparable to those of the single-crystal samples.[131] The Seebeck coefficient is inversely proportional to electrical conductivity due to the opposite dependence of carrier concentration, i.e., $S \sim \ln{(1/n)}$ in Eq. (1).[7]

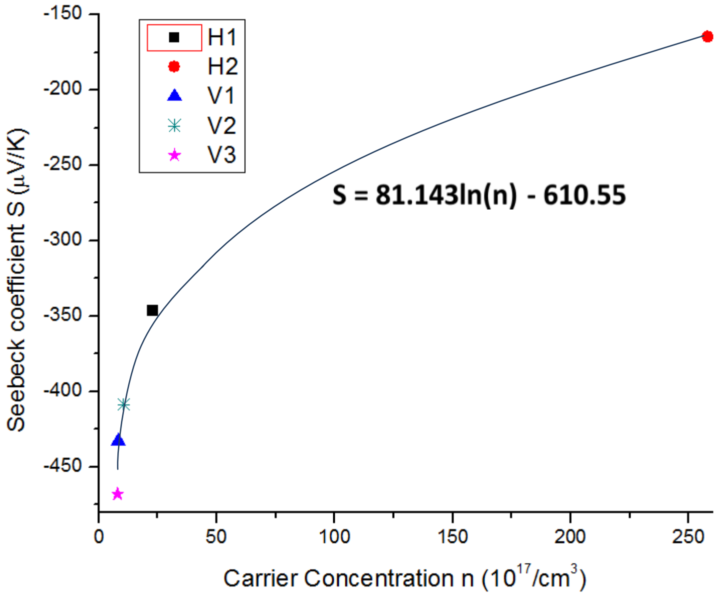

Figure 4.18 Seebeck coefficient variation due to carrier concentration change at room temperature

Figure 4.18 validates that the Seebeck coefficient decreases with increased carrier concentration. Generally as temperature increase, the Seebeck coefficient increase in magnitude because the ratio *Nc*/*n* is proportional to exp(*k*T) which given in Maxwell statistics. The negative Seebeck coefficient indicates that un-doped Mg_2Si is a *n*-type semiconductor.[79] The Seebeck coefficient of hot press sample (H2) is lowest because the carrier concentration is highest among all the samples. VPS sample with Mg rich powder (V2) has lower Seebeck coefficient than VPS samples with Mg nominal ratio powder because more Mg in the sample increase carrier concentration and dramatically decrease Seebeck coefficient.

For the hot-press samples, the Mg-rich sample H2 had a lower Seebeck coefficient because of its higher carrier concentration. The hot press samples had carrier concentrations higher than all of VPS samples V1, V2 and V3, and the Seebeck coefficient were lower than for VPS samples.

d) Figure of merit

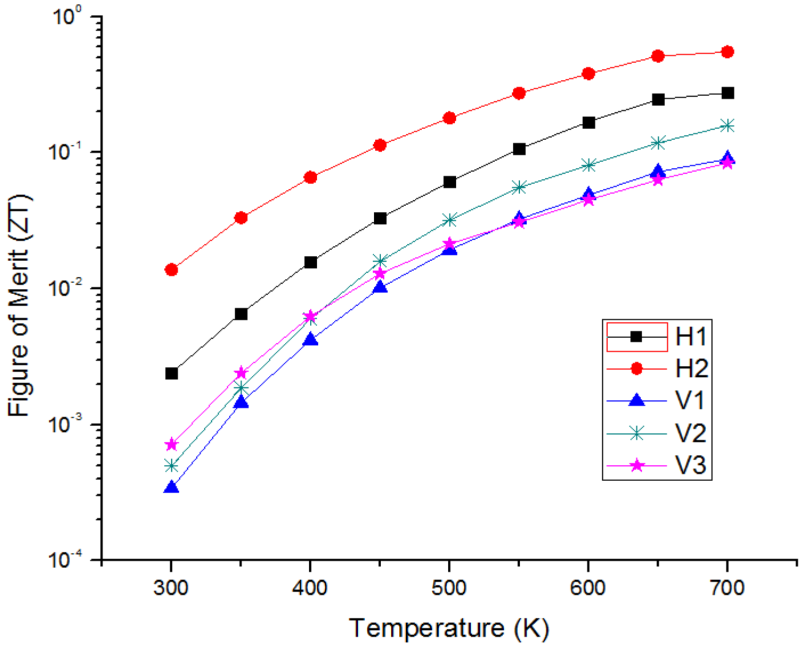

Figure 4.19 . ZT of Mg_2Si by VPS and hot press

Figure 4.19 shows the figure of merit *ZT* for the VPS and hot press samples. Overall, the VPS samples have a lower *ZT* than the hot press samples because of low carrier mobility, even though the VPS samples have a much lower thermal conductivity. VPS at 18kW with Mg rich powder V2 has a higher *ZT* as compared with the Mg nominal sample V1. Even though V1 has a little higher Seebeck coefficient than V2, the electrical conductivity of V1 is nearly half of V2. Also, the thermal conductivity of V2 is similar to the thermal conductivity of A1, which results in a higher *ZT* for V2. As Mg nominal ratio powder, ZT of 21kW sample (V3) is a little higher than that of 18kW sample (V1) at lower temperature and almost the same up to 700K.

For the hot press samples, the nominal-ratio-powder sample H1 has a lower *ZT* than the Mg-rich sample H2. H2 has much higher electrical conductivity than H1, and, noting that the Seebeck and thermal conductivity between them does not differ significantly, H2 has a higher *ZT* than H1. VPS samples with Mg rich powder at 18kW has highest figure of merit at higher temperature, and should be able to be further increased by proper doping. Increasing thermal spray power can increase the mobility, while appropriate doping can be used to tune the optimal carrier concentration to maximize the thermoelectric properties of VPS samples.

4.3.3 CONCLUSIONS

Vacuum Thermal Spray (VPS) is a rapid process. Magnesium silicide (Mg_2Si) samples have been successfully synthesized by VPS which has been shown to be an effective way to reduce the thermal conductivity of material compared with conventional hot press method. Even though Mg_2Si is extremely sensitive to oxygen and temperature, the VPS approach, using low power has successfully maintains the composition of the sample similar to feedstock powder. Beside the industrial scale production, thermal spray is flexible to directly spray thermoelectric material on any shape, i.e. cylindrical. In this work, the reduced thermal conductivity demonstrated in the Mg_2Si material is most likely due to phonon scattering by pores and cracks in the VPS samples. Carrier concentration represents a tradeoff between electrical conductivity and Seebeck coefficient. The Seebeck coefficient increases with a decrease in carrier concentration if the phase remains the same but electrical conductivity increase as carrier concentration increase when mobility doesn't change much. The low temperature electrical measurement also shows 3D variable hopping effect in hot press and VPS samples. IV curve measurement shows the low electrical conductivity is due to the existence of MgO insulation layer around the grain boundaries. VPS samples achieved ZT values approximate 30% those of hot-pressed samples with same starting powder. The work suggests that vacuum thermal spray can be a viable means to directly fabricate thermoelectric materials for high-volume applications.

4.4 Thermal Spray of Fe2Si and Thermoelectric Property

As we have discussed earlier, researchers from Japan and Germany have tried thermal spray with iron disilicide which has been introduced in section 2. Even we know the figure of merit of this material is not high. We still tried this material as a starting point since iron disilicide is much easier to handle compared with magnesium silicide in terms of oxidation or evaporation. Below are some results of our iron silicide.

4.4.1 Experiment

Iron silicide powder (P/N 7920204) was purchase from Steward and before thermal spray the powder was screen to 10 to 100 micron for better flow. Iron silicide was deposited on an aluminum substrate which has been degreased and gritted.

4.4.2 Results and discussion

To demonstrate the ability to form thick thermoelectric deposits, FeSi2 was sprayed to form thick rectangular pillars, as shown in Fig. 4.20. The material was sprayed using HVOF and the deposits were ~2 mm thick. Adhesion was good with the resulting pillars, with no indication of peeling or separation. No thermoelectric characterization was done on FeSi2, due to its poor potential for a thermoelectric, as discussed above. Thermal sprayed FeSi2 onto mild steel substrates to demonstrate thickness capability required for TE legs in a thermoelectric generator. Deposits are ~2 mm thick; grid spacing is 5 mm.

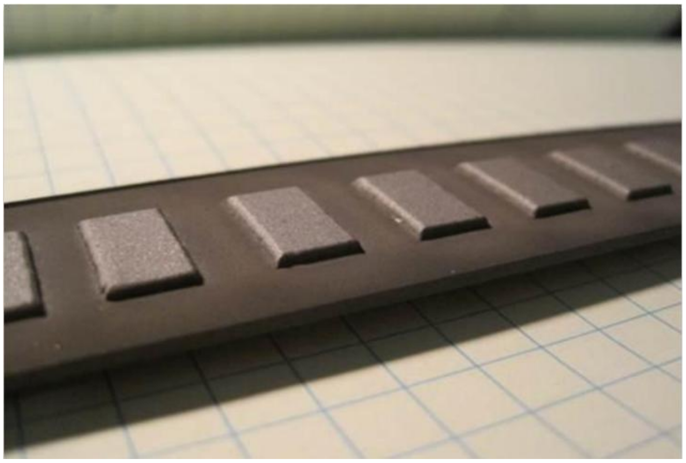

Figure 4.20 Thermal sprayed iron silicide (courtesy of Dr. Kentaro Shinoda and Prof Sanjay Sampath)

4.4.3 Conclusion

Thermal spray can deposit as thick as 2mm FeSi2 without any problem. The bonding is strong and no obvious oxidation or evaporation happens during thermal spray. It also shown that our HVOF facility is capable to form thermoelectric layer like iron silicide.

4.5 Thermal Spray of Filled Skutterudite and Thermoelectric Property

The material used in this work was FeCo4Sb12. There is significant interest in using filled skutterudites for automotive applications [1], however to the author's knowledge; these materials have never been thermal sprayed. Figure 4.21 showed the vapor pressure of most element contained in filled skutterudite versus the vapor pressure of magnesium. During our long time research on Mg_2Si, we found the high vapor pressure of Mg make thermal spray work much harder. As a comparison, antimony, the key element in filled skutterudite also had a high vapor pressure but not as high as Mg. As a result, thermal spray of filled skutterudite should be easier than Mg_2Si in terms of vapor pressure. Also, in the skutterudite, Sb is not in the atom element phase which indicate the feasibility of spray this material. One should notice that Sb and many of its compounds are toxic.

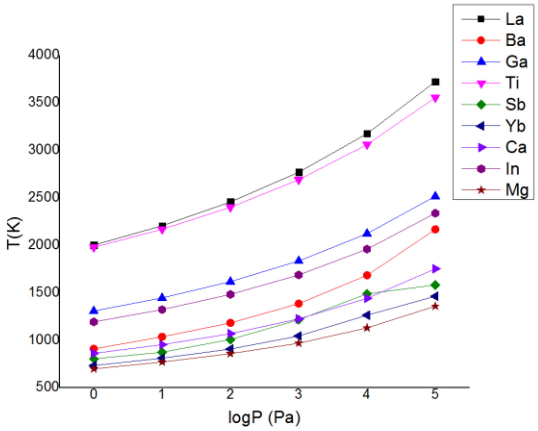

Figure 4.21 Vapor pressure of several element

4.5.1 Experiment

The filled FeCo4Sb12 skutterudites powders have not yet been thermally sprayed. SEM of the powder are shown in Fig. 4.22 The powder size ranges from 30–100 µm, and the particles are highly spherical, hence it is expected that this powder will spray well. The next steps are to spray splats and coatings for characterization.

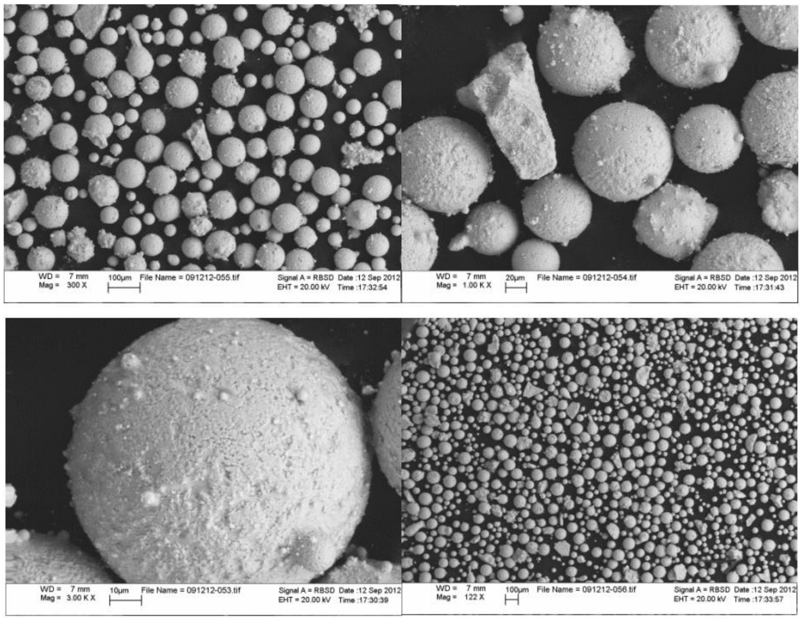

Figure 4.22 SEM of skutterudite powder

4.5.2 Results and discussion

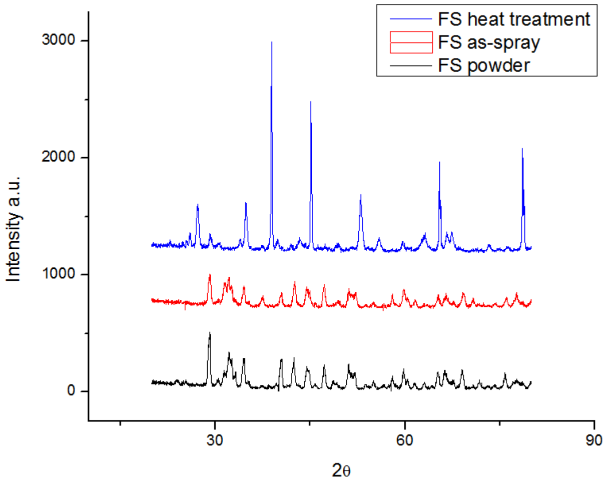

Figure 4.23 XRD of as quenched powder, as sprayed and heat treated samples

Figure 4.23 shows the XRD of as quenched powder, as sprayed and heat treated samples. As we can see, the phase doesn't change before and after thermal spray and this is expected since skutterudite phase is very hard to achieve and only by few minutes thermal spray process, it's impossible to get the correct phase. However, the idea is after quick deposition by thermal spray, appropriate heat treatment is need to obtain the skutterudite phase. Since we deposited as quenched powder on aluminium substrate and the thickness is only 100 microns. We did our heat treatment at 550C under flow of Argon for 24 hours. However, from the XRD we can see, after heat treatment, there is no skutterudite phase and lots of Al has diffused into as quenched powder.

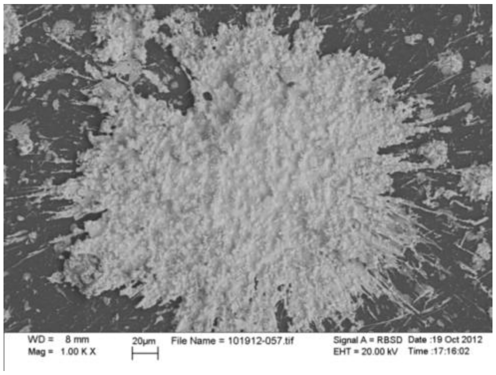

Figure 4.24 Splat of as quenched powder by APS

Even though the correct skutterudite phase didn't show in the heat treated sample, the microstructure of splat and cross section images of coating clearly showed the capability of thermal spray this material. The splat was fully melted and the coating was dense. The bonding within the coating showed good potential of spraying this material.

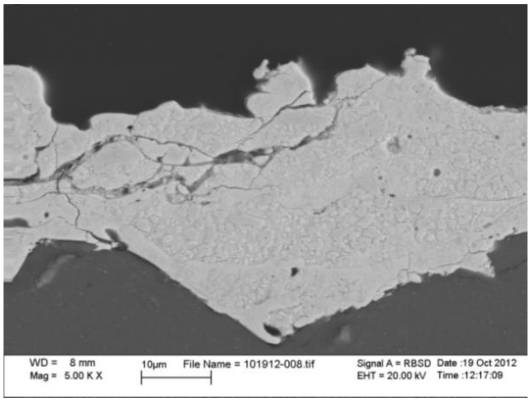

Figure 4.25 Cross section of skutterudite coating by APS

4.5.3 Conclusion

Thermal spray of filled skutterudite has been fish time tried and the as quenched material doesn’t decompose or get oxidized during thermal spray. Heat treatment was done but not in the optimal temperature because of the substrate. XRD showed the as sprayed sample had exactly the same phase as the feedstock powder. But heat treated sample showed some oxidation and diffusion of Al into the coating. Microstructure of splat showed this powder is fully melted and the flowability of this powder is good due to the uniform spherical shape. Cross section image of the coating indicated the bonding and adhesion of this coating is good and more thermal spray of this material should be tried.

5 DC-SPUTTERING OF FILLED SKUTTERUDITE

5.1 Experiment Methods

Four-inch-diameter un-doped <100> silicon wafers (University Wafer, Inc.) were used as the substrates in this research. The silicon wafers were 350- to 400-μm-thick and the resistivity is more than 1 MΩ·cm. The wafers were initially oxidized at 670K for 2 min to get a 240-nm-thick silicon dioxide layer using pressure enhanced chemical vapor deposition PECVD (Trion Technology, Inc.). The target material is purchased from LTS Research Laboratories, Inc. The films were deposited at room temperature without substrate heating.

The process chamber had a base pressure of 5 × 10-6 Torr with overnight pumping. The thickness of thin films was controlled by a film thickness monitor/controller during the deposition. Table 5-1 summaries most of the parameter used in the sputtering process.

Table 5-1 DC magnetron sputtering parameters

Sputtering gas	Ar
Sputtering power (W)	100
Base pressure (Torr)	5 × 10-6
Total gas pressure (Torr)	5 × 10-3
Substrate temperature (Ts)	Room temperature
Substrate to target distance (cm)	40
Substrate material	Oxidized silicon
Deposition rate (nm/s)	0.2

Table 5-2 summarizes all of the samples in this work including target and sputtered sample as well as their heat treated counterpart. The thickness of the film is measured by Stylus Profilometry (Bruker, IL, USA). Target material T1 is as-quenched filled skutterudite and 1020K heat treatment on target material with 120 hours is the T2 sample. Y1 is as sputtered filled skutterudite thin film and Y2~6 are the several thickness thin film samples at various heat treatment conditions.

Table 5-2 Sample synthesis method and post process.

Sample	Material	Condition	Heat treatment	Thickness (nm)
T1	Yb_xCoSb_3	Hot press	N/A	Target
T2	Yb_xCoSb_3	Hot press	1020K, 120 hours	Target
Y1	Yb_xCoSb_3	Sputtering	N/A, as deposited	860
Y2	Yb_xCoSb_3	Sputtering	620K, 2 hours	860
Y3	Yb_xCoSb_3	Sputtering	870K, 4 hours	860
Y4	Yb_xCoSb_3	Sputtering	1020K, 24 hours	860
Y5	Yb_xCoSb_3	Sputtering	1020K, 24 hours	300
Y6	Yb_xCoSb_3	Sputtering	1020K, 24 hours	130

The sample phase was analyzed by X-ray diffraction (XRD) (Ultimate III, Rigaku, TX, USA) utilizing Cu Kα radiation and energy-dispersive X-ray spectroscopy (EDS) (JEOL 7600F, Tokyo, JP). The surface morphologies of the sample were observed using a scanning electric microscope (SEM) (JEOL 7600F, Tokyo, JP). The electrical conductivity was measured using a Keithley digital multimeter (Model 2700, Keithley Instruments, Inc., OH, USA) and the sample was heated from 300 to 400K using a High Temperature Probe Station (MBE-Komponenten AO500, Germany). To investigate its contribution to electrical conductivity, the carrier concentration and Hall mobility were measured with a Hall Measurement System (8404, Lake Shore Cryotronics, Inc., OH, USA) using the Van der Pauw method. Seebeck coefficients were measured using a differential method under vacuum. Thermal conductivity was measured using 3ω method by a lock-in amplifier together with temperature coefficient of resistance (TCR) in high temperature probe station.

5.2 Results and Discussions

5.2.1 Phase composition of filled skutterudite thin film before and after heat treatment

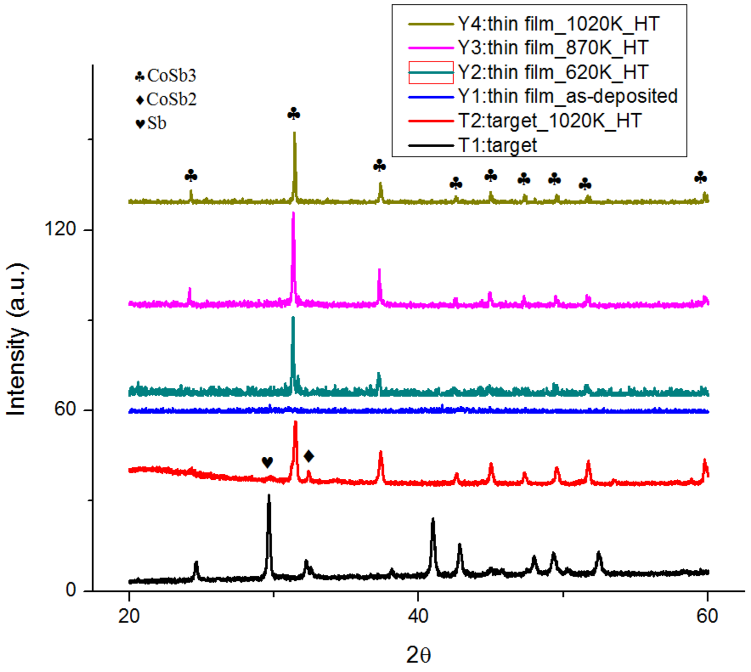

Figure 5.1 XRD of DC magnetron sputtered filled skutterudite thin film and target with different heat treatment

FIG. 5.1 shows the XRD of DC magnetron sputtered thin film as well as target before and after heat treatment. As can been seen from the figure, the as quenched target (T1)is basically contains Sb and CoSb2, instead of being in CoSb3 phase. The reason to choose as quenched target is a consideration of production availability and price. Heat treatment on the as quenched target material at 1020K (Y4) gives mainly CoSb3 phase with a little CoSb2 phase. The as-sputtered thin film (Y1) showed amorphous due to the substrate temperature is kept at room temperature when doing sputtering. Upon 620K heat treatment (Y2), the thin film turned from amorphous into crystalline. The crystallized thin film showed main peak of CoSb3 and this is quite different from the bulk material since bulk filled skutterudite needs higher and longer temperature to be fully turned into CoSb3 phase. The reason is thin film after sputtering process is more uniform and the diffusion is easier due to the lower dimension in thin film sample. Higher temperature heat treatment on 870K (Y3) and 1020K (Y4) can make the film fully crystalline and possibly facilitate the Yb diffusion into the CoSb3 cages. Overall, after 620K heat treatment, the thin film turned from amorphous into crystalline and 1020K with 24 hours heat treatment gives best electrical properties as shown in Table 5-3.

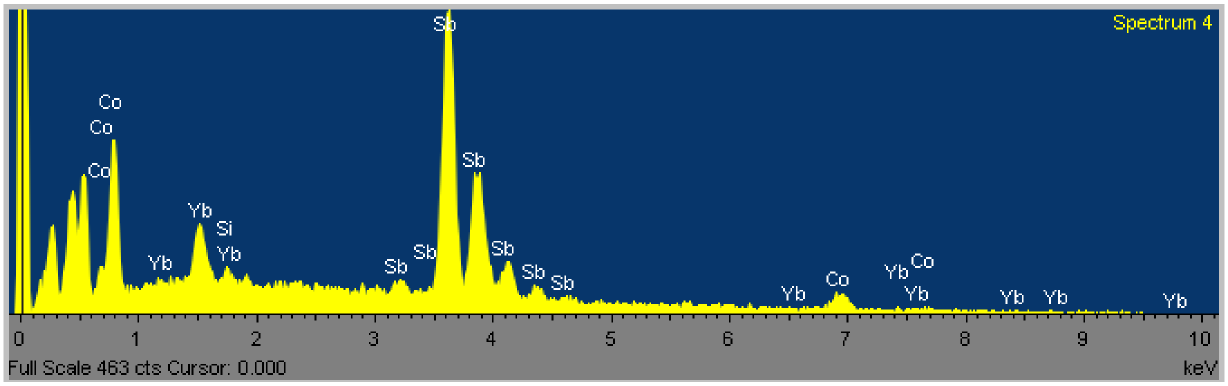

Figure 5.2 EDS of as-sputtered filled skutterudite thin film on Si substrate sample Y1

In FIG. 5.1, the trace Yb element is not found in the XRD result due to its low concentration. EDS is used to check the presence of Yb element as well as it's percentage through the quantitative analysis. EDS analysis (FIG. 5.2) shows the Yb content in the thin film is about 0.93% atomic corresponding to Yb0.15Co4Sb12 which gives N type electrical property.

5.2.2 SEM results of dc-sputtered filled skutterudite thin film samples

Heat treatment is significant for filled skutterudite sample in order to get correct phase and better thermoelectric properties. As shown in FIG. 5.3(a), the as-deposited material is amorphous because during sputtering the substrate is under room temperature. This is typically true for sputtering grown thin film. 620K heat treatment with 2 hours (Y2) turned the thin film into crystal as one can see from above XRD also. FIG. 5.3 (c) and (d) shows higher temperature heat treatment gives larger grain size which will enhance Hall mobility as we showed in Table 5-3.

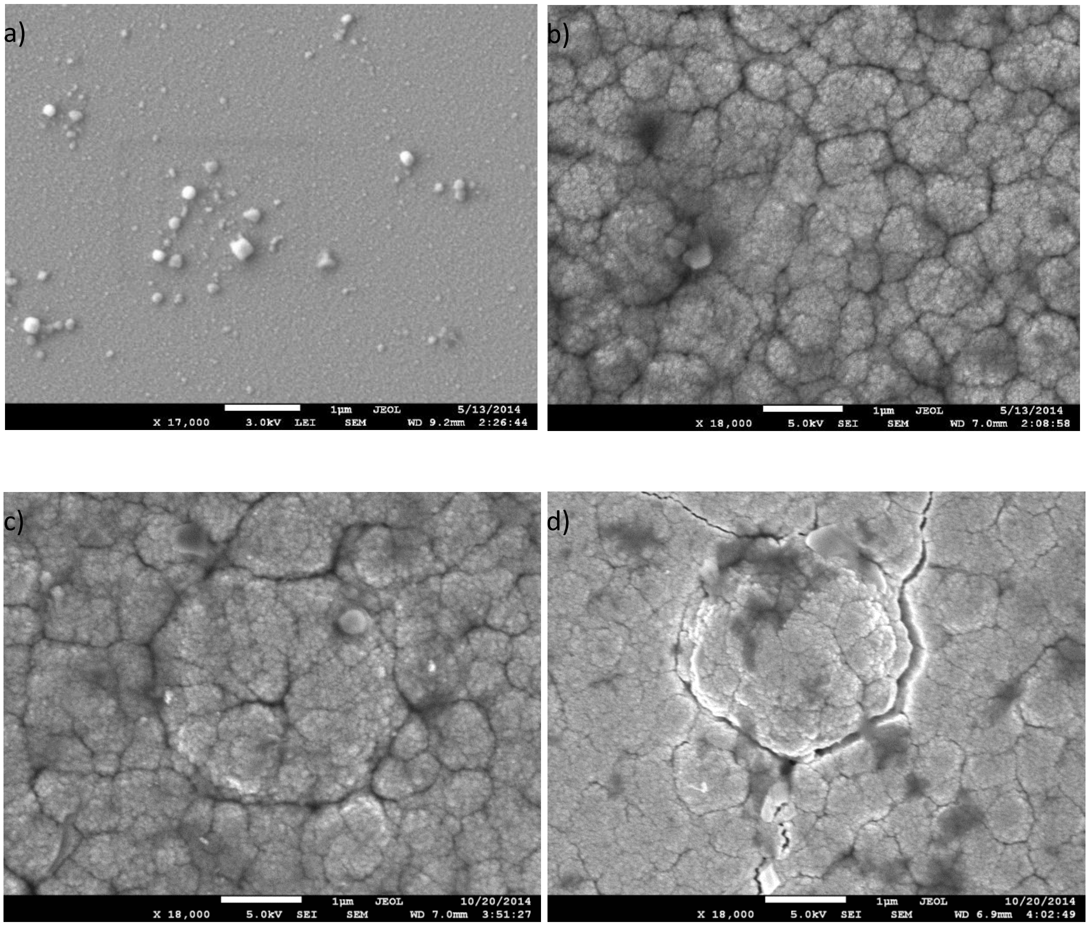

Figure 5.3 SEM surface image of filled skutterudite thin film a) as deposited Y1 sample, b) 620K heat treated Y2 sample, c) 870K HT Y3 sample and d) 1020K HT Y4 sample

5.2.3 Thermoelectric properties of dc-sputtered filled skutterudite thin film samples

5.2.3.1 *Electric properties*

Room temperature electrical conductivity as well as the carrier concentration and mobility were characterized using Van der Pauw method.

Table 5-3 Room temperature Hall Effect for 860nm thin film at different heat treatment temperature

Sample No.	Carrier concentration n ($10^{18}/cm^3$)	Hall mobility μ ($cm^2/V·s$)	Conductivity □= neμ ($10^4S/m$)
Y1	140000	0.07	16
Y2	5000	1.5	12
Y3	12	7.6	0.15
Y4	8.2	89	1.2

Table 5-3 shows the sputtered thin film electrical properties at different anneal temperature. As sputtered thin film sample shows a very high electrical conductivity due to high carrier concentration. The bonding between Co and Sb has not been fully formed which give thus high carrier concentration, while the mobility 0.07 cm2/V·s is very low. After 620K heat treatment for 2 hours (Y2), the CoSb3 phase started to accumulate as seen in FIG.1 and mobility increased to 1.5 cm2/V·s. Higher temperature heat treatment (Y3 and Y4) increased the mobility even more with some extent sacrifice of carrier concentration. Lower concentration will be beneficial to Seebeck coefficient as shown in Equation 1. In fact, 1020K heat treatment (Y4) can make sputtered thin film fully crystalized [52] and more importantly it has large carrier mobility. Thus from now on we chose 1020K heat treatment for our work.

Table 5-4 Room temperature Hall Effect for 1020K heat treated thin film at different thicknesses

Sample	Thickness (nm)	Carrier concentration n ($10^{18}/cm^3$)	Hall mobility μ ($cm^2/V·s$)	Conductivity □= neμ ($10^4S/m$)
Y4	860	8.2	89	1.2
Y5	300	17	46	1.3
Y6	130	4.8	80	0.61
Anno[52]	71	0.4	264	0.62

Thin films of different thickness have been deposit using DC magnetron sputtering machine with a constant sputtering rate. The values vary in electrical conductivity and Hall Effect measurement revealed carrier concentration and mobility both play important roles in electrical conductivity.

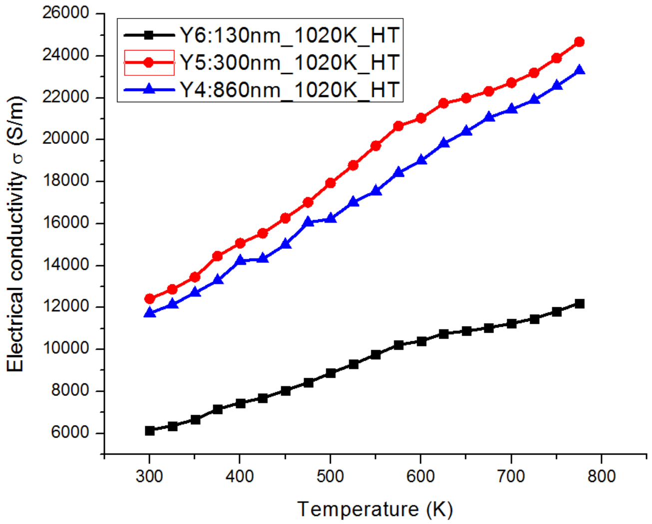

Figure 5.4 Electrical conductivity of 1020K heat treatment Yb doped CoSb3 thin film with different thicknesses

Electrical conductivity measurements for sample with 1020K heat treatment were made from 300 to 770K under vacuum. The measured electrical conductivities for sputtered thin film are shown in FIG.5.4. As can be seen, the variation in electrical conductivity is significant in different thickness samples. The 130nm thin film (Y6) has the smallest electrical conductivity due to its lower carrier concentration. The 300nm and 860nm thin films (Y5 and Y4) have higher conductivity with a higher carrier concentration level.

5.2.3.2 *Seebeck coefficient*

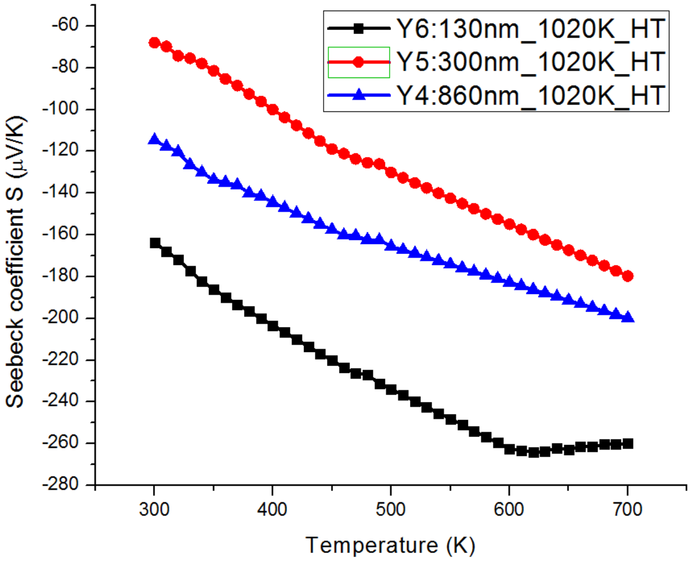

Figure 5.5 Seebeck of 1020K heat treatment Yb doped CoSb3 thin film with different thicknesses

FIG. 5.5 shows the measured Seebeck coefficients for filled skutterudite thin film with various film thicknesses. Seebeck coefficient is very sensitive to carrier concentration and is inversely proportional to electrical conductivity due to the opposite dependence of carrier concentration, i.e., S~ln (n) in Eq. (1).[7] FIG.5.5 shows the 130nm thick thin film (Y6) had a higher Seebeck coefficient because of its lower carrier concentration as shown in Table IV. As carrier concentration increase in Y4 and Y5 sample, the Seebeck coefficient starts to decrease. Generally as temperature increases, the Seebeck coefficient will increase in magnitude because the ratio of effective density of state to carrier concentration N_c/n in Eq. (1) is proportional to exp(kT). However for 130nm thin film (Y6) sample, the Seebeck coefficient starts to decrease around 600K which may due to the carrier energy filtering effect that has been caused by the potential barriers at grain boundaries[52]. The fact that the Seebeck coefficient is negative in FIG.5.5 indicates that Yb doped CoSb3 thin film is an n-type semiconductor, which also validates with the Hall Effect measurement.

5.2.3.3 *Thermal conductivity*

One popular technique for thermoelectric materials is a 3ω-method, in which a thin metal strip evaporated on the sample acts as heat source and a thermometer. Thermal conductivity was measured though 3ω method invented by Cahill et al.[136],[137] from room temperature up to 700K by depositing Au strip on top of sample. The heater is driven with AC current at frequency ω, which causes heat source to oscillate at frequency 2ω. By monitoring AC voltage as a function of the frequency of the applied AC current thermal conductivity can be determined. Prior to Au strip deposition, a thin layer of silicon oxidation layer is grown by PECVD for insulation.

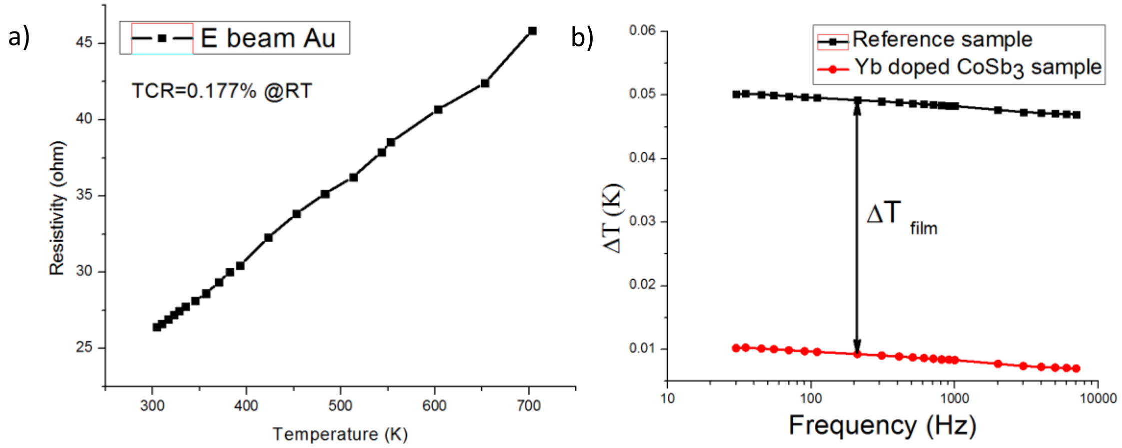

Figure 5.6 Thermal conductivity measurement including a)TCR of Au and b) example of temperature oscillations, ΔT, measured in the 3 ω method at 300 K on the Yb doped CoSb3 film and the reference sample

The calculations of the cross-plane thermal conductivity k_{film} of the thin films were carried out from the experimental data plotted in Fig.5.6(b) in accordance with Lee and Cahil [138] using a simplified one-dimensional model.

$$k_{film} = \frac{P_l \cdot t}{w \cdot \Delta T_{film}} \tag{2}$$

Where P_l is the supplied power per unit length of the narrow metal heater thermometer of the width w, t is the thickness of the tested thin film, ΔT_{film} is the increase of the temperature oscillations due to the thin film with respect to the reference sample. FIG.5.6 illustrates typical frequency dependent temperature oscillations in the sample containing the Yb filled CoSb3 thin film and in the reference sample. The calculation of the thermal conductivity using Eq.(2) gave the value of about 2~3W/mK at room temperature, which is 2 to 3 times lower than for the bulk material.

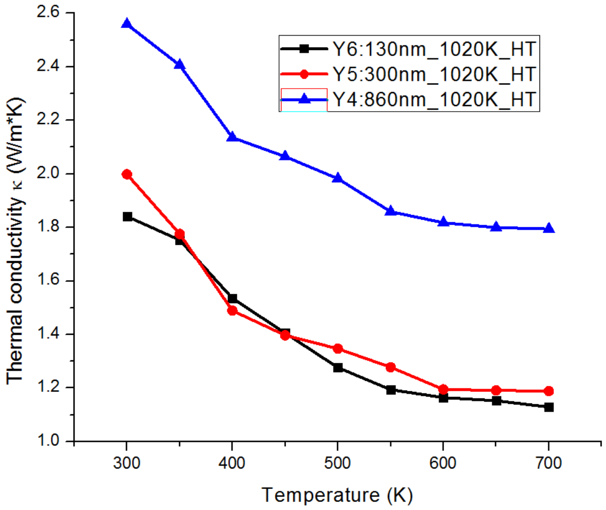

Figure 5.7 Thermal conductivity of Yb doped CoSb3 film with different thickness with temperature dependent

Temperature dependent thermal conductivity was measured similarly using 3ω method with the example shown in FIG. 6. At each temperature point, a frequency sweep is needed for the ΔT_{film} calculation for both thin film sample and reference sample. The TCR of e-beam evaporated gold is very stable up to 700K and the resistivity can be calculated based the measured TCR and room temperature resistivity. By applying the Eq. (2), thermal conductivity was calculated and plotted in FIG.5.7 for the thin films with different thickness. As temperature increases, all three films tend to decrease its thermal conductivity because the phonon scattering is enhanced at higher temperature. Thinner samples of 130nm and 300nm (Y6 and Y5) has a slightly lower thermal conductivity than 860nm thin film (Y4) which may be due to the enhanced phonon scattering by grain interface and boundary in thin films.

5.2.3.4 *Figure of merit, ZT*

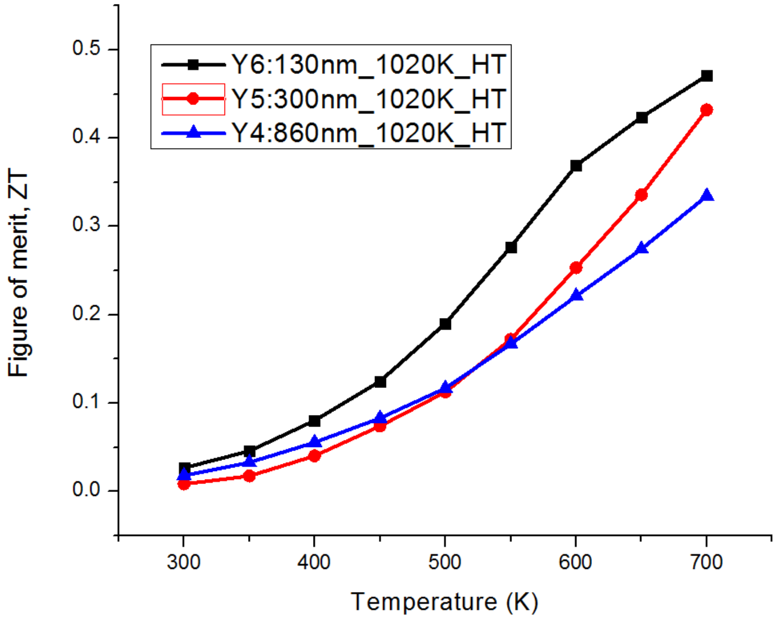

Figure 5.8 Figure of Merit, ZT of Yb filled CoSb3 films with different thicknesses

The figure of merit ZT value of the sample can be estimated by combining the electrical properties, Seebeck coefficient and thermal conductivity. FIG.5. 8 shows the ZT for Yb filled CoSb3 thin film with different thickness. The highest ZT is achieved with the 130nm sample (Y6) because it has much higher Seebeck coefficient even its electrical conductivity is slightly lower than other samples. Also, thermal conductivity of Y6 sample is lower than that of Y4 sample. The results show the figure of merit does not significantly depend on the thin film thickness at lower temperatures. While at each deposition and heat treatment, the carrier concentration and mobility do change a lot. Generally, with same carrier concentration and mobility, thinner film may have higher figure of merit due to lower thermal conductivity caused by enhanced phonon scattering by boundaries.

Sputtered Yb doped $CoSb_3$ figure of merit in this work is found to be between half to one third to its bulk material reported by Nolas et al.[44]. The lower ZT in thin film mainly comes from the lower mobility. As we saw in bulk material, the mobility can goes up to several thousand $cm^2/V{\cdot}s$ which is two magnitude higher than thin film in this work. Higher temperature with longer heat treatment may help increase the mobility but could also induce crack in the thin film if heating/cooling process is not well controlled.

5.3 Conclusions

Filled skutterudite is the state of art high temperature thermoelectric material and in this work for the first time Yb filled CoSb3 skutterudite thin film has been reported using DC magnetron sputtering method. The selection of using DC magnetron sputtering lies in its high deposition rate and it can maintain the target material composition. More importantly, magnetron sputtering provides denser microstructure which surpasses most of other thin film deposition techniques. The parameters of DC magnetron and post heat treatment on sputtered sample have been optimized experimentally and Yb filled $CoSb_3$ thermoelectric properties have been characterized.

Electrical conductivity, Seebeck coefficient, thermal conductivity, and figure of merit are characterized from 300K to 700K. XRD, SEM and EDS of the different thickness samples at three kinds of heat treatment conditions are obtained to assess the phase composition and crystallinity of thin film samples with different heat treatment temperatures. In this work, 1020K heat treatment was adopted for thin film post process due to thin film high degree of crystallinity as well as avoiding reverse heating effect. Carrier concentration and Hall mobility are obtained from Hall Effect measurements, which provide further insight into the electrical conductivity and Seebeck coefficient mechanisms. As-sputtered sample has huge carrier concentration which gives very high electrical conductivity. However, low Hall mobility in as sputtered sample makes it unsuitable for thermoelectric application. For three types of heat treatment, 1020K gives best Hall mobility. Seebeck coefficient is inversely dependent on carrier concentration, so the lower carrier concentration in 130nm sample increases Seebeck a lot and overall it gives the best figure of merit. Since the carrier concentration play trade-off role in thermoelectric material, it should be optimized to give better ZT. It seems in this work, the low carrier concentration is more favorable due to its large increase in Seebeck coefficient when conserving the square of Seebeck coefficient in the ZT equation. Thermal conductivity of thin film filled skutterudite was found to be much less compared with bulk Yb filled CoSb3 skutterudite which may be due to the enhanced phonon scattering by grain interface and boundary. 860nm sample is much thicker than the rest two samples and has a higher thermal conductivity. Different thickness thin film samples were prepared with same sputtering deposition rate and maximum ZT of 0.48 was achieve at 700K for 130nm thick sample. This value was between half and one third of bulk figure of merit which due to the lower Hall mobility in thin film samples.

6 PRELIMINARY THERMOELECTRIC GENERATOR DESIGN AND OPTIMIZATION IN AUTOMOBILE APPLICATION

6.1 Integrated Design of TEG

6.1.1 Heat transfer modeling

Our application of thermoelectric generator is on the exhaust pipe which means the geometry is cylindrical. This differs to most of the current modeling based on the thermal resistance network. First of all, our model has several layer which shows in figure 6.1.

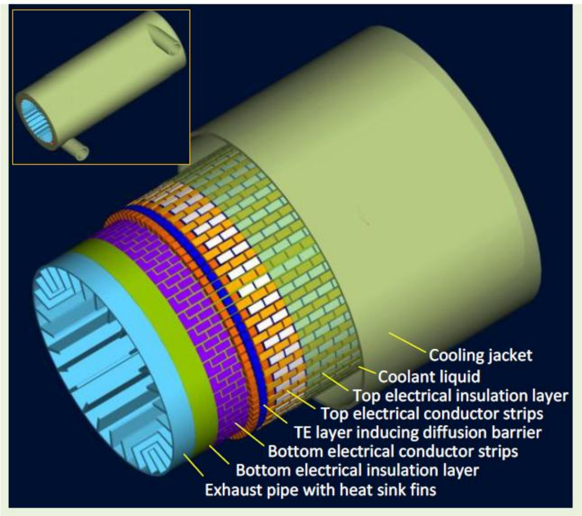

Figure 6.1 Integrated design concept (courtesy of Prof. Lei Zuo)

Starting from the exhaust pipe, a layer of insulator like alumina is thermal sprayed. Then a layer of conductor is right above the insulator to connect p and n type of thermo-element. On the other side of the thermo-element, another layer of conducting layer and insulation layer is sprayed. Outside is the cooling device which is important to improve the efficiency of the thermoelectric generator. The pipe is the heat source and cooling device is the heat sink.

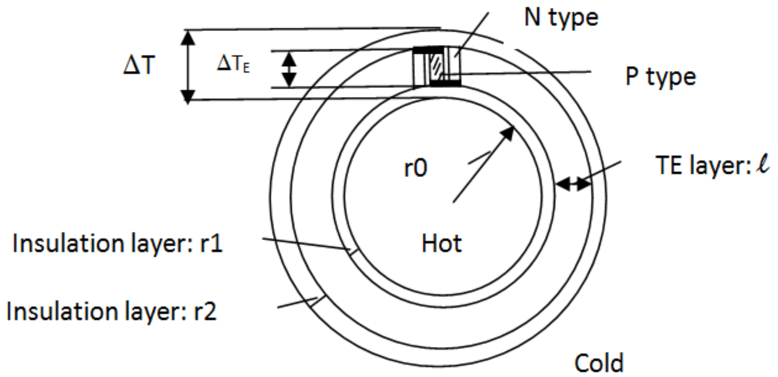

Figure 6.2 Scheme of the TEG layers

In the above figure 6.2, the inner pipe provides heat source to the thermoelectric generator and the cooling device outside draw the heat away. Some parameters of the model are the pipe radius is r0, the inner side insulation layer is r1, the insulation layer outside is r2 and the thermoelectric element layer has a leg length of L. N and P type TE legs are connected by conducting layer on both end. In this model authors just investigated the influence of the geometry of the insulation and thermoelectric. However the heat source and heat sink design will also influence the overall heat transfer in the system. Under this simplification, the assumption of constant temperature boundary condition is made.

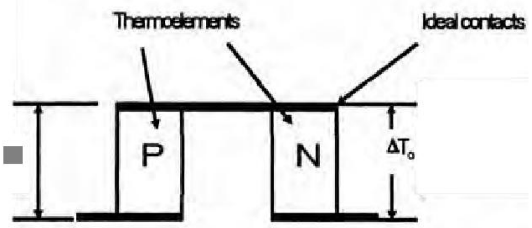

Figure 6.3 thermoelectric couple in the system

Although the overall geometry is cylindrical, the thermoelectric element can still be examined in one dimensional Cartesian coordinate. The reason lies that the thermoelectric element length is very small compared with pipe diameter which means the thermoelectric element on a circle which has an infinity radius. Another reason is the thermoelectric elements are separated into p and n type and they are not continuous. The local geometry of the thermoelectric element is not cylindrical. The accuracy of this assumption is affected by lots of factors, such as change in air gap/leg area ratio, length of legs and the advection effect in natural convection mode. For example, the increase in air gap/leg area ratio leads to more lateral heat transfer and the increased length of the legs will enhance the assumption that heat transfer is mainly in one-dimension. Based on this assumption our basic model using the thermal resistance network is established.

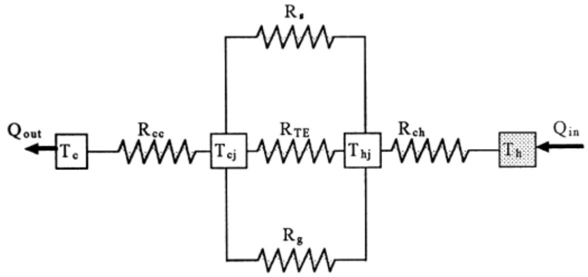

Figure 6.4 Thermal resistance network of the TEG module

Figure 6.4 is a typical resistance network that used in TGE modeling. Heat comes from the heat source and transfers through insulation layer, conducting layer, thermoelectric element layer, conducting layer, insulation layer again and goes out from the heat sink. The thermal resistance of conducting layer here can be neglected since the material be chosen is cooper which has very low thermal resistance compared to other parts. The parameters show above are: temperature of hot source and heat sink Th and Tc; thermal resistance of hot and cold side ceramic Rch and Rcc; temperature of hot and cold side of thermoelectric element Thj and Tcj. Thermal resistance of thermoelectric element RTE; thermoelectric of gas in the module gap between N, P thermoelectric element Rg; thermal resistance of the sealant used in the module Rs.

$$T_{hj} = T_h - \frac{R_{ch}\Delta T}{\sum R_{th}} \tag{6.1}$$

$$T_{cj} = T_c + \frac{R_{cc}\Delta T}{\sum R_{th}} \tag{6.2}$$

Here, $\sum \mathrm{R_{th}}$ is the total thermal resistance between Th and Tc in figure 6.3 above and $\Delta \mathrm{T} = \mathrm{T_h} - \mathrm{T_c}$.The total heat flux Q from the heat source to the heat sink through the thermoelectric module is given by

$$Q = \frac{\Delta T}{\sum R_{th}} \tag{6.3}$$

$$\sum R_{th} = R_{ch} + \left(\frac{1}{R_{TE}} + \frac{1}{R_g} + \frac{1}{R_s}\right)^{-1} + R_{cc} \tag{6.4}$$

From the geometry showed in figure 6.2, the thermal resistance of the insulation layer is given by

$$R_{ch} = \frac{\ln((r0+r1)/r0)}{2\pi L k_c} \tag{6.5}$$

$$R_{cc} = \frac{\ln((r0+r1+l+r2)/(r0+r1+l))}{2\pi L k_c} \tag{6.6}$$

The thermal resistance of the thermoelectric element is not hollow cylinder model any more. It is one dimension as shown in figure 6.2 and given by

$$R_{TE} = \frac{l}{Ak} \tag{6.7}$$

Here A is the cross section area of total thermoelectric element and k is the thermal conductivity of the thermometric material $\mathrm{k} = \mathrm{k_p} + \mathrm{k_n}$. Similarly, for the sealant when the area As and thermal conductivity ks is given. The thermal resistance is then given by

$$R_s = \frac{l}{A_s k_s} \tag{6.8}$$

The thermal resistance of air in the gap is a little different because beside conduction, radiation is another heat transfer method for heat goes through the module and it’s given by

$$R_g = \left[\frac{A_g k_g}{l} + \frac{\varepsilon \sigma A_g}{2-\varepsilon}\left(T_{hj}{}^2 + T_{cj}{}^2\right)\left(T_{hj} + T_{cj}\right)\right]^{-1} \tag{6.9}$$

where Ag and kg are the cross section area and thermal conductivity of air gas.
$\sigma = 5.67 \times 10^{-8} \mathrm{W\,m^{-2}K^{-4}}$ is the Stefan-Boltzmann constant and ε is the emmisivity of the ceramic plate surface. For simplicity, the emmisivity are assumed the same for hot and cold ceramic plates.

6.1.2 Electrical resistance modeling

For electrical resistance, the situation will be easier since only thermoelectric element and conducting layer are considered. Actually the resistance of conducting cooper layer can be neglected compared with the thermoelectric. But contact resistance is significant where contacting electrical resistance of the junction is given by

$$r = 2r_c + 2\rho\frac{l}{A} = \frac{2\rho(\rho_{oc}+l)}{A} \tag{6.10}$$

where $\rho = (\rho_n + \rho_p)/2$ is the electrical resistivity of the thermoelectric material and $r_c$is the contact electrical resistance at each junction. $\rho_{oc} = \rho_c/\rho$ is the ratio between contact resistivity and thermoelectric resistivity.

6.1.3 TEG module geometry optimization

Based on the above modeling, the optimal leg length is desired to save more energy. The criterion is to optimize the power per unit area which is an index for waste heat recovery since the cost of the heat source is not a concern. But under some other applications where heat source is not cost-free, a better model which includes the efficiency of the module should be established.

Under matched load, the voltage per unit couple of thermoelectric generator V is given by

$$V = \frac{\bar{S}}{2}\Delta T_E \tag{6.11}$$

The factor 2 in the above equation explains only half of the power can be used to generate power on the load while the other half is wasted as Joule heat. The current per unit area is the voltage divided by the internal resistance which is given by

$$I = \frac{V}{r} = \frac{\bar{S}}{4\rho(\rho_{oc}+l)}\Delta T_E \tag{6.12}$$

The power per unit couple generated then is

$$P = VI = \frac{\bar{S}^2}{8\rho(\rho_{oc}+l)}(\Delta T_E)^2 \tag{6.13}$$

where $\bar{S} = (S_n + S_p)/2$ is the average Seebeck coefficient of n, p type thermometric material. Optimization of the power according to leg length is based on the above equation. ΔT_E is also a function of leg length l. Combine equation (1), (2) and $\Delta T_E = T_{hj} - T_{cj}$, a more detailed equation of power per unit couple can be established.

$$\Delta T_E = \Delta T\left(1 - \frac{R_{ch} + R_{cc}}{\sum R_{th}}\right) \tag{6.14}$$

To simplify the model and also to make it solvable, the assumption $R_{ch} = R_{cc} = R_c$ should be made which means equation (6.5) equals to equation (6.6). This will give

$$r2 = \frac{r0 + r1 + l}{r0}\, r1 \tag{6.15}$$

Under this assumption, the equation (6.14) can be rearranged as

$$\Delta T_E = \Delta T\left(1 - \frac{2R_c}{\sum R_{th}}\right) \tag{6.16}$$

While

$$\frac{2R_c}{\sum R_{th}} = \frac{2R_c}{2R_c + \left(\frac{1}{R_{TE}} + \frac{1}{R_g} + \frac{1}{R_s}\right)^{-1}}$$

$$= \left\{1 + \left[\frac{\frac{2\ln\left((r0 + r1)\right)}{r0}}{lA_{oc}k_{oc}}\left(r0 + \frac{3r1}{2} + \frac{l}{2} + \frac{r2}{4}\right)X\right]^{-1}\right\}^{-1} \tag{6.17}$$

Where

$$X = 1 + A_{os}k_{os} + A_{og}k_{og} + \frac{\varepsilon\sigma A_g l}{(2-\varepsilon)k}\left({T_{hj}}^2 + {T_{cj}}^2\right)\left(T_{hj} + T_{cj}\right) \tag{6.18}$$

We also assume the width of the module L is the same for hot and cold ceramic plate

$$L = \frac{A_{hc}}{2\pi(r0 + r1/2)} = \frac{A_{cc}}{2\pi\left(r0 + r1 + l + \frac{r2}{2}\right)} \tag{6.19}$$

Although the two surface area of hot and cold ceramic plat is different, the difference is very small because $r1, l, r2$ are all small compared with $r0$. A reasonable simplification is to set $A_{hc} \cong A_{cc} = A_c$ then the L can be given as an average

$$L = \frac{A_c}{2\pi\left(r0 + \frac{3r1}{2} + \frac{l}{2} + \frac{r2}{4}\right)} \tag{6.20}$$

In the above equations, A_{oc}, k_{oc} are the ratio of cross section area and thermal conductivity between ceramic layer and thermoelectric element; A_{os}, k_{os} are the cross section area and thermal conductivity ratio between sealant and thermoelectric element; $A_{og}, k_{og}$are the ratio between air gap and thermoelectric element. Plug T_{hj} and T_{cj} in equation (6.1) and (6.2) into equation (6.18) will establish an equation of X

$$X = 1 + A_{os}k_{os} + A_{og}k_{og} +$$

$$\frac{\varepsilon\sigma A_g l}{(2-\varepsilon)k}\left({T_h}^2 + {T_c}^2 - \frac{\Delta T^2}{1+CX} + \frac{0.5\Delta T^2}{(1+CX)^2}\right)(T_h + T_c) \tag{6.21}$$

Where the coefficient C is

$$C = 1 + \frac{2ln\frac{(r0+r1)}{r0}}{lA_{oc}k_{oc}}\left(r0 + \frac{3r1}{2} + \frac{l}{2} + \frac{r2}{4}\right) \tag{6.22}$$

All the parameters except leg length are given to find the optimal leg length for maximum power density output. Plug equation (22) into equation (17), and combine equation (16) with (14). The power per unit area is given by

$$P = \frac{\overline{S}^2}{8\rho(\rho_{oc} + l)}(\Delta T)^2(1 + CX)^{-2} \tag{6.23}$$

After obtaining the optimal leg length, the leg length can be kept as a constant and vary the air gap ratio A_{og}. The equation is still the same to find the optimal air gap ratio. The reason for finding the influence of the air gap distance is related to our manufacturing process. For small gap, laser cutting is required and the cost of the manufacturing will be a little more. For large gap, conventional mechanical method, like milling can be implemented and thus reduces the cost as well.

6.1.4 Result and sensitivity analysis

Based on the heat transfer model, optimization of the leg length is made when all other parameters are kept constant. Table 6-1 shows the parameters when the oxide (T_iO_{2-x} and $C_oO(Li_{0.5})$) are used.

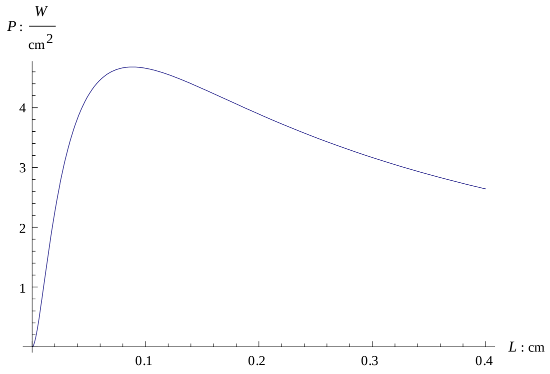

Figure 6.5 Optimal leg length for maximum power output

The result is reasonable since if the leg length is too small, the contact resistance will be sufficient large and if the leg length is too large the electrical resistance will be very large. According to the above equation, the air gap ratio Aog will influence the maximum output power per unit area. And as the ratio goes up, the heat conduction via air and radiation will increase which decrease the effective temperatureΔT_E. This model shows the air gap should be kept as small as possible.

Table 6-1 Parameters of the thermoelectric module

Para.	Value	Unit/ definition	Remarks
ρ_{oc}	0.1	ρ_c/ρ	Contact resistance ratio
ρ	0.0015	$(\rho_n + \rho_p)/2$	Ave. elec. resistivity
A_{oc}	1.5	A_c/A	ratio
k_{oc}	2.5	k_c/k	ratio
A_{os}	1/50	A_s/A	ratio
k_{os}	0.15	k_s/k	ratio
A_{og}	0.25	A_g/A	ratio
k_{og}	0.01	k_g/k	ratio
$r0$	3.2	cm	radius
$r1$	0.05	cm	length
σ	$5.67 \times 10^{(-12)}$	$\text{W m}^{-2}\text{K}^{-4}$	constant
$\overline{S}$	0.00045	V/K	Ave. Seebeck
k	0.024	W/(cm*K)	Ave. therm. Cond.
ε	0.3	1	ceramic plate
T_h	400	deg C	Hot side
T_c	100	deg C	Cold side

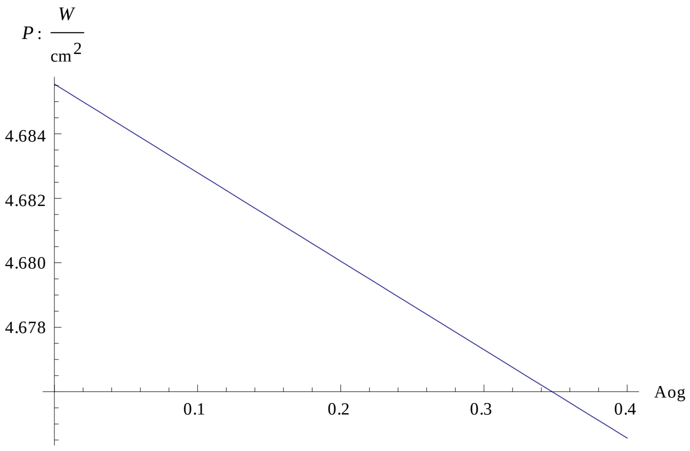

Figure 6.6 Optimal air gap for maximum power output

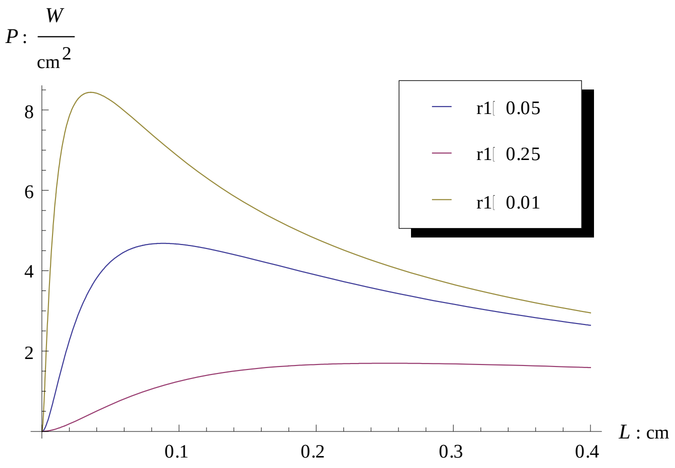

Figure 6.7 Sensitivity analysis of ceramic layer

The above figure shows the thicker ceramic layer is, the smaller optimal leg length will be. The change is obvious which means the optimal leg length is sensitive to the variation of ceramic layer. If the manufacturing process has some error on the thickness of thermal spray alumina, the optimal leg length will change a lot. So the thickness of ceramic layer should be control carefully to get an accurate optimal leg length.

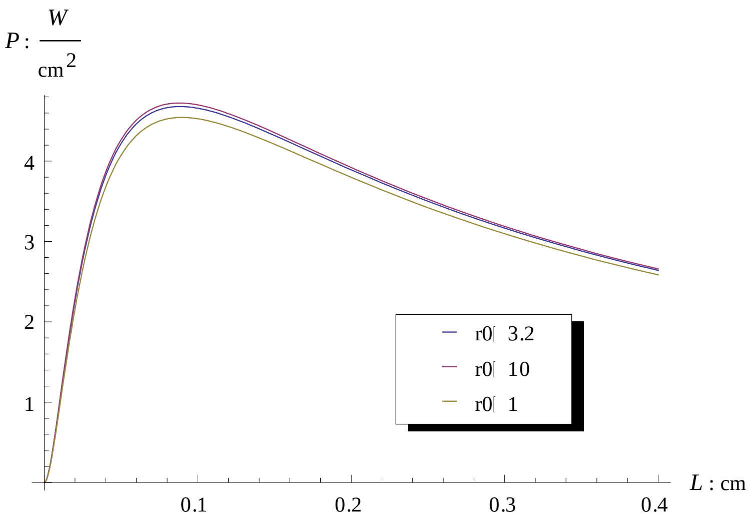

Figure 6.8 Sensitivity analysis of inner exhaust pipe radius

Figure 6.8 shows the optimal leg length is not very sensitive to the exhaust pipe diameter. The only concern is that the radius of the exhaust pipe should not be too small since the model is based on the assumption that ceramic layer is much smaller compared with the exhaust pipe diameter. For the manufacturing of exhaust pipe, the procedure is standard and the variation won't be that much. So this will not be a factor to influence optimal leg length.

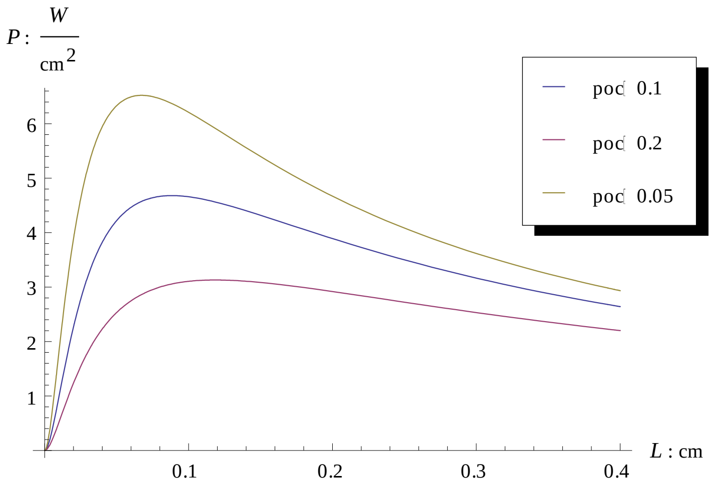

Figure 6.9 Sensitivity analysis of electrical contact resistance

Figure 6.9 shows the optimal leg length will be smaller if the electrical contact resistance can be reduced. This is due to the Joule heat loss on the conjunction. Basically, better contact is desired in the module fabrication, but it’s very hard to eliminate the influence of contact resistance.

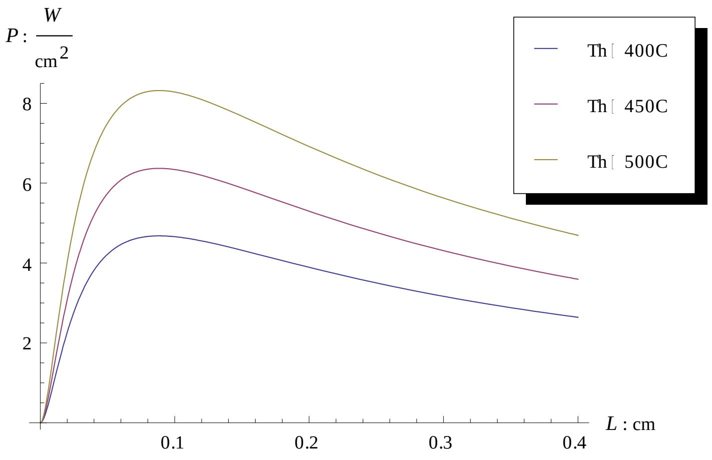

Figure 6.10 Influence of hot source temperature

Figure 6.10 investigated the heat source temperature influence on the optimal leg length. It’s important since the exhaust pipe has large variation of temperature due to all kinds of driving conditions and car size. Typically, larger car with higher driving speed will give higher temperature of exhaust. The authors have another review paper on the exhaust temperature and mass flow rate.

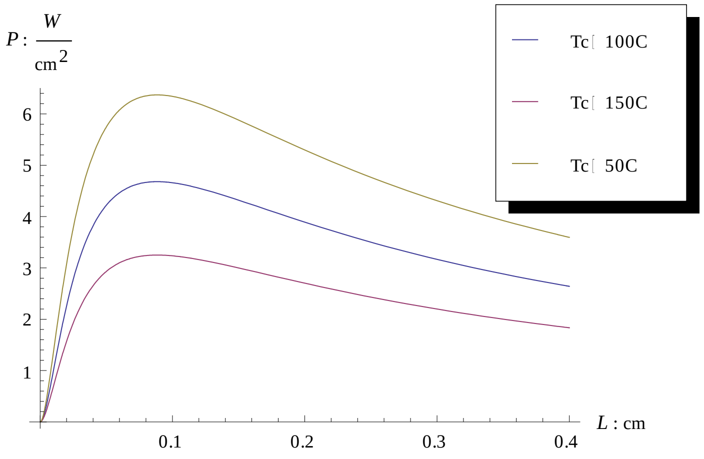

Figure 6.11 Influence of heat sink temperature to optimal leg length

Figure 6.11 is similar to figure 6.10 which shows the heat sink temperature also has influence on the optimization of leg length. Heat sink temperature is affected by the effective cooling device. Basically, increase the convection coefficient and contact area of the heat sink will make the cooling more efficient. At optimal leg length, lower the heat sink temperature, higher the output power.

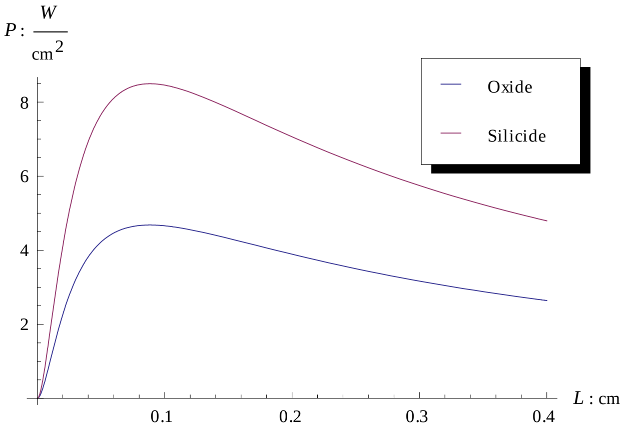

Figure 6.12 Different TE material influence on power output

Figure 6.12 shows how different materials influence the optimization process. The oxides are n-type T_iO_{2-x} and p-type $C_oO(Li_{0.5})$. While silicides like Mg_2Si and MnSi1.7 are also material that people have interests. Based on our thermal sprayed Mg_2Si sample, we got good result on the thermal conductivity and comparable result on electrical conductivity. But the Seebeck of the currently sprayed Mg_2Si is pretty low due to a lot of oxidation- MgO. The parameters used in the comparison are from other literature: $\overline{S}$ is 350μV/K and ρ is 0.0005Ωcm.

6.1.5 Conclusion

In this part, the heat transfer and electrical contact resistor model is established to find the optimal leg length and width based on the exhaust pipe geometry. Small leg length will increase the contact resistance and large leg length will increase the electrical resistivity of thermoelectric element. The tradeoff between these two factors is addressed and the optimal leg length is found to be around 0.85mm for oxide material (n-type T_iO_{2-x} and p-type$C_oO(Li_{0.5})$) and 0.9mm for Mg_2Si. The leg width is as smalls as possible to increase the output power except to separate the n, p type material. The sensitivity analysis shows:

The thicker ceramic layer, the smaller optimal leg length and the optimal leg length is sensitive to the variation of ceramic layer. So the thickness of ceramic layer should be control carefully to get an accurate optimal leg length during process. The optimal leg length is not very sensitive to the exhaust pipe diameter. The only concern is that the radius of the exhaust pipe should not be too small since the model is based on the assumption that ceramic layer is much smaller compared with the exhaust pipe diameter. The optimal leg length will be smaller if the electrical contact resistance can be reduced. Good contact of cooper layer is desired during thermal spray process.Heat source and heat sink temperature has influence on the output but is not sensitive to the optimal leg length. For module fabrication, the heat source temperature can be neglected.

The oxides are n-type $\mathrm{T_iO_{2-x}}$ and p-type$\mathrm{C_oO(Li_{0.5})}$ and Mg_2Si have different optimal leg length but the change is slight. So the optimization of the module can be done independent of material selection as long as the material is not at the abnormal level of thermoelectric property.

6.2 Fin design and electric output power estimation

6.2.1 Basic heat transfer calculations

Figure 6.13 shows the heat flow in a TEG device, where the exhaust gases (temperatures in and out denoted as “T in hot” and “T out hot”) and a coolant (temperatures in and out denoted as “T in cold” and “T out cold” flow in opposite directions to enhance heat transfer. The coolant is assumed to be normal engine coolant, routed from the radiator outlet to the TEG and then back through the radiator.

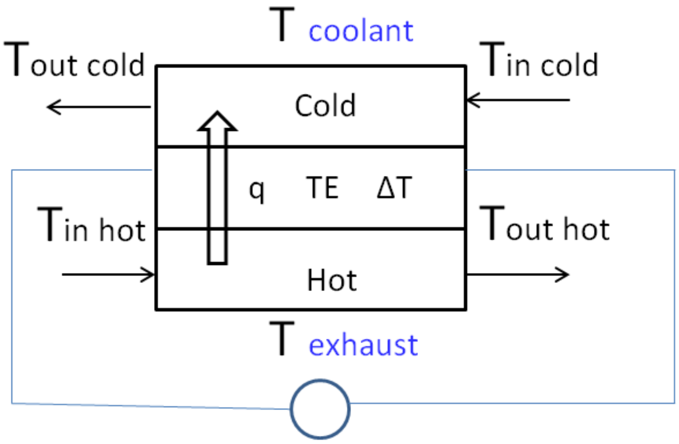

Figure 6.13 Heat flow through a TEG

Heat flux (q) through the TEG module is computed using equation 6.24, where ΔT is the effective temperature difference between the TEG hot side and cold side, k is the thermal conductivity of theTE material, A is the cross section area and Δx is the length of TE material.

$$q = \frac{kA}{\Delta x}\Delta T \tag{6.24}$$

Also, one can put the heat flux through the TEG in the form of overall heat transfer coefficient UA (U = heat transfer coefficient and A = contact area) as in equation 6.25.

$$q = UA\Delta T_m \tag{6.25}$$

While the ΔTm is the log mean temperature which is given by equation 6.26.

$$\Delta T_m = \frac{(T_{hi} - T_{ci}) - (T_{ho} - T_{co})}{\ln(T_{hi} - T_{ci})/(T_{ho} - T_{co})} \tag{6.26}$$

Typically, the inlet temperatures of the exhaust and coolant are known, but the outlet temperatures are not. So one needs to iteratively calculate the effective temperature to find a balance point where the heat lost by the exhaust gases equals the heat gained by the coolant.

An alternative way to do this calculation is by using Number of Transfer Units (NTU) Method [17] which is widely accepted in heat exchanger design. The NTU Method starts with equation 6.27, where q_{max} is the maximum heat transfer between the fluids and C_{min} is the smaller heat capacity rate (mass flow rate multiplied by specific heat).

$$q_{max} = C_{min}(T_{hi} - T_{ci}) \tag{6.27}$$

The effectiveness (E) of the heat exchanger is given by the ratio between actual heat transfer and the maximum theoretical heat transfer, as given by equation 6.28.

$$E = \frac{q}{q_{max}} \tag{6.28}$$

Effectiveness is a dimensionless quantity between 0 and 1. If we know E for a particular heat exchanger, and we know the inlet conditions of the two flow streams we can calculate the amount of heat being transferred between the fluids by using equation 6.29.

$$q = EC_{min}(T_{hi} - T_{ci}) \tag{6.29}$$

For any heat exchanger it can be shown that E can be expressed as in equation 6.30.

$$E = f(NTU, \frac{C_{min}}{C_{max}}) \tag{6.30}$$

For a given geometry, E can be calculated using correlations in terms of the heat capacity ratio (Cr), as in equation 6.31.

$$C_r = \frac{C_{min}}{C_{max}} \tag{6.31}$$

and the number of transfer units, NTU, is given by equation 6.32.

$$NTU = \frac{UA}{C_{min}} \tag{6.32}$$

For the present system, which is a counter-flow design, the effectiveness will be given by equation 6.33.

$$E = \frac{1-\exp[-NTU(1-C_r)]}{1-C_r\exp[-NTU(1-C_r)]} \tag{6.33}$$

Till now, combining the heat transfer equations and the NTU method, it is possible to calculate the effective temperature difference ΔT, but first the overall transfer coefficient UA should be determined.

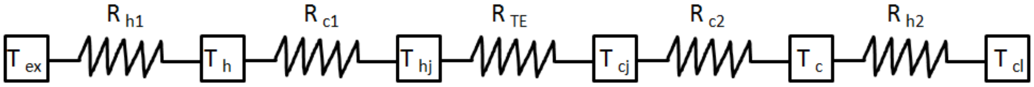

Figure 6.14 Thermal Resistance Network of TEG System

Figure 6.14 shows a typical TEG system thermal resistance network for each layer. Tex is the temperature of the exhaust, T_h and Tc are the hot and cold side on a ceramic layer, Thj and Tcj are the hot and cold side temperature on the TEG material, and Tcl is the coolant temperature. The overall heat transfer coefficient for the above system is given by:

$$UA = \frac{1}{R_{h1}+R_{c1}+R_{TE}+R_{c2}+R_{h2}} \tag{6.34}$$

Where Rh1 and Rh2 are the heat convective resistances, Rc1 and Rc2 are the conductive resistances of a ceramic layer, and RTE is the thermal resistance of the thermoelectric material layer.

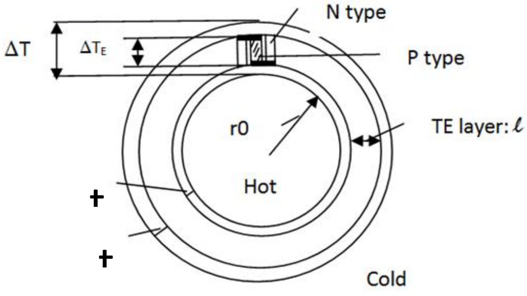

Figure 6.15 Diagram of cylindrical TEG System Cross Section

As shown in Figure 6.15, the assumed TEG geometry is cylindrical so the resistance has its own form. Equation 6.35 provides the actual overall heat transfer coefficient in this geometry.

$$\mathrm{UA} = \frac{1}{\frac{1}{h_o A_o} + \frac{\ln(r_1/r_i)}{2\pi k_o L} + \frac{\ln(r_2/r_1)}{2\pi k L} + \frac{\ln(r_o/r_2)}{2\pi k_o L} + \frac{1}{h_i A_i}} \tag{6.35}$$

Here the subscript ‘o’ denotes outer side and ‘i’ denotes inner side. Since the design includes placing fins inside the TEG to enhance heat transfer (see Figure 6.16) the inner side area will change. To define a complete overall heat transfer coefficient, it is then necessary to define the fin design.

6.2.2 Fin design

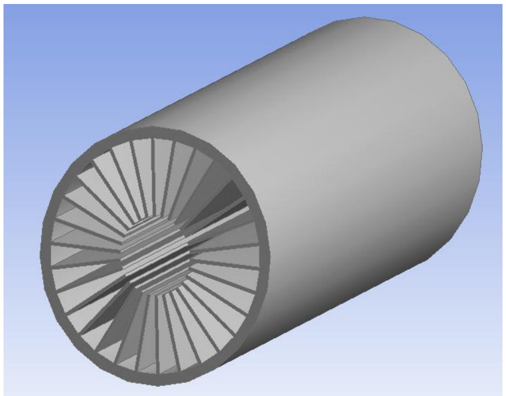

Figure 6.16 Example of Fin Design

In order to increase the extended surface area for heat transfer, a system of fins was designed as shown in Figure 6.16. For a long rectangular fin, Efficiency (η) is given by:

$$\eta = \frac{\tanh\,(\mathrm{mL})}{\mathrm{mL}} \tag{6.36}$$

And where:

$$\mathrm{m} = \sqrt{\frac{\mathrm{hP}}{\mathrm{kA_c}}} \tag{6.37}$$

Where L is the fin length; h is the film coefficient between exhaust and fin; P is the perimeter of fin; Ac is the cross section area of the fin; and k is the thermal conductivity of the fin. So after the fin design is defined, the overall heat transfer coefficient equation can be modified by insertion of “hi At” in place of “hi Ai”, where At is the total area of the fin surface.

6.2.3 Analytic solution of electric power output

Table 6-2 summarizes the heat exchanger/TEG design parameters, including exhaust entering at 600 deg C and coolant entering at 80 deg C. Based on these conditions, an integrated heat exchanger/TEG can be designed. The exhaust outlet temperature is calculated to be 390 deg C. The hot and cold sides of the TEG are at 330 deg C and 125 deg C, and the effective temperature difference is 205 deg C.

Table 6-2 Design Parameters of the Heat Exchanger

Item	**Value**	**Unit**	**Item**	**Value**	**Unit**
Pipe length(L)	12	inch	Exhaust mass flow rate ($\dot{m}_{hot}$)	20	g/s
Inner diameter(D_i)	3	inch	Coolant mass flow rate ($\dot{m}_{cold}$)	390	g/s
Outer diameter(D_o)	3.5	inch	Exhaust heat capacity($c_{p\ hot}$)	1.121	J/g*K
Thermal cond. (k)	2.4	W/m*K	coolant heat capacity($c_{p\ cold}$)	4.1806	J/g*K
Outer heat transfer (h_o)	2500	W/m^2*K	Exhaust inlet temperature ($T_{in\ hot}$)	600	deg C
inner heat transfer (h_{oi})	30	W/m^2*K	Coolant inlet temperature ($T_{in\ cold}$)	80	deg C
Fin Length	1.1	Inch	Fin width	0.04	inch
Average Seebeck ($\bar{S}$)	450	μV/K	Electrical resistivity ρ	0.0015	Ωcm
Ele. contact ratio(ρ_{oc})	0.1	cm	TEG length	1	cm

Using the effective temperature difference ΔT from the previous analytic model, the thermoelectric voltage (V) is given by:

$$\mathrm{V} = \frac{\bar{\mathrm{S}}}{2}\Delta \mathrm{T} \tag{6.38}$$

The current (I) is given by the voltage divided by the internal resistance (r):

$$\mathrm{I} = \frac{\mathrm{V}}{\mathrm{r}} = \frac{\bar{\mathrm{S}}}{4\rho(\rho_{\mathrm{oc}}+\mathrm{l})}\Delta\mathrm{T} \tag{6.39}$$

At matched load, which means the load resistance equals the internal resistance, the power density (P) is give by:

$$\mathrm{P} = \mathrm{VI} = \frac{\bar{\mathrm{S}}^2}{8\rho(\rho_{\mathrm{oc}}+\mathrm{l})}(\Delta\mathrm{T})^2 \tag{6.40}$$

6.2.4 FEA analysis and numerical results

In the above heat exchanger modeling, one-dimensional temperature distribution is assumed, which gives first order estimation. To make a more reasonable estimation of the effectiveness of the heat exchanger, a better model is needed. Here we assure the heat is uniformly distributed along the exhaust pipe. The governing equation for the two-dimensional heat transfers in the cylindrical coordinate is given by:

$$\frac{1}{\mathrm{r}}\frac{\partial}{\partial \mathrm{r}}\mathrm{r}\frac{\partial \mathrm{T}}{\partial \mathrm{r}} + \frac{\partial}{\partial \mathrm{z}}\frac{\partial \mathrm{T}}{\partial \mathrm{z}} = 0 \tag{6.41}$$

where T is the temperature and r is radius. To solve equation 6.41, separation of variables can be applied to render several ordinary differential equations. Since it is steady state, no initial condition is required but boundary conditions at inner and outer surfaces of the cylindrical exhaust pipe are needed.

$$-k_1\frac{\partial \mathrm{T}}{\partial \mathrm{r}}|\mathrm{r}_1 = \mathrm{h}_1(\mathrm{T} - \mathrm{T}_{1\infty}) \tag{6.42}$$

$$-\mathrm{k}_2\frac{\partial \mathrm{T}}{\partial \mathrm{r}}|\mathrm{r}_2 = \mathrm{h}_2(\mathrm{T} - \mathrm{T}_{2\infty}) \tag{6.43}$$

where the parameters k1 and k2 are the thermal conductivity of exhaust pipe at inner and outer surface, h1 and h2 are the convective heat transfer coefficient on each surface.

Several methods can be used to solve this problem, including finite element analysis (FEA) performed using ANSYS software. They can handle thermal properties as long as the problem is well defined and the boundary condition is given. The following figures show the temperature distribution of exhaust pipe with the TEG by solving the problem numerically using ANSYS. The parameters are provided by Table 6-2.

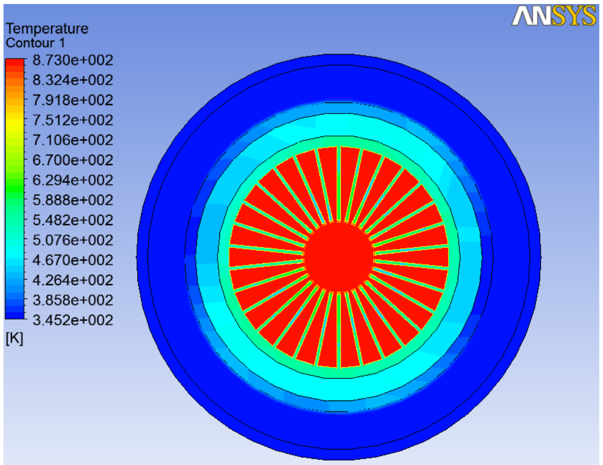

Figure 6.17 Temperature Distribution of Pipe with TEG at Entrance End

Figure 6.17 gives the temperature distribution in the cross section of the pipe with TEG at the entrance end. The hot and cold sides of the TEG are at 310 deg C and 120 deg C, and the effective temperature difference of TEG is 190 deg C, which is very close to that obtained using NTU method in Sections 7 and 8. Figure 6.18 gives the temperature distribution in the cross section of the pipe with TEG at the exit end. It shows that the hot and cold sides of the TEG are at 230 deg C and 90 deg C, yielding a temperature difference of around 140 deg C between the TEG hot and cold sides. To calculate the electrical output power, the average temperature difference between exhaust inlet side and exhaust outlet side was used. The average temperature difference is taken to be 165 deg C, i.e., (190 +140) / 2 = 165).

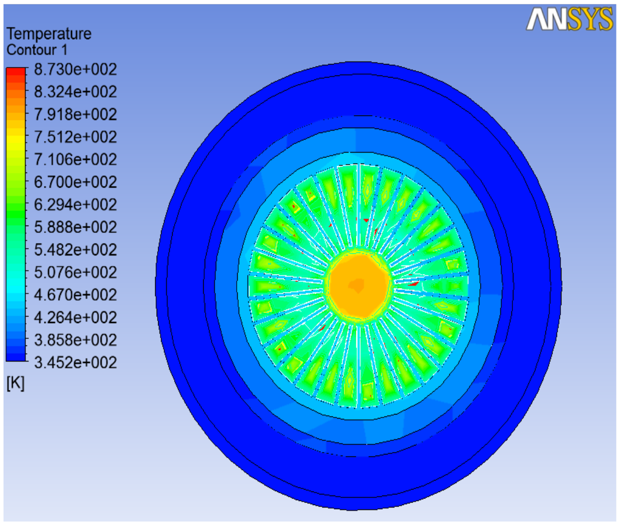

Figure 6.18 Temperature Distribution of Pipe with TEG at Exit End

Based on the temperature difference and equation 15, 16, 17, one can calculate the electrical output energy. The average temperature is 165 deg C. As a result, the total electrical output is calculated to be 526W, which is 4.2% of the waste heat energy, and correspond to a 5% fuel economy increase for a typical vehicle.

6.2.5 Conclusion

Based on this information, the authors designed an integrated TEG/heat exchanger. The heat transfer in this device was modeled using the Number of Transfer Units (NTU) method. A thermal resistance network was used to analyze the temperature at each junction. In order to improve the heat exchanger efficiency, fins were designed and incorporated into the design. The hot and cold sides of the TEG are at 330 deg C and 125 deg C, and the effective temperature difference is 205 deg C. The temperature distribution at the cross section of the TEG device was further estimated by finite element analysis (FEA) performed using ANSYS software, and the temperature difference at the entrance and exit ends were obtained. To calculate the potential electrical output power, the average temperature difference between exhaust inlet side and exhaust outlet side was used. The average temperature difference is taken to be 165 deg C. As a result, the total electrical output is calculated to be 526W, which is 4.2% of the waste heat power, and correspond to a 5% fuel economy increase for a typical vehicle.

7 THERMOELECTRIC GENERATOR APPLICATION AND RADIATION EFFECT IN NUCLEAR POWER PLANT

7.1 Overall Design

This work discusses the development of an independently powered sensor network that uses thermoelectric generators (TEGs) to provide power for monitoring and actuation in station blackout situations. Since heat is available at a variety of locations, using thermoelectrics for power generation provided a reliable source of power for sensor networks. The key idea is to combine multiple TEGs with power management circuits, sensors, microcontrollers, wireless transmitters, batteries, and possibly even actuators and installing them on steam pipes or other high-temperature nuclear plant components. Fig. 7.1 shows the key system components. During normal conditions, our TEG-based device will store electrical energy into batteries. During off-normal condition, they gather and deliver important parameters wirelessly. Heat passes from the hot pipe through the insulation using copper rods or heat pipes to thermoelectric generators on the outside surface of the insulation. The sensor package is similarly located on the outside, along with a wireless transceiver, data storage, and power management.

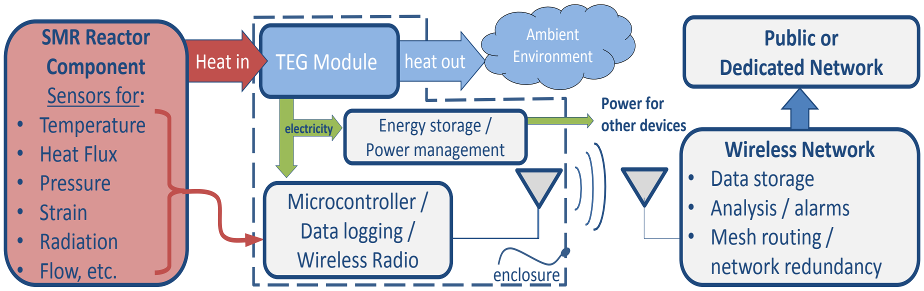

Figure 7.1 Operation during normal and off-normal conditions [8]

In this work, the principles of thermoelectric device are first introduced. Then, four design challenges: electrical loads, heat sources and thermal loads, environmental protection, and radiation effects, are discussed. An overview of the experimental testing facility under construction is discussed, followed by initial thermal analysis and designs for the TEG device discussed. Future work and expected outcomes are summarized in conclusion.

7.1.1 Design Challenges

7.1.1.1 *Electrical Loads*

The electrical load in this application is the system circuitry, including electrical power for sensors, signal conditioning, microcontrollers, wireless radios, and, when excess power is, available, energy storage via batteries or super-capacitors. Initial estimates of the power requirements are shown in Table 1. The power generated by TEGs will supply the system though a DC-DC converter. The system will measure any required parameters from the nuclear component and send the data to plant staff via wireless data transmitters. The appropriate sensors, e.g., for temperature, pressure, radiation, or flow rate, will provide electrical signals that are converted into digital format using industry-standard hardware. The wireless data transmitter is also a commercial mature product. One challenge for the system is the DC-DC converter and energy storage. A DC-DC converter design is being developed that adjusts to the TEG's output, as well as the selection of a reliable and long-life battery as the energy storage device. As shown in Table.7- 1, the total required electricity power is less than 7 W. The rest of the power can be used for energy storage and actuation.

Table 7-1 Electricity requirement for each circuit component

Circuit components	Required electricity (W)
Cooling fan for circuits	0.1 – 2.5
Microcontroller	< 0.5
Power management	< 1.0
Wireless data transmitter	0.5 – 3.0
Total	0.6 –7.0

7.1.1.2 *Heat Sources*

Determining the heat sources requires a comprehensive survey on the target SMR. The survey must provide the layout of the plant with dimensions and necessary parameters (e.g. temperature, pressure, flow rate, and radiation). There are four key measures of optimal heat source locations: (1) it must be easy and safe to be installed on. Some locations, even though can provide enough heat, are not desirable because the installation process may damage the structure of the nuclear reactor itself. The reactor core is a good example. (2) It must provide heat in a certain temperature range. Take a commercial TEG that has a thermal conductivity of 2.4 (W/m·K) for example, the ideal heat source must provide a heat flux of ~95 kW/m2, with a temperature lower than 250° C in order to achieve its maximum efficiency. (3) It must have enough space for installing electrical loads and heat sink. This can be verified once an actual SMR design is identified for the technology. (4) It needs to be close to reactor. The main function of the device is to sense the important parameters in reactor. Also, moderately high temperatures are required for the TEG devices to operate. Therefore, preferred location sites are close to reactor. These requirements narrow down possible locations.

7.1.1.3 *Environmental Protection*

The device must be sustainable in harsh environments, e.g. water, fire, shock, and high-dose radiation exposure. A design for an enclosure is derived from the design principles of an aviation "black box", or flight data recorder designed to survive in an event of a crash. Referring to Fig. 5, the environmental protection system will consist of a stainless steel/titanium alloy outer layer that is filled with a dry silica. The dry silica provides high-temperature insulation, which make it possible to tolerate fire at 1,100 ° C for one hour [139]. Additional inner layers will be included to shield the device from radiation. Example materials include Polysulfone (PSU) / Polyethersulfone (PES) / Polyphenylsulfone (PPSU), which are high-temperature polymers capable of blocking alpha and beta radiation. Lead sheet can be used to block gamma radiation and X-rays. Finally the electronics package resides in the center of the container (Fig. 7.2).

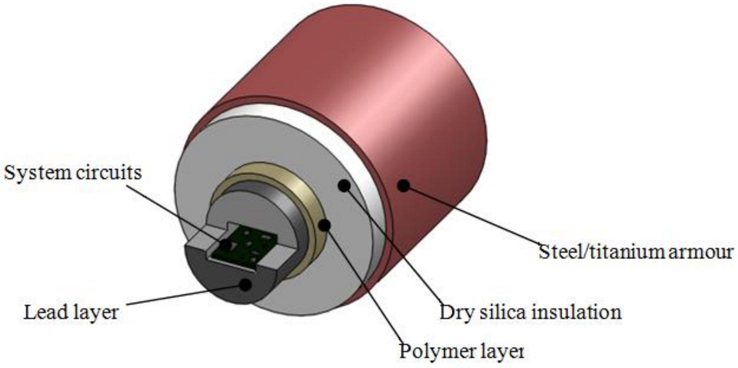

Figure 7.2 The enclosure for system circuits [8]

7.1.2 Experimental Setup

7.1.2.1 *Test Parameters*

To simulate the thermal loads associated with a nuclear reactor, an experiment has been designed and is being built that will provide the required heat flow for a commercial TEG device. A test stand has been designed to accommodate two different versions of commercial TEGs and provide measures of efficiency, power, and voltage to temperature difference. The target temperature differences between cold side and hot side of TEG in this experiment range from 0 to 146 ° C. Further experiments such as fin analysis, and electronic devices assembling are also underway. The TEGs under test sits on top of the Cu block each cartridge heater provides 200 Watts of heat, and is connected to a temperature controller with a thermocouple for feedback to maintain a constant temperature. Two water blocks are mounted on top of TEGs for heat removal. Each water block has a thermal resistance of 0.011 °C/W. The thermal resistance of water block is expressed as

$$R = \frac{\Delta T}{Q} \tag{7.1}$$

where ΔT is the temperature difference of copper block and entered water, and Q is the heat transferred from copper block to water block. The total amount of heat supplied by four cartridge heaters is 800 W.

A high-temperature insulation layer having a thermal conductivity of 0.79 W/(m • K) is used to minimize heat loss provide . Between the insulation and copper block is an air gap that also reduces conductive losses. The copper block is supported by four ceramic rods. A steel foil is covered on the inner wall of insulation layer for reducing heat loss by radiation.

7.1.2.2 *Simulation results*

A thermal simulation for the test stand had been performed before actual fabrication was started. Comsol version 4.2 was used for all analyses. The purpose of this simulation was to understand insulation performance and obtainable temperature difference between the cold side and hot side of the TEG. It is assumed that the entered water temperature is 20 °C. IN this case, the TEG cold-side temperature is 24.4 °C. By applying this temperature on the cold side of TEG, the temperature difference between cold side and hot side is about 138 °C. The total heat loss (by radiation, convection, and conduction) is about 40 W. The temperature distribution is shown in the following figure.

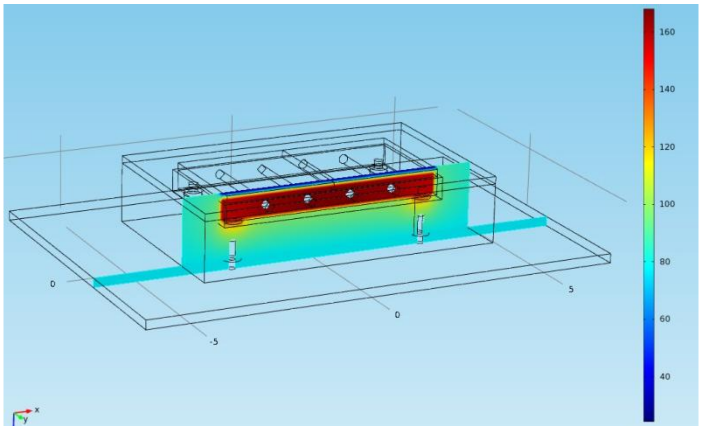

Figure 7.3 Temperature distribution along the test stand [8]

7.1.2.3 *Target Locations*

A preliminary survey on components temperature in different SMRs has also been performed. In light water reactors, the inlet and outlet pipe for reactor core and outlet pipe for steam generator typically have temperatures around 300 °C, and represent nearly ideal locations for TEG-based sensor packages. In non-water cooled reactors, the temperatures are generally higher. The inlet pipe for reactor core is considered to be a potential location. In Table 7-2, temperatures for several designs are shown. KLT-40S, System-integrated Modular Advanced *Reactor (*SMART), and *mPower* are light water reactors. The Pebble Bed Modular Reactor (PBMR) is a gas-cooled reactor cooled by Helium. Toshiba 4S (Super Safe, Small and Simple) is a fast neutron reactor cooled by liquid Sodium.

Table 7-2 Core and steam generator inlet/outlet temperature in different SMRs

SMR Location	KLT -40S	PB MR	SMART	4S	B&W *mPower*
Reactor Core: inlet/outlet (℃)	290/326	250/750	295.7/323	355/510	297/321
Steam generator: inlet/outlet (℃)	170/290	200/540	200/298	210/453	163/300

7.2 Nuclear Radiation

Different electronic components can handle varying degrees of radiation exposure, as shown in Table 7-3.

Table 7-3 Threshold of radiation for different electronic components

Component type	Damage threshold (Gy)
Resistors	102 — 106
Capacitors	102 — 108
Inductors	10 — 106
IC	102 — 104
Voltage regulator	103 — 106

Also, different locations and operating conditions result in different radiation level being produced (Table 7-4) [140].

Table 7-4 Radiation level at different locations in nuclear plants

Location	State of reactor	Gamma dose rate (Gy/h)	Neutron dose rate (Gy/h)
Inside the core	On load	10^{7}	10^{7}
	Shut-down	10^{4}	10^{-1}
Outside the radial shield	On load	10^{2}	10
	Shut-down	10^{-3}	Negligible
Above the pressure dome	On load	10	1
	Shut-down	5×10^{-3}	Negligible
Coolant loop	On load	5×10^{-1}	Negligible

Although radiation can cause negative effects in electronic circuits, radiation exposure is not necessary undesirable. The Seebeck coefficient has been found, for example, to actually improve after exposure to radiation. Take P-type PbTe thermoelectric material as an example, it has been found that its electrical resistivity increases by nearly four times, but the Seebeck coefficient increases by 2 to 3 percent by the effect of radiation. The figure of merit is reduced somewhat, but the offsetting effects of the Seebeck coefficient and the thermal conductivity reduce the net change [141].

7.2.1 Gamma and neutron radiation effect

7.2.1.1 *Experiment setup*

For thermoelectric material, The N material is iodine doped $Bi_2Te_{2.5}Se_{0.5}$ and the P material is lead doped Sb_2Se_3. The dopant in both cases amounts to much less than 1% thermoelectric material Bi_2Te_3. The sample size is thermal conductivity sample half-inch diameter with 2mm thick and Hall Effect sample size is 1 cm square with a thickness of 1mm. The sample has been irradiated with gamma ray up to 10M Rad. Thermal conductivity, electrical conductivity and Seebeck coefficient has been characterized and the change is not much. The sample has also been irradiate with neutron up to 1014/cm^2. The material is still radioactive and will characterize after radiation below background.

Besides the n, p type thermoelectric material described in the material level, the module consists of a liquid crystal polymer (brand name Zenite) eggcrate that supports the legs. A bond coat of Mo is applied to the legs and a conducting layer of aluminum is deposited on top of the Mo. The power leads are Cu with a Ni plated layer on top of the Cu and a layer of Sn plated on the Ni. The electronic board can be used to test the DC/DC converter. The purple wire is positive input for voltage from 3V to 20V. The white wile is ground/negative. Tow brown wires are the outputs of the converter. One is 5V and the other is 3.3V. During the radiation, certain voltage values can be applied to the input (purple (+) and white (-) wires). And measure the output voltage to see if they stay stable around 5V and 3.3V.

Both the TEG module and electronic board has been irradiated with neutron up to 1014/cm2 and due to the radioactive of the materials, we will characterize the items after radiation level drop down to below background. Also, we have been studying ion irradiation on n,p type Bi_2Te_3 material with a different dose from $5x10^{14}$ to 10^{16}/cm2. The electrical conductivity increases as the ion irradiation fluence increase until it saturate at $5x10^{15}$/cm2. This increase is due to the increase of carrier concentration created during ion bombardment.

7.2.1.2 *Results*

For thermoelectric material, The N material is iodine doped $Bi_2Te_{2.5}Se_{0.5}$ and the P material is lead doped Sb_2Se_3. The dopant in both cases amounts to much less than 1% thermoelectric material

Bi2Te3. The sample size is thermal conductivity sample half-inch diameter with 2mm thick and Hall Effect sample size is 1 cm square with a thickness of 1mm.

Gamma radiation from BNL 60-Co source with 1M and 10M Rad dose has been test on Bi2Te3 N type and Sb2Te3 P type material. Thermal conductivity, electrical conductivity resistivity including the carrier concentration or mobility and Seebeck coefficient has been characterized. The thermal conductivity measurement is done with flash method using TA instrument.

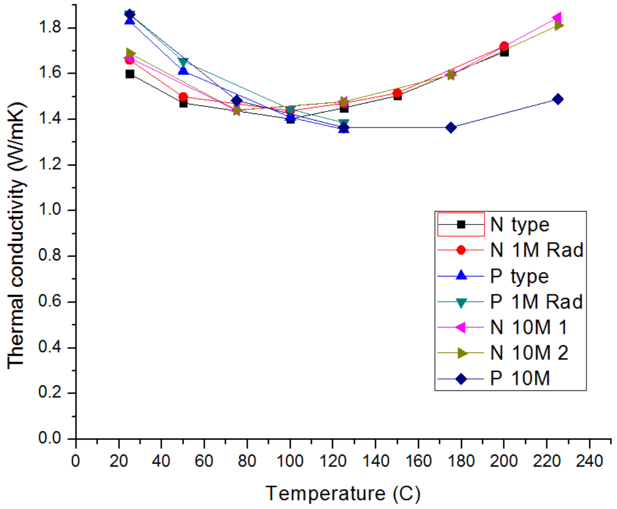

Figure 7.4 Thermal conductivity of N,P type material before and after gamma radiation.

As shown in figure 7.4, the thermal conductivity of both two types of material before radiation (N type, P type) doesn't change much after 1M or 10M Rad of gamma radiation. The difference is within the measurement error of the equipment.

Table 7-5 electrical properties of N, P type material before and after radiation

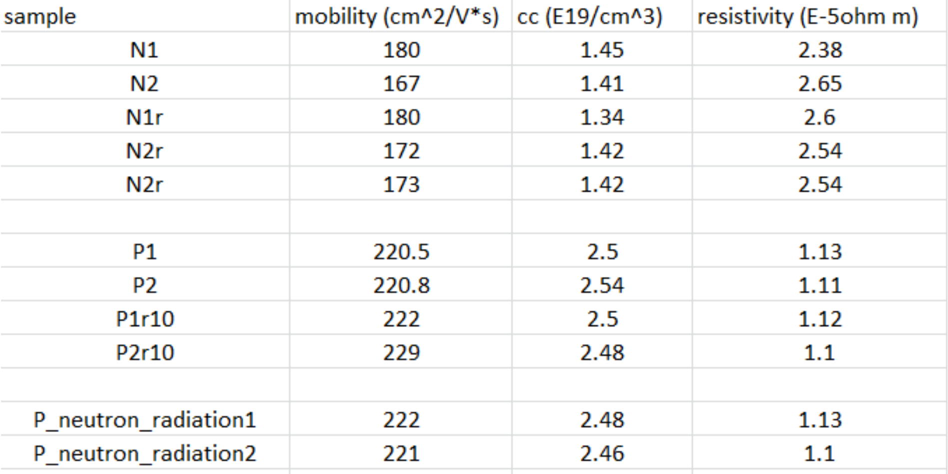

sample	mobility (cm^2/V*s)	cc (E19/cm^3)	resistivity (E-5ohm m)
N1	180	1.45	2.38
N2	167	1.41	2.65
N1r	180	1.34	2.6
N2r	172	1.42	2.54
N2r	173	1.42	2.54
P1	220.5	2.5	1.13
P2	220.8	2.54	1.11
P1r10	222	2.5	1.12
P2r10	229	2.48	1.1
P_neutron_radiation1	222	2.48	1.13
P_neutron_radiation2	221	2.46	1.1

Table 7-5 shows up to 10M Rad of gamma radiation the electrical properties don't change much. Furthermore, the carrier concentration and mobility of both materials has been characterize suing HMS4800 Hall Effect Measurement system and showed the change is negligible.

The sample has also been irradiate with neutron up to 10^{14}/cm^2 and as shown in Table 7-5 after this amount of neutron irradiation the electrical property doesn't change much. From literature, it's suggested to have high dose up to 10^{19}/cm^2 to give a measureable difference.

7.2.2 Ion beam radiation effect

7.2.2.1 *Experiment methods*

Three-inch-diameter boron-doped p-type <100> silicon wafers (Montoco Silicon Technologies, Inc.) are used as the substrates in this research. The silicon wafers are 350- to 400-µm-thick and the resistivity is in 1 to 5 Ω·cm range. The wafers are initially oxidized at 1100 oC for 60 mins to get a 0.5-µm-thick silicon dioxide layer using wet thermal oxidation. The Bi2Te3 and Sb2Te3 thin films are grown by e-beam evaporation deposition, using a Kurt J. Lesker PVD 75 E-beam/thermal evaporation system. Solid antimony (III) telluride and bismuth (III) telluride (99.999 % purity; Alfa Aesar Company) are evaporated for growth of the Bi2Te3 and Sb2Te3 thin films, respectively. The films are deposited at room temperature without substrate heating. The process chamber has a background pressure of 2 × 10-7 Torr.

The thickness of Bi2Te3 and Sb2Te3 thin films is controlled by an INFICON deposition monitor during the deposition, and measured by Stylus Profilometry (Bruker, IL, USA). Table I summarize all of the samples grown by e-beam evaporation and ion beam irradiation conditions.

The ion beam irradiations on thin film samples are performed at Ion Beam Lab of Los Alamos National Laboratory with 0.4 MeV Ne2+ ions using a 200 kV ion implanter. The ion irradiation is performed at room temperature without sample titling, and the samples are irradiated at different fluences from 0.5 x1015, 1 x1015, 5 x1015 and 10x1015 ions/cm2. The ion fluences are also converted to the unit of displacements per atom (dpa) using the Stopping and Range of Ions in Matter (SRIM)-2008 program based on the Kinchin-Pease model and full cascade calculations (Table 7-6).

Table 7-6 Sample synthesis method, ion fluence and displacements per atoms (dpa) based on SRIM-2008 calculation.

Sample	Material	Condition	Ion fluence (1015/cm2)	dpa
N0	Bi2Te3	E beam	0	0
P0	Sb2Te3	E beam	0	0
N1	Bi2Te3	E beam + ion beam	0.5	0.09
N2	Bi2Te3	E beam + ion beam	1	0.19
N3	Bi2Te3	E beam + ion beam	5	0.93
N4	Bi2Te3	E beam + ion beam	10	1.87
P1	Sb2Te3	E beam + ion beam	0.5	0.07
P2	Sb2Te3	E beam + ion beam	1	0.15
P3	Sb2Te3	E beam + ion beam	5	0.74
P4	Sb2Te3	E beam + ion beam	10	1.49

The displacement energy is 25 eV for all of the elements in Bi2Te3 and Sb2Te3. The ion ranges of the 400 keV Ne2+ in thermoelectric thin films were 493 nm for Bi2Te3 and 520 nm for Sb2Te3, respectively, significantly larger than that of the film thickness. These results suggest that most of the implanted Ne2+ penetrated through the film thickness such that the chemical effort on the electrical and thermoelectric properties of the films can be neglected. In addition, the electronic energy Se, nuclear energy loss Sn and the ENSP (electron to nuclear stopping power ratio) were estimated based on the average value across the depth of the thin film samples and the full cascade calculations of SRIM-2008.

Table 7-7 Ion irradiation parameter, ion range, electronic and nuclear energy loss and the ratio of the ENSP as evaluated by full cascade calculation based on SRIM-2008

Materials	Thickness (nm)	Ion sources	Se (eV/nm)	Sn (eV/nm)	ENSP	Ion Range
Bi2Te3	160	400 keV Ne2+	617	125	4.9	493 nm
Sb2Te3	100	400 keV Ne2+	595	106	5.6	520 nm

The phase composition of the samples before and after irradiations was analyzed with X-ray diffraction (XRD) (Ultimate III, Rigaku, TX, USA) utilizing Cu Kα radiation and energy-dispersive X-ray spectroscopy (EDS) (JEOL 7600F, Tokyo, JP). The cross-section morphologies of the sample were observed using a scanning electric microscope (SEM) (JEOL 7600F, Tokyo, JP). The electrical conductivity was measured using a Keithley digital multimeter (Model 2700, Keithley Instruments, Inc., OH, USA) and heated from 300 to 400 K using a High Temperature Probe Station (MBE-Komponenten AO500,, Germany). Seebeck coefficients were measured using a differential method under vacuum. To investigate its contribution to electrical conductivity, the carrier concentration and Hall mobility were measured with a Hall Measurement System (8404, Lake Shore Cryotronics, Inc., OH, USA) using the Van der Pauw method.

7.2.2.2 *Results and discussions*

7.2.2.2.1 *Phase composition of Bi2Te3/Sb2Te3 before and after ion radiation*

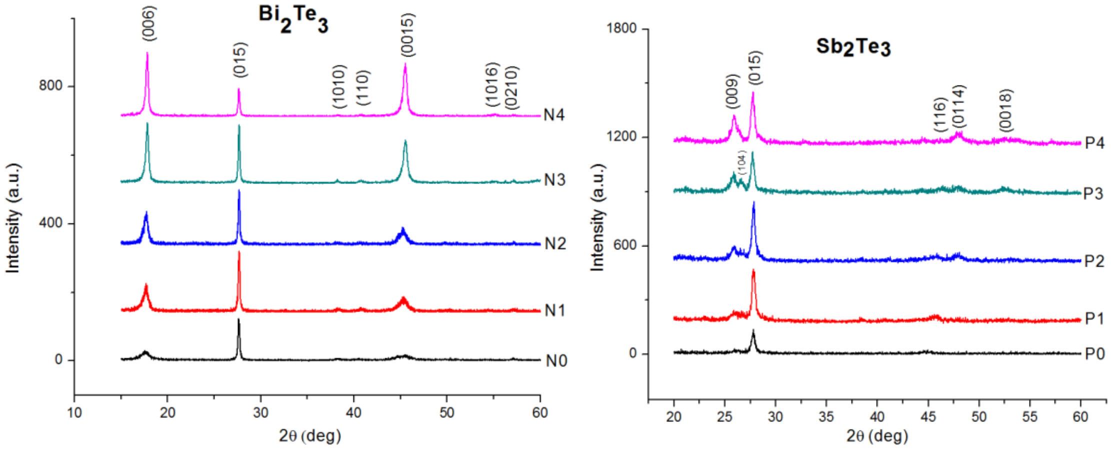

Figure 7.5 XRD of Bi2Te3 (left, a) and Sb2Te3 (right, b) thin film before and after ion beam irradiation shows an irradiation-induced reorientation and enhancement of crystallinity as the ion fluence increases

Figure 7.9 shows the XRD patterns of Bi2Te3 and Sb2Te3 thin films before and after ion bombardment. Sample N0 and P0 were as-grown n-type Bi2Te3 and p-type Sb2Te3 samples using e-beam evaporation; while the rest were bombarded with Ne2+ ion at different total fluences. For Bi2Te3, the as-grown thin film showed main phase orientation at direction (015). Upon 400 keV Ne ion irradiation, no irradiation-induced amorphization was observed, and both Bi2Te3 and Sb2Te3 samples remain highly crystalline as revealed by the XRD patterns. The increase in the ion fluence will further increase the crystallinity as evidenced by the peak narrowing of the XRD patterns. Additionally, an irradiation-induced reorientation occurred for both thin films, as evidenced by the increased intensity of the XRD diffraction peaks of (006) and (0015) for Bi2Te3 (Fig. 1a). A similar behavior was observed for Sb2Te3 film (see Fig. 1b). Before ion beam irradiation, the as-grown sample is located at mainly (015) direction and after the irradiation secondary preferred orientation in the direction of (009) is clearly visible as ion fluence increases.

The energy loss mechanism of the energetic ions is crucial in determining the irradiation damage process. The ballistic effect of nuclear energy loss (or nuclear stopping power: Sn) causes atomic displacements that can lead to amorphization of the irradiated materials. On the other hand, ionization radiation can promote defect recombination or recovery, even recrystallization of materials. A higher ENSP (electron to nuclear stopping power ratio) value may result in higher radiation defect recovery rate as compared with radiation damage accumulation, and hence enhanced radiation resistance. The radiation-enhanced crystallinity and reorientation of the thermoelectric thin films upon 400 keV Ne2+ suggests that the ionization radiation dominated radiation damage process. This is consistent with the relatively-small displacement damage created by the Ne2+ ions even at the highest ion fluences (1.87 and 1.49 dpa for Bi2Te3 and Sb2Te3, respectively), and significantly higher electronic energy loss Se and greater ENSP ratios for both Bi2Te3 and Sb2Te3. The ionization-radiation enhanced crystallinity and reorientation may also lead to the reduction of the defects upon irradiation and thus increases in the electrical conductivity upon initial ion irradiation as elaborated later.

7.2.2.2.2 TEM of Bi2Te3 and Sb2Te3 before and after ion beam irradiation

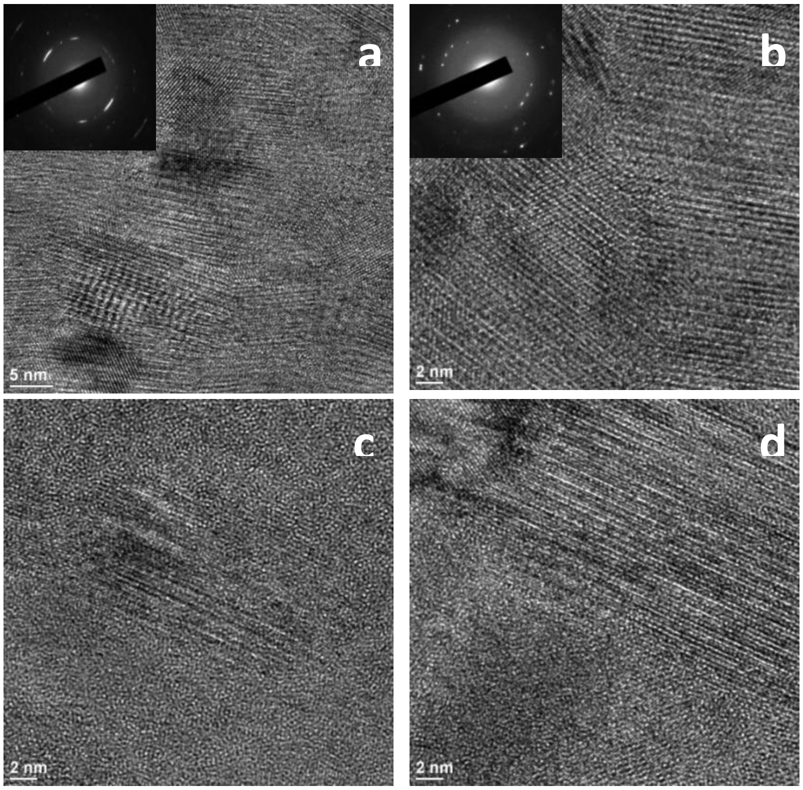

Figure 7.6 TEM of Bi2Te3 a) before radiation N0, b) after radiation N3 and Sb2Te3 c) before radiation P0, d) after radiation P3

Figure 7.10 shows the TEM images and diffraction patterns of two type samples before and after ion irradiation. The FIG. 2(a) shows a high magnificent TEM of as grown Bi2Te3 and FIG. 2 (b) shows the TEM of Bi2Te3 after 5x10^{15}/cm^{2} ion radiation N3 sample. As shown, the grain size increases in N3 suggesting the ionization radiation-induced defect recovery and grain growth, consistent with the XRD patterns. The selected electron diffraction pattern (SAED) of the as-grown Bi2Te3 film (inset in Fig. 7.10a) shows a ring pattern, a characteristic feature of the nanocrstyalline materials. A preferred orientation was observed as shown by the arc in the SAED which can be indexed as the (015) spacing based on structural data of Bi2Te3 (PDF#15-0874). Upon ion irradiation, the SAED pattern consists of discrete diffraction spots, inferring increased grain size upon ion irradiation. The originally preferred orientation of the (015) disappeared despite radiation-induced reorientation was observed, probably due to the different zone axis of the SAED pattern. Similar behavior occurred for Sb2Te3 film upon irradiation. Before irradiation, the Sb2Te3 thin film has a low degree of crystallinity, and nano-sized particles were embedded into an amorphous-dominated matrix (Fig. 7.10c). Ion irradiation significantly improves the crystallinity of the material as a result of the ionization radiation-induced defect recovery process. Overall, N type Bi2Te3 sample has better crystallinity than P type Sb2Te3 and TEM results are well correlated with XRD results showed before. The orientation changes after ion radiation implies the randomization happens during the process.

7.2.2.2.3 Transport properties of Bi2Te3 and Sb2Te3

A. Electrical conductivity variation upon ion irradiation

Electrical resistivity measurements were made from 300 to 400 K under vacuum. The measured electrical conductivities for both samples are shown in Figure 7.11, which indicates that the variation in electrical conductivity is significant upon ion radiation. In Figure 7.11(a), N0 which was as-grown sample, has a slightly higher resistivity than the rest Bi2Te3 samples with ion beam irradiations. For the Sb2Te3 thin film sample, the trend is similar as Bi2Te3 sample: P0 has higher electrical resistivity than P1~P4 upon ion beam irradiation, which is again likely due to the radiation induced ionization during ion radiation process. The decrease of electrical resistivity of both samples with increase of temperature is of the intrinsic semiconductor character.

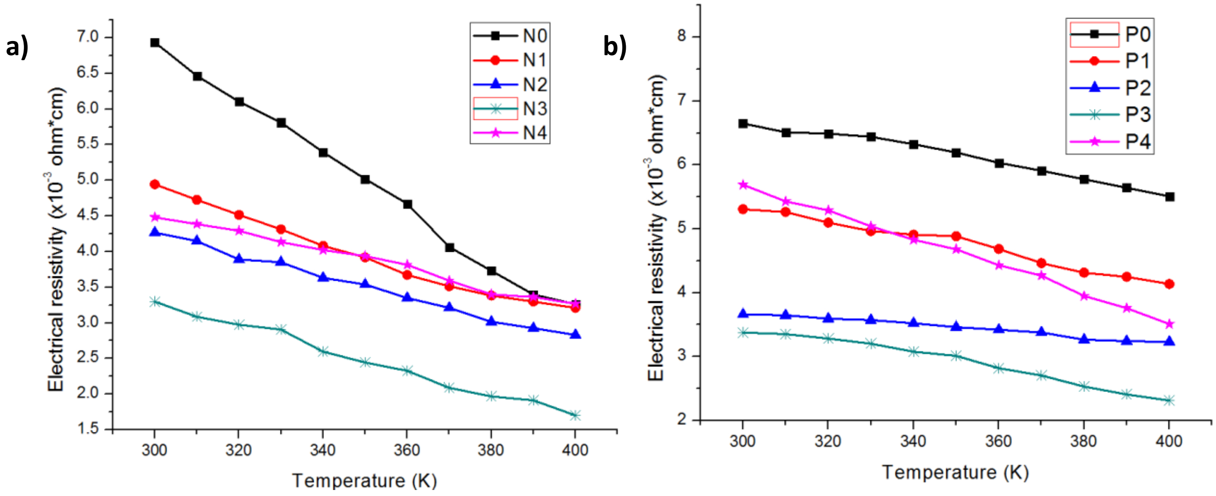

Figure 7.7 Electrical resistivities of Bi2Te3 (a) and Sb2Te3 (b) thin film after bombardment decrease to some extent and then increase after the ion fluence of 5x10^{15}/cm2

Figure 7.12 shows the variation of the electrical conductivity as a function of ion fluence. For both films, the as-grown samples have higher resistivity than the materials after ion beam irradiation, consistent with lower carrier concentration as referred from Hall Effect measurements (Table III). The improved electrical conductivity of both films with increased fluences may be attributed to the ionization-induced recovery of the intrinsic defects during film deposition process, and thus enhancement of the carrier concentration. With further increase of ion fluence above 5x10^{15} ions/cm2, the electrical conductivity decreases for both N4 and P4 samples as a result of the accumulation of displacement-induced defects in the thin film in which the displacement damage dominates over the ionization radiation.

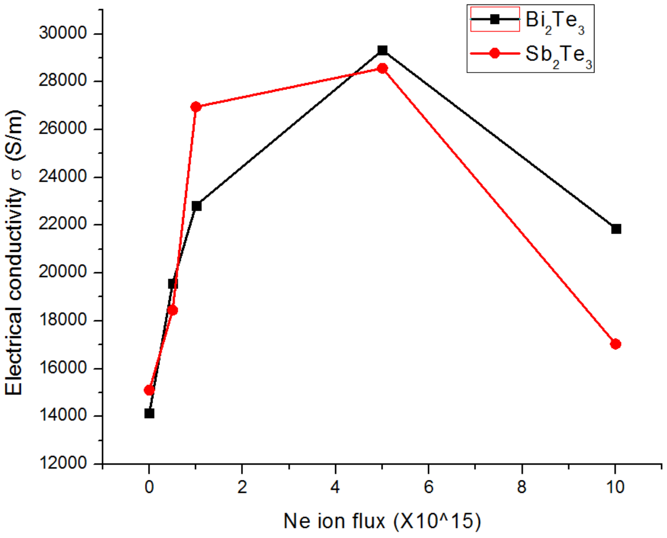

Figure 7.8 Room temperature electrical conductivity for Bi2Te3 and Sb2Te3 samples at various ion fluences

In order to understand the mechanisms and key parameters that affect electrical conductivity, Hall Effect measurements at room temperature were made with van der Pauw method and the results are shown in Table 7-8. The as-grown Bi2Te3 and Sb2Te3 thin film (N0 & P0) have lower carrier mobility than those of ion beam irradiated samples. As ion fluence increases before 5x10^{15}/cm^2, the carrier mobility in both Bi2Te3 and Sb2Te3 sample increases due to radiation induced defect recovery process showed in XRD result (see FIG. 7.9). After the ion fluence reaches 5x10^{15}/cm^2, higher fluence starts to decrease the mobility which may come from the accumulated defects generated by ion radiation. In Table 7-8, the carrier concentration of the Bi2T3 and Sb2Te3 samples starts to decrease at the beginning of ion radiation and it turns reversely at higher fluence. The carrier concentration by Hall Effect measurements matches well with the electrical resistivity using four-probe machine at room temperature. The change of the carrier concentration may also be associated with the mini-bands formation during ion radiation process.

Table 7-8 Room temperature Hall Effect for two type thin film at different fluence

Sample	Carrier concentration n (10^{20}/cm^3)	Hall mobility μ (cm^2/V·s)	Conductivity $\sigma = ne\mu$ (10^{4}S/m)
N0	5.78	1.50	1.4
N1	5.45	2.20	2.0
N2	5.11	2.74	2.3
N3	5.46	3.29	2.9
N4	5.04	2.66	2.1
P0	3.31	2.80	1.5

P1	3.23	3.50	1.8
P2	3.03	5.46	2.7
P3	3.18	5.50	2.8
P4	3.25	3.21	1.7

The samples in this study are non-stoichiometric and polycrystalline. The mobility is far less than that of stoichiometric Bi2Te3/Sb2Te3 single crystal, e.g., mobility of 313 cm^2/V*sec for thin films Bi2Te3 using metalorganic chemical vapor deposition[142] and 400 cm^2/V*sec for single crystal bulk Sb2Te3[143]. Generally, mobility is determined by phonon scattering at high temperatures and ionized impurity scattering at low temperatures for semiconductor materials.[134] For our samples, the increase of crystallization shown in XRD account for the increase of mobility and at higher fluence the accumulated defects decreased the mobility.

B. Seebeck coefficient

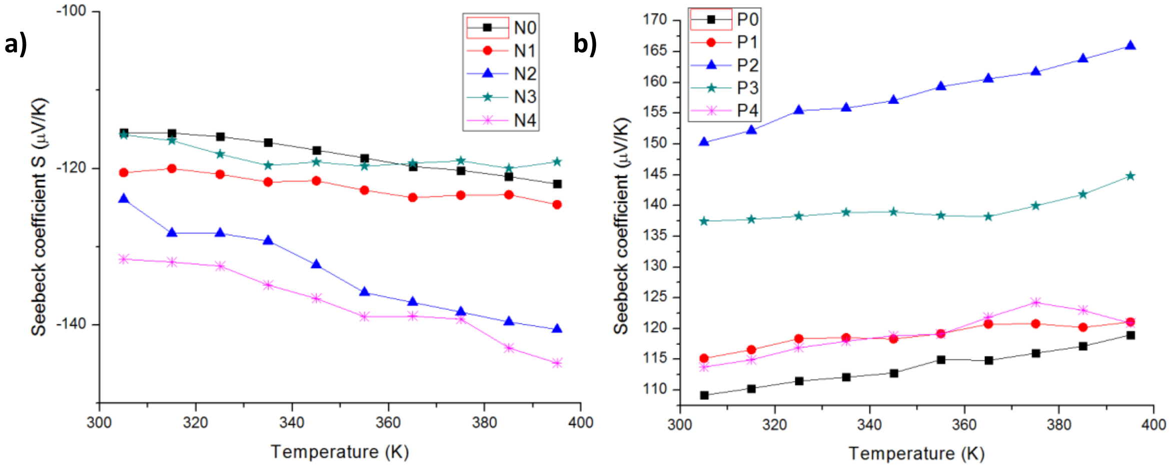

Figure 7.9 Seebeck of Bi2Te3 (a) and Sb2Te3 (b) thin film before and after bombardment

Figure 7.13 shows the measured Seebeck coefficients of Bi2Te3 and Sb2Te3 thin films before and after bombardment. Seebeck coefficient is very sensitive to carrier concentration and inversely proportional to electrical conductivity due to the opposite dependence of carrier concentration, i.e., S~ln (n) in Eq. (1).[7] Figure 7.13(a) shows that the un-irradiated sample N0 has a lower Seebeck coefficient because of its higher carrier concentration. As ion fluence increases from N0 to N2, the Seebeck coefficient increases since the carrier concentration continues to decrease. Figure 7.13(b) shows the similar trends for Sb2Te3 samples as P0 has a much higher carrier concentration than P1-P4.

Generally as temperature increases, the Seebeck coefficient will increase in magnitude because the ratio N_c/n in Eq. (1) is proportional to $\exp(kT)$. The fact that the Seebeck coefficient is negative in Figure 7.13(a) indicates that Bi2Te3 is an n-type semiconductor, and the positive Seebeck value in Figure 7.13(b) shows Sb2Te3 is a p-type semiconductor. This observation is consistent with the Hall Effect measurement.

C. Power factor (PF)

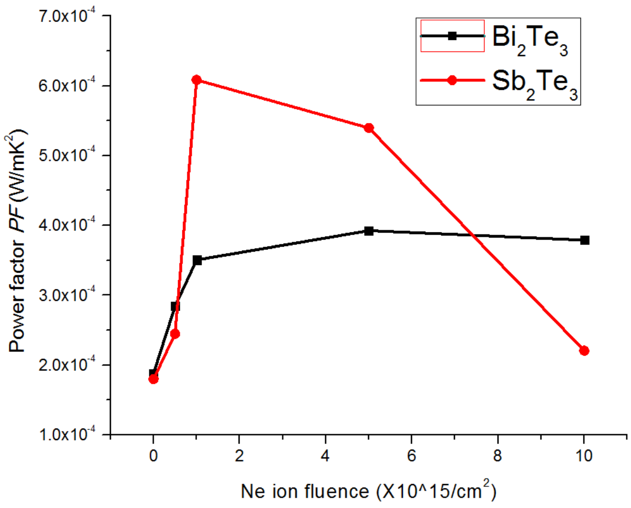

Figure 7.10 Room temperature PF of Bi2Te3 and Sb2Te3 thin film increases when ion fluence increases and the peak achieves between 1 and $5x10^{15}/cm^2$

The power factor value PF=S2σ of the sample can be estimated by combining the in-plane electrical properties σ and the in-plane Seebeck coefficient S. Figure 7.14 shows the in-plane power factors for Bi2Te3 and Sb2Te3 thin films before and after ion irradiation. Positive effects of ion irradiations from Ne2+ on thermoelectric material property are observed because of large improvements in electrical conductivity and Seebeck coefficient caused by carrier concentration and mobility change. Figure 7.14 shows the maximum PF for Bi2Te3 appeared at $5x10^{15}/cm^2$ Ne ion fluence, which increased to 208% compared with sample before ion radiation. For Sb2Te3 the maximum PF occurred at $1x10^{15}/cm^2$ Ne ion fluence, which increased to 337% compared with sample before radiation. However, under a higher fluence, $5x10^{15}/cm^2$ for Bi2Te3 and $1x10^{15}/cm^2$ for Sb2Te3, the power factor starts to decrease accordingly, limiting the enhancements of thermoelectric materials properties under intensive radiation environment. This is because at higher fluence, the mobility becomes smaller as the accumulation of defects generated by displacement damages to the materials and eventually the electrical conductivity starts to decrease.

7.2.2.3 *Conclusion*

Both thermoelectric material and device is not vulnerable to gamma radiation. Low dose neutron radiation has no obvious effect on thermoelectric device. In conclusion, thermoelectric Bi2Te3 and Sb2Te3 thin films prepared by E-beam evaporation were irradiated by 400 keV Ne2+ in order to investigate the radiation effects of the thermoelectric materials as energy harvester in nuclear environment. The microstructure evolution, phase/crystallinity and the thermoelectric properties were systematically investigated. An ionization radiation-induced defect recovery and reorientation were observed for both films as evidenced by XRD and TEM. A competition of the ionization radiation and displacement damage dominates the variations of the electrical and thermoelectric properties of materials. The electrical resistivity decreases in both materials upon ion irradiation due to the increase in carrier mobility and better crystallinity. The accumulated defects induced by displacement damage at higher ion fluence eventually result in the reduction of the mobility and electrical conductivity. Seebeck coefficient increases accordingly with ion radiation due to the reduction of carrier concentration and the charge mobility. Positive effects of ion irradiations from Ne2+ on thermoelectric materials are observed, which increases the power factors to 208% for Bi2Te3 and 337% for Sb2Te3 materials, respectively, consistent with the increase of the electrical conductivity as a result of ionization radiation-enhanced crystallinity. The peaks seem to happen at some place between 1 and 5 x1015/cm2, likely around 3 x1015/cm2 ion fluence. However, under a higher fluence, the power factor starts to decrease, limiting the enhancements of thermoelectrical material properties under intensive radiation environment.

7.3 Design Guideline for Radiation Shielding

Radiation can be a serious concern in nuclear power facilities, and a number of other circumstances. Containing radiation and preventing it from causing physical harm to employees or their surroundings is an important part of operating equipment that emits potentially hazardous rays. Preserving both human safety and structural material that may be compromised from radiation exposure are vital concerns, as well as shielding sensitive materials, such as electronic devices and photographic film. The process of regulating the effects and degree of penetration of radioactive rays varies according to the type of radiation involved. Indirectly ionizing radiation, which includes neutrons, gamma rays, and x-rays, is categorized separately from directly ionizing radiation, which involves charged particles. Different materials are better suited for certain types of radiation than others, as determined by the interaction between specific particles and the elemental properties of the shielding material. In our nuclear application, thermoelectric material and device may be affected at high dose level of nuclear radiation. Proper radiation shielding is needed in this application.

Radiation shielding is based on the principle of attenuation, which is the ability to reduce a wave's or ray's effect by blocking or bouncing particles through a barrier material. Charged particles may be attenuated by losing energy to reactions with electrons in the barrier, while x-ray and gamma radiation are attenuated through photoemission, scattering, or pair production. Neutrons can be made less harmful through a combination of elastic and inelastic scattering, and most neutron barriers are constructed with materials that encourage these processes. There are several factors that influence the selection and use of radioactive shielding materials. Considerations such as attenuation effectiveness, strength, resistance to damage, thermal properties, and cost efficiency can affect radiation protection in numerous ways. For example, metals are strong and resistant to radiation damage, but they undergo changes in their mechanical properties and degrade in certain ways from radiation exposure. Likewise, concretes are strong, durable, and relatively inexpensive to produce, but become weaker at elevated temperatures and less effective at blocking neutrons. The main types of radiation encountered in industrial projects are listed below.

7.3.1 Gamma and X-rays Shielding design

These are forms of electromagnetic radiation that occur with higher energy levels than those displayed by ultraviolet or visible light. In most cases, high-density materials are more effective than low-density alternatives for blocking or reducing the intensity of radiation. However, low-density materials can compensate for the disparity with increased thickness, which is as significant as density in shielding applications. Lead is particularly well-suited for lessening the effect of gamma rays and x-rays due to its high atomic number. This number refers to the amount of protons within an atom, so a lead atom has a relatively high number of protons along with a corresponding number of electrons. These electrons block many of the gamma and x-ray particles that try to pass through a lead barrier and the degree of protection can be compounded with thicker shielding barriers. However, it is important to remember that there is still potential for some rays making it through the shielding, and that an absolute barrier may not be possible in many situations.

Gamma ray attenuation is energy dependent and will depend on which of the three processes dominates. For lower energy gamma rays (less than 0.1 MeV), the photoelectric effect and pair production will play a significant role and heavy materials will attenuate substantially better than light materials. However, at energies above 5MeV, compton scattering dominates and material weight is less significant (note: gamma ray energy bursts in reactors near 7 MeV). The table below gives an idea of common numbers for these coefficients. Note that to first order, a carbon based shield with density about that of graphite has to be about 1.5 times as thick as a lead shield to attenuate gammas equally.

Table 7-9 Measured and predicted attenuation coefficients determined by photoelectric peaks (E. Bashandy, 1962)

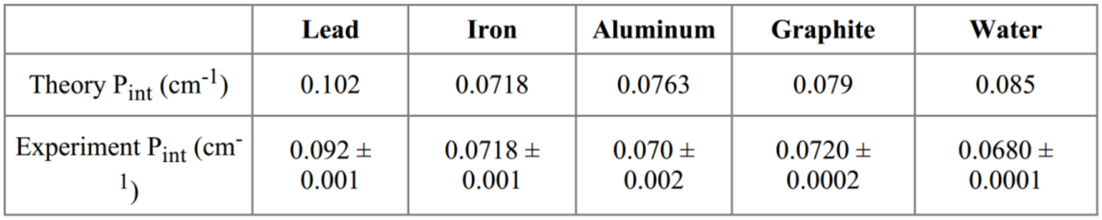

	Lead	Iron	Aluminum	Graphite	Water
Theory P_{int} (cm^{-1})	0.102	0.0718	0.0763	0.079	0.085
Experiment P_{int} (cm^{-1})	0.092 ± 0.001	0.0718 ± 0.001	0.070 ± 0.002	0.0720 ± 0.0002	0.0680 ± 0.0001

It is important that shielding materials do not become brittle and retain their compression strength after long exposure to violent core conditions. This was the impetus for using materials other than the historically popular cement and metal mixes. In fact, cured concrete used in early reactors operated at 50% of its nominal compression strength at temperatures around 450°C. Many fiber reinforced composites retain their mechanical properties (fracture toughness, elastic modulus) after being thermally aged at temperatures up to 1000°C. The ceramic materials, particularly carbon based composites, have many desirable structural properties for intense environments like those in nuclear reactors. It appears as if they should moderate neutrons and gamma radiation moderately well. However, further research into specific structures, their burn-up rates, and their effective cross-sections is necessary. Regardless of the results, they should be considered for intermediary layers in reactors designs to help mediate thermal fluxes and thermal expansion.

DUCRETE concrete mechanical properties have been determined in compression tests. Basically, the results show compressive strength similar to conventional concrete. In addition, if desired, the ratio of aggregate to the cement phase in the mixture can be varied to adjust the gamma and neutron attenuation characteristics. The steel shield has no neutron moderator and thus, the external dose is dominated by the effects of neutrons. Most shielding systems for gamma radiation use either steel or concrete because of their relatively low cost, wide availability, known fabrication characteristics, and radiation shielding effectiveness. For steel cask systems, separate neutron shields typically containing hydrogenous material are added since the thickness of steel required to attenuate neutrons to acceptable external doses is impractical. While concrete is not a particularly good gamma shield per unit thickness, it is cheap enough that the practical approach is to use lots of it. In sufficient thickness, it effectively shields both the neutron and gamma radiation effectively.

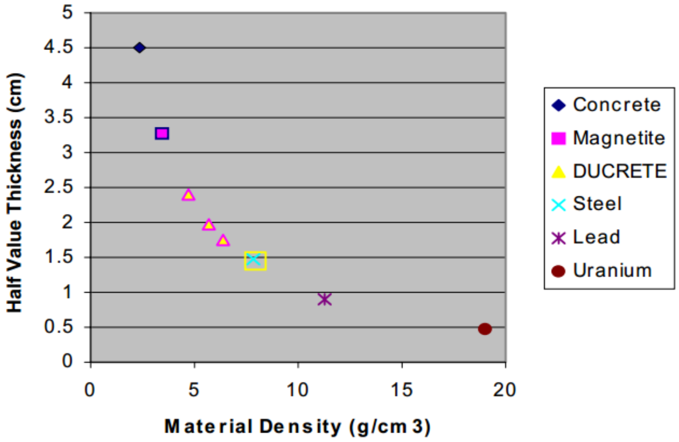

Figure 7.11 Half Value Layer Thickness for Shielding Materials Using a Cobalt 60 Source (courtesy of W. J. Quapp)

The best way to compare the total effectiveness of a shielding system would be to compare the final cost to the customer for systems having the same performance features. Such data are difficult to obtain because of business considerations. Lacking such data, one can compare the relative unit material costs and general fabrication costs per pound of material. However, it can be said that installed concrete costs about $0.12 per kg, steel costs about $1.10 per kg, DUCRETE considerably less than $2.00 per kg, lead about $1.65 per kg and depleted uranium metal at about $22 per kg. While fabrication cost for concrete and DUCRETE are low, fabrication cost for the metals are considerable. In addition, metal shielding systems will require additional neutron shields. Consequently, it will be shown that the overall cost effectiveness of DUCRETE is reasonable compared to concrete and considerably less than other materials for SNF and HLW storage applications.

7.3.2 Neutron shielding design

Neutrons are particles that have neither a positive nor a negative charge, and thus provide a wide range of energy and mass levels that must be blocked. Lead is quite ineffective for blocking neutron radiation, as neutrons are uncharged and can simply pass through dense materials. Materials composed of low atomic number elements are preferable for stopping this type of radiation because they have a higher probability of forming cross-sections that will interact with the neutrons. Hydrogen and hydrogen-based materials are well-suited for this task. Compounds with a high concentration of hydrogen atoms, such as water, form efficient neutron barriers in addition to being relatively inexpensive shielding substances. However, low density materials can emit gamma rays when blocking neutrons, meaning that neutron radiation shielding is most effective when it incorporates both high and low atomic number elements. The low-density material can disperse the neutrons through elastic scattering, while the high-density segments block the subsequent gamma rays with inelastic scattering.

The shielding of neutrons introduces many complications because of the wide range of energy that must be considered. At low energies (less than 0.1 MeV), low mass number materials, such as hydrogen in H_2O, are best for slowing down neutrons. At these energies, the cross section for interaction with hydrogen is high (approximately 20 barns), and the energy loss in a collision is high. Materials containing hydrogen are known as hydrogenous material, and their value as a neutron shield is determined by their hydrogen content. Water ranks high and is probably the best neutron shield material with the advantage of low cost, although it is a poor absorber of gamma radiation.

Water also provides a ready means for removing the heat generated by radiation absorption. At higher energies (10 MeV), the cross section for interaction with hydrogen (1 barn) is not as effective in slowing down neutrons. To offset this decrease in cross section with increased neutron energy, materials with good inelastic scattering properties, such as iron, are used. These materials cause a large change in neutron energy after collision for high energy neutrons but have little effect on neutrons at lower energy, below 0.1 MeV.

Iron, as carbon steel or stainless steel, has been commonly used as the material for thermal shields. Such shields can absorb a considerable proportion of the energy of fast neutrons and gamma rays escaping from the reactor core. By making shields composed of iron and water, it is possible to utilize the properties of both of these materials. PWRs utilize two or three layers of steel with water between them as a very effective shield for both neutrons and gamma rays. The interaction (inelastic scattering) of high energy neutrons occurs mostly with iron, which degrades the neutron to a much lower energy, where the water is more effective for slowing down (elastic scattering) neutrons. Once the neutron is slowed down to thermal energy, it diffuses through the shield medium for a small distance and is captured by the shielding material, resulting in a neutron-gamma (n,γ) reaction. These gamma rays represent a secondary source of radiation.

Iron turnings or punching and iron oxide have been incorporated into heavy concrete for shielding purposes also. Concrete with seven weight percent or greater of water appears to be adequate for neutron attenuation. However, an increase in the water content has the disadvantage of decreasing both the density and structural strength of ordinary concrete. With heavy concretes, a given amount of attenuation of both neutrons and gamma rays can be achieved by means of a thinner shield than is possible with ordinary concrete. Various kinds of heavy concretes used for shielding include barytes concrete, iron concrete, and ferrophosphorus concrete with various modified concretes and related mixtures. Boron compounds have also been added to concretes to increase the probability of neutron capture without high-energy gamma-ray production.

Boron has been included as a neutron absorber in various materials in addition to concrete. For example, borated graphite, a mixture of elemental boron and graphite, has been used in fast-reactor shields. Boral, consisting of boron carbide (B_4C) and aluminum, and epoxy resins and resin-impregnated wood laminates incorporating boron have been used for local shielding purposes. Boron has also been added to steel for shield structures to reduce secondary gamma ray production. In special situations, where a shield has consisted of a heavy metal and water, it has been beneficial to add a soluble boron compound to the water.

The hydrogen-containing materials, however, spread the neutron population over all energies in the spectrum because of the large average energy loss per interaction. The additives introduced into the hydrogenous material (boron, beryllium, and lithium) ultimately reduce the number of neutrons at the lower energies because of the reduced density of hydrogen in the materials and the absorption properties of the additives. The material that spreads more neutrons over all energies is pure polyethylene. This material is also the one with the largest hydrogen density. The composite material has the lowest hydrogen density, and even though neutrons are spread over all energies, the number of neutrons at the lower energies is an order of magnitude lower than for polyethylene.

The hydrogen-bearing materials reduce the number of higher energy neutrons in the 500 keV to 20 MeV energy ranges that penetrate the shield materials considered. In fact, the more hydrogen, the better the overall shielding characteristics. It means that if neutron absorbers are added to the hydrogen-bearing material, then fewer neutrons penetrate the shield. If a polymeric composite material is added, then a better higher energy reflecting characteristic could be achieved.

Heavier elements, like lead, generally have high cross sections for inelastic reactions of high-energy neutrons and can therefore be assumed to be an efficient shielding of high-energy neutrons. However, as the neutrons are attenuated, there is a considerable build-up of low-energy neutrons that will dominate the contributions to the effective dose. For this reason, lead could not be used as shielding alone, but might, if followed by a layer of some hydrogenous material, such as concrete, significantly improve the overall shielding properties. Iron is also a material known for having favorable shielding features, but with similar properties as lead of producing low-energy neutrons. The microscopic cross-sections for high-energy neutrons in iron are lower than in lead, but the atomic density is higher by a factor of 2.5. Therefore, iron can actually be expected to attenuate the high-energy neutrons more efficiently than lead.

7.3.3 Alpha and Beta Particles shielding design

Alpha particles are positively charged helium nuclei, and are relatively easy to block, while beta particles are negatively charged electrons that are more difficult to shield against. While density remains an important characteristic for blocking alpha and beta radiation, thickness is less of a concern. A single centimeter of plastic is sufficient for shielding against alpha particles, as is a half-inch of paper. In some cases, lead is ineffective in stopping beta particles because they can produce secondary radiation when passing through elements with a high atomic number and density. Instead, plastic can be used to form an efficient barrier for dealing with high-energy beta radiation. When negatively charged beta particles hit a high-density material, such as tungsten, the electrons are blocked, but the target which the barrier is intended to protect can actually become irradiated.

α particle can be stopped after traveling through 3 centimeters (about 1.2 inches) of air, 0.2 millimeters (about 0.008 inches) of water, or a piece of paper or skin. A thin piece of paper, or even the dead cells in the outer layer of human skin provides adequate shielding because alpha particles can't penetrate it. However, living tissue inside the body offers no protection against inhaled or ingested alpha emitters.

β particle can only be stopped after traveling through 3 meters (about 10 feet) of air, a few centimeters (less than 2 inches) of water, or a thin layer of glass or metal. Additional covering, for example heavy clothing, is necessary to protect against beta- emitters. Some beta particles can penetrate and burn the skin.

Since both alpha and beta particle are pretty easy to block and the damage to our proposed TEG application systems is negligible, the discussion is mainly on gamma and neutron radiation shielding.

7.3.4 Shielding design guideline

The overall systems including the energy harvesting and electronics must be packaged well for hardening against temperature and radiation. The beta radiation can be shielded easily by a thin layer of metal. Lead or tungsten can be used for gamma ray shielding. Based on the radiation study, various thickness of metal can be used. If intensive protection, especially for neutron impact, is needed, we may design a multilayer radiation shielding system of B4C and WC. The optimized thickness of the B4C and WC will be determined from the Monte Carlo N-Particle (MCNP) and Fluktuierende Kaskade (FLUKA) calculation in simulating neutron transport inside materials based on the conventional neutron flux and energy spectrum. The effectiveness of shielding protection can be verified using MCNP and FLUKA simulation and validated in the various radiation facilities available.

In proposed thermoelectric energy harvesting from nuclear environment, proper radiation shield is need with the following guideline:

- Gamma radiation shielding design is no need up to 10M Rad for thermoelectric material or module.
- Gamma radiation shielding design for DC-DC converter is needed.
- Gamma radiation shielding design for wireless communication system is no need.
- Neutron radiation shielding design is no need for dose low than $10^{14}/cm^2$.
- Ion radiation shielding design is need for dose larger than $10^{15}/cm^2$.
- Alpha and beta radiation shielding design is no need for the system.

8 CONCLUSION

Overall, this dissertation addresses the critical issue of energy crisis by proposing thermal energy harvesting through thermoelectric materials and device. By using thermoelectric material, the wasted heat energy could be converted into electricity to increase vehicle fuel efficiency and to power sensors, depends on the quality and quantity of input heat energy. The scientific innovation is based on recent advance on various kinds of thermoelectric material and novel fabrication method to increase energy efficiency of different situations. The thermoelectric material has been intensively studied in this work and depends on different application the appropriate materials are selected for each application. The importance of this works lies on the novel design/fabrication of thermoelectric material using new method, like thermal spray, physical sputtering. The process parameters are investigated to give best thermoelectric performance. More scientifically, the phase structure, microstructure and interface are examined to study the influence on thermal conductivity, electrical conductivity as well Seebeck coefficient, the most important parameter for thermoelectric material. Interface problems are crucial in material science, especially as the development of nano-structure material. This work targets to provide more fundamentals from the material science point of review of solving energy crisis. Besides, this dissertation also presents some novel designs to harvesting waste energy from different source, example nuclear environment, where a huge heat is lost especially during disaster. The design take advantages of current commercial available thermoelectric module and the novel design of heat exchange/power electronic from this group. The application of thermoelectric will enhance the thermoelectric topic and attract more research to work on this topic. Our work proved the potential application of thermoelectric for energy harvesting to power sensor and it can be more widely used with larger scale harvester.

8.1 Exhaust Heat Review

In summary, the average exhaust temperatures at highway driving cycle and city driving cycle are around 500~650 degree Celsius and 200~400 degrees Celsius. The mass flow rate changes a lot according to vehicle size. Typically, the mass flow rate is around 10~25 g/s but the exception occurs when heavy duty trucks are taken into consideration. The thermal power calculated based on the collected data is 3~10 kilowatts. To make meaningful contribution to the fuel efficiency improvement, the conversion efficiency of TEG devices needs to be 8~10% or more since several hundreds of watts of electricity is effective for application. As the exhaust changes in large range at different driving conditions, the TEG is hard to replace the alternator even though the average output of the electrical power from TEG can be several hundred watts. To install the TEG module, locations should be chosen at downstream of catalytic converter since the heat quantity and quality satisfy the requirement for intermediate temperature thermoelectric material and there is no increased pollution due to extracting heat from upstream of catalytic converter.

8.2 Thermal Spray of Magnesium Silicide

On the thermoelectric material synthesis side, magnesium silicide (Mg_2Si) layers have been firstly synthesized by Atmospheric Plasma Spray (APS), which has been shown to be an effective way to reduce the thermal conductivity of material compared with conventional hot press method. Even though Mg_2Si is very sensitive to air and temperature, the APS using SG100 gun very successfully keeps the composition the same as raw powder. In our investigation, reduced thermal conductivity of Mg_2Si material is obtained most likely due to phonon scattering by pores and cracks in the APS samples. Thermal conductivity, electrical conductivity, Seebeck coefficient and figure of merit are all compared between APS and hot press from 300K to 390K. Carrier concentration and hall mobility are measured to understand influence of electrical conductivity by different methods. Carrier concentration is a tradeoff between electrical conductivity and Seebeck coefficient. Heat treatment under vacuum at 400 degree Celsius helps to tune the concentration but doesn't change mobility significantly. Seebeck coefficient increases with the decrease of carrier concentration if phase remain the same. Thermal conductivity of APS is lower than hot press samples. Vacuum annealed APS sample gives very high Seebeck coefficient. Carrier concentration need to be tuned and carrier mobility need to be increased to achieve a better ZT. As a preliminary result, APS achieved 10% in ZT compared with hot pressed sample and higher percentage will obtained by properly control carrier concentration and higher temperature annealing of APS sample. Besides mass production and cost effective, thermal spray can directly fabricate thermoelectric material on exhaust pipe which makes it worth of more investigation. Vacuum Thermal Spray (VPS) is a rapid process and also magnesium silicide samples have been successfully synthesized by VPS. Even though Mg_2Si is extremely sensitive to oxygen and temperature, the VPS approach, using low power has successfully maintains the composition of the sample similar to feedstock powder. Beside the industrial scale production, thermal spray is flexible to directly spray thermoelectric material on any shape, i.e. cylindrical. In this work, the reduced thermal conductivity demonstrated in the Mg_2Si material is most likely due to phonon scattering by pores and cracks in the VPS samples. Carrier concentration represents a tradeoff between electrical conductivity and Seebeck coefficient. The Seebeck coefficient increases with a decrease in carrier concentration if the phase remains the same but electrical conductivity increase as carrier concentration increase when mobility doesn’t change much. The low temperature electrical measurement also shows 3D variable hopping effect in hot press and VPS samples. IV curve measurement shows the low electrical conductivity is due to the existence of MgO insulation layer around the grain boundaries. VPS samples achieved ZT values approximate 30% those of hot-pressed samples with same starting powder. The work suggests that vacuum thermal spray can be a viable means to directly fabricate thermoelectric materials for high-volume applications. Thermal spray of filled skutterudite has been first time tried and the as quenched powder doesn’t decompose or get oxidized during thermal spray. Heat treatment was done but not in the optimal temperature because of the Al substrate. XRD showed the as sprayed sample had exactly the same phase as the feedstock powder. But heat treated sample showed some oxidation and diffusion of Al into the coating. Microstructure of splat showed this powder is fully melted and the flowability of this powder is good due to the uniform spherical shape. Cross section image of the coating indicated the bonding and adhesion of this coating is good and more thermal spray of this material is needed.

8.3 Thermoelectric Generator Model and Design

On the thermoelectric module modeling and optimization side, heat transfer and electrical contact resistor model is established to find the optimal leg length and width based on the exhaust pipe geometry. Small leg length will increase the contact resistance and large leg length will increase the electrical resistivity of thermoelectric element. The tradeoff between these two factors is addressed and the optimal leg length is found to be around 0.85mm for oxide material (n-type $\mathrm{T_iO_{2-x}}$ and p-type$\mathrm{C_oO(Li_{0.5})}$) and 0.9mm for $\mathrm{Mg_2Si}$. The leg width is as smalls as possible to increase the output power except to separate the n, p type material. The sensitivity analysis shows: A) The thicker ceramic layer, the smaller optimal leg length and the optimal leg length is sensitive to the variation of ceramic layer. So the thickness of ceramic layer should be control carefully to get an accurate optimal leg length during process. B) The optimal leg length is not very sensitive to the exhaust pipe diameter. The only concern is that the radius of the exhaust pipe should not be too small since the model is based on the assumption that ceramic layer is much smaller compared with the exhaust pipe diameter. C) The optimal leg length will be smaller if the electrical contact resistance can be reduced. Good contact of cooper layer is desired during thermal spray process. D) Heat source and heat sink temperature has influence on the output but is not sensitive to the optimal leg length. For module fabrication, the heat source temperature can be neglected. E) The oxides are n-type $\mathrm{T_iO_{2-x}}$ and p-type$\mathrm{C_oO(Li_{0.5})}$ and $\mathrm{Mg_2Si}$ have different optimal leg length but the change is slight. So the optimization of the module can be done independent of material selection as long as the material is not at the abnormal level of thermoelectric property. We designed an integrated TEG/heat exchanger. The heat transfer in this device was modeled using the Number of Transfer Units (NTU) method. A thermal resistance network was used to analyze the temperature at each junction. In order to improve the heat exchanger efficiency, fins were designed and incorporated into the design. The hot and cold sides of the TEG are at 330 degree C and 125 degree C, and the effective temperature difference is 205 degree C. The temperature distribution at the cross section of the TEG device was further estimated by finite element analysis (FEA) performed using ANSYS software, and the temperature difference at the entrance and exit ends were obtained. To calculate the potential electrical output power, the average temperature difference between exhaust inlet side and exhaust outlet side was used. The average temperature difference is taken to be 165 degree C. As a result, the total electrical output is calculated to be 526W, which is 4.2% of the waste heat power, and correspond to a 5% fuel economy increase for a typical vehicle.

8.4 Thin Film Thermoelectric Material Fabrication

On thin film filled skutterudite, the state of art high temperature thermoelectric material for the first time Yb filled CoSb3 skutterudite thin film has been reported using DC magnetron sputtering method. The selection of using DC magnetron sputtering lies in its high deposition rate and it can maintain the target material composition. More importantly, magnetron sputtering provides denser microstructure which surpasses most of other thin film deposition techniques. The parameters of DC magnetron and post heat treatment on sputtered sample have been optimized experimentally and Yb filled CoSb3 thermoelectric properties have been characterized. Electrical conductivity, Seebeck coefficient, thermal conductivity, and figure of merit are characterized from 300K to 700K. XRD, SEM and EDS of the different thickness samples at three kinds of heat treatment conditions are obtained to assess the phase composition and crystallinity of thin film samples with different heat treatment temperatures. In this work, 1020K heat treatment was adopted for thin film post process due to thin film high degree of crystallinity as well as avoiding reverse heating effect. Carrier concentration and Hall mobility are obtained from Hall

Effect measurements, which provide further insight into the electrical conductivity and Seebeck coefficient mechanisms. As-sputtered sample has huge carrier concentration which gives very high electrical conductivity. However, low Hall mobility in as sputtered sample makes it unsuitable for thermoelectric application. For three types of heat treatment, 1020K gives best Hall mobility. Seebeck coefficient is inversely dependent on carrier concentration, so the lower carrier concentration in 130nm sample increases Seebeck a lot and overall it gives the best figure of merit. Since the carrier concentration play trade-off role in thermoelectric material, it should be optimized to give better ZT. It seems in this work, the low carrier concentration is more favorable due to its large increase in Seebeck coefficient when conserving the square of Seebeck coefficient in the ZT equation. Thermal conductivity of thin film filled skutterudite was found to be much less compared with bulk Yb filled CoSb3 skutterudite which may be due to the enhanced phonon scattering by grain interface and boundary. 860nm sample is much thicker than the rest two sample and has a higher thermal conductivity. Different thickness thin film samples were prepared with same sputtering deposition rate and maximum ZT of 0.48 was achieve at 700K for 130nm thick sample. This value was between half and one third of bulk figure of merit which due to the lower Hall mobility in thin film samples.

8.5 Radiation Influence on TEG Application in Nuclear Environment

On nuclear radiation on material, thermoelectric Bi2Te3 and Sb2Te3 thin films prepared by E-beam evaporation were irradiated by 400 keV Ne2+ in order to investigate the radiation effects of the thermoelectrical materials as energy harvester in nuclear environment. The microstructure evolution, phase/crystallinity and the thermoelectrical properties were systematically investigated. An ionization radiation-induced defect recovery and reorientation were observed for both films as evidenced by XRD and TEM. A competition of the ionization radiation and displacement damage dominates the variations of the electrical and thermoelectrical properties of materials. The electrical resistivity decreases in both materials upon ion irradiation due to the increase in carrier mobility and better crystallinity. The accumulated defects induced by displacement damage at higher ion fluence eventually result in the reduction of the mobility and electrical conductivity. Seebeck coefficient increases accordingly with ion radiation due to the reduction of carrier concentration and the charge mobility. Positive effects of ion irradiations from Ne2+ on thermoelectric materials are observed, which increases the power factors to 208% for Bi2Te3 and 337% for Sb2Te3 materials, respectively, consistent with the increase of the electrical conductivity as a result of ionization radiation-enhanced crystallinity. The peaks seem to happen at some place between 1 and 5 x1015/cm2, likely around 3 x1015/cm2 ion fluence. However, under a higher fluence, the power factor starts to decrease, limiting the enhancements of thermoelectrical material properties under intensive radiation environment.

9 FUTURE WORK

This dissertation provides lots of scientific finding including the thermal spray related microstructure and interface on the influence of thermoelectric properties as well as the radiation effect on the phase and microstructure change for thermoelectric materials. In future, the author would like to present more scientific results of thermoelectric fabrication and application in the following aspects:

- The phase change of filled skutterudite material during thermal spray;
- How microstructure evolves during different temperature heat treatment;
- Different thermoelectric properties for in-plane and through-thickness direction;
- How microstructure and interface influence carrier concentration and Hall mobility.
- How nuclear radiation change the phase and microstructure of thermoelectric material.
- What is the change of carrier concentration by ionized radiation on thermoelectric material?
- How thin film thermoelectric thickness affects phonon transport.
- How to reduce electron scattering of thermal sprayed sample without change the phonon scattering.

9.1 Thermal Spray of Other Materials

9.1.1 Filled skutterudite thermal spray

Filled skutterudite has always been an attractive thermoelectric material due to its high figure of merit. By our several trials on this material, we found the parameter to control the phase composition and find the proper post treatment method. Skutterudite has first time been synthesized by thermal spray method. XRD and SEM are used to characterize the phase and microstructure of skutterudite sample. As-sprayed skutterudite is followed with heat treatment and the correct phase can be obtained. With high velocity and low temperature thermal spray, the as quenched powder is not oxidized and the evaporation of Sb is also suppressed. The microstructure of thermal sprayed skutterudite shows lots of pore/cracks that can enhance the phonon scattering. Thermal conductivity of our sample is lower than by conventional method because of enhanced phonon scattering.

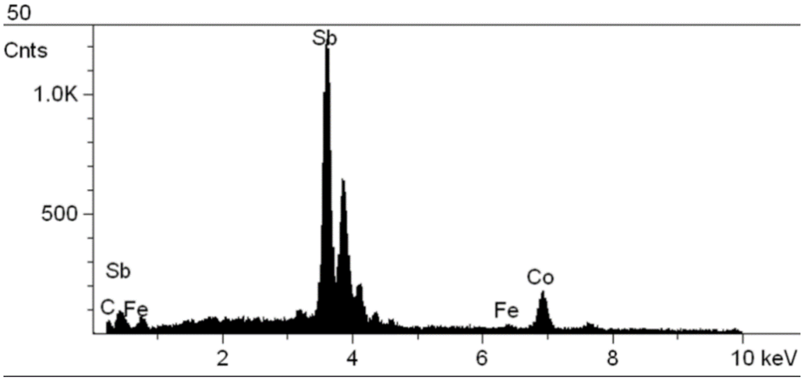

Figure 9.1 EDX of as-sprayed skutterudite

Figure 8.3 is the EDX of the as sprayed skutterudite. One should notice that it's as quench phase however the results show no oxidation or contamination occurs during thermal spray.

Also, we are trying to spray this material with VPS and followed by heat treatment with oxygen getter in quartz tube. Seebeck coefficient will be measured under vacuum. If the coating is thick enough, thermal and electrical conductivity can be measured from room temperature up to 700K.

9.1.2 Higher manganese silicide and oxides

In the introduction section, the significance of HMS has been addressed due to its high figure of merit and superior thermal spray property than Mg_2Si since Mg is too sensitive to oxygen and temperature. We are seeking HMS powder appropriate for thermal spray and struggled for a long time. Commercially, there is not higher manganese silicide powder available. In several research labs, they make HMS for their own experiment which is far less for thermal spray. One spray just for very thin layer need at least 500 grams. Due to our successful trial on spray of Mg_2Si, a good thermoelectric property of HMS is expected. During thermal spray, HMS will not react with oxygen as much as Mg_2Si do. This gives us plenty of flexibility, say, APS with different nozzles can be used. Beside, HVOF can be another viable method if oxidation is not a concern. As we all know, HVOF makes denser coating than other method due to its high velocity.

9.1.3 Oxides

Another material that we have discussed at beginning of this project is oxide material. We know that thermal spray is a mass production method and hard to isolate air. But oxides are perfect candidates in terms of oxidation during thermal spray. The only problem with oxides is their relative low figure of merit. Lots of researches are ongoing to increase its efficiency. During the introduction, several oxidation materials have been discussed. Furthermore, oxygen deficiency titanium oxide (i.e. $TiO_{1.9}$) is a good thermoelectric candidate. But attention still needs to pay to the constitution of each element because TiO1.9 could become TiO2 by oxidation which decreases its figure of merit. Beside, BiCuSeO oxide is also a popular thermoelectric material. As long as the powder is available, good phase and thermoelectric properties could be achieved with thermal spray technology.

9.2 Optimize Thin Film Filled Skutterudite Thermoelectric

On thin film filled skutterudite, the state of art high temperature thermoelectric material for the first time Yb filled CoSb3 skutterudite thin film has been reported using DC magnetron sputtering method. But the figure of merit of this work is not high for wide application. On the target side, more selection of chemistry composition is needed including doping element amount. A more comprehensive study on how each element and doping amount in filled skutterudite system will influenced the overall figure of merit is needed. The relationship between thin film thickness and thermal conductivity, electrical conductivity and Seebeck should be investigated from the phonon and electron scattering point of view. The microstructure and interface control and the influence on carrier concentration and Hall mobility should be addressed also. On the fabrication side, more film thickness and operating power should be evaluated in term of measured thermoelectric properties including thermal, electrical and Seebeck coefficient.

More importantly, the application of the thin film thermoelectric should be specified by doing more research on heat related problems in IC chips. The feasibility study of those applications should be carried out in order to evaluate the potential benefit of thin film application in localized cooling or energy harvesting from hot spot in IC chips. Only by expand the niche application of thin film thermoelectric application, the research on this topic can be hot as in other application including automobile and nuclear.

The most important character of thin film thermoelectric material lies in the potential high figure of merit engineering through nano-technology. However, the application of thin film energy depends on the overall efficiency of thin film material based device fabrication. Our work has initiated MEMS based manufacturing of thermoelectric material; however on the device side, innovative design and fabrication method should be addressed in order to cut the cost and meet the industrial requirement.

9.3 Through thickness measurement

Due to our integrated design of thermoelectric generator, through thickness electrical conductivity and Seebeck coefficient will be used to calculate figure of merit. For thermal conductivity, in plane value will be used. As know, thermal sprayed samples have large anisotropic for in plane and through thickness direction which is the intrinsic properties. We didn’t measure through thickness Seebeck coefficient because the sprayed sample was not long enough. For our Seebeck equipment, at least four millimeter is need on the spray direction for through thickness Seebeck characterization. For electrical conductivity, we got some preliminary result.

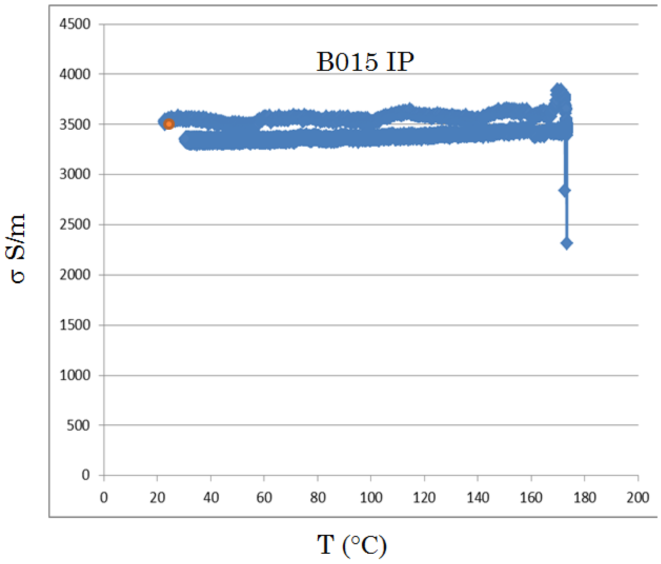

Figure 9.2 In plane electrical conductivity of Mg2Si by APS

Figure 9.1 showed the in plane electrical conductivity of Mg_2Si by APS (SG100). We should notice that the equipment we used is home build Keithley digital multi-meter, the accuracy is not as good as the one we used in BNL. Basically, the nano-meter and lock-in amplifier in BNL gives much more reliable measurement. However, as a comparison between in plane and through thickness measurement, it's enough to conclude.

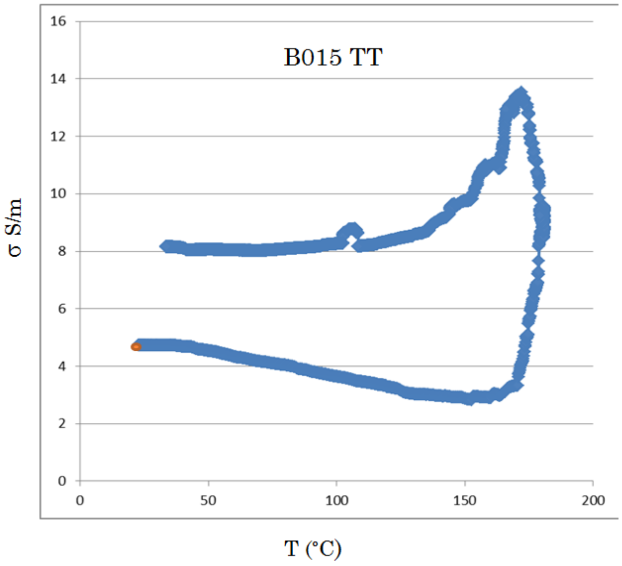

Figure 9.3 Through thickness electrical conductivity of Mg2Si by APS

Compare Figure 9.2 and 9.3, one can clearly see the electrical conductivity decreases more than two magnitude from in plane to through thickness. This is expected because thermal sprayed samples have better bonding perpendicular to the spray direction. Most of the void, cracks or other defects are accumulated in the spray direction. Both two figures show the electrical conductivity change during one thermal cycle from room temperature to 175°C. The starting point is indicated by an orange dot. The difference between temperature rise and fall may due to evaporation of Mg, anneal of the defects or measurement error. To make a useful device, through thickness properties should be increased either by heat treatment or other method that can increase the bonding ratio. Due to thermal sprayed sample's thickness, several through thickness properties cannot be measured now, in the future, we need to spray longer sample or find better equipment to do through thickness measurement.

9.4 Thermoelectric Prototype Shielding Design in Nuclear Application

Radiation can be a serious concern in nuclear power facilities and a number of other circumstances. Containing radiation and preventing it from causing physical harm to employees or their surroundings is an important part of operating equipment that emits potentially hazardous rays. Preserving both human safety and structural material that may be compromised from radiation exposure are vital concerns, as well as shielding sensitive materials, such as electronic devices and photographic film. The process of regulating the effects and degree of penetration of radioactive rays varies according to the type of radiation involved. Indirectly ionizing radiation, which includes neutrons, gamma rays, and x-rays, is categorized separately from directly ionizing radiation, which involves charged particles. Different materials are better suited for certain types of radiation than others, as determined by the interaction between specific particles and the elemental properties of the shielding material. In our nuclear application, thermoelectric material and device may be affected at high dose level of nuclear radiation. Proper radiation shielding is needed in this application.

Part of this work showed that high dose nuclear radiation will have influence on both thermoelectric material and electronics. Proper shielding especially for neutron radiation is highly desirable for the degradation on the overall performance of the system. Gamma radiation effect seems not affect thermoelectric material but can be a problem for DC-DC converter. A complete shielding design will contains mechanical support for the device and prevent it from radiation in nuclear environment. The device must be sustainable in harsh environments, e.g. water, fire, shock, and high-dose radiation exposure. The environmental protection system will consist of a stainless steel/titanium alloy outer layer that is filled with dry silica. The dry silica provides high-temperature insulation, which make it possible to tolerate fire at 1,100 ° C for one hour. Additional inner layers will be included to shield the device from radiation. Example materials include Polysulfone (PSU) / Polyethersulfone (PES) / Polyphenylsulfone (PPSU), which are high-temperature polymers capable of blocking alpha and beta radiation. Lead sheet can be used to block gamma radiation and X-rays.

REFERENCE

1. Geballe, T.H., *The Seebeck Effect in Germanium.* Physical Review, 1953. **92**(3): p. 857-857.
2. Martin, G., *The Peltier effect and low-temperature research.* Nature, 1921. **107**: p. 43-43.
3. Bevan, P.V., *On the Joule-Thomson effect.* Proceedings of the Cambridge Philosophical Society, 1904. **12**: p. 127-134.
4. Broido, D.A. and T.L. Reinecke, *Effect of Superlattice Structure on the Thermoelectric Figure of Merit.* Physical Review B, 1995. **51**(19): p. 13797-13800.
5. Mensah, S.Y. and G.K. Kangah, *The Thermoelectric Effect in a Semiconductor Superlattice in a Non-Quantized Electric-Field.* Journal of Physics-Condensed Matter, 1992. **4**(3): p. 919-922.
6. Broido, D.A. and T.L. Reinecke, *Thermoelectric power factor in superlattice systems.* Applied Physics Letters, 2000. **77**(5): p. 705-707.
7. Busch, G. and U. Winkler, *Elektrische Leitfahigkeit Und Hall-Effekt Intermetallischer Verbindungen.* Helvetica Physica Acta, 1953. **26**(3-4): p. 395-399.
8. Lin, C., H. Chen, M. Tewolde, G. Fu, D. Liu, T. Zhang, T. He, C. Nie, W. Zheng, F. Liu, L. Zuo, D. Hwang, J. Longtin, *THERMOELECTRICALLY POWERED SENSING FOR SMALL MODULAR REACTORS*, in *ASME 2013 Summer Heat Transfer Conference*2013: Mineapolis, Minnesota, USA.
9. Yang, J.H. and F.R. Stabler, *Automotive Applications of Thermoelectric Materials.* Journal of Electronic Materials, 2009. **38**(7): p. 1245-1251.
10. Wei, D.H., et al., *Performance analysis and optimization of organic Rankine cycle (ORC) for waste heat recovery.* Energy Conversion and Management, 2007. **48**(4): p. 1113-1119.
11. Ishikawa, N., *A study on emissions improvement of a diesel engine equipped with a mechanical supercharger.* International Journal of Engine Research, 2012. **13**(2): p. 99-107.

12. Katrasnik, T., et al., *Improvement of the dynamic characteristic of an automotive engine by a turbocharger assisted by an electric motor.* Journal of Engineering for Gas Turbines and Power-Transactions of the Asme, 2003. **125**(2): p. 590-595.
13. Bell, L.E., *Cooling, heating, generating power, and recovering waste heat with thermoelectric systems.* Science, 2008. **321**(5895): p. 1457-61.
14. Patel, P. *Powering Your Car with Waste Heat*. MIT Technology Review, 2011.
15. Li, Q., Z.W. Lin, and J. Zhou, *Thermoelectric Materials with Potential High Power Factors for Electricity Generation.* Journal of Electronic Materials, 2009. **38**(7): p. 1268-1272.
16. Makita, Y.T., H.; Shibata, H; Kobayashi, N; Hasegawa, M; Kimura, S; Obara, A; Tanabe, J.; Uekusa, S *Optical, electrical and structural properties of polycrystallinel beta-FeSi2 thin films fabricated by electron beam evaporation of ferrosilicon*. in *15th International Conference on Thermoelectrics*. 1996.
17. Sodeoka, S.S., M; Tsutsumi, A; Kuramoto, K; Sawazaki, J; Yoshida, K; Huang, H.; Nagai, K.; Kondo, H.; Nakahama, S. . *Fabrication of large size FeSi2 thermoelectric device by thermal spraying process*. in *17th International Conference on Thermoelectrics*. 1998.
18. Cherigui, M., N.E. Fenineche, and C. Coddet, *Structural study of iron-based microstructured and nanostructured powders sprayed by HVOF thermal spraying.* Surface & Coatings Technology, 2005. **192**(1): p. 19-26.
19. Schilz, J., et al., *On the thermoelectric performance of plasma spray-formed iron disilicide.* Journal of Materials Science Letters, 1998. **17**(17): p. 1487-1490.
20. Corelli, J.C. and R.T. Frost, *The Effects of Reactor Irradiation on the Thermoelectric Properties of Lead and Bismuth Tellurides*, 1960, Knolls Atomic Power Lab., Schenectady, N.Y.
21. Kilp, G.R. and P.V. Mitchell, *RADIATION EFFECTS ON THERMOELECTRIC MATEFlIATS*, 1961, Westinghouse: UNITED STATES ATOMIC ENERGY COMMISSION.
22. Carstens, T., et al., *Gamma Radiation Influence on Thermoelectric Powered Wireless Sensors for Dry-Cask Storage.* Electrical and Power Engineering Frontier, 2013. **2**(2): p. 7.
23. Espinosa, N., et al., *Modeling a Thermoelectric Generator Applied to Diesel Automotive Heat Recovery.* Journal of Electronic Materials, 2010. **39**(9): p. 1446-1455.
24. Lewis, B.G. and D.C. Paine, *Applications and processing of transparent conducting oxides.* Mrs Bulletin, 2000. **25**(8): p. 22-27.
25. Kelly, P.J. and R.D. Arnell, *Magnetron sputtering: a review of recent developments and applications.* Vacuum, 2000. **56**(3): p. 159-172.
26. LaGrandeur, J., D. Crane, A. Eder, , *Vehicle Fuel Economy Improvement through Thermoelectric Waste Heat Recovery*, in *DEER Conference*2005.
27. Andreas Eder, M.L. *Efficient and Dynamic - The BMW Group Roadmap for the Application of Thermoelectric Generators*. in *Thermoelectrics Applications Workshop*. 2011.
28. J. LaGrandeur, D.C., S. Hung, B. Mazar and A. Eder, *Automotive Waste Heat Conversion to Electric Power using Skutterudite, TAGS, PbTe and BiTe.* International Conference on Thermoelectrics, 2006.
29. D. M. Smith, J.T., G. Min, *Weight Penalty Incurred in Thermoelectric Recovery of Automobile Exhaust Heat.* Journal of Electronic Material, 2011. **40**(5): p. 784-788.
30. Yang, J. *Engineering and Material for Automotive Thermoelectric Application*. in *Thermoelectric Applications Workshop*. 2009.
31. Thacher, E.F., et al., *Testing of an automobile exhaust thermoelectric generator in a light truck.* Proceedings of the Institution of Mechanical Engineers Part D-Journal of Automobile Engineering, 2007. **221**(D1): p. 95-107.
32. J. Bass, A.K., N. Elsner. *Thermoelectric Generator (TEG) for Heavy Diesel Trucks*. in *International Conference on Thermoelectrics*. 2001.

33. Yigit, K.S., *Experimental investigation of a comfort heating system for a passenger vehicle with an air-cooled engine.* Applied Thermal Engineering, 2005. **25**(17-18): p. 2790-2799.
34. Talbi, M. and B. Agnew, *Energy recovery from diesel engine exhaust gases for performance enhancement and air conditioning.* Applied Thermal Engineering, 2002. **22**(6): p. 693-702.
35. D. T. Hountalas, C.O.K., D. A. Kouremenos, E. D. Rogdakis, *Study of available exhaust gas heat recovery technologies for HD diesel engine applications.* International Journal of Alternative Propulsion, 2007.
36. Lineykin, S. and S. Ben-Yaakov, *Modeling and analysis of thermoelectric modules.* Ieee Transactions on Industry Applications, 2007. **43**(2): p. 505-512.
37. Yim, W.M. and F.D. Rosi, *Compound Tellurides and Their Alloys for Peltier Cooling - Review.* Solid-State Electronics, 1972. **15**(10): p. 1121-&.
38. Chowdhury, I., et al., *On-chip cooling by superlattice-based thin-film thermoelectrics.* Nature Nanotechnology, 2009. **4**(4): p. 235-238.
39. Stordeur, M. and I. Stark, *Low power thermoelectric generator - self-sufficient energy supply for micro systems.* Proceedings Ict'97 - Xvi International Conference on Thermoelectrics, 1997: p. 575-577.
40. Dresselhaus, M.S., et al., *New directions for low-dimensional thermoelectric materials.* Advanced Materials, 2007. **19**(8): p. 1043-1053.
41. Miorandi, D., et al., *Internet of things: Vision, applications and research challenges.* Ad Hoc Networks, 2012. **10**(7): p. 1497-1516.
42. Venkatasubramanian, R., et al., *Thin-film thermoelectric devices with high room-temperature figures of merit.* Nature, 2001. **413**(6856): p. 597-602.
43. Nolas, G.S., D.T. Morelli, and T.M. Tritt, *Skutterudites: A phonon-glass-electron crystal approach to advanced thermoelectric energy conversion applications.* Annual Review of Materials Science, 1999. **29**: p. 89-116.
44. Nolas, G.S., et al., *High figure of merit in partially filled ytterbium skutterudite materials.* Applied Physics Letters, 2000. **77**(12): p. 1855-1857.
45. Shi, X., et al., *Multiple-Filled Skutterudites: High Thermoelectric Figure of Merit through Separately Optimizing Electrical and Thermal Transports (vol 133, pg 7837, 2011).* Journal of the American Chemical Society, 2012. **134**(5): p. 2842-2842.
46. Venkatasubramanian, R., *Phonon blocking electron transmitting superlattice structures as advanced thin film thermoelectric materials.* Recent Trends in Thermoelectric Materials Research Iii, 2001. **71**: p. 175-201.
47. Venkatasubramanian, R. and T. Colpitts, *Enhancement in figure-of-merit with superlattice structures for thin-film thermoelectric devices.* Thermoelectric Materials - New Directions and Approaches, 1997. **478**: p. 73-84.
48. Venkatasubramanian, R., et al., *Superlattice thin-film thermoelectric materials and devices.* Thermoelectric Materials 2003-Research and Applications, 2004. **793**: p. 51-58.
49. Xu, L., et al., *Enhancement in Thermoelectric Properties Using a P-type and N-type Thin-Film Device Structure.* Polymer Composites, 2013. **34**(10): p. 1728-1734.
50. Kim, M.Y. and T.S. Oh, *Thermoelectric Power Generation Characteristics of a Thin-Film Device Consisting of Electrodeposited n-Bi2Te3 and p-Sb2Te3 Thin-Film Legs.* Journal of Electronic Materials, 2013. **42**(9): p. 2752-2757.
51. Anno, H., et al. *Thermoelectric properties of rf-sputtered CoSb₃ films*. in *Thermoelectrics, 1996., Fifteenth International Conference on*. 1996.
52. Anno, H., et al. *Preparation and thermoelectric properties of CoSb₃ thin films on GaAs(100) substrate*. in *Thermoelectrics, 1997. Proceedings ICT '97. XVI International Conference on*. 1997.

53. Savchuk, V., et al., *Transport and structural properties of binary skutterudite CoSb3 thin films grown by dc magnetron sputtering technique.* Journal of Applied Physics, 2002. **92**(9): p. 5319-5326.
54. Caylor, J.C., et al., *Pulsed laser deposition of thin-film skutterudite thermoelectrics.* Abstracts of Papers of the American Chemical Society, 2000. **219**: p. U883-U883.
55. Zeipl, R., et al., *Thin layers prepared by pulsed laser deposition from Yb0.19Co4Sb12 target.* ICT'06: XXV International Conference on Thermoelectrics, Proceedings, 2006: p. 451-454.
56. Zeipl, R., et al., *Properties of thin N-type Yb(0.14)Co(4)Sb(12) and P-type Ce(0.09)Fe(0.67)Co(3.33)Sb(12) skutterudite layers prepared by laser ablation.* Journal of Vacuum Science & Technology A, 2010. **28**(4): p. 523-527.
57. Kumar, S.R.S., et al., *Pulsed laser deposition and thermoelectric properties of In- and Yb-doped CoSb3 skutterudite thin films.* Journal of Materials Research, 2011. **26**(15): p. 1836-1841.
58. Yakabe, H.K., K.; Terasaki, I.; Sasago, Y., *Thermoelectric properties of transition-metal oxide NaCo2O4 system*, in *Thermoelectrics*1997.
59. S.A. Eide, C.D.G., T.E. Wierman, INL and N. D.M. Rasmuson, *Reevaluation of Station Blackout Risk at Nuclear Power Plants* 2005: p. 13-17.
60. Kuan, P., D.J. Hanson, and F. Odar, *Managing water addition to a degraded core*1991, EG and G Idaho, Inc., Idaho Falls, ID. Medium: ED; Size: Pages: (19 p).
61. Clapier, F. and C.S. Zaidins, *Neutron Dose Equivalent Rates Due to Heavy-Ion Beams.* Nuclear Instruments & Methods in Physics Research, 1983. **217**(3): p. 489-494.
62. Vizkelethy, G., et al., *Simulation of Neutron Displacement Damage in Bipolar Junction Transistors Using High-Energy Heavy Ion Beams*, 2006, Sandia National Laboratories
63. Lewis, M.B., et al., *Improved Techniques for Heavy-Ion Simulation of Neutron Radiation-Damage.* Nuclear Instruments & Methods, 1979. **167**(2): p. 233-247.
64. Kulcinsk.Gl, Wittkowe.Ab, and G. Ryding, *Use of Heavy Ions from a Tandem Accelerator to Simulate High Fluence, Fast Neutron Damage in Metals.* Nuclear Instruments & Methods, 1971. **94**(2): p. 365-&.
65. Abromeit, C., *Aspects of Simulation of Neutron Damage by Ion Irradiation.* Journal of Nuclear Materials, 1994. **216**: p. 78-96.
66. Guner, S., et al., *Effects of MeV Si ions bombardment on the thermoelectric properties of Zn4Sb3 and CeFe2Co2Sb12 thin films.* Surface & Coatings Technology, 2009. **203**(17-18): p. 2664-2666.
67. Zheng, B., et al., *Improvement on thermoelectric properties of multilayered Si1-xGex/Si by ion beam bombardment.* Nuclear Instruments & Methods in Physics Research Section B-Beam Interactions with Materials and Atoms, 2008. **266**(1): p. 73-78.
68. Budak, S., et al., *MeV Si ion beam modification effects on the thermoelectric generator from Er0.1Fe1.9SbGe0.4 thin film.* Nuclear Instruments & Methods in Physics Research Section B-Beam Interactions with Materials and Atoms, 2009. **267**(8-9): p. 1592-1595.
69. Xiao, Z., et al., *MeV Si ion bombardments of thermoelectric BixTe3/Sb2Te3 multilayer thin films for reducing thermal conductivity.* Nuclear Instruments & Methods in Physics Research Section B-Beam Interactions with Materials and Atoms, 2005. **241**(1-4): p. 568-572.
70. Budak, S., et al., *MeV Si ions bombardments effects on thermoelectric properties of SiO2/SiO2 + Ge nanolayers.* Radiation Physics and Chemistry, 2012. **81**(4): p. 410-413.
71. Zheng, B., et al., *Thermoelectric properties of MeV Si ion bombarded Bi2Te3/Sb2Te3 superlattice deposited by magnetron sputtering.* Surface & Coatings Technology, 2009. **203**(17-18): p. 2682-2686.
72. Zaitsev, V.K., et al., *Highly effective Mg2Si1-xSnx thermoelectrics.* Physical Review B, 2006. **74**(4).

73. V. K. Zaitsev, M.I.F., I. S. Eremin and E. A. Gurieva, *Thermoelectrics Handbook: Macro to Nano-Structured Materials*2005: CRC press, New York.
74. Michael Riffel, J.S., *Mechanically alloyed Mg2Si1-xSnx solid solution as thermoelectric materials*, in *International Conference on Thermoelectrics - ICT*1996.
75. Kieback, B., *Hagen Symposium Reports: Nanostructured PM Materials*, 2010.
76. Jung, J.Y. and I.H. Kim, *Synthesis and Thermoelectric Properties of n-Type Mg2Si.* Electronic Materials Letters, 2010. **6**(4): p. 187-191.
77. T. Kajikawa, K.S., S. Sugihara, M. Ohmori, *Thermoelectric properties of magnesium silicide processed by powdered elements plasma activated sintering method*, in *Thermoelectrics*1997.
78. T. Kajikawa, K.S., *Thermoelectric figure of merit of impurity doped and hot-pressed magnesium silicide elements*, in *Thermoelectrics*1998.
79. Tani, J. and H. Kido, *Thermoelectric properties of bi-doped Mg2Si semiconductors.* Physica B-Condensed Matter, 2005. **364**(1-4): p. 218-224.
80. Akasaka, M., et al., *Non-wetting crystal growth of Mg2Si by vertical Bridgman method and thermoelectric characteristics.* Journal of Crystal Growth, 2007. **304**(1): p. 196-201.
81. Tamura, D., et al., *Melt growth and characterization of Mg2Si bulk crystals.* Thin Solid Films, 2007. **515**(22): p. 8272-8276.
82. R. M. Ware, B.S., A.R.I.C., and D. J. McNeill, B.Sc., A. Inst. P., *Iron disilicide as a thermoelectric generator material*, in *Electrical Engineers*1964.
83. Starke, U., et al., *Structural and compositional reversible phase transitions on low-index Fe3Si surfaces.* Europhysics Letters, 2001. **56**(6): p. 822-828.
84. Yoshikawa, T., et al., *Thermodynamics of impurity elements in solid silicon.* Journal of Alloys and Compounds, 2010. **490**(1-2): p. 31-41.
85. Kojima, T., I. Nishida, and T. Sakata, *Crystal-Growth of Mn15si26.* Journal of Crystal Growth, 1979. **47**(4): p. 589-592.
86. Higgins, J.M., et al., *Higher manganese silicide nanowires of Nowotny chimney ladder phase.* J Am Chem Soc, 2008. **130**(47): p. 16086-94.
87. Jeitschko, W. and D. Braun, *Lafe4p12 with Filled Coas3-Type Structure and Isotypic Lanthanoid-Transition Metal Polyphosphides.* Acta Crystallographica Section B-Structural Science, 1977. **33**(Nov): p. 3401-3406.
88. Lutz, H.D. and G. Kliche, *Lattice Vibration-Spectra .26. Far-Infrared Spectra of the Ternary Skutterudites Cop3-Xasx, Coas3-Xsbx, and Mge1.5y1.5 (M=Co,Rh,Ir, Y=S,Se).* Journal of Solid State Chemistry, 1981. **40**(1): p. 64-68.
89. Borshchevsky, A.C., T.; Fleurial, J.-P., *Solid solution formation: improving the thermoelectric properties of skutterudites*, in *Thermoelectrics*1996.
90. Sharp, J.W., et al., *Thermoelectric Properties of Cosb3 and Related Alloys.* Journal of Applied Physics, 1995. **78**(2): p. 1013-1018.
91. Chen, L.D.T., X.F.; Kawahara, T.; Dyck, J.S., *Multi-filling approach for the improvement of thermoelectric properties of skutterudites*, in *Thermoelectrics*2001.
92. Rowe, D.M.K., V.L.; Kuznetsova, L.A., *Thermoelectric properties of the Ce1-xLnxFe4Sb12 (Ln=rare earth) skutterudites*, in *Thermoelectrics*1998.
93. Berardan, D., et al., *Chemical properties and thermopower of the new series of skutterudite Ce1-pYbpFe4Sb12.* Journal of Alloys and Compounds, 2003. **351**(1-2): p. 18-23.
94. Giri, R.Y., N.; Sekine, C.; Shirotani, I., *La doping effect in thermoelectric properties of skutterudite compound CeRu4P12*, in *Thermoelectrics*2002.
95. Sharp, J.W., Poon, S.J. and Goldsmid, H.J., *Boundary scattering of phonons: a new approach.*, in *Thermoelectrics*2000.

96. Bertini, L., et al., *Nanostructured Co1-xNixSb3 skutterudites: Synthesis, thermoelectric properties, and theoretical modeling.* Journal of Applied Physics, 2003. **93**(1): p. 438-447.
97. Kumari, L., et al., *Solvothermal Synthesis, Structure and Optical Property of Nanosized CoSb3 Skutterudite.* Nanoscale Research Letters, 2010. **5**(10): p. 1698-1705.
98. Terasaki, I., Y. Sasago, and K. Uchinokura, *Large thermoelectric power in NaCo2O4 single crystals.* Physical Review B, 1997. **56**(20): p. 12685-12687.
99. Funahashi, R., et al., *An oxide single crystal with high thermoelectric performance in air.* Japanese Journal of Applied Physics Part 2-Letters, 2000. **39**(11B): p. L1127-L1129.
100. Ohtaki, M., Nojiri, Y., and Maeda, E.,, *Improved thermoelectric performance of sintered NaCo2O4with enhanced 2-dimensional microstructure*, in *International conference on Thermoelectrics*2000.
101. Shin, W. and N. Murayama, *Thermoelectric properties of (Bi,Pb)-Sr-Co-O oxide.* Journal of Materials Research, 2000. **15**(2): p. 382-386.
102. Miyazaki, Y., et al., *Low-temperature thermoelectric properties of the composite crystal [Ca2CoO3.34](0.614)[CoO2].* Japanese Journal of Applied Physics Part 2-Letters, 2000. **39**(6A): p. L531-L533.
103. Ohtaki, M., et al., *High-temperature thermoelectric properties of (Zn1-xAlx)O.* Journal of Applied Physics, 1996. **79**(3): p. 1816-1818.
104. Ohta, H., W.S. Seo, and K. Koumoto, *Thermoelectric properties of homologous compounds in the ZnO-In2O3 system.* Journal of the American Ceramic Society, 1996. **79**(8): p. 2193-2196.
105. Isobe, S., et al., *Thermoelectric performance of yttrium-substituted (ZnO)(5)In2O3 improved through ceramic texturing.* Japanese Journal of Applied Physics Part 1-Regular Papers Short Notes & Review Papers, 2002. **41**(2A): p. 731-732.
106. Malochkin, O., W.S. Se, and K. Koumoto, *Thermoelectric properties of (ZnO)(5)In2O3 single crystal grown by a flux method.* Japanese Journal of Applied Physics Part 2-Letters, 2004. **43**(2A): p. L194-L196.
107. Koumoto, K., *A challenge to create novel oxide thermoelectrics.*, in *International conference on Thermoelectrics*2004.
108. Theodore J. Abraham, D.R.M.a.J.M.P., *High Seebeck coefficient redox ionic liquid electrolytes for thermal energy harvesting.* Energy & Environmental Science, 2013.
109. Metco, S., *An Introduction to Thermal Spary.*
110. Hall, A., et al., *The Effect of Torch Hardware on Particle Temperature and Particle Velocity Distributions in the Powder Flame Spray Process.* Journal of Thermal Spray Technology, 2010. **19**(4): p. 824-827.
111. Bradley, E.L. and S.D. Stoddard, *A Flame Spray and Arc Spray Powder Feeder for Ultra-Fine Materials.* American Ceramic Society Bulletin, 1965. **44**(9): p. 730-&.
112. Kharlamov, Y.A., *Mechanism of Plastic-Deformation in Formation of Flame Spray Coatings.* Soviet Powder Metallurgy and Metal Ceramics, 1988. **27**(12): p. 947-952.
113. Mcgeary, T.C., *Spray Coatings by Detonation Gun and Plasma Devices.* American Ceramic Society Bulletin, 1965. **44**(8): p. 629-&.
114. Vinayo, M.E., et al., *Plasma Sprayed Wc-Co Coatings - Influence of Spray Conditions (Atmospheric and Low-Pressure Plasma Spraying) on the Crystal-Structure, Porosity, and Hardness.* Journal of Vacuum Science & Technology a-Vacuum Surfaces and Films, 1985. **3**(6): p. 2483-2489.
115. Gruner, H., *Vacuum Plasma Spray Quality-Control.* Thin Solid Films, 1984. **118**(4): p. 409-420.
116. Parker, D.W. and G.L. Kutner, *Hvof-Spray Technology Poised for Growth.* Advanced Materials & Processes, 1991. **139**(4): p. 68-&.

117. Karthikeyan, J., *Cold spray technology.* Advanced Materials & Processes, 2005. **163**(3): p. 33-35.
118. Wolfers, F., *The diffusion of X-rays and Bragg's law.* Comptes Rendus Hebdomadaires Des Seances De L Academie Des Sciences, 1923. **177**: p. 759-762.
119. *CRAIN'S PETROPHYSICAL HANDBOOK*.
120. Hurley, J.P., Dagragna.Vl, and Mathiese.Jm, *Energy-Dispersive X-Ray Spectroscopy.* Research-Development, 1970. **21**(12): p. 14-&.
121. *Laser flash technique measures thermal conductivity.* Insight, 1996. **38**(4): p. 278-278.
122. Kodaira, T. *Present Status of PIE Techniques in Tokai Hot Cell Facilities*. in *The 5th Asia Symposium on Research Reactors*. 1996.
123. Parker, W.J., et al., *Flash Method of Determining Thermal Diffusivity, Heat Capacity, and Thermal Conductivity.* Journal of Applied Physics, 1961. **32**(9): p. 1679-&.
124. Cowan, R.D., *Pulse Method of Measuring Thermal Diffusivity at High Temperatures.* Journal of Applied Physics, 1963. **34**(4): p. 926-&.
125. *Jandel Multiheight Probe Instructions*.
126. F.M.Smith, *Measurement of Sheet Resisitivities with the Four-Point Probe.* The Bell System Technical Jounal, 1958. **37**: p. 711-718.
127. Hall, E., *On a New Action of the Magnet on Electric Currents.* American Journal of Mathematics, 1879.
128. Biji, H.J.v.d. *Theory and Operating Characteristics of the Themionic Amplifier*. in *Institute of Radio Engineers*. 1919.
129. Technologies, M., *Seebeck Effect Software MMR-Tech.*
130. Chi, W.G., S. Sampath, and H. Wang, *Microstructure-thermal conductivity relationships for plasma-sprayed yttria-stabilized zirconia coatings.* Journal of the American Ceramic Society, 2008. **91**(8): p. 2636-2645.
131. Hu, Y.F., et al., *Thermoelectric properties and microstructure of c-axis-oriented Ca3Co4O9 thin films on glass substrates.* Applied Physics Letters, 2005. **87**(17).
132. Padture, N.P., M. Gell, and E.H. Jordan, *Materials science - Thermal barrier coatings for gas-turbine engine applications.* Science, 2002. **296**(5566): p. 280-284.
133. Pawlowski, L., *The science and engineering of thermal spray coatings*2008.
134. Arora, N.D.H., J. R. Roulston, D. J., *Electron and hole mobilities in silicon as a function of concentration and temperature.* IEEE Transaction on Electron Devices, 1982. **29**(2): p. 292-295.
135. Seliuta, D., et al., *Terahertz sensing with carbon nanotube layers coated on silica fibers: Carrier transport versus nanoantenna effects.* Applied Physics Letters, 2010. **97**(7).
136. Cahill, D.G., *Thermal-Conductivity Measurement from 30-K to 750-K - the 3-Omega Method.* Review of Scientific Instruments, 1990. **61**(2): p. 802-808.
137. Cahill, D.G., *Thermal conductivity measurement from 30 to 750 K: The 3 omega method (vol 61, pg 802, 1990).* Review of Scientific Instruments, 2002. **73**(10): p. 3701-3701.
138. Lee, S.M., D.G. Cahill, and T.H. Allen, *Thermal-Conductivity of Sputtered Oxide-Films.* Physical Review B, 1995. **52**(1): p. 253-257.
139. Bonsor, K. *How Black Boxes Work*. 2001; Available from: http://science.howstuffworks.com/transport/flight/modern/black-box.htm.
140. Houssay, L.P., *Robotics and radiation hardening in the nuclear industry*, 2000, University of Florida: Gainesville, FL. p. 3.
141. Mitchell, G.R.K.a.P.V., *Radiation Effects of Thermoelectric Materials*, 1961, Westinghouse Electric Corp., Atomic Power Dept.: Pittsburgh,PA.

142. Venkatasubramanian, R., et al., *Low-temperature organometallic epitaxy and its application to superlattice structures in thermoelectrics.* Applied Physics Letters, 1999. **75**(8): p. 1104-1106.
143. H.Scherrer and S. Scherrer, *CRC Handbook of Thermoelectrics*, in *CRC Press*, D.M. Rowe, Editor 1995: Boca Raton, FL.